

Regional Mapping of the Crustal Structure in Southern California

Thesis by
Zhimei Yan

In Partial Fulfillment of the Requirements
for the Degree of
Doctor of Philosophy



California Institute of Technology
Pasadena, California

2007
(Defended June 5, 2006)

© 2007

Zhimei Yan

All Rights Reserved

To My Parents

Acknowledgements

First, I would like to thank my thesis advisor, Robert Clayton, for his continual support, guidance, and encouragement. For these past six years, I have drawn a lot of comfort and pleasure from his patience, encouragements, and his valuable input about scientific issues. Without him, I may have been able to come this far, but it might not have been such a pleasant experience. I would also like to thank the friendly atmosphere of the lab maintained by the faculty, staff and students. It makes me feel strong to know that there is always someone out there who is willing and able to provide some insights about the problems that I meet in my research. Through the years, I have benefitted a lot through the discussions about the geology and tectonic problems of Southern California with Professor Saleeby and Wernicke, about seismological issues with Professor Kanamori, Helmberger, and colleagues, including Jascha Polet, Chen Ji, Stone Ni, Brian Savage, Alex Song, Min Chen, and Vala Hjorleifsdottir.

I would like to thank the Resources Seminars and Brian Savage, Chen Ji, Stone Ni, Jascha Polet, Vala Hjorleifsdottir, Lupei Zhu, Lijie Han, Qinya Liu, Javier Favela, Eh Tan, Daoyuan Sun and Juliette Artru for their generous help with various script writing. I would also like to thank the secretaries - Elisa Loeffen, Viola Carter, Elizabeth Camarena and Evelina Cui for their kind help, and the its staff - Mike Black, and Ken Ou for their help with various computer problems.

I would also like to thank my other thesis committee members - Mark Simons for his assist in choosing courses and his helpful advice of writing down a summary for the papers that I have read, Jason Saleeby for his extensive help in revising the manuscript of the LARSE II refraction paper, Jean-Philippe Avouac for the very informative GE277 seminars, and Don Helmberger for his entertaining way of doing science. I would also like to thank Joann for taking me along on an amazing geophysical cruise crossing the Atlantic Ocean and the short visit to the two countries that I had never dreamed of - South Africa and Chile.

I would like say thanks to all my officemates - Javier, Brian, Nathan, Rowena, Daoyuan, Qinya, Sarah, Sonja and Ting for their company and the fun they brought to the office. I would

like to say special thanks to Javier, Brian, Chen, Stone, Anu and Leo for their warm welcome when I started my graduate life at SeismoLab.

I would like thank my apartmentmates Min, Debbie, and Yizhen for their company, their kind help and for the joy they brought to my life. I enjoyed sharing an apartment with each of you and have learned something from each of you! I would also like to thank Rebecca Flowers for sharing her experience about seeking postdoc and faculty positions.

I have made great friends during my graduate life. Many thanks to Chen Ji and Min Li, Jiao Lin and Yayun Liu, Daoyuan Sun and Min Chen, Kaiwen Xia and Fengrui, Stone Ni and Dongdong, Jing Liu and Lingsen, Junjun and Linfen, Huiyu, Weijun and Hua for their support, encouragement, and for being there when I needed them. I would like to thank my great old friends from high school and college - Jinyu Piao, Bailing Shen , Lilia, Daming Wang, and Xuan Zhang for always being there to hear me complain, share my joy and remind me how lucky I am.

I would also like to thank CaltechC. It is like a big family in CaltechC. I enjoyed the mutual help among C members, and the various activities organized by C. I would like to thank my hiking friends - Yizhen, Weijun, Xiaoliang and Min Tao for the fun we shared and the support we offered when conquering the high mountains. I would also like to thank my loyal badminton partner, Yaru Hsu, for all the practices and the fun. I would also like to thank Wen Chen, Jiao Lin and Xiaolan Hu for their coaching in badminton.

Last but definitely not least, I would like to thank my parents for their most passionate support of my pursuit for higher and better education. They have been with me through thick and thin with their timeless love and unfailing encouragement. I would also like to thank my brother and two sisters for their continual support, trust, encouragements and their being there for my parents all the time. They have been very dependable supporters. I owe my family the deepest thankfulness.

Abstract

This thesis presents a study of the lateral variations of the crustal structure in Southern California from the waveform data recorded by the Southern California Seismic Network (SCSN) stations, the LARSE I and II surveys. The Receiver Function method is used to process the teleseismic waveform data to image the lateral variations of the crustal structure. A first arrival analysis of the LARSE II refraction data is used to determine the upper crustal velocity structure (less than 4 km).

A 2-D upper crustal structure with seven steeply dipping faults was constructed from the LARSE II seismic refraction survey. A new method was developed to identify faults from the densely distributed receivers and sources on the profile. Typical velocity values of 2.2–2.3 km/s, 3.7–4.3 km/s, and 6.0 km/s are observed for the Pliocene to recent sediments, upper plate basement granitic and gneissic crystalline rocks, and the lower plate Pelona schist (Rand schist) respectively. The regional upper plate complexes of the granitic and gneissic crystalline rocks are observed to yield consistently anomalous low seismic velocities of 3.7–4.3 km/s as compared with the expected velocities for the constituent rock types, which is inferred to result from the extreme shearing, brittle fracturing and related retrogressive hydration reactions during and after the Laramide flat subduction of the Farallon plate. The faults were identified from distinctive features in the first arrival data and they correlate very well with geologically mapped faults, which include the Pelona fault, the San Francisquito Fault, the Clearwater Fault and the San Andreas Fault and two buried normal faults in the west Antelope basin.

Lateral variations of the crustal structure in Southern California are imaged from the back-azimuthal-grouped receiver functions (RFs) of the SCSN stations and the LARSE I, II passive stations. Large rapid variations in the crust are commonly observed beneath the San Gabriel Mountains (SGM), the western Peninsula Ranges (WPR), and the eastern Mojave Desert (EMD), such as the transition from 2-layered crustal structure to 3-layered from the eastern to the western SGM, and the large offsets among the different back-azimuthal groups of several stations. Deep Moho of 34–39 km is observed beneath the western Peninsula Ranges,

Sierra Nevada and the San Bernardino Mountains and no regional, but local deep Moho exists beneath the SGM. Shallow and relatively flat Moho of 28-30 km is observed beneath the western Mojave Desert (WMD) and the Coso geothermal area in the southern Sierra Nevada. Large difference in the crustal structure is observed between the western and the eastern Mojave Desert. Moho is relatively simple and flat beneath the WMD, but is more complicated beneath the EMD. Two stations (DAN and LDF) in the EMD show very anomalous receiver functions and a Moho step of 8–10 km is inferred between the NW and SE group of station DAN.

Synthetic waveform modeling of the anomalous features in the RFs for two stations (TA2 and BFS) in the eastern San Gabriel Mountains indicates the existence of a flat-topped notch structure on the Moho. Moho is inferred to get shallowed from 37–39 km north of the San Andreas Fault, 33–35 km south of the San Gabriel Fault to a depth of ~ 29 km beneath the Mt. Baldy block.

Contents

Acknowledgements	iv
Abstract	vi
1 Introduction	1
2 Seismic Refraction Evidence for Steep Faults Cutting Highly Attenuated Continental Basement in the Central Transverse Ranges, California	4
2.1 Introduction	6
2.2 Analysis of the Refraction Data	9
2.3 Correlation of Seismic and Geologic Structure	18
2.4 Conclusions	28
3 Regional Mapping of Crustal Structure in Southern California from Receiver Functions	32
3.1 Introduction	34
3.2 Data and Analysis	36
3.3 Results	43
3.3.1 Southern Sierra Nevada and Walker Lane Belt	43
3.3.2 Peninsula Range and the Salton Sea	46
3.3.3 Mojave Desert and San Bernardino Mountains	47
3.3.4 San Gabriel Mountains	54
3.4 Discussion	60
3.5 Conclusions	64
4 A Notch Structure on the Moho beneath the Eastern San Gabriel Mountains	67
4.1 Introduction	68

4.2	Data	70
4.3	Synthetic Models	77
4.4	Discussion	80
4.5	Conclusions	83
5	Conclusion	84
A	Effect of Faults on First Arrivals	87
B	Receiver Functions for Individual Stations in the San Gabriel Mountains	93
C	Receiver Functions for Stations across the Salton Trough	101
C.1	Asymmetric Extension of the Salton Trough	101
C.2	RFs for Station JCS and Nearby Stations	102
D	Anomalous Receiver Functions for Stations in the Mojave Desert and Sierra Nevada	107
D.1	Mojave Desert Stations	107
D.2	Sierra Nevada Stations	111
E	Moho Depth and Vp/Vs Ratio for the Regional RF Study	123

List of Figures

1.1	Distribution of the SCSN stations on the geological map of Southern California	3
2.1	Topographic relief map along the LARSE II line	8
2.2	One typical shot gather (# 8411) in the study area	10
2.3	First arrivals for a sequence of shot gathers	10
2.4	Synthetic wavefield of two shots for a faulted structure	12
2.5	Typical synthetic first arrivals for a sequence of shots gathers for a faulted structure	13
2.6	Observed first arrivals of some representative shot gathers	14
2.7	Comparison of synthetic first arrivals from the preliminary model with data	16
2.8	Comparison of synthetic first arrivals from the refined model with data	17
2.9	Synthetic first arrivals of the best fitting model for the real data	19
2.10	Comparison of the shallow crustal seismic velocity model with a geologic cross-section	21
3.1	Station map for the regional RF study	35
3.2	Events map for the regional RF study	38
3.3	Receiver functions for station VCS	39
3.4	Exmaple of unsuccessful stacking—SW group of VCS	41
3.5	Example of successful stacking—NW group of PAS	42
3.6	Regional Moho depth map	44
3.7	RF profile across the southern Sierra Nevada and Walker Lane Belt	46
3.8	RF profile across the western Peninsula Ranges and Salton Trough	47
3.9	Station and Moho piercing points map in the Mojave Desert	48
3.10	RFs along the three west-east profiles in the Mojave Desert	49
3.11	RFs along the two south-north profiles in the Mojave Desert	51
3.12	Correlations of the stations showing anomalous RFs with a 2-D kinematic model in the Mojave Desert	53

3.13	Station and Moho piercing point map in the San Gabriel Mountains	54
3.14	RFs along the four south-north profiles in the San Gabriel Mountains	55
3.15	RF profiles for the SE and SW group of the LARSE II	58
3.16	Radial and tangential RFs for station MWC indicating the existence of a SW dipping velocity-decrease interface	59
3.17	Correlation of the subsurface structure with the terrane distribution in the San Gabriel Mountains	61
4.1	Topographic and revised geologic maps for the San Gabriel Mountains	69
4.2	Radial RFs for station TA2 showing a large offset across SAF	71
4.3	NW RF group of station BFS showing variation of the RFs with ray parameter	73
4.4	Synthetic RFs for a wedge-inserted model	74
4.5	RF profiles along the LARSE I and the SCSN lines and two representative stacking groups	75
4.6	Summary of the data	77
4.7	Synthetic RFs for a notch and a step model	78
4.8	Geometries of four different models	79
4.9	Synthetic receiver functions for the four models	80
4.10	Alignment of the shallow Moho with the Mt. Baldy block	82
5.1	Complete Bouguer gravity anomaly for the study area	86
A.1	Synthetic first arrivals for normal and thrust faults	89
A.2	Amplitude comparison of the segment F2 for a normal and a thrust faulted structure	92
B.1	Radial and tangential RFs for station CHF	94
B.2	Radial and tangential RFs for station MWC	95
B.3	Radial and tangential RFs for station BFS	96
B.4	Radial and tangential RFs for station TA2	97
B.5	Radial and tangential RFs for station PDU	98
B.6	Radial and tangential RFs for station BTP	99
B.7	Radial and tangential RFs for station PAS	100
C.1	Distribution of the SCSN stations on a geological map in the Peninsula Ranges	102

C.2	RF profiles in the Peninsula Ranges	103
C.3	Radial and tangential RFs for station JCS	105
C.4	Radial RFs for station DPP and JCS	106
D.1	Radial and tangential RFs for station DAN	108
D.2	Stacking of the SE group for station DAN	109
D.3	Stacking of the NW group for station DAN	110
D.4	Radial and tangential RFs for station LDF	112
D.5	Stacking of the NW group for station LDF	113
D.6	Stacking of the SE group for station LDF	114
D.7	Radial and tangential RFs for station ISA	115
D.8	Radial and tangential RFs for station WBS	116
D.9	Radial and tangential RFs for station FUR	118
D.10	Stacking of the SE group for station FUR	119
D.11	Stacking of the SW group for station FUR	120
D.12	Radial and tangential RFs for station CGO	121
D.13	Radial and tangential RFs for station CWC	122
E.1	Vp/Vs ratios for the station groups in Figure 3.6	124

List of Tables

E.1	Moho depth for the station groups from RF study	125
-----	---	-----

Chapter 1

Introduction

The degree to which the continental crust/lithosphere is involved during large-scale deformation, as well as the strength of the crust/lithosphere, is of fundamental importance in geodynamics. The current crustal structure is a key to its past role. By studying the current crustal structure, important insights and constraints can be gained for the above questions. The main focus of this thesis is to study the lateral variations of the crustal structure in Southern California.

Southern California is a tectonically very unique area since it records the transition of the plate boundary from an Andean-type convergent system between the Farallon plate and the North America plate, to the current San Andreas Fault strike-slip system between the Pacific plate and the North America plate at ~ 30 Ma. Segmentation of the Farallon slab at Laramide time (~ 70 Ma) is proposed by Saleeby (2003). Flat shallow subduction is inferred for a segment corresponding to the restored Salina-Mojave Desert block and steep subduction for the Sierra Nevada segment to the north and the Peninsula Ranges to the south. Due to the difference in the slab geometry, response of the upper plate to the subduction in the corresponding regions differs—lithosphere beneath the greater Sierra Nevada batholith and the Peninsula Ranges remains relatively intact, while the overlain batholithic crust was strongly deformed and disrupted for the Salina and Mojave Desert blocks. Thick layers of the lower plate Pelona Schist formed as a result of the flat subduction beneath the Salina and Mojave Desert block and were subsequently uplifted and exposed on the surface.

Due to the transition in the plate boundary, the stress field in Southern California changed accordingly (from mainly compression to transtension), which results in a dramatic change in the deformation styles of the continental crust in North America. Extension in the Basin and Range, formation of the San Andreas Fault strike-slip system, opening of the Gulf of California and extension in the Borderland occurred as a result. During these dominant extensional deformation events, upper crust in some areas, such as the Basin and Range, and the Mojave

Desert, was highly extended and disrupted, while some blocks, such as the Great Valley and Sierra Nevada, and the western Peninsula Ranges, remain almost intact (Figure 1.1). Thus, the contrast in the continental deformation in different sub-provinces provides a very good natural laboratory to study the response of continental crust to large-scale deformation and the involvement of the lower crust in the observed upper crustal deformations.

In this thesis, the receiver function method is applied to the densely distributed SCSN stations (Figure 1.1) to study the lateral variation of the crustal structure in Southern California. Moho depth variations among different provinces, as well as the variations of the mid-crustal interfaces within the central Transverse Ranges and the Mojave Desert are investigated. Generally, deep Moho is observed in the relatively undeformed western Peninsula Ranges block (WPR), western Sierra Nevada (SN) and the San Bernardino Mountains. Relatively shallow Moho is observed in the western Mojave Desert and the Coso Geothermal area in the Walker Lane belt (Figure 3.6). The shallowest Moho is observed in the currently extending Salton Trough and the southern extension of the Death Valley Fault Zone in the Mojave Desert. Thus, the overall large-scale Moho depth variation supports the strong coupling between the upper and lower crust, especially from the deep Moho for the relatively intact SN and WPR blocks and their relatively sharp transition to the shallow Moho in the nearby highly extended domains. Exceptions to this pattern, however, are observed in several station groups in the highly extended Walker Lane belt where a deep Moho of 36–39 km is obtained (Appendix D) indicating some decoupling between the upper and lower crust.

Strong attenuation of the upper crust in the central Transverse Ranges and the western Mojave Desert is evident from the LARSE II refraction study (Chapter 2), where a 2-D upper crustal structure (≤ 4 km) is constructed and consistently anomalous low velocities of 3.7–4.3 km/s are observed for the upper plate granitic and gneissic crystalline rocks.

A case study of refining models of 2-D structure by synthetic waveform modeling of variations of the receiver functions with back azimuth and ray parameter is presented in Chapter 4, where a notch structure on the Moho is inferred for the Mt. Baldy block, which is bounded by the San Andreas Fault on the north and the San Gabriel Fault on the south.

Large difference in the Pms arrivals is observed at several neighboring stations and among the different back azimuthal groups of some stations. Details of the receiver functions for these station groups are presented in the appendixes.

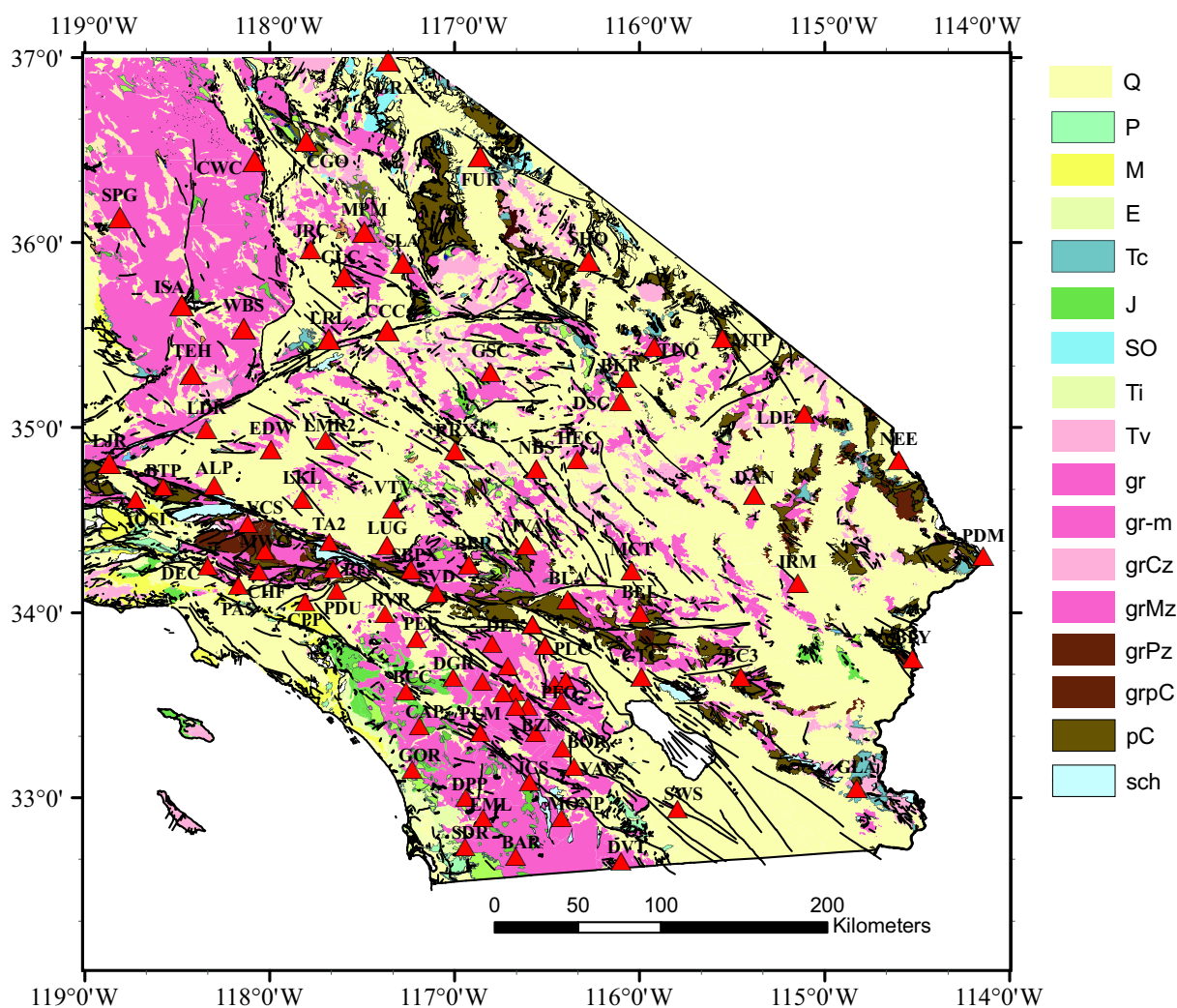


Figure 1.1 Geological map of Southern California with hard-rock SCSN stations marked. Colors represent the rock types and the red triangles are the SCSN stations along with their names. Q, P, M, E, Tc are Cenozoic sedimentary rocks. J and SO are Mesozoic and Paleozoic sedimentary rocks; Ti and Tv are Tertiary intrusive and volcanic flow rocks; gr, gr-m, grCz, grMz, grPz, and grPc are granitic rocks of different ages; pC is precambrian igneous and metamorphic rocks; sch is the lower plate schist of various types and ages.

Chapter 2

Seismic Refraction Evidence for Steep Faults Cutting Highly Attenuated Continental Basement in the Central Transverse Ranges, California

Abstract

A 2-D upper crustal structural profile with seven steeply dipping faults was constructed from the LARSE II seismic refraction data recorded over the north central Transverse Ranges and adjacent Mojave Desert in southern California. The profile extends to a depth of about 4 km. The faults were identified from distinctive features in the seismic first arrival data, while the velocity structure was determined from travel times and refined by forward modelling. The resulting seismic velocity structure is correlative to the geologic structure along the profile, and is used to help constrain a geologic cross-section. Six of the seven faults detected from the seismic data correspond directly to geologically mapped faults in the central Transverse Ranges and adjacent Mojave Desert. From south to north, they are the Pelona fault, the San Francisquito fault, the Clearwater fault, the San Andreas Fault, and two faults that cut the Portal Ridge. The seventh fault is buried beneath Quaternary deposits of the western Mojave Desert, and appears to correlate with an additional fault that cuts Portal Ridge out of the section line. The southernmost fault (the Pelona fault) separates the younger Vasquez formation on the south, from the Pelona schist on the north and is determined to be an intermediate (40° – 60°) south-dipping normal fault. This coupled with field observations indicate that the Pelona fault was instrumental in the late Oligocene–early Miocene formation of the Soledad basin, and the structural ascent and exhumation of the Pelona schist along the proto-Sierra Pelona intra-basin ridge. Analogous Neogene extensional deformation is found to have affected the western Mojave Desert region, where faults 6 and 7 appear to have had north side down normal

displacement, and to have been instrumental in forming the western Antelope basin. A 6.0 km/sec basal layer to our shallow seismic structure is correlated with the Pelona schist south of the San Andreas Fault, and to the tectonically related Rand schist beneath the western Mojave Desert. Granitic and gneissic crystalline rocks, which form regional upper plate complexes along the Vincent thrust above the Pelona schist, and along the Rand thrust above the Rand schist, yield consistently low seismic velocities as compared to the expected velocities for the constituent rock types. These anomalous velocities are reconciled by the degraded structural and textural state of the upper plate crystalline rocks that resulted from extreme shearing, brittle fracturing and related retrogressive hydration reactions starting during or shortly after the latest Cretaceous–early Paleocene underthrusting of the schists. Extension, translation along the San Andreas transform system, and compressional faulting with the uplift of the Transverse Ranges further accentuated the basement deformations. The integrated result is that the survival of the Precambrian through Mesozoic granitic crust of the region became a rootless and highly attenuated upper crustal layer.

2.1 Introduction

The Transverse Ranges of Southern California is a structurally complex region that records a protracted history of interactions between the North America plate edge and the Farallon plate and subsequently with the East Pacific Rise with the demise of the Farallon plate [Atwater and Severinghaus 1989; Atwater 1989; Atwater and Stock 1998; Crouch and Suppe 1993; Dickinson 1981, 1996; Jacobson et al. 1996; Nicholson et al. 1994; Ingersoll and Rumelhart 1999]. The pre-Cenozoic basement rocks of the region record the subduction of the Farallon plate along an Andean-type arc-trench system that can be traced continuously from the northern Sierra Nevada to the central Baja California regions [Crouch and Suppe 1993; Saleeby 2003]. Late Cretaceous to Cenozoic rocks of the Transverse Ranges, however, record a uniquely complex tectonic overprinting history on this regionally extensive Andean-type system. The first overprint entailed the latest Cretaceous–early Palaeogene subduction of a shallow segment of the Farallon plate [Saleeby 2003]. This resulted in the shearing off of the sub-continental lithosphere mantle beneath the corresponding segment of the magmatic arc, and the tectonic emplacement of subduction accretion assemblages directly beneath rocks belonging to the axial region of the arc [Jacobson et al. 1996]. These events not only profoundly affected the deep crust–upper mantle regime, but also highly deformed rocks of the magmatic arc, and disrupted depositional patterns of the adjacent fore-arc basin. The early Neogene encroachment of the East Pacific Rise into the southern California plate edge environment instigated yet another disruptive tectonic regime in what was to become the modern Transverse Ranges. Most important are ~ 255 km of right slip on the San Andreas and ~ 60 km on the San Gabriel faults [Dickinson 1981, 1996].

This study focuses on a north-south transect across the north–central Transverse Ranges and adjacent western Mojave Desert. The principal geographic features of the Transverse Ranges that are traversed include the Santa Susana–San Gabriel Mountains transition in the San Fernando pass area, the Santa Clarita Valley and the adjacent westernmost Soledad Basin, the Sierra Pelona, the Liebre and Sawmill Mountain blocks, and the Portal Ridge (Figure 2.1). Basement rocks along this transect are part of the greater San Gabriel Mountains igneous and metamorphic complex of Precambrian and Mesozoic age, and Mesozoic magmatic arc rocks of the western Mojave Desert. Both of these basement complexes record shallow slab segment subduction along the regionally extensive Vincent and Rand thrust systems [Cheadle et al. 1986; Li et al. 1992; Malin et al. 1995; Jacobsen et al. 1996; Fuis et al. 2001; Saleeby, 2003].

These thrust systems placed subduction accretion assemblages of the Pelona and Rand schists beneath Mesozoic magmatic arc rocks and their continental crystalline host rocks during latest Cretaceous–Paleocene time. Scattered remnants of uppermost Cretaceous to mid-Eocene strata of the transect and of adjacent regions record subsidence of the Vincent-Rand thrust complexes to marine conditions in response to extensional collapse of the shallow slab segment orogen [Malin et al. 1995; Saleeby 2003]. In late Eocene through much of Oligocene time the study area sat in the fore-arc region of a diffuse magmatic arc that was well inland of the plate edge environment, which marks the re-establishment of subduction related magmatism in the wake of shallow slab segment subduction [Burchfiel et al. 1992; Saleeby 2003]. Upper Oligocene to mid-Miocene strata of the region record extension and volcanism related to the encroachment of the East Pacific Rise into the plate edge environment [Hendrix and Ingersoll 1987; Dickinson 1981]. By mid-Miocene time significant transrotations began to affect the region as the San Andreas transform system developed [Luyendyk et al. 1980; Luyendyk 1991; Bird and Rosenstock 1984; Hornafius et al. 1986; Humphreys and Hager 1990; Dickinson 1996]. Further evolution of this system involves transpression that deformed and uplifted the Transverse Ranges to their current active state.

The LARSE II transect (Los Angeles Region Seismic Experiment Phase II) extends northward from the Santa Monica Mountains coast, through the Transverse Ranges and western Mojave Desert and into the southernmost Sierra Nevada. It provides a large scale, high-resolution seismic data set across the Transverse Ranges part of the modern plate edge. Along the main line of the survey, over 1000 seismographs were deployed at 100 m spacing, and shot points were spaced approximately 1 km apart (Figure 2.1). The focus of this study is on the segment that runs between San Fernando pass and the western Mojave Desert. In this study, we present the inversion of the upper crustal structure based on first arrivals of a sequence of shots from the Santa Susana Mountains to the western Mojave Desert. Of particular interests are the identification of major faults, and construction of a 2-D velocity structure model. This 2-D structure can be correlated to the first-order structural features that record the geological development of the region. Most importantly, the 2-D seismic structure model resolves several well-mapped faults, which include the Pelona, San Francisquito, Clearwater and San Andreas faults. Each of these faults is known to cut basement and to juxtapose fundamentally different rock types at the Earth's surface. The 2-D structure model places constraints on the geometry of these and

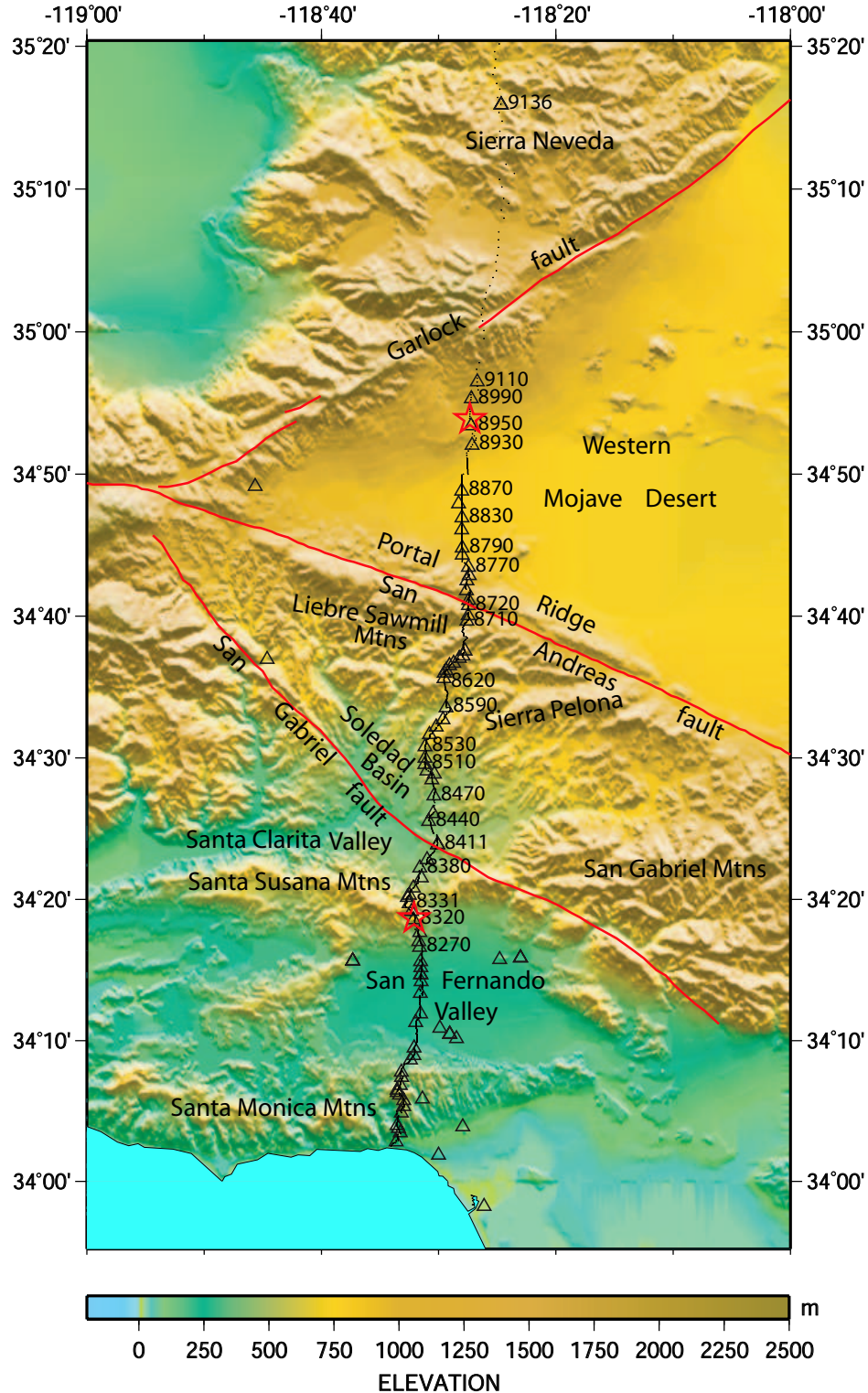


Figure 2.1 Topographic relief in Southern California. Triangles represent shots with shot numbers of several selected shots beside them. Shot numbers generally increase from south to north. Little dots are receivers. Nearly 100 shots and 1400 receivers were deployed along the main line. Two stars represent the end points of the profile in this study.

other recognized faults at depth, as well as on the pre-existing regional structure cut by these steep faults. These constraints are used in the construction of a geologic cross section along the seismic line, which is constructed mainly from published mapping and our own unpublished topical mapping.

2.2 Analysis of the Refraction Data

The first arrivals on the LARSE II survey generally appear as three branches as is evident on a typical shot gather shown in Figure 2.2. The first branch has a velocity of 2.0–2.5 km/s, and is due to a slow sedimentary layer that is prominent in the San Fernando Valley and the Mojave Desert. The second branch is due to broken upper plate basement rocks and Early Neogene to Cretaceous sedimentary rocks and has a velocity around 4.0 km/s. The final segment has a velocity of 6.0 km/s and is the normal mid-crustal velocity in Southern California. Of particular interest in the first arrival data is the reverse branch that is labelled as AB in Figure 2.2. The slope of this segment implies an apparent velocity that is too large to be a reasonable velocity for the study area. This feature is prominent on all south-to-north profiles across the Santa Clarita Valley (see Figure 2.3, shots #8331 to #8520). It is fixed to the same ground point rather than a particular source-receiver offset. On the reverse profile through this region (north to south), the travel time curves all converge to a single 3.5 km/s branch. This velocity is lower than that of the near offset part of shot #8590. These two features are characteristic of an abrupt lateral change in properties that is usually caused by a steep fault. In this case, it is the Pelona Fault that juxtaposes slow Vasquez formation on the south against the fast Pelona Schist on the north.

In order to study the typical signatures that a fault imparts on first arrivals and to provide a method to invert velocity structure from these anomalous first arrivals, a simple faulted two-layered model is examined. Synthetic arrival times from 17 shots were calculated using an acoustic finite difference method. The model and two synthetic seismograms that illustrate the above two features are shown in Figure 2.4. The upper panel shows the synthetics for a shot on the footwall. It shows the prominent negative-slope branch CD similar to AB in the real data (Figure 2.2). This reverse branch exists on all the shots far away from the fault on the footwall (see Figure 2.5). The middle panel shows the synthetics for a shot on the hanging wall. It has an unusual velocity variation pattern, which is closely related to the fault. The apparent

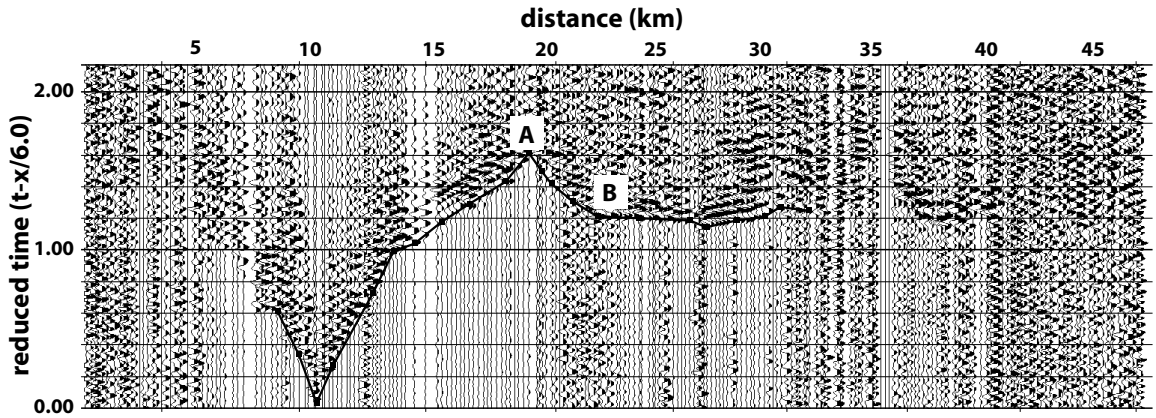


Figure 2.2 One typical shot gather (# 8411) in the study area. Travel times are reduced by 6.0 km/s. Black line is the first arrival picks. The first arrival branch of # 8411 has three normal segments, which have positive or zero slopes. Velocities of the three segments are 2.4 km/s, 4.3 km/s and 6.0 km/s respectively. The unusual thing about this shot gather is the negative slope segment (AB) between the second and third segments, which indicate an apparent velocity too large to be a reasonable true velocity for the study area.

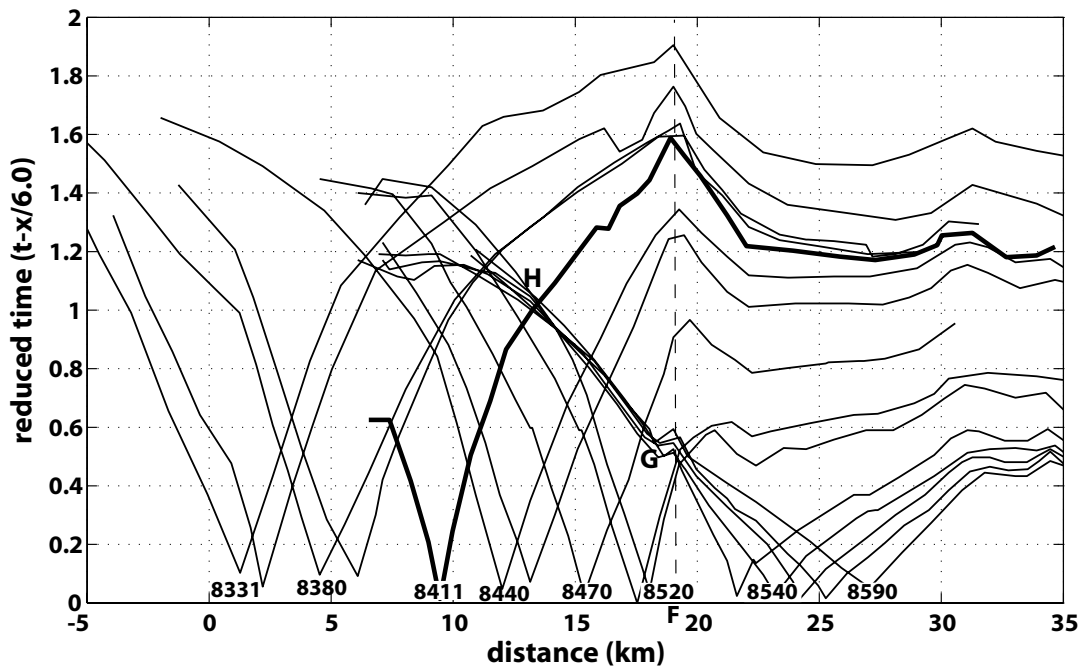


Figure 2.3 First arrivals for a sequence of shot gathers. The heavy solid line represents first arrival picks for the previous shot # 8411. A negative-slope segment exists on every shot south of # 8520, a peak point thus appears and they are almost aligned to the same ground point. For shots north of shot # 8520, first arrivals of their south branches converge to each other to the south of the fault and adopt a similar low velocity (GH). The above two features are both offset independent, but location dependent, indicating the existence of an abrupt lateral velocity change around shot #8520.

velocity changes from 4.0 km/s to 6.0 km/s, then back to 4.0 km/s, and 6.0 km/s. Left branches of the first arrivals for all the shots on the hanging wall (see Figure 2.5) share similar velocity variation patterns and the second 4 km/s branch (unusual low velocity branch) all converge to each other on the footwall side of the fault. This convergent unusual low-velocity branch feature matches the convergent segment labelled as GH in the real data (Figure 2.5). A third feature that a fault imparts on first arrivals is a group of apparent headwave branches like L1, L2, and L3 in Figure 2.5, whose arrival times increase systematically with distance away from the fault. They occur on shots close to the fault on the footwall. Feature F2 exists on the opposite side of the fault from features F1 and F3. These three features are useful in identifying faults from the seismic data and a further explanation of them is given in Appendix A.

Using the three features described above, we identified 6 faults from the central Transverse Ranges and western Mojave Desert portion of the LARSE II line. First arrivals for several selected shots and the identified faults are shown in Figure 2.6. Features related to faults in the real data are not as obvious as that for a single faulted situation because the patterns for neighboring faults interact with each other. However, each fault we identified has its corresponding diagnostic features, with fault 1 having the most obvious features. It has both the negative-slope segments for shots from the south side and the convergent low-velocity segments for shots from the north side, indicating that a large velocity contrast occurs across this fault and low velocity materials accumulated on the south side. Features related to faults 2, 3 and 4 are not obvious due to strong interaction effects, but we can see the systematic increasing “pseudo” head branches related to fault 3 and 4 for shots from south and north side respectively, and the low-velocity segments related to fault 2 and 3. The features indicate that higher velocity material (a shallower interface) exists between fault 3 and 4, while lower velocity material (a deeper interface) is present in the blocks between faults 2 and 3, and between faults 4 and 6. Low velocity segments are obvious on the north side of both fault 6 and 7 in the Mojave Desert, indicating a relative accumulation of low-velocity sediments on the north side of both faults.

In this densely faulted area, a number of the first arrival kinks appear due to lateral velocity variations, so care is needed when using the kinks to estimate thickness of layers. In this study, thickness of layers is assumed to remain almost constant between faults, and the kink points, which are least influenced by lateral velocity variations, are used to estimate the thickness. Usually, the kink point of the farthest shot away from the fault is used. For example, for the

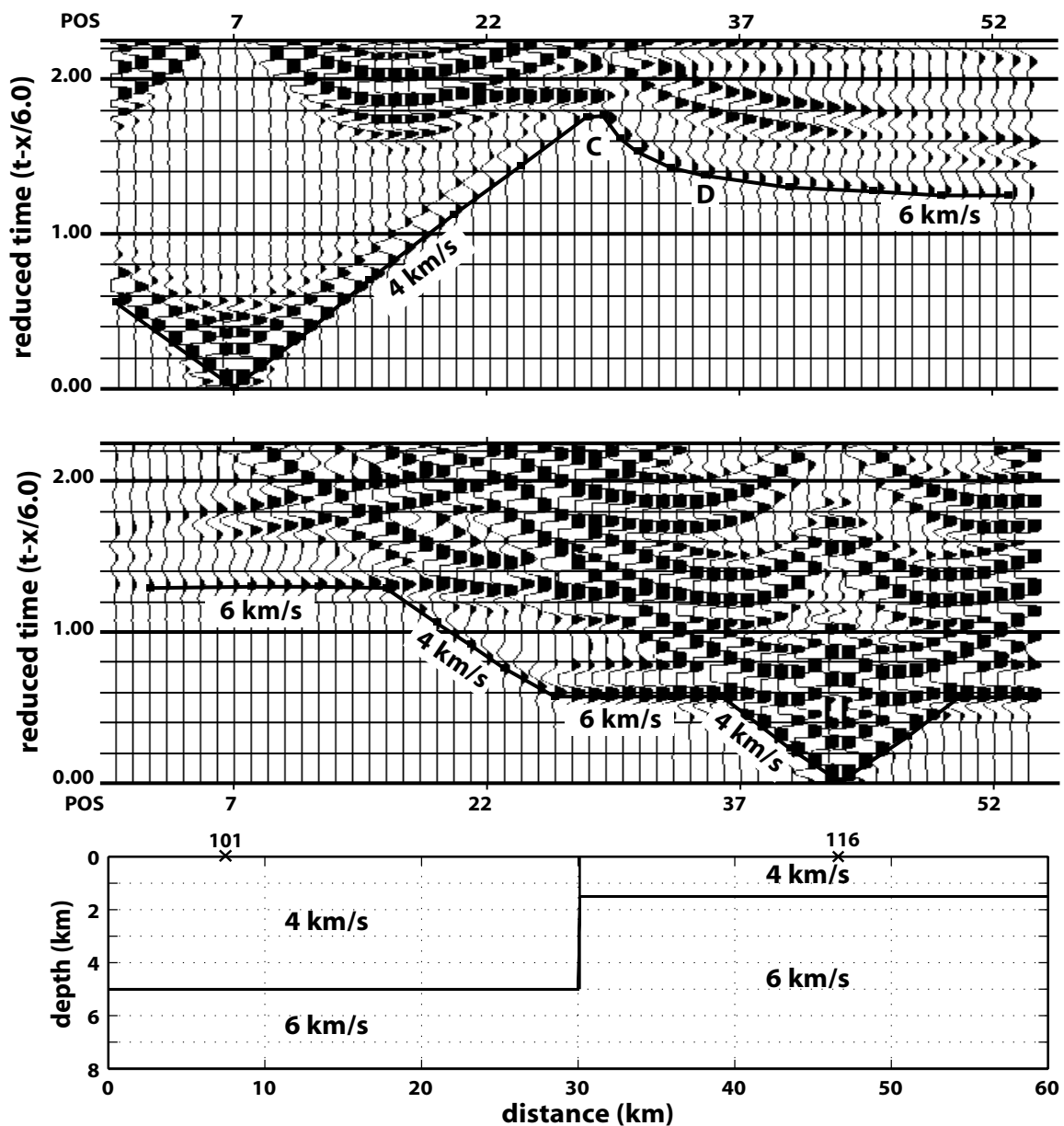


Figure 2.4 A single faulted one-layer over a half space velocity model and two synthetic seismograms for two shots on either side of the fault. Synthetic waveforms were computed using a full waveform finite-difference method. In the bottom panel, x on the top surface of the model represent the two shots. Synthetic seismograms of the two shots are shown in the top and middle panels. The top one is the synthetic seismogram for shot #101, which is on the footwall. The negative-slope segment feature (CD) similar to AB of shot #8411 is observed to the right of the fault. The middle panel is the synthetic seismogram for shot #116, which is on the hanging wall. The unusual low velocity segment (the second 4 km/s segment away from the shot) is observed to the left of the fault.

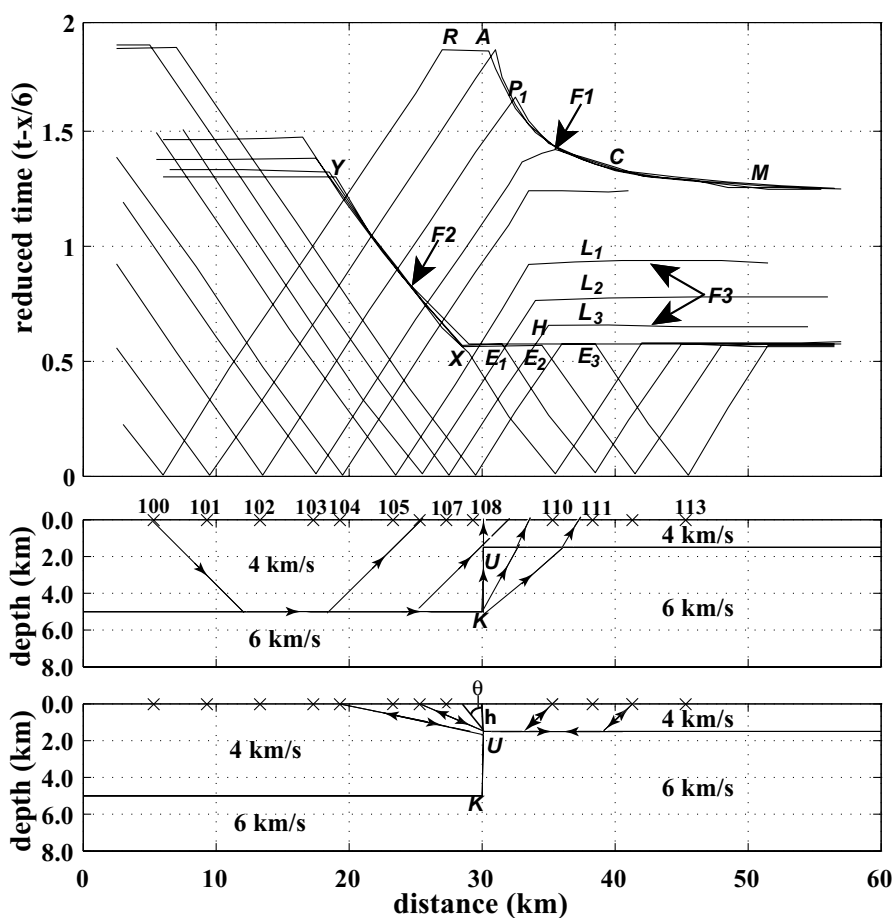


Figure 2.5 Velocity structure and first arrival picks for the single faulted one layer over a half space model. Velocity structure with typical ray paths for the first arrival phases of the three groups of shots is shown in the middle and bottom panels. First arrival picks are shown in the top panel. The first arrivals show three features that are diagnostic of a fault. They are: F1: Negative-slope segments (AC). Time decreases with offset along this segment and a peak point shows up. It exists on shots on the footwall far away from the fault. F2: Convergent unusual low velocity segment (XY). First arrivals of a sequence of shots adopt a similar low velocity and converge to each other along this segment. They exist on shots from the hanging wall. F3: Systematic time-increasing pseudo head wave branches. They exist on shots from the footwall close to the fault (shot #105, #107 and #108). Apparent kink points of these shots are not depth-dependent, but related to the shot distance away from the fault instead. Typical ray paths for shots far away from the fault on the footwall are shown in the middle panel. Note that the rays that first travel along the left interface, then diffract from point K are the rays that produce the negative-slope segments (F1). Hence, the negative-slope segment does not represent a true velocity of the sampled area. In the bottom panel, the rays that first travel along the right interface, then diffract from point U are the rays that appear as convergent low-velocity segments (F2) for shots from the hanging wall. Rays that travel along the same path, but reverse direction, i.e. for shots on the footwall, appear as the systematic time-increasing pseudo head wave branches (F3). Here h is the top layer thickness of the hanging wall. θ is the critical angle.

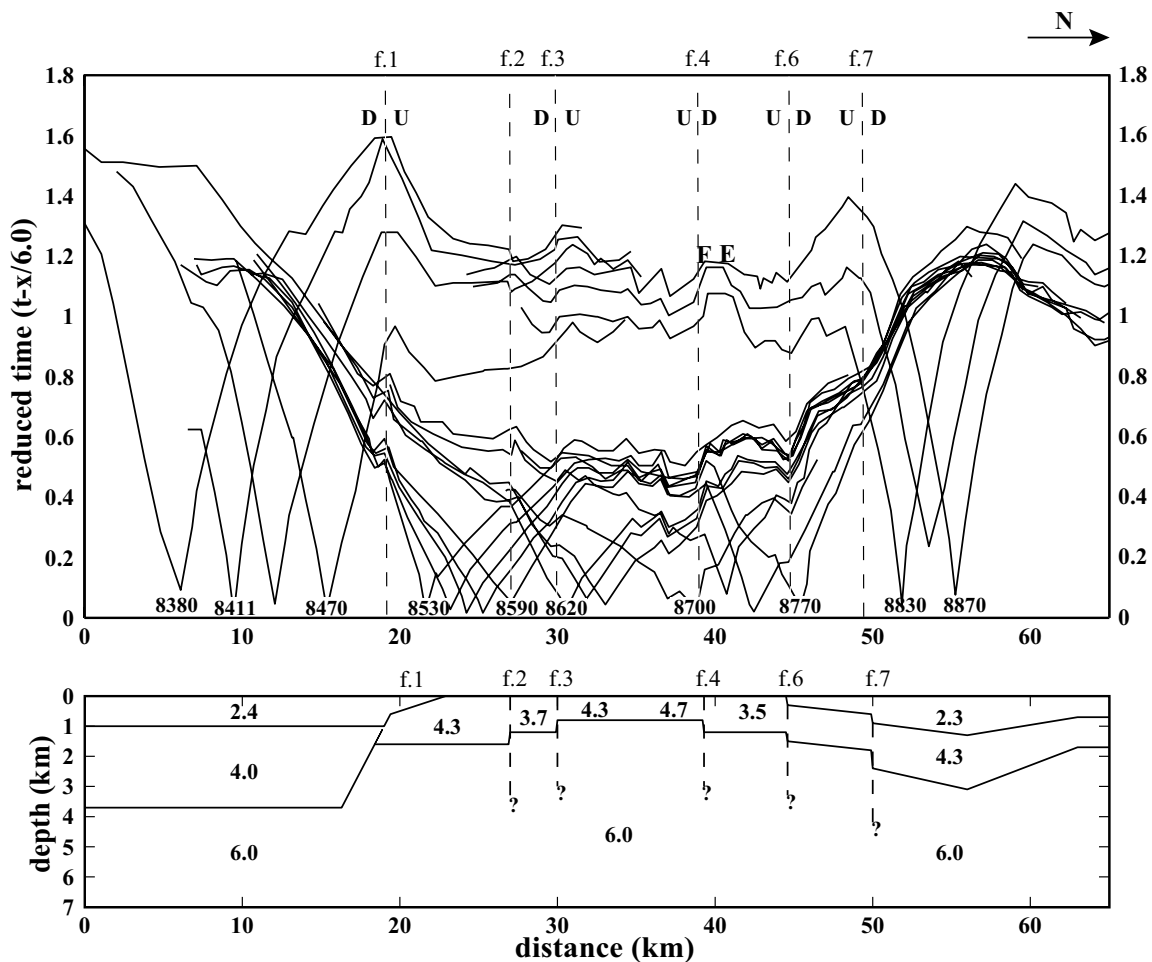


Figure 2.6 The upper panel is the first arrival picks of several selected shots (with shot numbers beneath) for the study area and the bottom panel is the preliminary velocity structure inverted from the first arrival data. Six faults were identified from the three distinctive features in the arrival time data. Each identified fault has its own characteristic features though attributes related to fault 1 are the most prominent. U or D on either side of the faults represents the hanging wall (shallower interface), or the footwall (deeper interface) respectively. Thickness of the velocity layers is estimated from appropriate crossover points under the assumption that thickness of the layers does not change significantly between faults. The dip angle of fault 1 is determined to be around $40^{\circ} - 60^{\circ}$ to the south. A question mark is put beneath each fault because the depth extension is indeterminate.

block south of the fault 1, only the second intercept point of the north branch of shot #8331 is used to calculate the thickness of the second layer. The kink point of the nearest shot to the fault on the footwall is also used to estimate the layer thickness for the hanging wall. For example, the kink point for the north branch of #8590 is used to determine the thickness of the block between faults 2 and 3. The influence of faults on first arrival branches and the rationale behind our kink point selection process are discussed in the Appendix A. The shallow velocities are determined from the near offset part of the first arrival data. The velocity of the second layer is assumed to be 6.0 km/s in the central area. The resulting model is shown in Figure 2.6.

In order to test the validity of this method, arrivals of several shots from the top surface of this velocity structure are computed using an acoustic finite-difference method. The acoustic approximation is used because the data are recorded on vertical seismometers and the sources are explosions, which means that the main energy recorded by the seismometers is P-waves. The finite difference method can handle models of arbitrary complexity. Comparison of the synthetic first arrivals of several selected shots with the observed data for corresponding shots is shown in Figure 2.7. From these, we can see that synthetic first arrivals match the large-scale features of the data at far offsets and compare well with the details of the observed data at near offsets. But, the arrival times at far offset are poorly modelled, which means that we need to further refine the deeper structure.

To further refine the structure by including the far offset part of the data, we find that we need to accurately correct the influence of topography. Topography is relatively flat in the southern and northern parts of the study area, but varies substantially in the central part. The elevation increases by 0.6 km in less than 10 km distance, and the arrival time changes by 0.15-0.3 sec accordingly. The standard static elevation correction does not work well for such rapid variations. To properly account for topography, we added variations in the source and receiver elevations into the finite-difference modelling program. We then refine the model by trial-and-error modelling until the fit of the synthetics to the data is significantly improved. The resulting model and comparison of the synthetic first arrivals with data are shown in Figure 2.8. The major difference between this model and the preliminary one is that we add a second layer with a velocity around 5.0 km/s in the Liebre-Sawmill Mountain block (from 27 to 38 km in Figure 2.8) since all the synthetic first arrivals from farther shots for the preliminary model are faster than the observed data in this area.

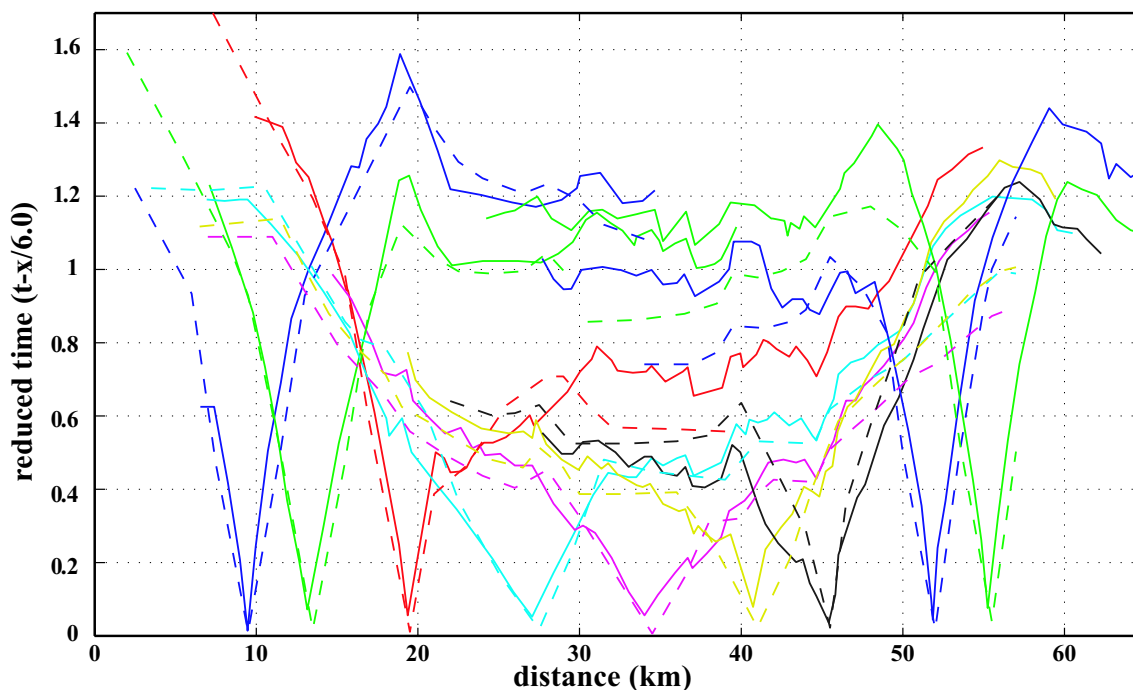


Figure 2.7 Comparison of synthetic first arrivals (dashes) for several shots from the preliminary model in Figure 2.6 with the observed arrivals (solid) of corresponding shots. The synthetics generally fit the data well in the near-offset. Big features similar to the real data show up in the far offset, but arrival times are poorly modelled.

With this further refinement, we find that an additional fault (fault 5) exists to the north of San Andreas Fault and that rocks between these two faults have relatively low velocity. In the area near the San Andreas Fault (around 40 km in Figure 2.6), the first arrivals for several shots from the Mojave Desert are around 0.1 second slower than that in the surrounding area, such as segment EF in the first arrival curve of shot #8830. For shots from the south, such as #8530 to #8590 at distances from 20 to 28 km, first arrivals increase about 0.05 second across this narrow zone. From these features, we deduce that this narrow zone is a low-velocity zone. An additional fault (fault 5) bounds its north boundary. From our simulation, this zone is 2-2.5 km wide and extends to at least 1.5 km deep from the surface. This zone geologically corresponds to a fault sliver between the San Andreas Fault and fault 5. It is associated with movements along the San Andreas Fault and is characterized by highly fractured granitic basement rocks with zones of fault gouge.

In the Sierra Pelona (the block between 20 and 27 km in Figure 2.8), the refracted wave increases in velocity with distance away from the Pelona Fault (from shot #8510 to #8440), so we deduce that velocity increases with depth in this area. A linear gradient of the velocity from

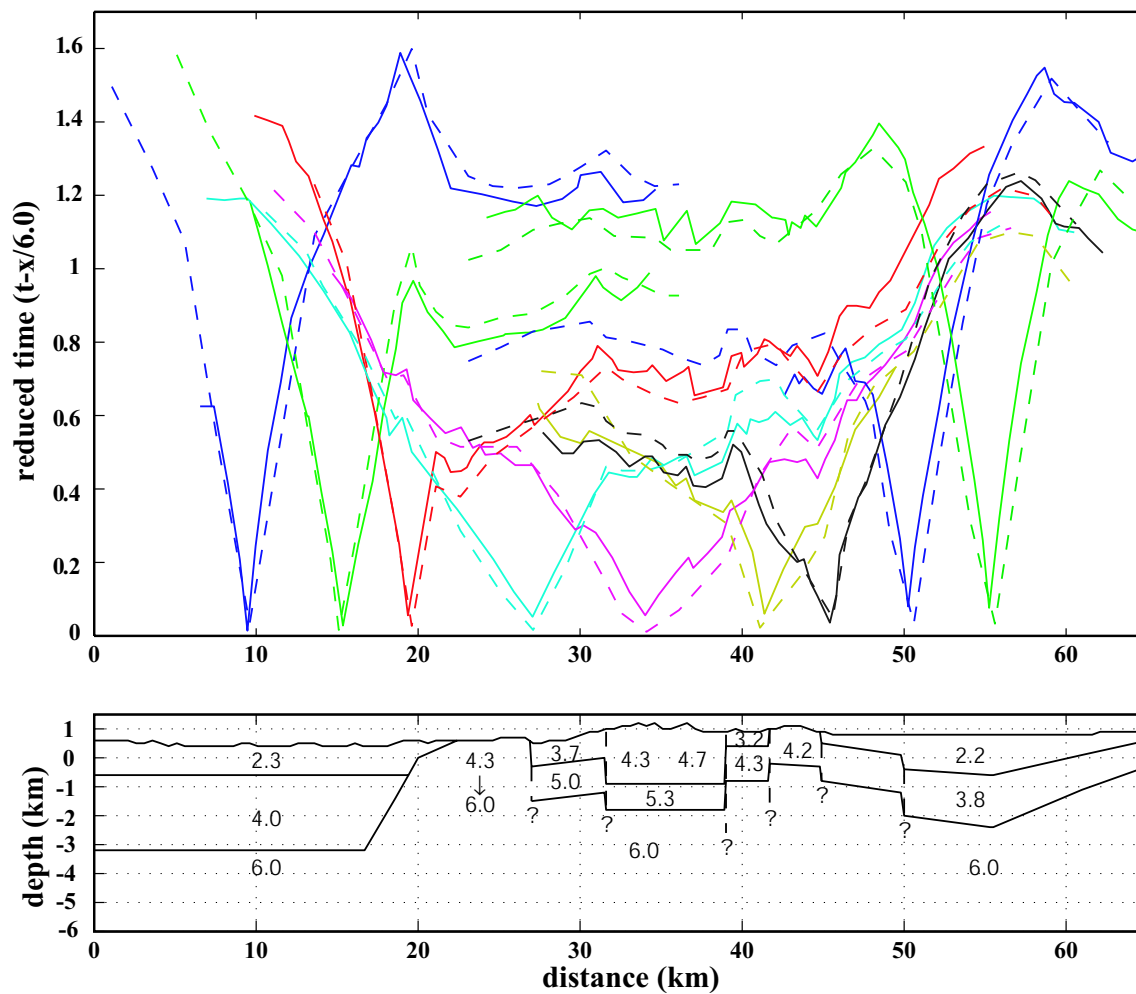


Figure 2.8 Comparison of synthetic first arrivals (dashes) for several shots from the improved model from trial and error modelling with the observed data (solid) of corresponding shots. The fit between the synthetics and the observed data, especially at far offset, is significantly improved compared with the preliminary model.

4.3 km/s at depth 0.5 km to 6.0 km/s at depth 2.0 km significantly improves the fit to the data. In the Mojave Desert, we find that a velocity value of 3.2 km/s for the second layer increases the fit of the synthetics for shots from #8530 to #8590, but the synthetic first arrivals for shots from #8770 to #8870 are too late compared to the data. A velocity value of 3.8 km/s gives an overall better fit. The refined velocity model is shown in Figure 2.8.

Features related to Fault 1 are very prominent (Figure 2.3). It has both the negative-slope segments for shots from the south side and the unusual low-velocity segments for shots from the north side. The unusual attribute about this fault is that the peak points of the regressive segments are almost aligned to the same ground point, instead of being distributed along a diffraction curve for a vertical fault (compare with Figure 2.5). As discussed in the appendix, relative location of the peak point and the kink point indicates that this fault is moderately dipping to the south. A dip angle around $40^\circ - 60^\circ$ makes the synthetic first arrivals best fit the data. The best-fitting model and synthetic first arrivals for several shots are shown in Figure 2.9. Peak points of the regressive segments in the synthetic data are almost aligned, which matches the real data. So we deduce that dip angle of the Pelona fault is around $40^\circ - 60^\circ$ to the south.

2.3 Correlation of Seismic and Geologic Structure

The shallow crustal velocity structure deduced from the LARSE II seismic data is used to help constrain a geologic cross section constructed from published geologic mapping and drill hole data [Dibblee 1967, 1982a, 1982b, 1992, 1996, 1997a, 1997b; Wright 1991], and our own topical mapping (J. Saleeby, unpub. data). The geologic section and seismic velocity section are shown at 1:1 scale along with a geologic strip map in Figure 2.10. All the faults interpreted from the LARSE II seismic data have corresponding structures in field and are shown on the cross-section. From south to north, they are the Pelona fault (1), the San Francisquito fault (2), the Clearwater fault (3) the San Andreas Fault (4) two unnamed faults (5, 6) which cut Portal Ridge, and a buried fault (7) in the adjacent Mojave Desert. Velocity values determined from seismic data can be compared with the general rock types and their textural states in the geologic cross section, recognizing that in some areas there are thickness and velocity trade-offs in the seismic structure. Additionally, the Figure 2.10 cross-section correlates our shallow velocity structure for the western Mojave Desert region with buried fault and basin structure

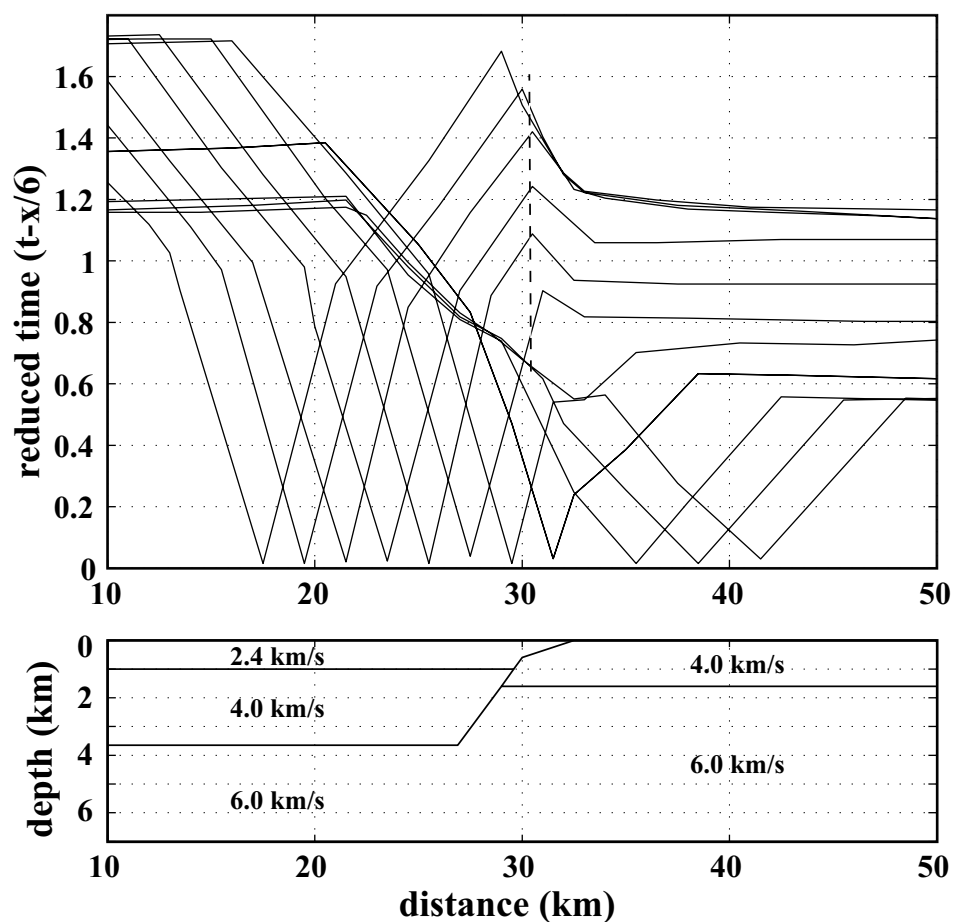


Figure 2.9 Synthetic first arrivals of the best fitting model for the real data set shown in Figure 2.3 related to the Pelona fault. The fault here dips to the south at an angle of 45° . Note the kink points for the shots south of the fault are almost aligned to the same ground point, similar to the observed features in real data. The similarity between these two arrivals indicates that this fault dips to the south and the dip angle is around 45° .

determined along the nearby Mojave Desert COCORP 1 line [Li et al. 1992]. Resolution of fault structures in the southern Santa Clarita Valley to San Fernando Pass region is poor for this segment of the LARSE II data that we have processed, a point that we will return to below.

The most distinctive structure that our LARSE II data analysis has resolved is the Pelona fault (Figure 2.10). Pelona schist has moved up along the footwall of this fault relative to hanging wall strata of the Soledad basin. The Soledad basin is defined as a depocenter principally by a thick (locally up to 5000m) section of volcanic and alluvial deposits of the upper Oligocene-lower Miocene Vasquez Formation [Hendrix and Ingersoll 1987]. The surficial low velocity lens which extends northward over the Pelona fault corresponds to upper Miocene strata which unconformably overlap the Vasquez Formation as well as lap across the western end of the Pelona fault. The Pelona fault was thus rendered inactive by upper Miocene time. From our study, we have determined that this fault dips between 40° and 60° to the south placing the Vasquez Formation in the hanging wall above footwall Pelona Schist. Field observations of the fault as exposed several kilometers east of the transect line indicate that it has had a complex movement history involving mainly south side down normal displacement. Thin selvages of cataclastic granitic rock lie along the fault between the schist and the Vasquez Formation. We interpret these to be disrupted vestiges of the Vincent thrust upper plate, which was attenuated in part by the extension related to the Pelona fault. Normal displacement along this fault is interpreted to have begun during late Oligocene-early Miocene formation of the Soledad basin. This fault appears to have been instrumental in the formation of internal sub-basins within the Soledad basin with the uplift of the proto-Sierra Pelona as an intra-basin ridge [Muehlberger 1958; Hendrix and Ingersoll 1987]. Hanging wall basement rocks above the Pelona fault were broken by north dipping imbricate normal faults, which also gave the floor of the Soledad basin considerable topographic and structural relief. Footwall rocks of the Pelona schist are deformed into a broad antiform, which is interpreted to have developed by isostatically driven uplift and attendant flexure in response to crustal unloading along the fault [cf. Wernicke and Axen 1988]. Net extension by normal displacement along the Pelona fault and attenuation of upper plate basement rocks beneath the Soledad basin may have been large (15) km considering that Vasquez Formation strata lie conformably on the Paleocene San Francisquito Formation north of the Sierra Pelona, but are unconformable on denuded upper plate basement rocks to the south.

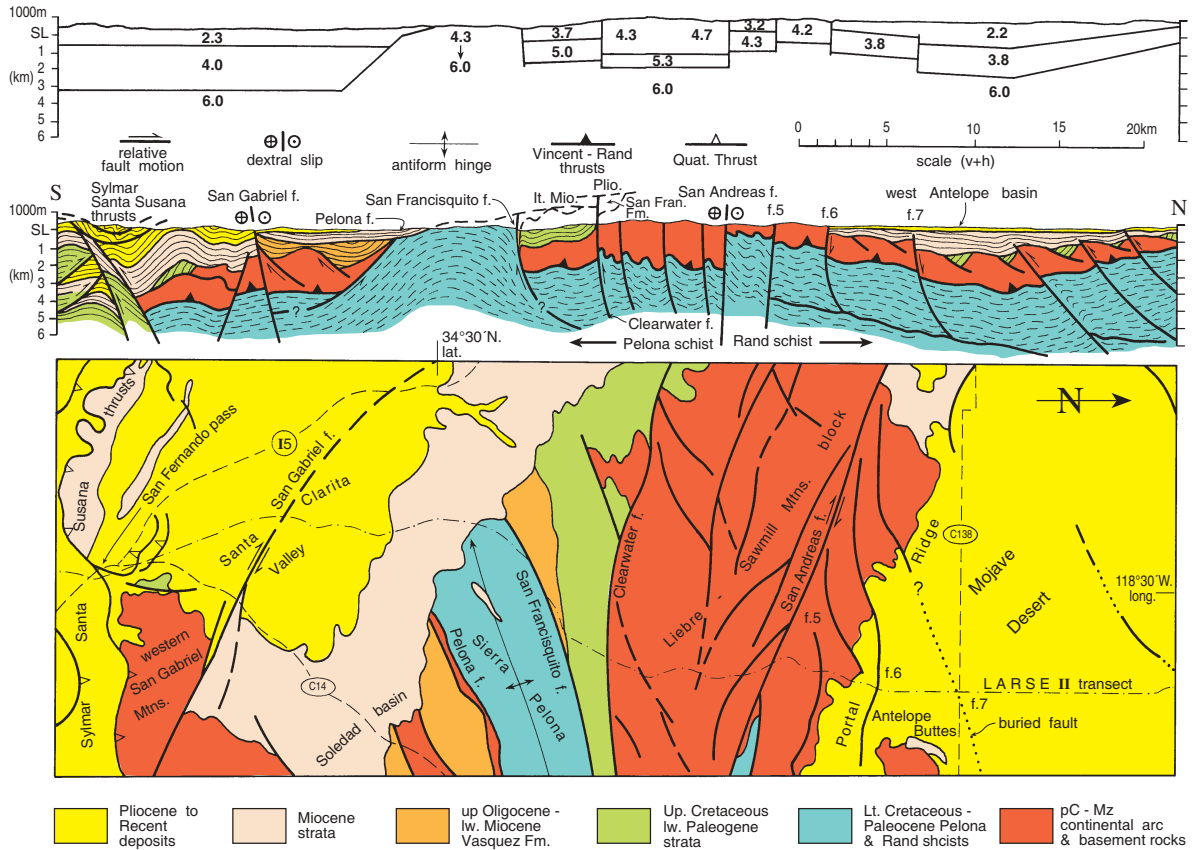


Figure 2.10 Shallow crustal seismic velocity structure, geologic cross section and geologic strip map drawn at 1:1 scale along northern segment of LARSE II transect. Geology is after Dibblee [1967, 1992, 1996 and 1997 a and b]; and J. Saleeby (unpub. data). Geologic cross section is registered in space to surface or near surface expression of steep faults imaged by seismic refraction data. Structure under Mojave Desert is diagrammatic, and in part constrained by projection of COCORP Mojave Desert line 1 data onto section plane [after Li et al. 1992]. Location of LARSE II transect shown by dot-dash line. Locations of Interstate 5, California State routes 14 and 138 are shown by dashed lines. Note that north is to the right in strip map.

The northern margin of the Sierra Pelona is bounded by the San Francisquito fault (fault 2), which is shown to be a steep structure by both the LARSE II seismic data and its linear geomorphic expression along much of its length. Locally, however, it assumes a $\sim 70^\circ$ N. dip with hanging wall Tertiary strata dropped down relative to the footwall Pelona schist. This fault is constrained to be upper Oligocene-early Miocene in age by its cutting of the Vaquez Formation, and its depositional overlap by the same upper Miocene strata that lap across the Pelona fault (see the attached geologic map in Figure 2.10). Our interpretation of the San Francisquito fault is that it was an intra-Soledad basin normal fault, which in part accommodated the rise of the Sierra Pelona ridge and was instrumental in the partition of the basin into sub-basins. As discussed below, however, the San Francisquito fault may have been inverted to a modest high-angle reverse slip fault during the mid-Miocene demise of the Soledad basin as a distinct depocenter.

The relationship between the velocity structure and the geologic structure of the Sierra Pelona is of significance. A velocity gradient from a surficial value of 4.3 km/sec to 6.0 km/sec at ~ 2 km depth is resolved in the LARSE II data. The geologic structure consists of a broad west-plunging antiform. The LARSE II transect crosses the western envelope of the antiform where fractured metaclastic rocks dominate the surface exposures. To the east along the core area of the antiform, metabasaltic rocks are more abundant, and at the deepest exposed structural level, weakly schistose amphibolitic metabasalt with relict pillow structures is well exposed. Laboratory measurements of average P-wave velocities for the Pelona schist sampled in the eastern San Gabriel Mountains range from 5.8 km/sec for metaclastic rocks to 6.4 km/sec for metabasaltic rocks [Pellerin and Christensen, 1998]. Accepting that the relatively low metaclastic surface velocities of 4.3 km/sec reflect the fractured and related weathered state of the surficial schist exposures, the geologic structure of the Sierra Pelona antiform correlates quite well with the LARSE II and laboratory velocity data. The shallow metaclastic rich envelope of the antiform yields low velocities, whereas the deeper more metabasaltic core yields higher velocities.

The block between the Sierra Pelona north bounding San Francisquito fault and the San Andreas Fault (fault 4) consists two eastward tapering structural wedges (Figure 2.10). The first wedge lies between the San Francisquito fault and the steeply dipping Clearwater fault (fault 3), and consists of folded Tertiary strata with an unconformable inlier of gneissic and granitic

basement. The second wedge lies to the north between the Clearwater and San Andreas faults. It constitutes the Liebre-Sawmill Mountain block and consists of highly fractured and faulted gneissic and granitic basement with small unconformable infolds of the Tertiary strata. The juxtaposition of basement rock with infolds of cover strata against the same cover strata with a basement rock inlier indicate an important north side up slip component for the steeply dipping Clearwater fault. This presumably occurred in conjunction with the folding of the Tertiary strata and its basement. The Clearwater fault dies out up section within overlapping Pliocene strata to the west of the study area, and merges eastward with the San Francisquito fault. The Liebre-Sawmill Mountain block is characterized by numerous steeply dipping internal faults and a near pervasive steeply dipping brittle-ductile shear fabric. These basement rocks and the equivalent basement inlier within the adjacent sediment wedge are also interpreted as part of the attenuated upper plate of the Vincent thrust. The low seismic velocities deduced from the LARSE II data for surface exposures of these rocks (4.3 to 4.7 km/sec and also 5.0 km/sec for rocks beneath the Tertiary strata) as compared to laboratory velocities measured on more coherent samples scattered throughout the San Gabriel Mountains basement complex (5.7 to 6.2 km/sec; Pellerin and Christensen 1998] are reconciled by the highly degraded textural state of the Liebre-Sawmill basement rocks. The interface from the 5.0 km/sec layer to the 6.0km/sec layer beneath the sediment wedge is correlated with the Vincent thrust. The deformed remnants of the thrust are in turn displaced up along the Clearwater fault and are correlated with the 5.3km/sec layer of the Liebre-Sawmill Mountain block. This velocity is interpreted as the mark of superposed deformation and retrograding of both the upper and lower plates along the thrust. To the south of the San Francisquito fault the Vincent thrust has been completely eroded away above the Sierra Pelona antiform. Significant erosional breaching through the upper plate began by mid-Miocene time as indicated by the appearance of appreciable schist detritus in the sedimentary record. Local breachment by late Oligocene-early Miocene time is indicated by rare schist clasts in the Vasquez Formation [Muehlberger 1958; J. Saleeby, unpub. data].

Open folding of the Vasquez Formation, and its San Francisquito Formation/granitic basement substrates marks the disruption of the Soledad basin in Miocene time. These events are accentuated by the mid to upper Miocene unconformity shown on the geologic cross section. Structural relations in the Vasquez Formation suggest that the proto-Sierra Pelona intra-basin ridge acted as a structural buttress during this compressional deformation. Adjacent to both the

Pelona fault and the San Francisquito fault the otherwise openly-folded Vasquez Formation is rotated to near vertical and steeply overturned dips. Modest tightening and the development of second order open folds (not present in the cross section plane) in the Sierra Pelona antiform may have accompanied folding of the Vasquez cover strata. Inversion of the San Francisquito fault to a modest reverse slip component is also considered to have accompanied this folding event as suggested by the adjacent overturning of the Vasquez Formation. The steeply dipping shear fabric and internal faults of the Liebre-Sawmill Mountain block in general parallel the axial planar trend of folds in the cover strata. The implicit strain of this fault and rock fabric system appears much greater than that exhibited by the open folding of the cover strata. This suggests that the fabrics, and perhaps the faults, are inherited from earlier tectonic regime(s) and that perhaps they too have inverted their kinematic role from earlier extensional to later compressional behavior. The tapering of the Liebre-Sawmill Mountain basement wedge and the adjacent San Francisquito Formation wedge into the proximity of the San Andreas Fault raises the possibility that the San Francisquito and Clearwater faults once had significant strike-slip components as part of the early San Andreas transrotational regime. Offset markers or shear sense indicators along these faults indicating such have yet to be observed, however. The Liebre-Sawmill Mountain block is the highest topographic feature of the region by roughly 500 m. This is interpreted as the mark of uplift related to the late Neogene compressional deformation as well. The San Francisquito and presumably the Vasquez equivalent strata were eroded off the basement block as it was uplifted.

The geologic analysis of the velocity structure offered above begs the question as to what is the appropriate average P-wave velocity for the Pelona schist. In their analysis of laboratory seismic velocity data, Pellerin and Christensen [1998] assumed a 9:1 ratio of metaclastic to metabasaltic rocks, and derived an average P-wave velocity of 5.8 km/sec. This lithologic ratio is too high for the core area of the Sierra Pelona, which could be more representative of the schist at depth. An average P-wave velocity of 6.0 km/sec, as suggested by this study, appears more appropriate, although large transposed layers of pure metaclastic or pure metabasaltic rocks could yield velocity domains that deviate significantly in either direction from this value. Average P-wave velocities in the range of 6.2 to 6.5 km/sec for the schist and 5.5 to 6.1 km/sec for upper plate basement rocks were deduced for the Rand thrust complex of the Tehachapi Mountains [Malin et al. 1995]. The Rand schist in the Tehachapi Mountains contains abundant

metabasalt as well as the ubiquitous metaclastic rocks. The cogent point here is that depending on the actual metabasalt to metaclastic ratio of a given domain of the schist under investigation, it may or may not be distinguishable by seismic velocities from texturally and structurally coherent basement rocks of the respective upper plate [cf. Pellerin and Christensen, 1998; Table 3].

The 6.0 km/sec layer of our shallow crustal model to the southwest San Andreas Fault is correlated to the Pelona schist. Such a correlation for the 6.0 km/sec layer to the northeast of the fault, if correct, carries important implications for the geological interpretation of our shallower velocity structure model. Seismic reflection data for the western Mojave Desert show the Rand schist at shallow crustal levels throughout much of the region [Cheadle et al. 1986; Li et al. 1992; Malin et al. 1995]. These data also show the schist and its tectonically overlying granitic basement plate ramping up southward towards the San Andreas Fault. The ramping structure is confirmed by surface exposures of the schist in small hills ~6 km north of the San Andreas fault, east of the study area, and by an ~25 km long fault sliver of schist lying along the north wall of the fault. This fault sliver underlies much of Portal Ridge [Dibblee 1967], and the terminus of its surface exposure is 2 km southwest of the LARSE II transect (Figure 2.10 map).

The 6.0 km/sec basal layer of our shallow crustal model in the western Mojave Desert is tentatively correlated with the Rand schist. As discussed above, the Rand schist is in regional tectonic terms correlative with the Pelona schist, although their immediate proximity as expressed along the LARSE II transect is a result of ~255 km right slip on the San Andreas fault. The problem that arises from a simple correlation of the 6.0 km/sec layer with the Rand schist is in the implied velocity of its upper granitic plate (3.8 km/sec). As aberrant as this velocity seems, the presence of such basement rocks at depths which correspond to the boundary between our 2.2 km/sec and 3.8 km/sec layers is corroborated by stratigraphic, drill hole, gravity and seismic reflection data [Dibblee 1967; Li et al. 1992]. As discussed below the geologic structure of the 3.8 km/sec layer is suggested to be highly complex, and characterized by shattered, retrograded and highly attenuated granitic basement rock.

Faults 5 and 6 constitute part of the high angle fault system that obliquely transects Portal Ridge. The surface exposures between the San Andreas Fault and fault 5 consist of highly shattered granitic rocks with zones of fault gouge. These rocks correspond to the 3.2 km/sec layer,

and the underlying 4.3 km/sec layer is interpreted as highly fractured Rand schist projected beneath the shattered granitic rocks from schist exposures to the southeast. Surface exposures between faults 5 and 6 consist of shattered upper plate granitic rocks that correspond to the 4.2 km/sec layer. Beneath these rocks at shallow levels presumably lies the Rand schist. The velocity variations between the faults 5 and 6 sliver and the San Andreas-fault 5 sliver reflect the brittle deformation overprint of the San Andreas Fault zone.

Fault 7 is buried beneath Quaternary deposits of the Mojave Desert, but is well defined in the seismic data. Bedrock exposures in the nearby Antelope Buttes, to the east of the transect, correlate well with the seismic structure deduced between faults 6 and 7. The 2.2 km/sec layer principally corresponds to a relatively thin section of Neogene strata exposed along the western edge of the Buttes, and the 3.8 km/sec layer corresponds to its underlying shattered basement. Fault 7 is correlated with a well expressed fault that obliquely transects the western end of Portal Ridge (Figure 2.10 map). The correlation is based on the fact that the shattered granitic basement exposed to the north of the exposed fault constitutes the depositional substrate for a thick Neogene section. Fault 7 in the subsurface defines a basement scarp across which the Neogene section thickens abruptly. Thus the stratigraphic changes that occur across the exposed fault, between the Antelope Buttes block and the western end of Portal Ridge, match those seismically imaged across the buried fault 7. Hence the correlation.

The shallow seismic velocity structure deduced along the LARSE II line for the western Mojave Desert region clearly defines the west Antelope basin, an east-west trending shallow trough which extends to the western tip of the Mojave Desert [Dibblee 1967]. Except for sparse drill hole data and gravity data [Dibblee 1967], and our shallow velocity model, constraints for the subsurface geologic structure are sparse. The geologic structure shown for the basin on Figure 2.10 is constrained by these data, and by the projection of COCORP seismic reflection data westward onto the LARSE II transect from a parallel line located 10 km to the east of our transect. The COCORP data show a modest north-dipping fault, which corresponds spatially to the eastward extension of either fault 6 or 7. In addition to the Rand thrust ramping up to the south the COCORP data also show a strong reflector internal to the schist which also ramps up to the south at a depth of ~ 4 km beneath the thrust. Our interpretation is that faults 6 and 7 are basin bounding normal faults which root into a detachment fault that corresponds to the reflector within the schist. Fault 5 may have had a similar origin, but it is shown on the cross

section as having been partly remobilized as part of the San Andreas Fault zone. The COCORP data also show two distinctive north-dipping reverse faults at the northern end of their transect. These two faults and a third reverse fault, expressed as a dissected scarp and adjacent broad folding of Quaternary strata, are shown deforming the northern margin of the West Antelope basin. The northward ramping up of our shallow velocity structure under the northern West Antelope basin is attributed to this young, and possibly active, distributed compressive deformation. The COCORP data show additional north dipping faults, which appear to offset the top of the basement in an opposite sense as the reverse faults. These are interpreted as older basin floor normal faults.

The shallow 3.8 km/sec layer that extends across the west Antelope basin floor merits special attention. Neogene stratigraphic thicknesses, sparse drill hole data, and seismic reflection data [Dibblee 1967; Li et al. 1992] all point to this layer as upper plate granitic rock of the Rand thrust system. The 3.8 km/sec velocity deduced for this layer seems excessively low, although velocities of 4.2 km/sec and 3.2 km/sec were deduced for the apparent southward continuation of this layer where such basement rocks constitute the surface exposures. The interpretation offered here, and shown diagrammatically on the geologic section, is that this layer is highly attenuated, shattered and retrograded upper plate granitic rock. This layer may also contain vestigial lenses of early Palaeogene strata, such as the Golar Formation that is depositional on upper plate granitic rocks adjacent to the Garlock fault [Dibblee 1967]. In this interpretation these lenses have been dispersed by Neogene extension and overlapped along with their adjacent denuded basement by the Neogene basin fill. The extreme attenuation of the western Mojave Desert upper granitic plate is considered a result of the superposing of Neogene extension over the effects of latest Cretaceous-early Palaeogene extensional collapse of the Rand thrust complex [cf. Saleeby 2003].

An alternative interpretation to that offered above for the 3.8 km/sec layer is that it represents primarily a thick Palaeogene section of Golar Formation affinity strata beneath the Neogene section. This is possible [cf. Saleeby 2003], but there are no surface exposures or drill hole data to support this view. In this interpretation, the Rand thrust would be opaque to our velocity data, and it would perhaps correspond to the deeper reflector imaged by the COCORP data [Li et al. 1992]. The favored interpretation, however, is that most of the Palaeogene that may have existed beneath the west Antelope Basin region has been removed by a combination of

extensional tectonic denudation and erosion, and for the most part syn- and post-extensional Neogene strata of the basin lie unconformably on highly attenuated and shattered basement.

Final discussion focuses on the relatively simple seismic velocity structure derived for the southern end of our transect beneath the southern part of Santa Clarita Valley and the San Fernando Pass areas. As shown on the geologic cross section the structure is much more complex than that of the seismic velocity model. Most notable is a lack of any signature for the San Gabriel fault, nor the Santa Susana-Sylmar thrust system. Nor is there any expression of the considerable basement relief beneath the Neogene strata of the area that is documented by drill hole data. In addition to the problem of poor resolution at the extremities of our seismic model, the most viable explanation for this is that upper plate crystalline rocks above the Vincent thrust of this region are also highly fractured and hydrated, and thus yield seismic velocities in a range below those of coherent basement rocks and overlapping with those of clastic sedimentary rocks. Such a textural state is born out by observations of crystalline rocks which constitute the western end of the San Gabriel Mountains, and which project westwards beneath the adjacent San Fernando Pass area. As noted earlier the history of upper plate crystalline rock fracturing, hydration and attenuation began during or shortly after initial schist underthrusting, and has been accentuated by Neogene to Recent extensional, strike-slip and compressional deformations. The effects of this near pervasive textural and structural degradation of much of the Southern California region crystalline basement are well expressed along the entire length of our transect by their consistently low P-wave velocities as compared to what is known to typify texturally and structurally coherent continental basement rocks.

2.4 Conclusions

We recognized three characteristic features of faults in densely sampled seismic refraction data and these features were used to identify six faults in the north-central Transverse Ranges and adjacent Mojave Desert portion of the LARSE II transect. We also estimated the influence of faults (lateral velocity variations) on first arrivals, especially on kink points, which enables us to discriminate between different kinds of apparent kink points and to determine which apparent kink point is appropriate to derive a good estimate of P-wave velocity layer thickness. We locally used a simple 1-D depth-inversion method on these appropriate kink points to determine

the thickness of different velocity layers for blocks between faults under the assumption that the thickness does not change dramatically between faults. A 2-D velocity structure was thus constructed as a preliminary model from the near offset part of the data. We then refined this preliminary model using test and trial modelling for the synthetic first arrivals to fit all the data. An additional fault (fault 5) was detected from this trial-and-error modelling. The synthetic first arrivals generally compare well with the recorded data. The velocity structure we constructed from the seismic data compare reasonably well with the known geologic structure, constituent rock type and textural state data.

Locations of these 7 faults are fairly well defined from the seismic data and they compare well with geologically mapped faults. From south to north, they are the Pelona fault, the San Francisquito fault (south and north bounding faults of Sierra Pelona), the Clearwater fault, the San Andreas fault, two faults associated with Portal Ridge, and a fault buried beneath Quaternary deposits within the western Mojave Desert. Features related to the Pelona fault are most prominent, and indicate that the velocity structure changes markedly across this fault from the Santa Clarity Valley and underlying western Soledad basin to the Sierra Pelona.

The Pelona fault was a major active south-dipping normal fault during the late Oligocene-early Miocene formation of the Soledad basin. Footwall rocks of the Pelona schist were flexed into a broad open antiform probably as a result of isostatic response to crustal unloading along the Pelona fault. South side up normal displacement of the San Francisquito fault is interpreted to have in part accommodated the rise and flexure of the Sierra Pelona antiform. Between the San Francisquito fault and the San Andreas Fault lies an elevated area characterized by intense brittle deformation of upper plate basement rocks of the Vincent thrust, and the folding of its Tertiary cover strata. This block was folded and uplifted in mid-Miocene to earliest Pliocene time by compressive deformation probably in response to transpression along the San Andreas fault, and as part of the regional uplift of the Transverse Ranges.

The LARSE II transect in conjunction with COCORP reflection data of the western Mojave Desert have identified structures that played a key role in the development of the west Antelope basin. The southern margin of this basin is controlled by steeply dipping Miocene (?) normal faults, which apparently root into a low north dipping detachment surface. Mio-Pliocene basin fill thickens northward across these normal faults. The northern margin of the basin is deformed by north-dipping reverse faults, some of which may be active.

The shallow crustal seismic velocity structure determined by the LARSE II data defines a regional pattern of surficial low-velocity sedimentary rock lenses, which represent the remnants of larger Cenozoic sedimentary basins. Constituent Palaeogene to lower Neogene strata were deposited and subsequently disrupted in extensional tectonic environments. Pliocene to Recent strata are deposited in the remnants of early Neogene extension-related basins, and are also in part deformed and uplifted along Pliocene to Recent compressive deformation zones. Our shallow seismic structure does not distinguish these contrasting settings for the Pliocene to Recent deposits. The Pelona and Rand schists form a basal high velocity layer beneath the entire region at relatively shallow crustal levels. Between the schists and the Cenozoic strata lie highly attenuated, intensely fractured, and variably hydrated remnants of the upper “granitic” crystalline plates of the Vincent and Rand thrust systems. These rocks consistently yield low P-wave velocities as compared to what would be expected for fresh coherent basement rocks. These low velocities reflect the highly degraded structural and textural state of the upper plate basement rocks in response to multiple extensional and subsequent compressive deformation events. Such degradation of these basement rocks is in places so extreme as to prohibit the seismic resolution of depositional contacts with their overlying Cenozoic cover strata

In our analysis of the fault structure of the north central Transverse Ranges and adjacent western Mojave Desert, we have placed important constraints on vertical slip components. Neither the seismic data, nor the presence of offset geologic markers or shear sense indicators in the study area has offered constraints on possible strike-slip components. The history of transrotation, transtension and transpression in the Transverse Ranges region [Luyendyk 1991; Dickinson 1996; Ingersoll and Rumelhart 1999] leaves open the possibility of significant strike-slip components on some of the steep faults that we have resolved, in addition to that of the San Andreas fault.

Acknowledgements

We thank the many volunteers who helped with the LARSE II experiment. We would like to thank Jascha Polet, Vala Hjorleifsdottir, and Javier Favela for their reviews and comments. Helpful reviews by Walter Mooney and an anonymous referee are gratefully acknowledged. This research was supported by the Southern California Earthquake Center. SCEC is funded by NSF Cooperative Agreement EAR-0106924 and USGS Cooperative Agreement 02HQAG0008.

This paper is SCEC contribution number 736 and the Division of Geological and Planetary Sciences, Caltech, contribution 8972. J. Saleeby acknowledges support under NSF grant EAR-0087347.

Chapter 3

Regional Mapping of Crustal Structure in Southern California from Receiver Functions

Abstract

Lateral variations of the crustal structure in Southern California are determined from receiver functions using data from the broadband stations of the Southern California Seismic Network (SCSN) and LARSE surveys. The results include crustal thickness estimates at the stations themselves, and where possible, cross-sections within different geomorphic provinces are drawn to show the lateral variations of crustal structure. Crustal structure beneath the central Transverse Ranges is strongly heterogeneous and has some large rapid lateral variations. A relatively shallow Moho of 31–34 km is observed for the eastern San Gabriel and Liebre-Sawmill Mountains, and most station groups in the western San Gabriel Mountains. However, a deep Moho of 36–39 is inferred for several station groups in the western San Gabriel Mountains. Thus, no regional root is observed for the San Gabriel Mountains. Strong lateral heterogeneity in the subsurface structure correlates well with the surficial geology as evidenced by the observation that the station groups that show very different receiver function patterns sit on distinctive allochthonous terranes. The Moho is relatively flat in the Coso geothermal area and the western Mojave Desert with a depth of 28–32 km, but it shallows to the east in the Mojave Desert and reaches 22–25 km at the southern extension of the Death Valley fault zone (DVFZ). Crustal structure is more complicated in the eastern Mojave Desert where large variations in the Moho depth are observed beneath two stations. An anomalous jump of ~ 8 –10 km is determined for one station (DAN) beneath the Fenner Valley, east of Amboy, CA, where events from NW indicate a shallow Moho of 22–24 km, and events from SE indicate a deep Moho of 30–32 km, over a horizontal distance of no more than 15 km. A deep Moho of 34–38 km is observed

along a sliver with a width of 30–40 km in the western Peninsula Ranges, and the sharp transition from this thick crust to the thin crust on the east beneath the Salton Trough indicates that movement of the western Peninsula block involves the whole continental crust and that strong coupling exists between the upper and lower crust. Asymmetric extension of Salton Sea is also observed: the Moho thins gradually from 20–22 km in the Salton Trough to 25–28 km to the east in the Mojave Desert at ~ 100 km away, but transitions sharply to 34–38 km thickness in the west within a distance of ~ 50 km. A deep Moho of 35–39 km is observed beneath the west Sierra Nevada, northern Death Valley Fault zone and the San Bernardino Mountains.

3.1 Introduction

Lateral variations of the crustal structure are of fundamental importance to understanding the tectonic evolution and the current status of the lithosphere, and the comparison of the subsurface structure with surficial deformation can provide important insight into the coupling relationship between the upper and lower crust, and thus the strength of the lower crust. Surficial geology in the Southern California indicates that large-scale deformations have occurred during and after the transition of the plate boundary from a convergent one to a strike-slip one. Examples of the deformation include block rotation of the central and western Transverse Ranges, opening of the Gulf of California, and the large-scale extension in the Basin and Range province. Thus, Southern California provides a very natural laboratory to investigate these problems.

Extensive efforts have been made to investigate the crustal structure in Southern California. These include an early study of local refraction studies and teleseismic P travel time delays by Hadley [1978] and Hadley and Kanamori [1977,1979], who built a standard regional model for Southern California and found a high velocity body in the upper mantle beneath the Transverse Ranges. A kinematic model which proposes that the crust and upper mantle are decoupled across the Southern California and that the plate boundary is shifted to the east beneath the Eastern California Shear Zone in the upper mantle was inspired by the fact that this upper mantle high velocity body is continuous across the San Andreas Fault and its spatial extension to the active Helendale-Lenwood fault zone [Hadley and Kanamori 1979]. This high velocity anomaly was further refined by tomography studies and its spatial dimension was constrained to be ~ 80 km in N-S direction, ~ 150 km in E-W direction and extends to ~ 200 – 250 km in depth with a 2%–3% P velocity anomaly [Humphreys et al. 1984; Humphreys and Clayton 1990; Kohler 1999]. Common explanation for this high upper mantle velocity body is that it is caused by sub-crustal lithosphere downwelling [Humphreys and Hager 1990; Kohler 1999]. For the involvement of the crust, however, different kinematic models have been proposed and the two end members are complete decoupling of the crust and upper mantle, in which the crust remains flat [Humphreys and Hager 1990; Humphreys 1995], and strong coupling between the crust and the upper mantle, in which the crust deepens accordingly [Houseman et al. 2000; Kohler 1999]. The key to solving this mystery lies in the crustal thickness beneath the San Gabriel Mountains, which is still in debate.

The studies that support shallow Moho beneath the San Gabriel Mountains include Zhu

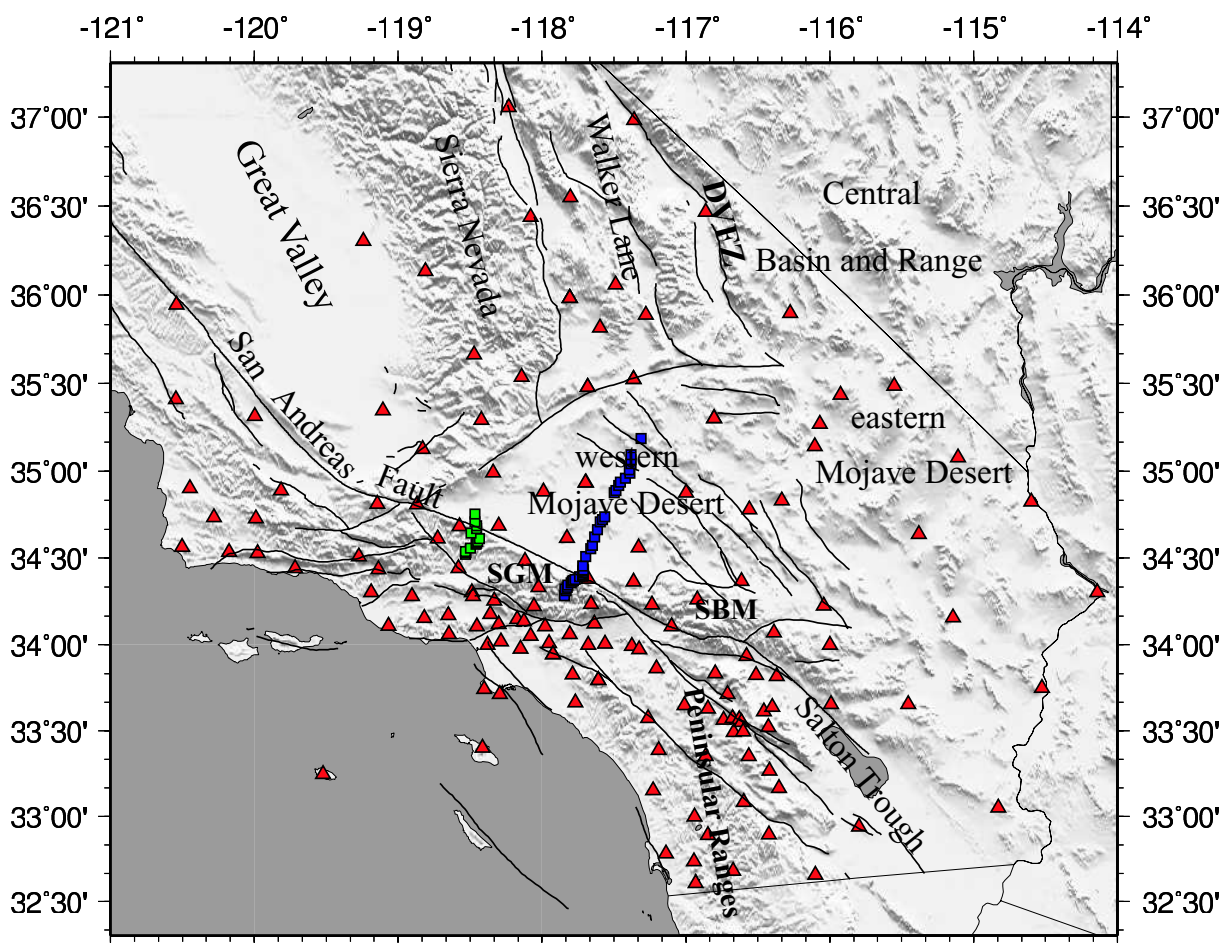


Figure 3.1 Map showing the stations used in this study, along with major faults in Southern California [Jennings and George 1994]. Red triangles are SCSN stations, blue squares are LARSE I stations, and green squares are LARSE II stations. SGM, San Gabriel Mountains. SBM, San Bernardino Mountains. DVFZ, Death Valley fault zone.

and Kanamori's [2000] teleseismic receiver function (RF) studies from 65 TriNet broadband stations, Zhu's [2000] teleseismic receiver function studies from the LARSE I passive stations, and Richards-Dinger and Shearer's PmP - P differential time studies [1997]. These studies all infer a shallow crust of 28–31 km for the central Transverse Ranges. In contrast, Kohler and Davis [1997] inferred the existence of a deep root of 40 km centered at the San Andreas Fault from teleseismic travel time studies of the LARSE I passive stations. A feature that further complicates the interpretation is that two interfaces are apparent in Zhu's [2000] teleseismic receiver function image along the LARSE I line. Zhu [2000] picked the shallower one at 25–29 km to be the Moho, while others argue that the deeper interface at around 40 km with slightly smaller amplitude could be the Moho instead. All these indicate that further study of the crustal structure beneath the San Gabriel Mountains is needed to resolve the controversy.

Broadband stations in Southern California (Figure 3.1) have been nearly tripled since 2001 after Zhu and Kanamori's study [2000]. Also with this previous study, the RFs from all back azimuths were stacked together to give an estimate of the averaged Moho depth beneath a station, while large variations in the Pms arrival times are observed for most stations beneath the San Gabriel Mountains. Events from different directions pierce the Moho at different points that are separated from each other by as much as 15–20 km laterally, so the difference in the Pms arrivals for different back azimuthal groups can be exploited to find rapid variations in crustal structure.

The RF method has the advantage of providing very good localized estimate of the crustal structure beneath a station. In this study, we will take the advantage of this property to develop a relatively high-resolution regional map of the Southern California crustal structure. We will exploit the higher density of broadband stations in Southern California, and the large number of suitable teleseismic events to increase the resolution especially beneath individual stations by stacking the RFs only over restricted back azimuthal ranges. This will allow us to identify lateral variations of the structure beneath individual stations, which is particularly important for stations near major faults. Compared with other techniques, such as wide-angle reflection and refraction studies, the local and relative timing nature of the RF method makes the results less dependent on lateral and vertical variations in the velocity structure. The estimate only depends weakly on the average crustal P velocity and an uncertainty in the average V_p of 0.1 km/s will result in an uncertainty of less than 0.5 km in the Moho depth for a 30 km thick crust [Zhu and Kanamori 2000]. However, the relative timing nature of RF makes them highly dependent on the average crustal V_p/V_s ratio [Zhu and Kanamori 2000]. In this paper, we use the stacking algorithm developed by Zhu and Kanamori [2000], which uses multiples of the Pms phase to estimate the crustal thickness and V_p/V_s ratio.

3.2 Data and Analysis

To produce a detailed map of lateral variations in the crustal structure of Southern California, 164 non-basin broadband stations of the SCSN (Southern California Seismic Network) were used along with the stations from the passive component of LARSE I [Kohler and Davis 1997; Zhu 2000] and LARSE II [Fuis et al. 2001, Zhu 2002] surveys. Locations of the SCSN stations

and LARSE surveys are shown in Figure 3.1. A total of 144 teleseismic earthquakes recorded by the SCSN stations with magnitude larger than 5.5, and a distance between 30° and 95° were used (Figure 3.2). The actual numbers of events for individual stations vary from 20 to 140, depending on the signal-to-noise level of the waveform data, and the recording period of the station. Over the deployment period, the LARSE I stations recorded 12 good events from the NW back azimuth. For LARSE II, 3-6 high signal-to-noise ratio events from SW and SE respectively were used (Figure 3.2).

Teleseismic waveform data with signal-to-noise ratios higher than 3 were selected. The records were time windowed to 90 sec, starting 15 sec before the P-wave onset, band-pass filtered (0.02–2 Hz), and the two horizontal components were rotated to the radial and tangential directions. Two types of deconvolution techniques were used to deconvolve the vertical component from the radial and tangential components. A frequency domain deconvolution [e.g., Langston 1977, 1989; Owens et al. 1984; Ammon et al. 1990] using spectral division with water levels 0.001, 0.01, 0.1 and Gaussian filter parameters of 2.5 and 5.0 were used for the LARSE I and LARSE II passive data. Selection of the water level and Gaussian parameters for each record is determined by the pre-signal noise levels. For RFs with sufficiently low pre-signal noise levels, the RF with the lowest water level and higher Gaussian parameter is selected. An iterative time-domain deconvolution technique [Ligorria and Ammon 1999; Kikuchi and Kanamori 1982] was used for the broadband SCSN data.

The signal-to-noise ratio is increased by stacking the RFs grouped by their conversion points (back azimuth). Although the variation of the RFs over the whole back azimuth range is large, they are very similar to each other within a limited azimuthal range (see Figure 3.3). The RFs for each station are divided into 9 azimuth groups, and the stacking grid-search algorithm of Zhu and Kanamori [2000] was applied to groups with more than 5 RFs to get an estimate on the Moho depth, H , and the V_p/V_s ratio, κ , at the surface projection of conversion point at the Moho. The conversion point is normally 7–10 km away (in the back azimuth direction) from the receiving station, depending on the ray parameter. Since estimates of the Moho depth depend only weakly on the average crustal P velocity, it is assumed to be 6.3 km/s for all stations for simplicity and consistency. The search range of H and κ for most azimuthal station groups are $H \in [25, 45]$, and $\kappa \in [1.65, 1.90]$. In regions where Moho depth deviates substantially from 28 to 38 km, the searching range for H is modified accordingly. For example, the searching

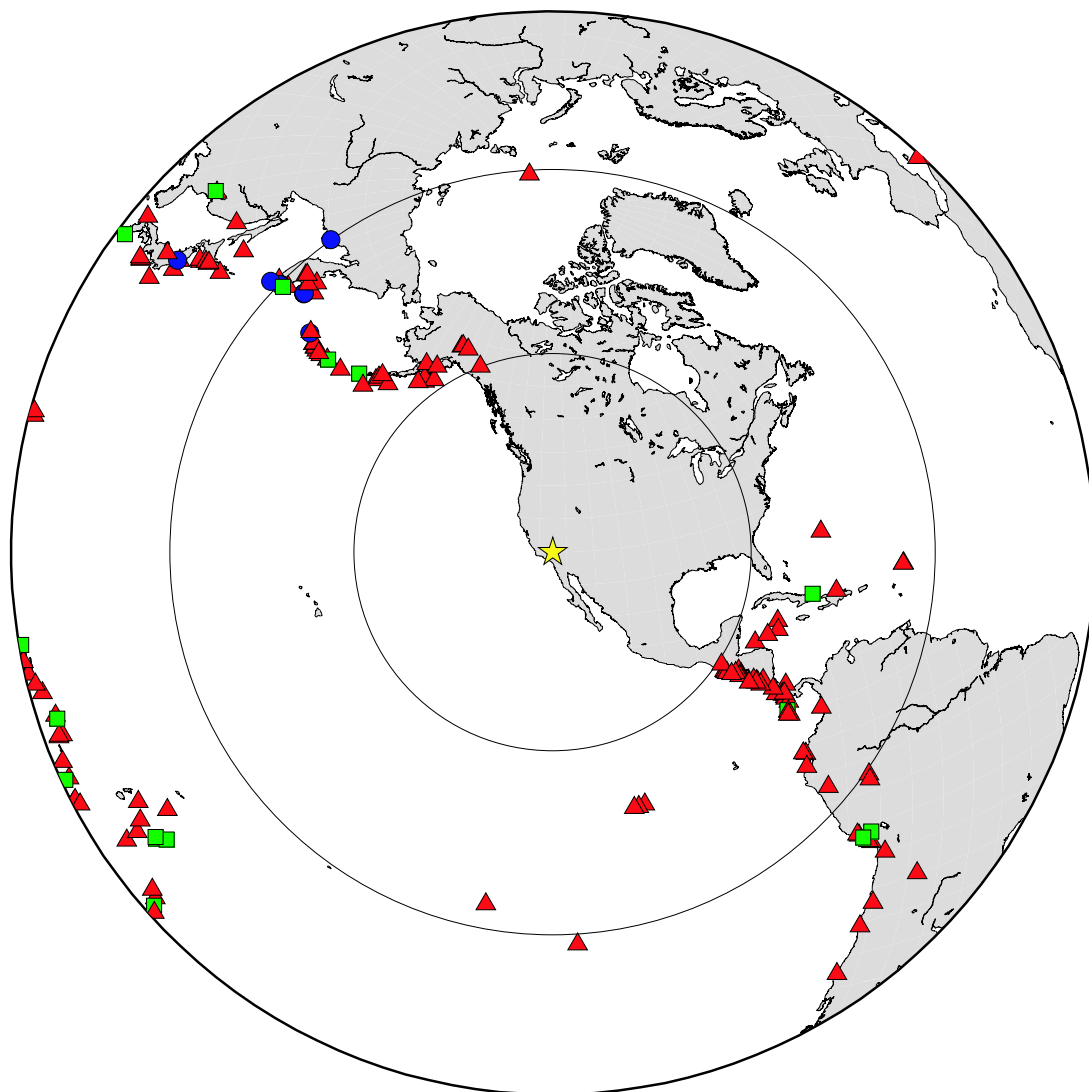


Figure 3.2 Map showing the distribution of the events used for this study, which include ~ 145 events for the SCSN stations (red triangles), 12 events for the LARSE I survey (blue circles) and 17 events for the LARSE II survey (green squares). Yellow star represents the SCSN station TA2 at Table Mountain, Wrightwood. The three common-centered circles represent the 30° , 60° and 90° distances away from station TA2.

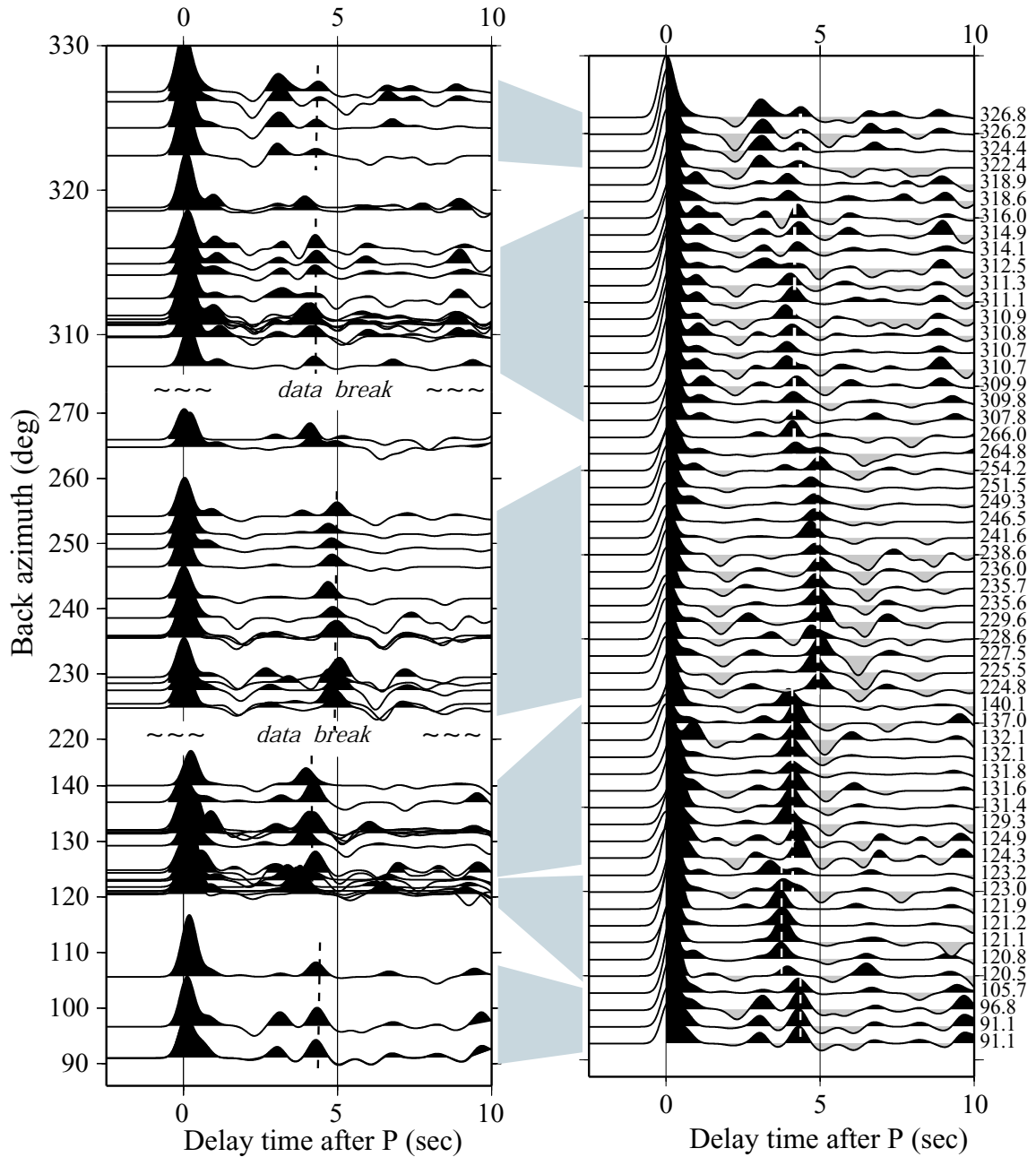


Figure 3.3 All the receiver functions for station VCS (Vincent Substation). On the left the RFs are plotted as a function of back azimuth, on the right, the RFs are evenly spaced, but in the order of increasing back azimuth from bottom to top. The RFs show large variations within the whole back azimuth range, but share large amount of similarities among RFs with similar back azimuths. Note the late Pms arrivals (4.8 sec) for events from SW, and nearly constant arrivals of 4.0-4.2 sec for other directions. The prominent negative phase arriving at 2.0 sec and 1.5 sec for events from NW and SW respectively represents a velocity decrease interface, which could be correlated with similar phases observed at other stations, such as MWC and CHF (Figure 3.14).

range for H is 15–30 km for stations close to the Salton Sea. Uncertainty estimates for the grid search is taken to be the 95% maximum contour for the purpose of distinguishing RF groups with relatively well-developed multiples. Comparing with the uncertainty estimation method of Zhu and Kanamori [2000], this estimate has the advantage of being able to determine how well developed the multiples are from the geometry of the contours, which in turn will be used to select well-constrained data points from all the stacking azimuthal groups.

When the 95% contour of the (H, κ) grid search is broad in any direction (Figure 3.4) or has more than one local maximum, it indicates that either the amplitude of the multiples is too small to be distinguished from background noise or that several reverberations exist in the data and it is difficult to tell which one is the true multiple. In both cases, the grid search algorithm does not work since well-developed multiples are required for it to be successful. An example of a successful stacking group is shown in Figure 3.5, which shows clear PpPms multiples although the PsPms multiples are a little bit delayed due to minor lateral variations in the crustal structure. The selection criteria used to distinguish well-constrained data points from all the stacking station groups are: only one 95% contour exists, uncertainty range for κ is less than 0.15, and 100% of the polarities for the primary phase, more than 50% of the polarities for both multiples are correct. Only station groups that meet the above criteria are included in the Moho depth mapping of Figure 3.6. For groups that fail these criteria, but have prominent and consistent Pms phases, such as the SW station group of VCS (Figure 3.4), the averaged stack traces are included in the cross-sections of the corresponding provinces (such as Figure 3.7). For the LARSE I and LARSE II passive data, continuity of the Moho interface with nearby stations is assumed, and RFs from neighboring stations were referenced in constraining the Pms pick when multiple Ps phases exist between 3 and 5.5 seconds.

In summary, procedures for this RF study are as follows. (1) For all the available waveforms for each event, data were selected according to the signal-to-noise ratio, only stations with signal-to-noise ratios higher than 3.0 were retained. (2) The vertical component is deconvolved from the radial and tangential components to get the radial and tangential RFs for each station of each event. (3) All the available RFs for each station from different events were then divided into 9 groups according to back azimuth, and the grid-search algorithm is applied for groups with more than 5 events to get a point estimate the H and κ . (4) Groups with good multiples were then selected for the Moho-depth mapping. (5) Cross-sections are drawn for the relatively

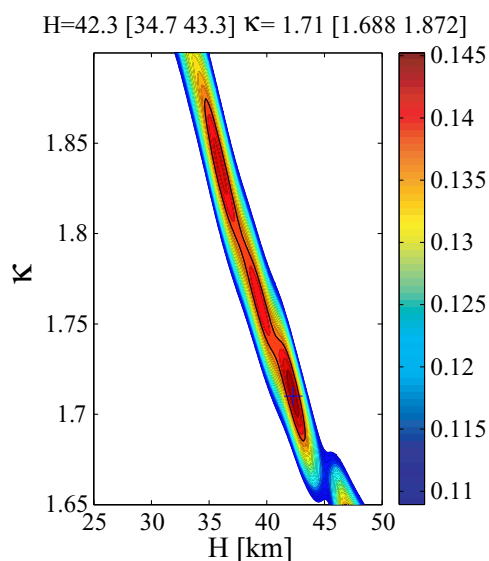
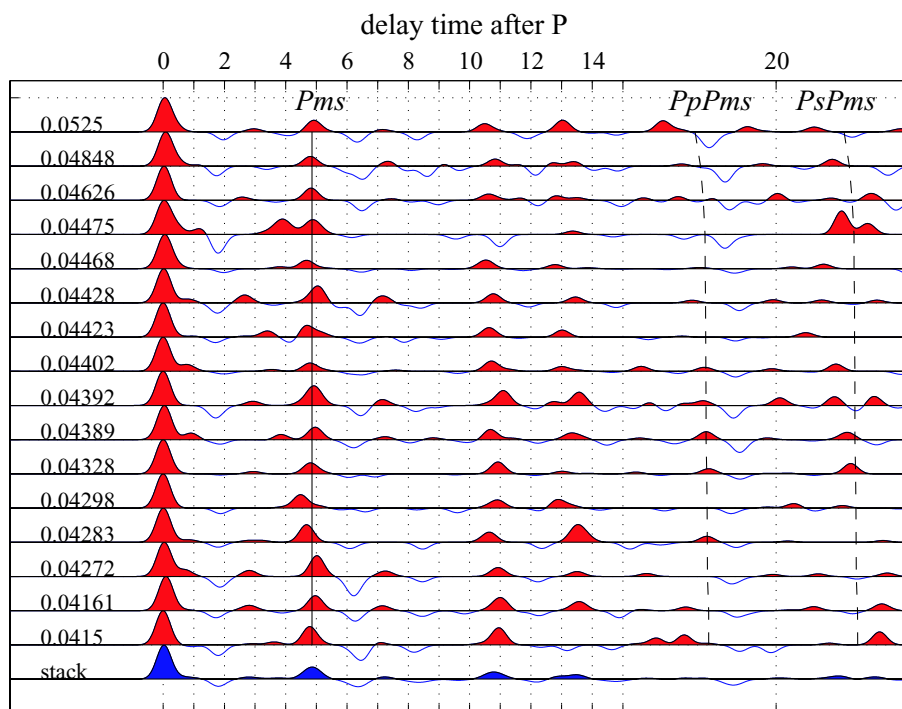
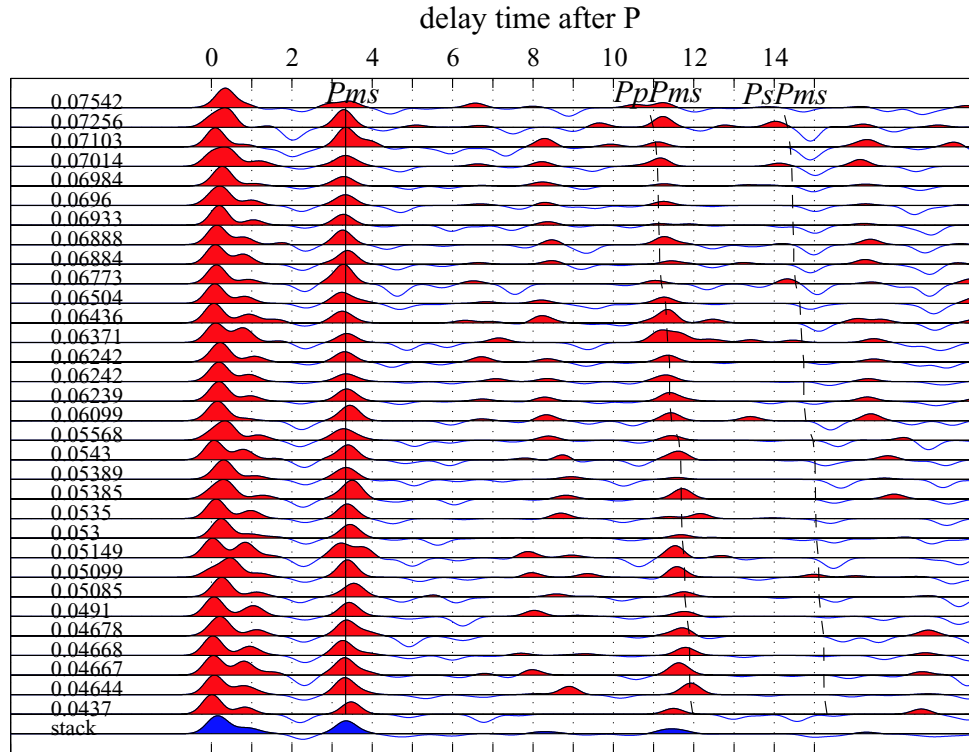


Figure 3.4 Bottom panel shows the $[H, \kappa]$ grid search function for the SW RF group of station VCS. The black cross shows the best estimated (H, κ) , which maximize the weighted summation function of Zhu and Kanamori [2000]. Colors represent the amplitudes of the function. The black contour line is the 95% maximum contour, which represents the uncertainty estimate for the picked (H, κ) . For this group of data, the 95% contour is very broad in the κ direction and the $[H, \kappa]$ domain grid search is not considered successful. Individual traces for this station group are shown on top, with the predicted arrival times from the picked (H, κ) marked by the dash lines. Multiples for this group are not well developed and this serves as an example of poor stacking groups. Station groups with similar attributes are excluded from the regional Moho mapping of Figure 3.6, but the bottom averaged stacked trace (the blue trace) is included in the following cross-sections.



$H=28.4$ [27.3 30.3] $\kappa=1.727$ [1.678 1.767]

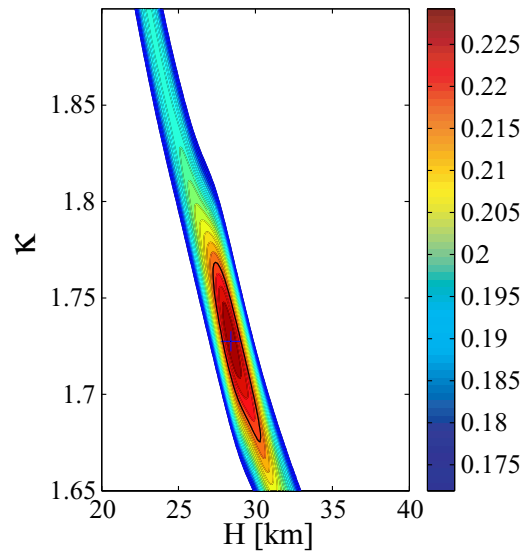


Figure 3.5 Similar to Figure 3.4, except this is an example of successful grid-search group. This group of RFs is the NW group of station PAS. For this group, the estimated Moho depth is 28.4 km, with uncertainty range [27.3, 30.3]. V_p/V_s ratio, κ , is estimated to be around 1.727, with uncertainty range [1.678, 1.767]. Note the V_p/V_s ratio is not very well constrained with this method. Individual traces of the RFs are shown on top, sorted according to ray parameter, and arrival times for the three phases Pms, PpPms and PsPms are marked by the dashed lines. Note that the Pms and PpPms are very well determined from this grid-search method. True arrival times for PsPms are a little bit later than those predicted from the picked (H , κ), probably due to small lateral heterogeneity in the crustal structure.

densely sampled areas.

3.3 Results

A total of ~ 250 stacking groups with well developed multiples were selected from more than 700 stacking groups for the SCSN data. None of the LARSE I or LARSE II passive station groups were selected due to the small number of available events and no distinguishing multiples. The Moho depth map derived from these well-constrained data points is shown in Figure 3.6. The final Moho depth, V_p/V_s ratio results for these good data points are listed in Table 1 of Appendix E. A large portion of the station groups in the western Peninsula Ranges, Mojave Desert, Southern Sierra and Walker Lane area are selected reflecting the relatively smoothness of the Moho interface in these areas. Most station groups in the western San Gabriel Mountains do not meet the selection criteria due to strong lateral heterogeneity in the crustal structure, and are thus excluded from the map. Several cross-sections are drawn to show the lateral variations of the crustal structure and are discussed in later sub-sections. Stations in the Great Valley, Salton Trough and the Los Angeles Basin were not included in this study due to complications in the RFs from resonances in the low-velocity sediments.

This study imaged similar broad-scale features reported in other studies [Cheadle et al. 1986, Li et al. 1992, Richards-Dinger and Shearer 1997, Zhu and Kanamori 2000]. Thinner crust of 20–22 km and 25–27 km exists close to the Salton Trough, and the eastern Mojave Desert respectively. The Moho is relatively flat in the western Mojave Desert and southern Walker Lane area with a depth of 28–31 km. Thick crust of 34–38 km is observed beneath the western Peninsula Ranges, the San Bernardino Mountains, and the western Sierra Nevada Mountains. In this study, however, the density of RF station groups provides more details of the crustal structure. In the following, results will be discussed in sub-sections according to geographical areas.

3.3.1 Southern Sierra Nevada and Walker Lane Belt

Substantial variations in the Moho depth are imaged beneath the southern Sierra Nevada and nearby Walker Lane fault zone. A deep Moho of 35–39 km is imaged beneath the western Sierra and the northern Walker Lane. The imaged deep Moho beneath the western Sierra Nevada and

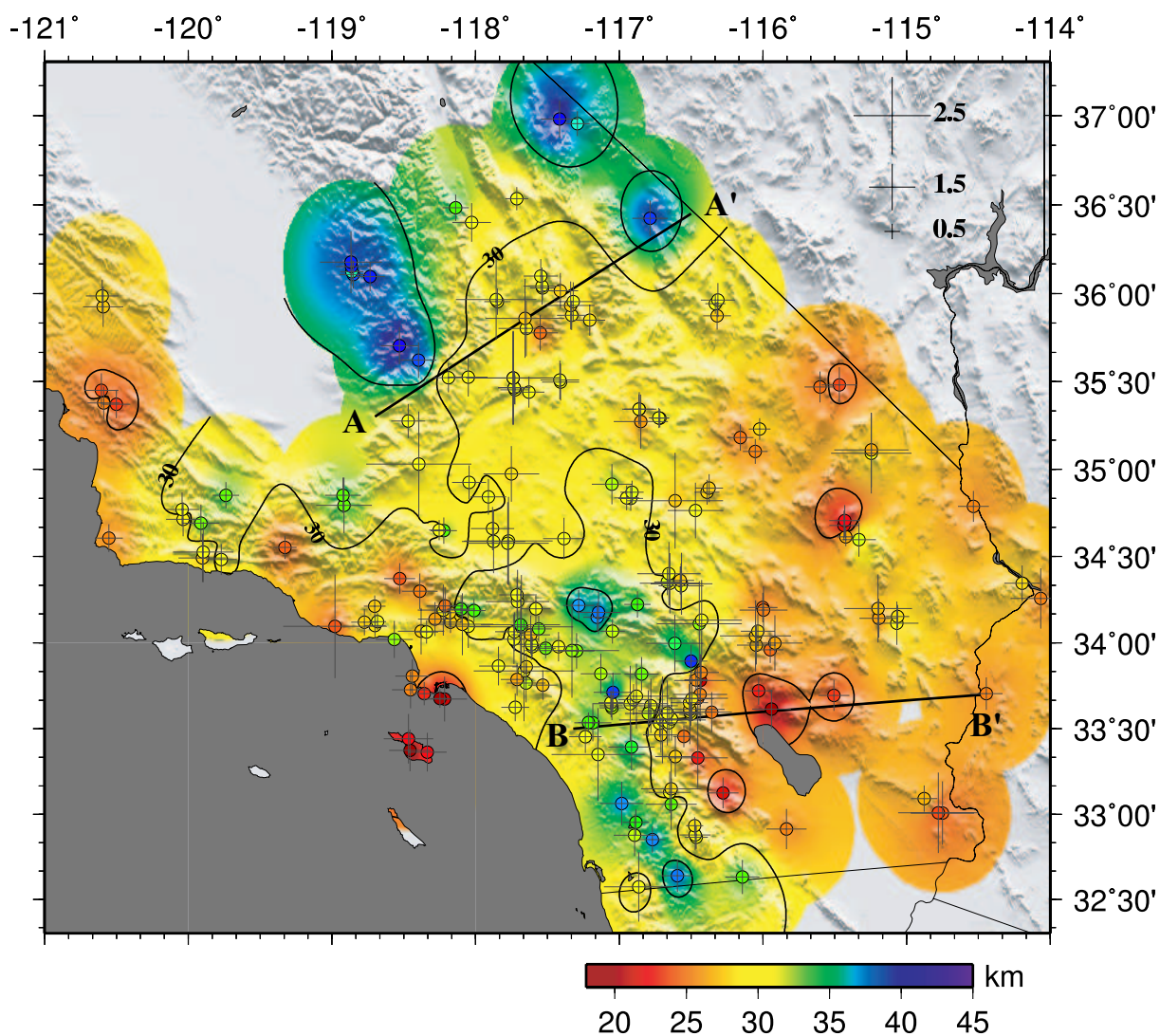


Figure 3.6 Map showing the interpolated Moho depth for the study area from selected data points that show distinguishable multiples. Circles represent the Moho conversion data points. An inverse distance algorithm is used to interpolate the data points over an area that is the union of all the circles centered at each data point with a radius of 30 km. Crosses at each circle represents the uncertainty of the Moho depth estimation at that data point from the 95% contour of the grid search. The uncertainty scale is given in the upper-right corner. The two black lines represent the locations of the two cross-sections in Figure 3.7 and Figure 3.8 respectively. AA' is the Sierra Nevada cross-section and BB' is the western Peninsula to Salton Sea cross-section.

its transition to shallower Moho to the east are similar to the RF studies by Jones and Phinney [1998] and the travel time tomography studies by Fliedner et al. [2000]. Large differences in the Pms arrivals are observed at station FUR, Furnace Creek, Death Valley (Figure 3.7 and Figure D.9), with a late Pms arrival at 5.0 sec for the SW group. Moho depth of 40 km and V_p/V_s ratio of 1.775 are inferred from the $H-\kappa$ domain grid-search algorithm for this group, with very well developed PpPms multiples (Figure D.11). The PsPms multiples are not well-developed and thus this group is not included in the regional map of Figure 3.6. For the SE group, a Moho depth of 38.8 and V_p/V_s ratio of 1.68 is inferred (Figure D.10), which share a similar deep Moho with the SW group but have a much lower V_p/V_s ratio. Similar deep Moho was previously imaged by the seismic travel-time tomography studies (line P3 of Fliedner et al. [2000]). The deep Moho imaged beneath the Death Valley by these two studies is very different from the shallow and flat Moho at ~ 30 km inferred from previous COCORP reflection studies [Allmendinger et al. 1983, 1987; Hauge et al. 1987; Hauser et al. 1987]. One possible reason for the difference is that the Moho may be below the illumination zone of the reflection studies. The difference in the picked V_p/V_s ratio for these two station groups of FUR indicates that there may be a problem with the Moho depth result beneath this station, but the clearly delayed prominent Pms phase for the SW group of station FUR relative to other station groups in the Coso geothermal area (Figure 3.7) does indicate the existence of a deeper Moho here.

The Moho seems to have a major step across latitude 36.5° , as it is relatively shallow at a depth of 28–31 km to the south in the Coso geothermal area, but deepens to the north. The shallow Moho in the Coso geothermal area is in accordance with previous tomography studies [Fliedner et al. 2000; Jones et al. 1994; Jones 1987] and COCORP reflection studies [Klemperer et al. 1986; Hauge et al. 1987; Hauser et al. 1987]. The deep Moho to the north in the eastern Sierra Nevada is similar to the 34 km Moho imaged by Fliedner et al. [2000] from local travel time tomography studies, but differs from the shallow Moho of 30 km imaged by Zandt et al. [2004]. This is probably due to the fact that some stations that show a deeper Moho, (such as CGO, where the Moho depth is about 33–35 km) were not included in Zandt et al. [2004] because they were not in operation during the PASSCAL experiment period. A cross-section with all the nearby station groups showing a consistent and prominent Pms phase is shown in Figure 3.7. Location of the profile is shown in Figure 3.6. It clearly shows the Moho depth variation pattern: deeper at both ends, and shallower in the Coso geothermal area. For this and

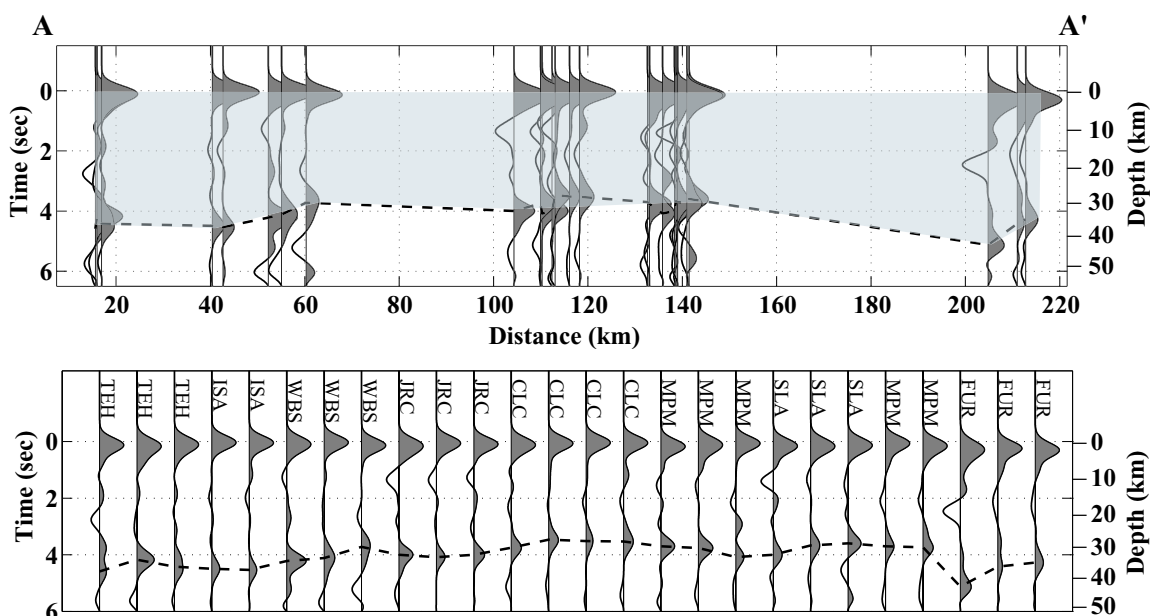


Figure 3.7 The average stacked RFs along the Sierra Nevada cross-section AA' in Figure 3.6. On the top, the traces are plotted according to their distances from point A. On the bottom, the traces are evenly spaced. The dash line represents the Moho P-to-S converted phase, Pms. The marked depth on the right is “pseudo” depth obtained by migrating the Ps-P time using the standard iasp91 model and it could be slightly different from the best-estimated depth from the grid-search algorithm because the velocity model used for the migration is not constant. Shallow Moho or earlier Pms arrival time is observed for stations in the central portion of the profile (JRC, CLC, and MPM), which locate very close to the Coso geothermal field.

the following profiles, the time-domain RFs were migrated into depth domain assuming the standard iasp91 velocity model.

3.3.2 Peninsula Range and the Salton Sea

In the Peninsula Range and Salton Sea area, the Moho depth pattern is similar to studies by Lewis et al. [2000, 2001] and Ichinose et al. [1996]. A sliver of deep Moho at 34–38 km is observed in the western Peninsula Ranges, and a shallow Moho of 20–25 km is found at the station groups surrounding the Salton Trough. The transition from the thick crust along the sliver in the western Peninsula to the thin crust surrounding the Salton Trough is relatively sharp, and the Moho is observed to get thinned from 34–38 km to 20–25 km within a lateral distance of less than 50 km (Figure 3.6). The relatively sharp transition of the Moho depth from the western Peninsula Ranges (WPR) to the Salton Trough and the fact that thick crust exists beneath the WPR, which was transferred onto the Pacific oceanic plate during the formation

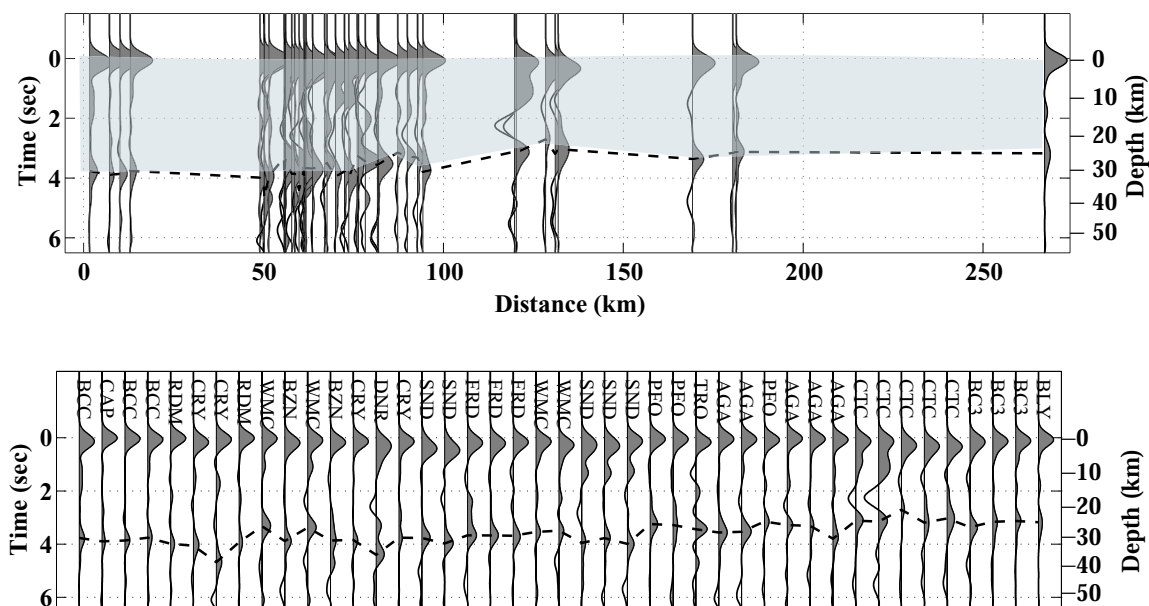


Figure 3.8 The average stacked RFs along the Peninsula-Salton Sea cross-section BB' in Figure 3.6. Similar to Figure 3.7, the traces are plotted with distance away from point B on the top, and are evenly spaced on the bottom. The shallowest Moho is observed on the northern tip of the Salton Sea at about 128km along the profile. Rapid variations in the Moho depth is observed on the west from western Peninsula Ranges to the western margin of the Salton Trough, while gradual shallowing of the Moho is observed on the east from the Salton Trough to the eastern Mojave Desert. An asymmetric extension of the Salton Trough is inferred.

of the San Andreas strike-slip fault system, indicates that the crust beneath the WPR is of continental origin and that the western movement of this block away from the stable North American continent involves the whole crust. A cross-section along 33.6° shows the lateral variations of the crustal structure across the Salton Trough (Figure 3.8). We extended the profile of Lewis et al. [2000] further east to a station at the California-Arizona border to show the asymmetric extension of the Salton Sea. A sharp transition is observed on the west, but a more gradual variation is found to the east and a relatively shallower Moho depth of 25–28 km is observed ~ 100 km to the east in the Mojave Desert. No prominent midcrustal interface is found along this profile. More details of the asymmetric extension of the Salton Trough and Moho depth variation in the western Peninsula Ranges are shown in Appendix C.

3.3.3 Mojave Desert and San Bernardino Mountains

For the Mojave Desert, a relatively flat Moho of 28–32 km is observed in the west, and slightly shallower Moho of 26–28 km is found for most station groups in the east across the southern

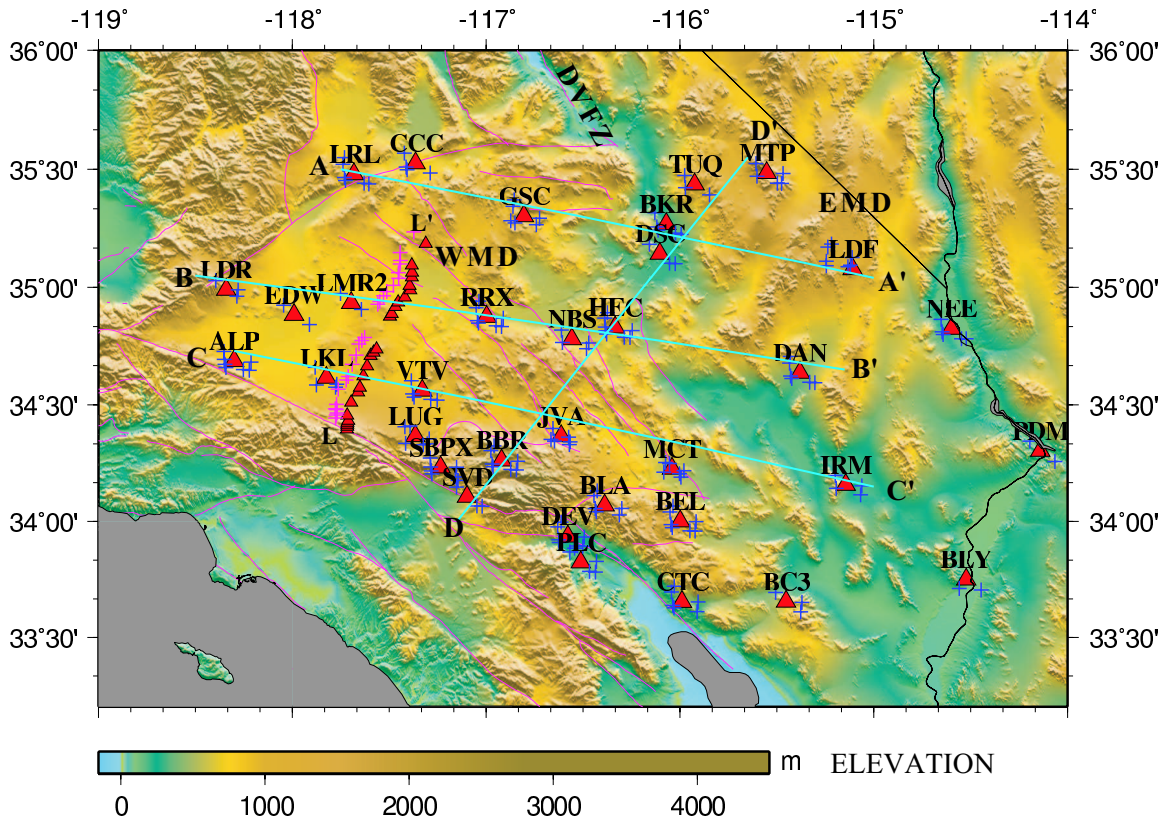


Figure 3.9 Topographic map of the Mojave Desert along with the stations and the surface projections of the Moho piercing points. Large triangles represent the SCSN stations with station names marked. Blue crosses are the surface projection of the Moho piercing points for different station groups. Small red triangles are LARSE I passive stations and crosses are the surface projection of the Moho piercing points for the NW event group. The green lines are the four cross-sections along which averaged stacked RFs are plotted in the following figures. WMD, Western Mojave Desert. EMD, Eastern Mojave Desert. DVFZ, Death Valley Extensional Zone. It is clear from this topographic map that the Western Mojave Desert and the Eastern Mojave Desert are separated by the topographic low of the southern extension of the Death Valley fault zone.

extension of the Death Valley fault zone, where the shallowest Moho within the province of $\sim 23\text{--}25$ km is inferred. A deep Moho of $34\text{--}39$ km is observed beneath the San Bernardino Mountains. Three E-W profiles and one N-S profile were constructed (Figure 3.9) to show the lateral variations of the crustal structure.

For the northern E-W cross-section AA' (Figure 3.10), Moho is flat beneath stations LRL and CCC at a depth of $29\text{--}31$ km, gets shallower beneath stations GSC and BKR, and reaches its minimum value of $23\text{--}25$ km beneath the eastern azimuth groups of BKR and DSC. Moho deepens and gets complicated further to the east, especially beneath the easternmost station LDF. A midcrustal negative pulse (corresponding to a negative-gradient velocity interface) in

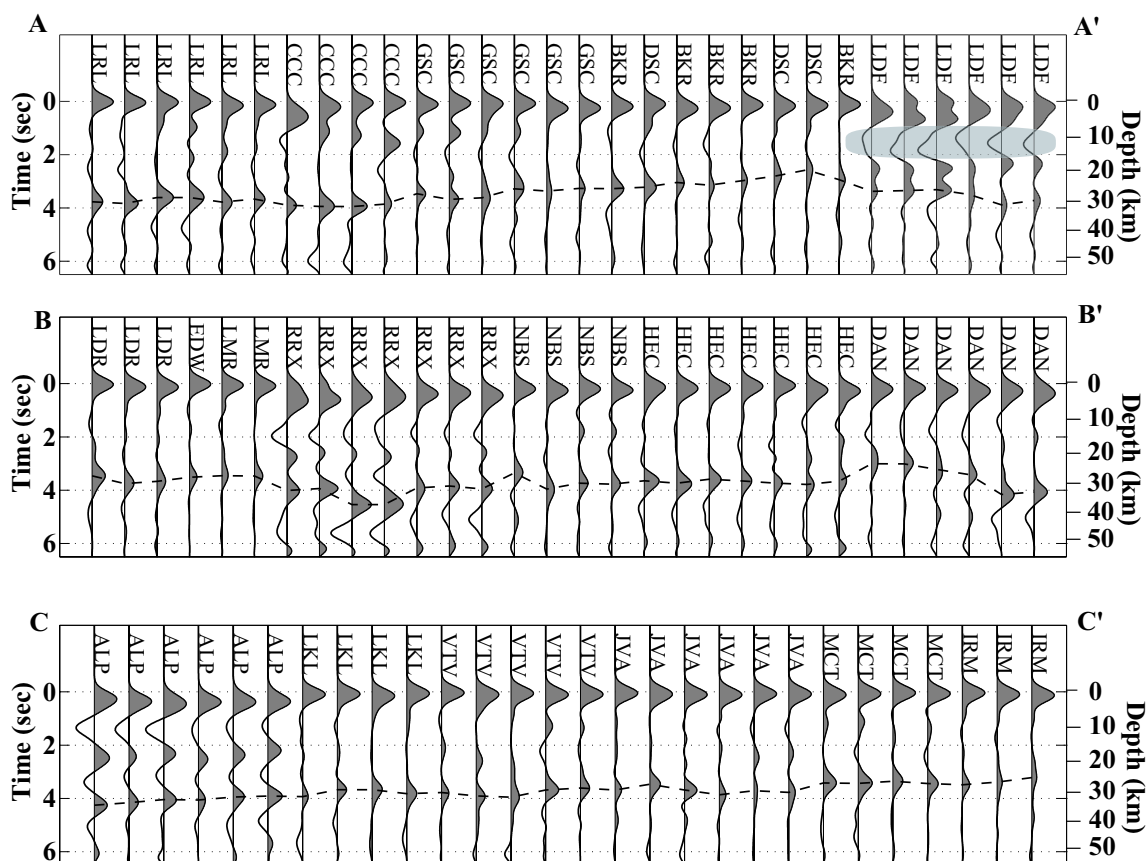


Figure 3.10 RFs along the three east-west profiles of Figure 3.9. From top to bottom, they are profiles AA' , BB' , and CC' respectively. The RFs are evenly spaced but sorted according their distance from the west end points. The dashed lines at around 3.5 to 5 sec are the Pms picks. The light gray shaded negative pulse on the east side of profile AA' represents a low-velocity zone beneath this local area. Note the shallowing of the Moho at GSC, BKR and DSC on the top profile and at DAN on the central profile. A sharp Moho depth jump is observed beneath station DAN. The apparent sudden Moho jump from HEC to DAN is not as sudden as it appears since the piercing points for these two groups are ~ 90 km apart.

the RFs is observed at ~ 1.5 sec (10–12 km) at station LDF, as well as an additional positive pulse at ~ 20 km (Figure D.4). The Pms arrival time for this station shows some large difference between events from NW and those from SE, with later arrivals observed for events from SE. The unusual RFs at station LDF indicate that the crustal structure in the east Mojave Desert beneath station LDF is different from that in the west and that the crustal structure is more complicated.

For the central line, the Pms has a relatively constant arrival time of 3.7–3.8 sec for most station groups except for station RRX and DAN. For station RRX, the Pms arrivals show large variations with back azimuth and a very late arrival time of 4.3–4.5 sec is observed for the two

SW groups. Multiple reverberations exist for these two groups and the two multiple phases — PpPms and PsPms are not clear, so the very late Pms arrival time could be the result of complications from the low-velocity sediments that are inferred to exist beneath this station from the apparent delay of the direct P wave in the radial RFs. A similar anomalous Pms arrival is observed for a LARSE I passive station and will be discussed later. At station DAN, a very large difference in the Pms arrival time is observed (Figure D.1), with a similar pattern to station LDF on the top profile. For events from NW, Pms has an very early arrival time of ~ 3 sec, corresponding to a Moho depth of ~ 20.5 – 22.5 km, but for events from the SE (Figure D.2), Pms arrives at 4.2 sec and a Moho depth of ~ 30.5 – 33.5 km is inferred (Figure D.3). This implies a ~ 8 – 10 km Moho offset between these two station groups over a lateral distance less than 15 km. For events from the SW direction, an intermediate Pms arrival time of 3.5 sec is observed. Clear PpPms multiples are observed for both the NW and SE groups, and the picked Vp/Vs ratios from the grid search are: 1.845 for the NW group and 1.805 for the SE group, which are very close to each other. This indicates that the imaged Moho step beneath this station is real and that the structure to either side of this station is relatively smooth. Also, the shallow Moho on the west side of station DAN is confirmed by the SmS-S travel time difference from the Hector Mine aftershock sequences by Hjorleifsdottir and Helmberger [2001]. Teleseismic travel times show that both P and S arrivals are delayed in the NW back azimuth, but have an earlier arrival time for events from SE, which excludes the possibility of ascribing the observed differential Pms arrival times to lateral variations in the crustal velocities and confirms the requirement of Moho step.

For the southern E-W line, the Moho is essentially flat and gets slightly shallower to the east beneath station MCT and IRM. A very prominent midcrustal interface is observed at the westernmost station ALP, which is similar to the midcrustal interface observed along the LARSE I line (discussed later).

The shallow Moho in the eastern Mojave desert was previously imaged by several studies [Zhu and Kanamori 2000; Richards-Dinger and Shearer 1997; Hearn and Clayton 1986b], but more details are presented here. The thinnest Moho in this region seems to correlate very well with the topographic low (Figure 3.9) of the southern extension of Death Valley fault zone. This confirms previous observations that active extension zones normally correlate with thin Moho and high geothermal activities [Abers et al. 2002]. Extensive Quaternary volcanic activity is

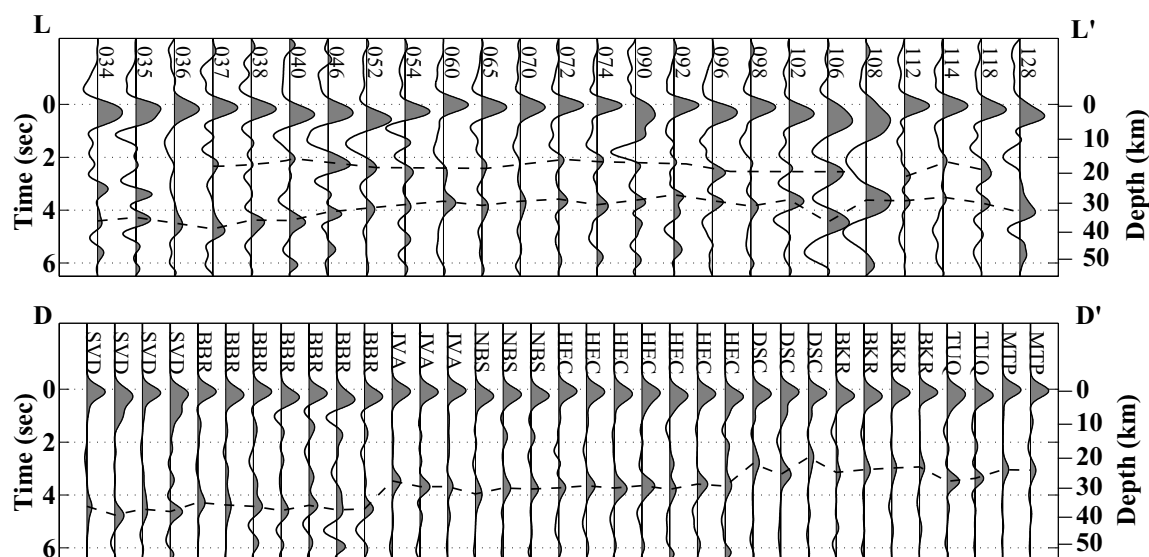


Figure 3.11 RFs along the LARSE I line and the N-S SCSN profile DD' in Figure 3.9. A deep Moho is observed at the southern station groups on both profiles (from 034 to 040 on the LARSE I profile and from SVD to BBR on the profile DD'). A consistent midcrustal interface is present along the LARSE I profile at about 2 sec. Note the two steps on the Moho along the profile DD' — from BBR to JVA, and then from HEC to DSC. The shallowest Moho on this profile (around DSC) correlates very well with the topography low at the southern extension of the Death Valley fault zone (Figure 3.9).

observed in the eastern Mojave Desert [Jennings 1975; Jennings and George 1994; Kaufman and Royden 1994], but is absent in the western Mojave Desert. These indicate that the eastern Mojave Desert is a very different tectonic province [Snow and Wernicke 2000] from the western Mojave Desert. The southern extension of the Death Valley zone in the Mojave Desert, however, seems to share some similarity with the active Salton Trough extensional zone. This could also be inferred from the high P_n velocities and early P_n arrivals the two regions share from the local P_n wave studies of Hearn and Clayton [1986b]. Whether the two fault zones are connected or not is not resolved here.

A negative phase (corresponding to a negative-gradient velocity interface) is observed just beneath the Moho on the SE groups of station DAN (BB' in Figure 3.10), which could be the upper boundary of a magma chamber or might indicate that the upper mantle lithosphere is thin in this area, similar to the thin warm lithosphere observed beneath the eastern Sierra [Wang et al. 2002].

A deep Moho of 34–39 km is observed beneath the San Bernardino Mountain along the SCSN N-S profile and its northern extension along the LARSE I profile (Figure 3.11). For the

SCSN station profile (DD'), two groups of a flat/ramp/flat pattern are observed at the Moho depth. A deep Moho of 34–39 km is observed beneath station SVD and BBR in the San Bernardino Mountains, which then shallows to 29–31 km in the western Mojave Desert beneath stations JVA, NBS and HEC, and reaches a depth of 23–26 km beneath station DSC and BKR in the southern extension of the Death Valley shear zone, and finally slightly deepens to 26–28 km further to the north. For the LARSE I profile, only the first step related to the shallowing from the northern extension of the San Bernardino Mountain root to the western Mojave Desert is observed. A flat Moho at 29–31 km and a low-amplitude midcrustal interface at \sim 18–20 km is consistently observed for most LARSE I stations (from station 037 to the north). The midcrustal interface might be correlated with the regional 6.3/6.7 interface determined by Hadley [1978]. Exceptions to the pattern are stations 106 and 108, which show very different RF waveforms and will be discussed in the following paragraph. The deep Moho imaged under the San Bernardino Mountains and the Mojave side of the LARSE I profile is most likely connected with each other at depth due to their close proximity, which indicates that the deep root of the San Bernardino Mountains extend further to the north, where no surface topographic high exists. A similar deep Moho is inferred by Zhu [2000] and Kohler and Davis [1997] from RF and teleseismic P travel-time studies respectively. However, there are some differences between these two studies concerning the San Gabriel Mountains part of the root, which will be discussed in the following sub-section.

Unusual RFs are observed at LARSE I stations 106 and 108, and SCSN station RRX. The Pms has a very late arrival time of 4.5 sec for station 106, and the Ps arrival time for the midcrustal interface is also delayed comparing with other western Mojave stations. This pattern is similar to the anomalous RFs observed at SCSN station RRX. For station 108, no midcrustal interface is observed and the Pms phase is much wider than others. If the stations are overlaid on the 2-D kinematic model [Dokka and Ross 1995], the two LARSE I stations fall on one of the openings between rotated blocks (Figure 3.12) and station RRX is on the junction of this NW oriented transtensional zone and another E-W one to the east. This indicates that either a deep basin develops in this opening or that the block rotation does involve the Moho. Another transtensional zone exists beneath station 096, but RFs for this station do not show any anomaly (Figure 3.12), which indicate that depth extension of the openings in Dokka's kinematic model are different.

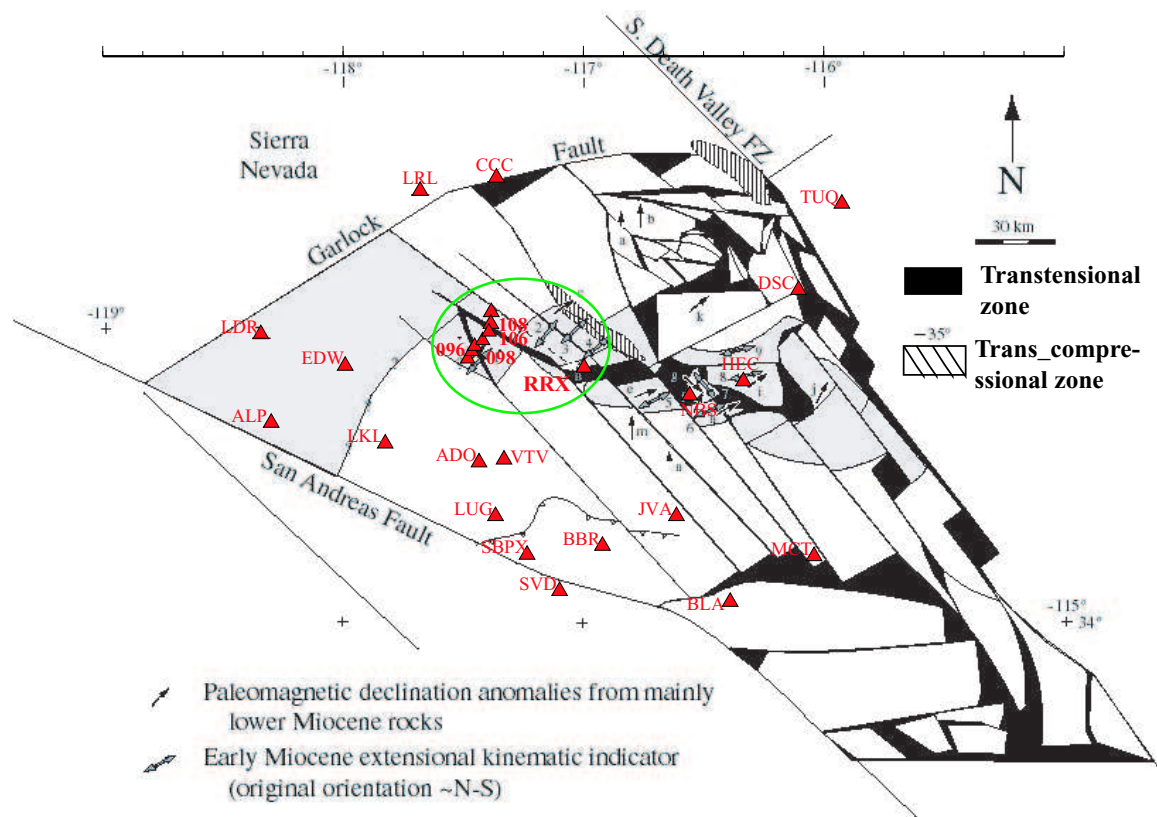


Figure 3.12 Stations in the Mojave Desert were plotted on the 2-D kinematic model [Dokka and Ross 1995] to show the coincidence of the three stations (106, 108 and RRX within the green circle) that show unusual RFs with the narrow transtensional zones in Dokka's kinematic model. Note that another LARSE I station 096 also sits on a narrow transtensional zone to the south of where 106 and 108 sit, but RFs for this station are similar to those of other stations, indicating that differences exist among these transtensional zones.

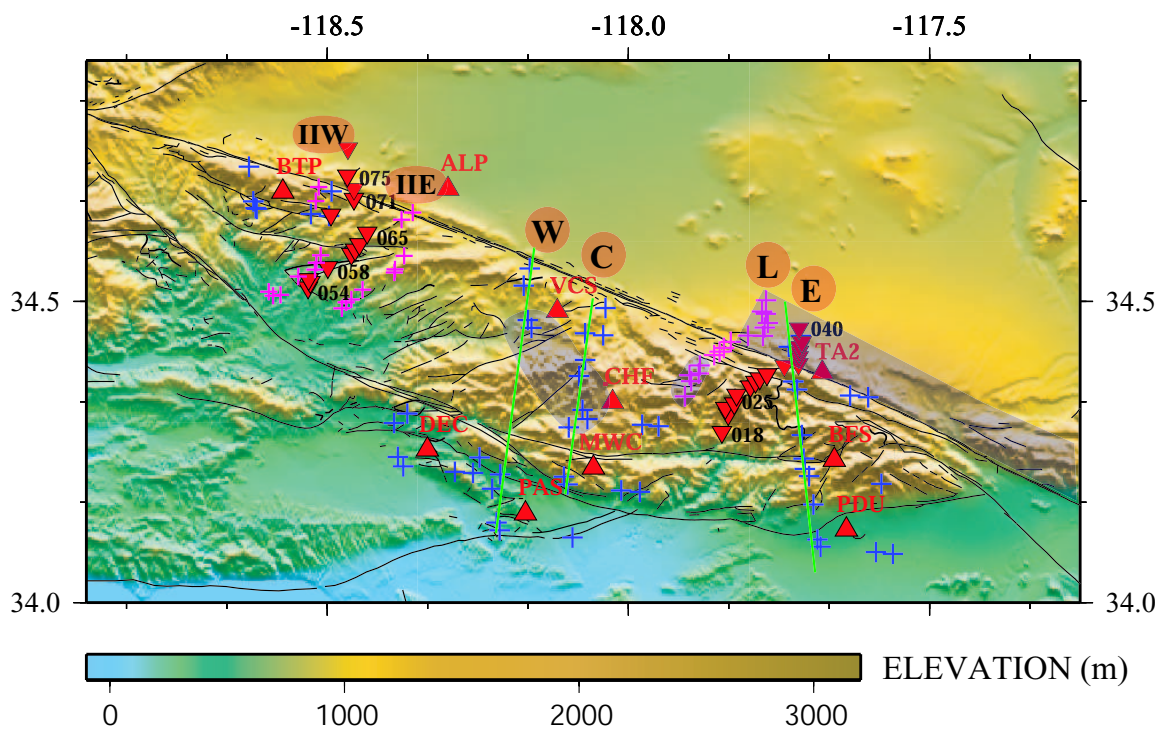


Figure 3.13 Topographic map of the San Gabriel Mountains along with the stations and surface projection of the Moho piercing points. Red triangles are the SCSN stations and inverted triangles are the LARSE passive stations, with station names marked for all the SCSN stations and representative LARSE stations. Crosses are the surface projection of the Moho piercing points, with blue ones for the SCSN stations, pink ones for the LARSE stations. The three green lines are the three profiles along which RFs are plotted in Figure 3.14. The shaded areas represent the local mountain roots imaged by this study and the large one to the north of the San Andreas Fault is related to the San Bernardino Mountain. Station groups in the non-shaded area have a relatively shallow Moho of 30–34 km.

3.3.4 San Gabriel Mountains

Most stations in the San Gabriel Mountains show large variations in the Pms arrival times with back azimuth (Details are shown in Appendix B). RFs for a typical station, VCS, are shown in Figure 3.3. Pms has an early arrival time of 3.7–4.0 sec for events from SE and NW, but has a late arrival time of 4.8 sec for events from SW. No clear multiples are observed for any of the three groups. Other station groups in the western San Gabriel Mountains are also missing multiples, and consequently none of the station groups are qualified for the Moho depth mapping in Figure 3.6. Since clear Pms arrivals and other midcrustal phases are prominent for these station groups, three N-S cross-sections were constructed from the SCSN stations, as well as 3 profiles from the LARSE stations (Figure 3.13).

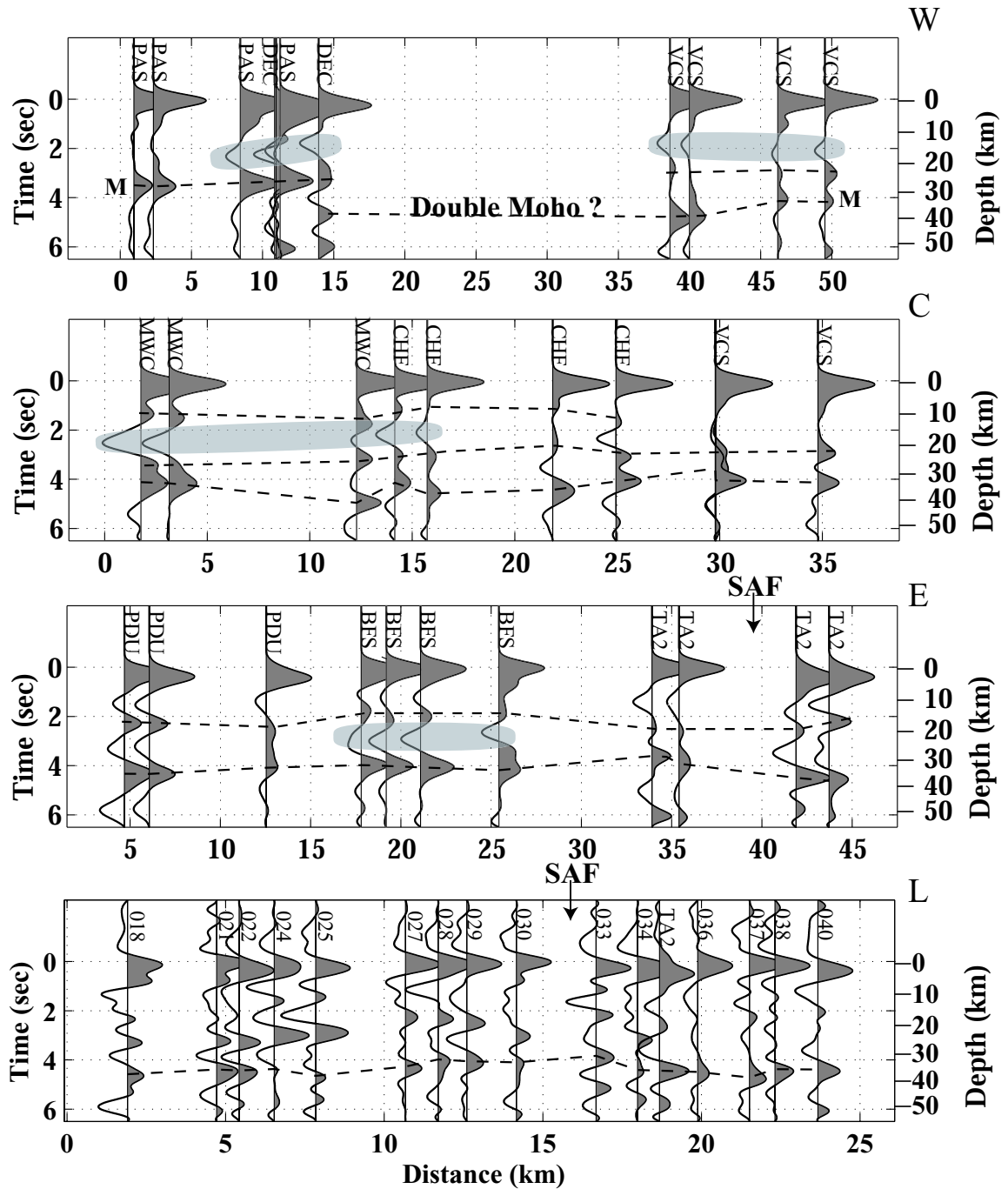


Figure 3.14 RFs along the three N-S profiles of the SCSN station groups and the LARSE I profile. From top to bottom, they are for the Western, Central, Eastern and LARSE I profiles. Moho Pms phases and midcrustal interfaces Ps phases are marked by the dashed lines. The shaded areas show the negative velocity-gradient interface. Note the large differences in the RFs along the LARSE I profile, between the southern and the northern station groups along the western profile and those between the central and eastern profiles.

Large variation in the crustal structure is inferred by comparing RFs along the four profiles in Figure 3.14, especially from those between the north and south station groups on the western profile and those between the eastern and central profiles. For the eastern profile, only one midcrustal interface at about 16–18 km is commonly observed, which corresponds to a two-layered crustal structure. Two midcrustal interfaces, however, are imaged for the central profile, corresponding to a 3-layered crustal structure. Depths to the two interfaces are 8–10 km and 22–25 km respectively. The midcrustal interface on the eastern line has a similar depth to the midcrustal interface (6.3/6.7 interface) of the Hadley and Kanamori [1979] standard Southern California model. For the central profile, the second positive midcrustal interface that is immediately below a prominent negative pulse is almost constant in time for all the RF groups, indicating a flat interface at 22–25 km. There is a fairly well-resolved image of the transition from the 3-layered structure to the 2-layered structure along the LARSE I profile (Figure 3.14 L). The second midcrustal interface shows up very clearly at stations 018 to 025, as well as the top one at stations 021, 024 and 025, but only one midcrustal interface is apparent at about 2.2–2.3 sec for stations 027–029, which is similar to the RFs on the eastern profile. Arrival times for the Pms phase, and thus the Moho depths, are also different for these two profiles, as well as for stations along the LARSE I profile. The Moho is relatively flat at 32–34 km for the southern groups of the east profile, and shallows to 29–31 km for groups close to the San Andreas Fault, but it is rougher and has a local deep Moho of 35–38 km in the middle part of the central profile. The southern station groups (018–022) of the LARSE I profile also show a deep Moho of 35–38 km, but the interpretation of the two further north stations, 024 and 025, is controversial. If Moho Pms is the phase that has the largest amplitude between 2.5 and 5.0 sec, then the lower midcrustal interface at 2.7–3.0 sec should be the Moho Pms and thus a very shallow Moho of 23–25 km is inferred, as interpreted by Zhu [2000]. However, if continuity of the interfaces is assumed, then this large amplitude interface seems to correlate very well with the 2.8–3.0 lower crustal interfaces for stations 018–021, and the later interface, which has a much smaller amplitude, arriving at 4.8–5.0 sec is interpreted to be the Moho Pms. A relatively deep Moho of 35–38 km is thus inferred for these two stations, similar to the stations further to the south (018–021). On the LARSE II profile, Zhu [2002] found that there was significant amplitude contrast for the Pms phase across the San Andreas Fault, with a low amplitude Pms phase imaged beneath the Liebre-Sawmill Mountains. Complications in the crustal

structure beneath the San Gabriel Mountains may also contribute to the low-amplitude of the Pms phase due to diffraction. Consequently the deeper low-amplitude interface on 024–025 can be a candidate for the Moho, which is our preferred interpretation. For the 4 further north stations (027–030), Moho is relatively flat at a depth of 32–34 km, similar to that inferred for the eastern profile. The large variations in the RFs along the LARSE I profile confirm that large lateral heterogeneity exists in the crustal structure beneath the San Gabriel Mountains.

Dramatic changes in the Pms arrivals are observed between the northern and southern station groups along the western profile (Figure 3.14). Pms has an early arrival time of 3.6–3.8 sec for the southern station groups, corresponding to a Moho depth of 27–29 km, but changes to a value of 4.8 sec, corresponding to a Moho depth of \sim 38 km, beneath the SW station groups of VCS in the middle, and then back to 4.0 sec further to the north for the NW groups of stations VCS. A midcrustal interface at about 23 km is observed for all the station groups of VCS, which is absent for the southern groups. A deep interface at about 5.0 sec is observed for the northern station group of DEC, which could be linked to the Pms phases for the SW groups of VCS to the north. The midcrustal interface at \sim 3.0 sec in the north may also be linked with the Pms phase for the southern groups if a south-dipping interface is assumed. One interpretation for this "double Pms" feature is a double Moho structure, the top one corresponds to the oceanic Moho and the lower one corresponds to the continental Moho. This might be a reasonable interpretation since oceanic crust is inferred to exist in this area indicated by the wide-spread surface exposure of lower plate Pelona Schist [Malin et al. 1995]. Similar structure has been imaged from RF studies beneath Himalaya by Schulte-Pelkum et al. [2005]. Since no in-between stations exist, it is difficult to draw a definite conclusion on this.

The SW and SE back azimuth groups for some of the LARSE II passive stations are shown in Figure 3.15, as well as the E groups of SCSN station BTP. A flat Moho of 31–33 km is seen for the SW groups and 28–31 km for the SE group. The four southern most stations on the SW group show complicated RFs probably due to the influence from the nearby Soledad basin (Figure 3.15). A 3-layered structure is inferred for most station groups for both profiles and a prominent negative pulse is observed on station 073 and 075 on the SW profile, as well as two SE groups of station BTP. The arrival time of this negative phase indicate that it is at a depth of \sim 15 km, which is similar to those observed along other profiles, which are discussed below. Amplitudes for the receiver functions for events from the NW direction are generally low as

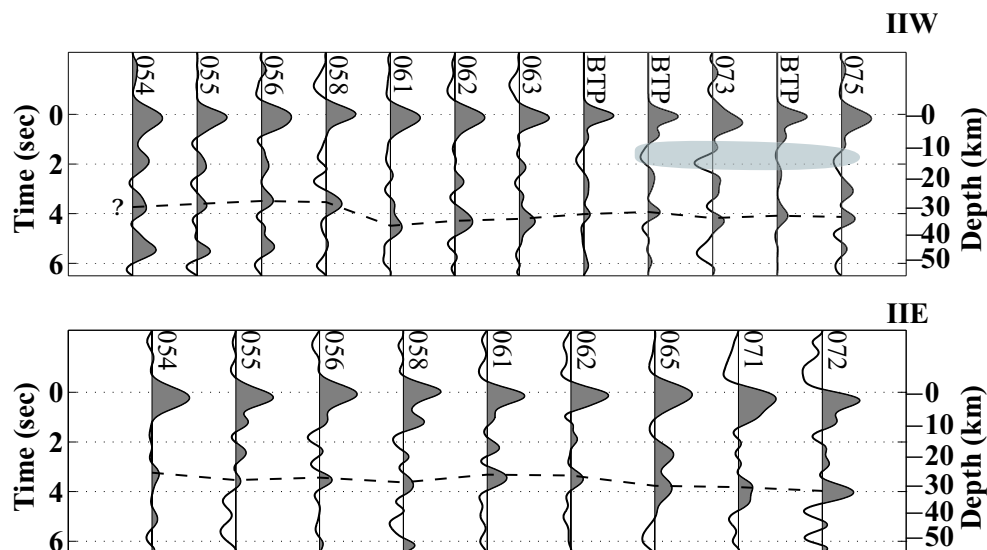


Figure 3.15 RF profiles for the SE and SW group of the LARSE II stations. Note the similarity among the SE group receiver functions and SCSN station BTP. They all show 3-layered structure. The SE station groups sample the deep structure beneath the Pelona Schist. Also, note the difference in the RFs for station BTP with those for station ALP in the Mojave Desert (Figure 3.10), indicating the difference in the crustal structure beneath the San Gabriel Mountain to that beneath the Mojave Desert across the San Andreas Fault.

described by Zhu [2002], so, they are not presented in this study.

A midcrustal negative pulse is commonly observed on the station groups along the three SCSN profiles (Figure 3.14). Arrival times for this pulse vary from 1.9 to 3.0 sec, corresponding to a depth of 15 km to 24 km, which is very similar to the bright spot in the San Gabriel Mountain imaged by Ryberg and Fuis [1998] on the LARSE I reflection profile. In this study, this bright interface is determined to be locally dipping to the SW-S from both the arrival times of this interface along the profiles and the amplitude variations of this interface on the radial and tangential components of the RFs for stations MWC and CHF. RFs for station MWC are shown in Figure 3.16. Three reflectors were imaged at the top of the bright reflective zone by Ryberg and Fuis [1998], and they were interpreted to be gently north dipping based on the clear north dip of the northern portion of the interface. However, gently S dipping of the interface is actually clear from their image for the southern portion of the interface [Ryberg and Fuis 1998] and thus it is in agreement with this study. This indicates that the bright spot is probably not a simple planar interface, but probably forms a dome shape, as indicated by the reflection image [Ryberg and Fuis, 1998]. No clear corresponding negative pulse is observed in the LARSE

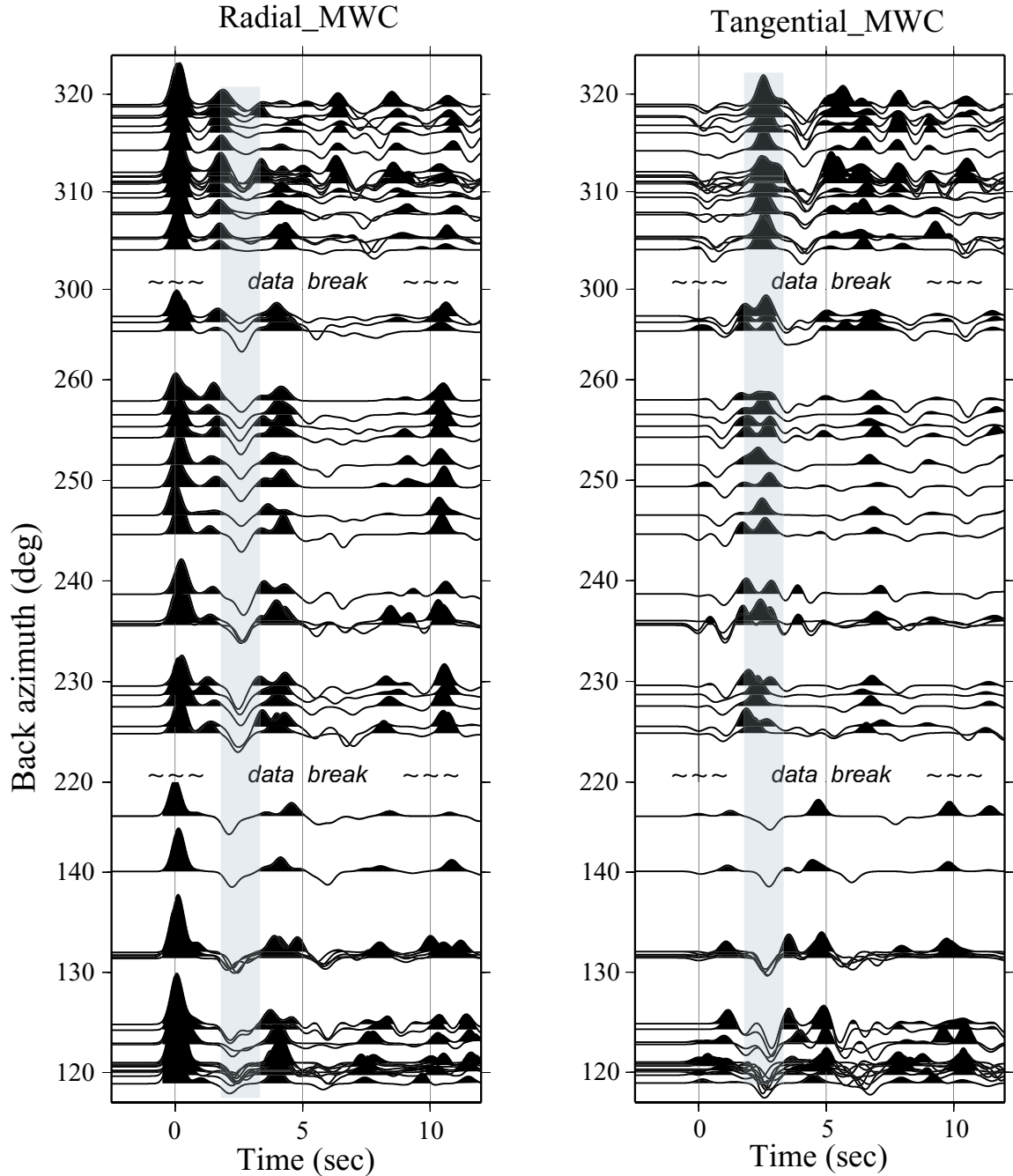


Figure 3.16 Radial and tangential RFs for station MWC (Mount Wilson) in the San Gabriel Mountains. Note the amplitude variation of the midcrustal interface at 1.8–2.0 sec (shaded). The amplitude of this phase is largest for RFs at back azimuth ~ 220 – 230 on the radial component, and diminishes for the SE and is almost zero for the NW. For the tangential component, the amplitude of this phase is higher for the back azimuthal groups of 300 – 320 and 120 – 145 , with reversed polarity, and a much smaller amplitude is observed on the back azimuth range 225 – 260 . The amplitude variation of this phase on both components indicates that it is a SW-S dipping interface. Since there are some gaps on the back azimuthal coverage, the exact dip direction is not very well constrained.

I profile probably due the fact the events we use here are from the updip direction (NW) of this interface, which, in theory, has a small or zero amplitude [Savage 1998]. This bright spot (negative pulse) is interpreted, by Ryberg and Fuis [1998], to be a 'master' decollement that separates the Pelona Schist from lower continental crustal rocks. It is also imaged at the SE station groups of station BTP and the SW groups of some LARSE II passive stations (073 and 075) in the Liebre-Sawmill Mountains (Figure 3.15). Arrival time for the interface is slightly smaller at ~ 2 sec, (13–15km). Thus, the bright spot seems to be a common feature beneath the Central Transverse Ranges. Ryberg and Fuis [1998] also imaged a positive polarity event for shot 8330 along the LARSE I profile at 0.2 sec later than the bright reflector and thus constrain the thickness of the low-velocity layer to be around 500 m. An approximate constraint on the thickness of this layer can be made from this study if the positive phase below the bright spot along the central SCSN profile (Figure 3.14) is assumed to be the bottom of the Pelona Schist — the depth distribution of the Pelona Schist is then constrained to be between 19–21 km and 23–25 km, a thickness that is much larger than that from the reflection study [Ryberg and Fuis 1998].

3.4 Discussion

By observing the available RF station groups in the San Gabriel Mountains, one common conclusion can be drawn—the crustal structure in the San Gabriel Mountains is strongly lateral heterogeneous, which is indicated by the following evidence: (1) Large variations of the Pms arrival time with back azimuth for stations in the western San Gabriel Mountains (such as VCS and CHF); (2) No prominent primary Pms phases for some station groups and no well-developed multiples exist for most station groups in the western Gabriel Mountains; (3) A transition from 2-layered to 3-layered crustal structure from eastern to western San Gabriel Mountains; (4) Large variations in the RF station groups along the LARSE I profile and the western SCSN profile (Figure 3.14). Another indication of the complicated crustal structure beneath the San Gabriel Mountains is the observation of systematic variations of the RFs with ray parameter for certain station groups. An example is the WNW station group of BFS. For this group, a single larger amplitude Pms phase is observed for RFs with small ray-parameter (close to station BFS) branches into two smaller amplitude phases for RFs with larger ray pa-

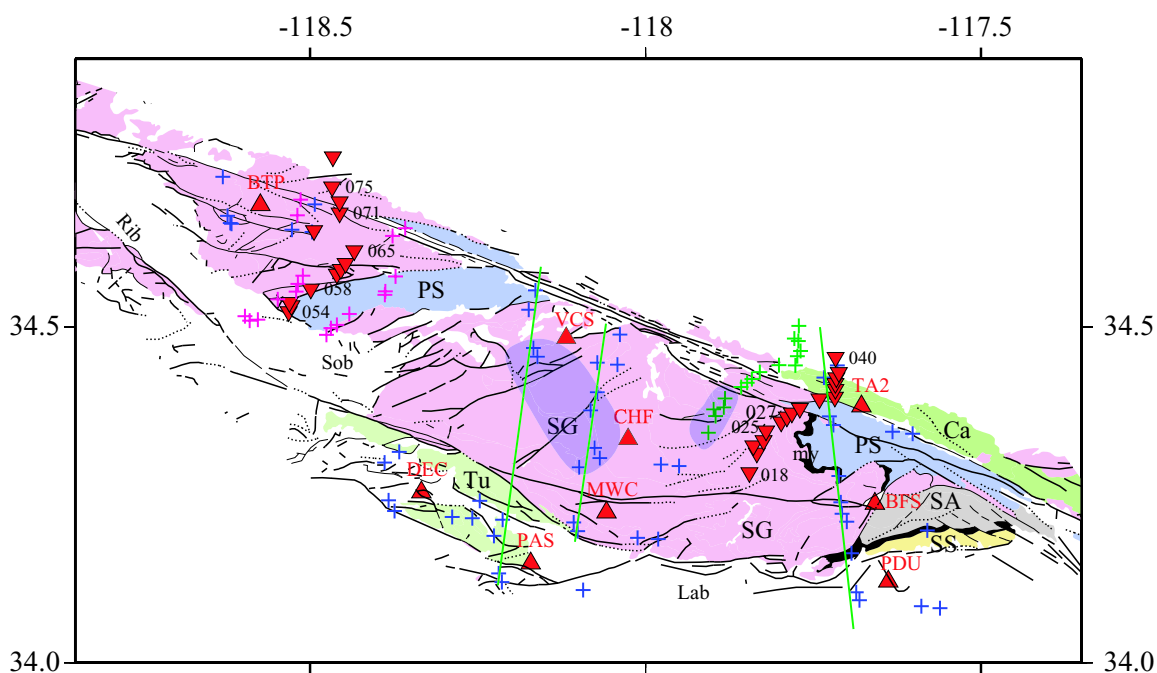


Figure 3.17 Stations and their piercing points were mapped onto revised geological terrane map of Dibblee [1982b]. Symbols are the same as those in Figure 3.13. The bold black characters are basement terrane names. SG, San Gabriel terrane; SA, San Antonio terrane; SS San Se-vaine terrane; Tu, Tujunga terrane; my, mylonite; PS, Pelona Schist terrane; Ca, Cajon terrane. Cenozoic sedimentary basins are also marked. Lab, Los Angeles basin; Sob Soledad basin; Rib, Rideg basin. Shaded areas are the local deep Moho imaged from this study.

rameters (≥ 0.065). This is caused by the existence of a notch structure on the Moho and details are discussed in Chapter 4.

Complications in the subsurface structure seem to correlate very well with the surficial geology of the basement terrane map [Dibblee 1982b] for the San Gabriel Mountains (Figure 3.17). One example is the WNW station group of BFS. BFS sits slightly to the south of the Vincent Thrust Fault—the fault that separates the lower plate Pelona Schist terrane from the San Antonio terrane. A large contrast in the crustal structure is thus inferred across this station, with the lower plate Pelona Schist to the north and Mesozoic granite rocks to the south. Complications in the Pms phase on the WNW RF group of station BFS and its inference of a Moho step across the depth extension of the San Gabriel Fault (Chapter 4) with shallower Moho in the north correlates with the surficial geology of lower plate Pelona Schist being either exposed at surface or residing at shallow depth north of station BFS very well. Stations on the eastern and central profiles are also mapped onto different terranes, which can explain the large contrast in the crustal structure between these two profiles. Though the three stations on the

central profile all sit on the San Gabriel terrane, some major faults, such as the Pelona fault to the WNW of station VCS, cut through their piercing points, which could contribute to large variations in the Pms arrival times at these stations. The northern and southern groups of the station groups along the western line also sit on different terranes. The different terranes were proposed to have distinctive tectonic evolution history and were juxtaposed together from distant locations [Ehlig 1981; Dibblee 1982]. Hence, the crustal structure imaged from RFs in this study shows some correlation with the surficial geological data, which indicates that strong coupling probably exists between the upper and lower crust beneath the San Gabriel Mountains and that the pre-juxtaposition structures of the different terranes have strong influence on the current subsurface crustal structure in this area.

There have been some controversial results on whether the San Gabriel Mountains have a root. Kohler and Davis [1997] inferred that a deep root of 40 km centered at the San Andreas Fault from teleseismic P arrival time residuals along the LARSE I line. Zhu [2000] imaged a shallow Moho of 24–31 km for the San Gabriel side, and a deep Moho of 37–40 km for the Mojave side along the LARSE I profile from teleseismic RF studies. Results from this study indicate that there are large lateral variations in the crustal structure beneath the San Gabriel Mountains and that the Moho reaches a depth of 35–39 km beneath some local areas in the western San Gabriel Mountains. Location of the inferred deep Moho is shown in Figure 3.13. No regional deep root exists beneath the San Gabriel Mountains, especially beneath the highest eastern San Gabriel Mountains, where a Moho depth of only 32–34 km is determined. The teleseismic P travel delay patterns observed by Kohler and Davis [1997] can be partially explained by the large upper mantle high velocity anomaly beneath the Transverse Ranges imaged by Humphreys et al. [1984] and Kohler [1999]. Existence of such a large narrow high velocity anomaly will certainly contribute to the earlier arrivals for stations passing through it. The absence of a regional root is consistent with the complete Bouguer gravity anomaly in this area [Langenheim 1999; Wooley and Langenheim 2001]. The wide existence of a shallow Moho beneath most station groups in the San Gabriel Mountains indicates that the crust of the SGM is most probably not involved in the down-welling of the sub-crustal lithosphere and thus supports the decoupling kinematic model of Humphreys and Hager [1990].

This study confirms the result of the previous study by Zhu [2000] that the San Andreas Fault as well as the San Gabriel Fault and some other major faults in the San Gabriel Mountains

does extend to the Moho and cut through the whole crust. Large offset in the Moho is observed both across some major faults, such as the San Andreas Fault, and beneath some individual stations where no major faults exist on the surface. Examples for the former case include the large variations in the RFs among stations along the LARSE I profile, among different back azimuth groups for stations TA2, VCS and other SCSN stations in the San Gabriel Mountains (Figure 3.14). Evidence for the depth extension of the major faults to the Moho is also apparent from the differences in the RFs for nearby stations that are separated by the major faults. One example is for station ALP (Mojave side, Figure 3.10) and BTP (San Gabriel side, Figure 3.15), which are separated by the San Andreas Fault and are ~ 25 km apart. For station BTP, two midcrustal interfaces exist at depths 10–12 km and ~ 20 km, and Moho is relatively shallow at about 31 km. For station ALP (Figure 3.10), only one large amplitude midcrustal interface is observed and Moho is about 34 km deep, indicating the large difference in the crustal structure beneath these two stations. An example of large offset on the Moho, where no major fault is evident on the surface, is station DAN in the eastern Mojave Desert (Figure 3.10), where a large offset of 8–10 km is observed between the NW and SE RF groups. Large variations in the lower crustal structure can also be inferred from the RF data, such as the transition from 2-layered structure on the eastern profile to 3-layered structure in the central profile beneath the San Gabriel Mountain (Figure 3.14), and the sudden appearance of an additional lower-crustal interface at ~ 20 km beneath station LDF in the eastern Mojave Desert (Figure 3.10). All these large lateral variations in the lower crust and the Moho indicate that either the lower crust or the upper mantle are sufficiently strong to resist the shear stresses induced by lateral heterogeneity in the lower crust and the Moho.

On the regional map of Figure 3.6, uncertainty in the Moho depth from the grid-search algorithm, which is less than 2 km for most station groups, is shown. Another source of uncertainty for the Moho depth estimation is from the average crustal P velocities. For consistency, the average crustal velocity is assumed to be 6.3 km/s for all stations. However, from studies of Hadley [1978], Hearn and Clayton [1986a, 1986b], Hauksson [2000] and Godfrey et al. [2002], the average crustal V_p varies from about 6.2 beneath the Sierra Nevada to about 6.5 km/s beneath the San Gabriel Mountains and the western Peninsula Ranges. So, uncertainty in the average V_p will add approximately additional ± 1.0 km in the Moho depth estimation. This additional ± 1.0 km will not change the lateral variation pattern of the regional Moho map in

Figure 3.6, since most of the large variations in the Moho depth are more than 4 km. Another issue for the study area is the influence of low-velocity sediments on the receiver functions and their further influence on the estimation of Moho depth. For stations sitting on thick sediments, especially those with complicated geometries (stations in the Los Angeles Basin for example), poor quality RFs were produced due to scattering and reverberations and consequently were not included in this study. For stations covered with thin sediments, such as ALP (Figure 3.10), reasonable RFs are produced, but the primary P arrivals in the RFs are shifted from zero due to the large amplitudes of the P to S conversions from the sediment-basement interface and its closeness in arrival time with the direct P. Under this situation, arrival time of the Pms phase is not influenced, the estimate of the average crustal V_p might be slightly overestimated since the existence of the sediments will reduce actual average V_p . The Moho depth will be overestimated by a maximum of 0.5 km and the Moho depth variation pattern in Figure 3.6 will only be slightly altered.

One general problem for all the profiles is lateral variations in the V_p/V_s ratio. Large deviations of the V_p/V_s ratio from the standard iasp91 model can change the migrated depth domain RFs, such that the large differences in the Pms arrival times could be explained by lateral variations in the V_p/V_s ratio instead. However, it is very unlikely for the different Pms times to be caused by large variations in the V_p/V_s ratio alone, especially for those RF groups for the same station (such as the Moho jump inferred for station DAN), because rays from different directions converge to each other at shallower depth (≤ 10 km) and V_p/V_s ratios for the different rock types, except the San Gabriel anorthosite complex, all lie within the range of 1.67–1.756 (converted from the Poisson's ratio of Pellerin and Christensen 1998).

3.5 Conclusions

High resolution lateral variations of the crustal structure in Southern California are imaged from back azimuth grouped receiver function studies for both the SCSN stations and LARSE passive stations. Large lateral variations in the crustal structure are imaged both beneath individual geographic provinces and across the major faults that separate the different provinces. Large variations in the crustal structure are especially prominent beneath the San Gabriel Mountains, across the San Andreas Fault, across the southern extension of the Death Valley fault zone in

the Mojave Desert and in the transition from western Peninsula Ranges to the Salton Trough.

Large lateral variations beneath the San Gabriel Mountains (SGM) are inferred from several types of evidence: (1) The existence of local deep Moho beneath some station groups in the western SGM and the absence of it beneath other stations as well as beneath the eastern SGM and Liebre-Sawmill Mountains. (2) Large variations in the Pms arrival times with back azimuth for the same station. (3) Systematic variations of the Moho Pms phase with ray-parameter for the certain station groups. (4) No well developed multiples for most station groups in the western San Gabriel Mountains. (5) A transition from 2-layered crustal structure to a 3-layered structure from eastern SGM to western SGM. The correlation of the complicated RF variation pattern with the surficial basement terrane distribution indicates that strong coupling exists between the upper crust and lower crust in this area, and the crustal structure (Moho depth) inherits a lot from the original terranes. The absence of a deep Moho beneath a large portion of the station groups in the San Gabriel Mountains indicates that no regional-scale deep root exists in this area and thus weak coupling or decoupling is inferred on a 20–30 km scale for the crust and upper mantle in this area. This study also indicates a wide spatial distribution of the bright spot beneath the San Gabriel Mountains with a dip direction of SE-SW in the southern part of the western San Gabriel Mountains.

RFs in the western Mojave Desert are generally simple and do not show significant variation with the back azimuth indicating a relatively simple and flat Moho. The absence of midcrustal interfaces in most SCSN stations and a relatively low-amplitude midcrustal interface for the LARSE I passive stations indicate that crustal structure in the western Mojave Desert is significantly different from that beneath the San Gabriel Mountains. Depth of the Moho is generally 29–31 km in the western Mojave Desert. Shallower Moho of 23–26 km is observed beneath the topography low, corresponding to the southern extension of the Death Valley fault zone in the Mojave Desert, indicating that large-scale extension is probably occurring in this area. The crustal structure is complicated in the eastern Mojave Desert, especially beneath stations LDF and DAN. At DAN, a Moho step of 8–10 km is determined over a horizontal distance of no more than 15 km. The appearance of a midcrustal negative velocity-gradient interface at 12–15 km and a following positive one at ~20 km beneath station LDF indicate complications in the crustal structure beneath the eastern Mojave Desert and the existence of large lateral variations in the lower crust. Deep Moho of 35–39 km is observed beneath the San Bernardino Mountains

and its extension to the NW along the San Andreas Fault.

Deep Moho of 35–39 km is observed along a sliver in the western Peninsula Ranges and the sharp transition from the deep Moho here to shallow Moho of 19–22 km to the east close to the Salton Trough indicates that the crust of the western Peninsula Ranges is of continental origin and that the movement of the western Peninsula Ranges away from main body of the North American plate most probably involves the whole crust.

Large lateral variations in the crustal structure also exist beneath the Sierra Nevada and nearby Walker Lane area. A deep Moho of 36–39 is observed in the western Sierra Nevada and two stations in the Death Valley fault zone, while flat shallow Moho of 28–31 km is observed beneath the Coso geothermal area and the southernmost Walker Lane area. Existence of a deep Moho beneath the Walker Lane area indicates that the Moho is probably not as flat as previous reflection studies indicate beneath the Basin and Range.

Acknowledgements

We thank the Southern California Seismic Network and the Southern California Earthquake Data Center for providing the network data, IRIS data center and Kohler for providing the LARSE data. This research is partially support by USGS Contract 04HQAG0010.

Chapter 4

A Notch Structure on the Moho beneath the Eastern San Gabriel Mountains

Abstract

Anomalous features in the receiver functions for two stations in the eastern San Gabriel Mountains indicate the existence of a notch structure on the Moho beneath the Mt. Baldy block, which is bounded by the San Andreas Fault (SAF) in the north and the San Gabriel Fault (SGF) in the south. The Moho shallows from a depth of 37–39 km north of the SAF and 33–35 km south of the SGF to ~ 29 km beneath the Mt. Baldy block. Surface projection of this block with the shallow Moho corresponds very well with the area where the lower plate Pelona Schist is either exposed at the surface or resides at very shallow depth. Synthetic receiver function waveform modeling for six different Moho geometries indicates that a flat-topped notch structure on the Moho is required to fit the data. The notch structure is also supported by the Pms arrival times along the LARSE I profile.

4.1 Introduction

The San Gabriel Mountains (SGM) is an east-west trending range formed from basement rocks uplifted along the SW side of the 'big bend' portion of the San Andreas Fault (SAF) (Figure 4.1a). Uplift began several million years ago and is still going on as a product of the transcompression from the left-step in the right-lateral strike-slip SAF system. The uplift was accomplished by reverse faulting along the Sierra Madre and related faults on its southern margin and broad arching in the interior against the Mojave Desert block on the north [Dibblee 1982c; Ehlig 1981].

Basement rocks exposed within the range mainly consist of Precambrian to Mesozoic igneous and metamorphic rocks of upper North American continental affinity and lower plate Mesozoic Pelona Schist (Figure 4.1b). The two different rock units are separated by the Vincent Thrust on the eastern SGM, which was proposed to be the interface along which the lower Farallon plate subducted beneath the upper North American plate during the Mesozoic [Dibblee 1982c; Ehlig 1981; Saleeby 2003]. The Pelona Schist is a late Cretaceous-early Tertiary (60-70 Ma) well-foliated, greenschist facies, metamorphic rock [Ehlig 1968]. It consists of oceanic rocks that were metamorphosed in response to deep burial beneath the Vincent thrust fault during the Laramide flat subduction [Jacobson et al. 1996; Ehlig 1981; Malin et al. 1995; Saleeby 2003]. It was subsequently uplifted, deeply eroded, and was brought to the surface or just below the surface during middle Tertiary extension [Jacobson et al. 1996].

Recent fission track and U-Th/He analyses by Blythe et al. [2000] indicate that the high elevation (1.5–3 km) of the San Gabriel Mountain is largely uplifted within the most recent 7 Ma. The supporting mechanism for the high elevations in this range, however, has remained controversial. Previous receiver function studies [Zhu and Kanamori 2000; Zhu 2000] and PmP-P differential time studies [Richards-Dinger and Shearer 1997] indicate that a shallow crust of 28–31 km exists for the central Transverse Ranges and thus a regional or dynamic supporting mechanism for the topography is inferred. However, Kohler and Davis [1997] inferred the existence of a deep root of 40 km centered on the San Andreas Fault from teleseismic travel time studies of the LARSE I passive stations and thus deduced an airy isostatic compensation mechanism. A feature that further complicates the interpretation is that two interfaces appear in Zhu's [2000] LARSE I teleseismic receiver function studies south of the San Andreas Fault. The shallower one at 25–29 km was picked to be the Moho by Zhu [2000], while others argue

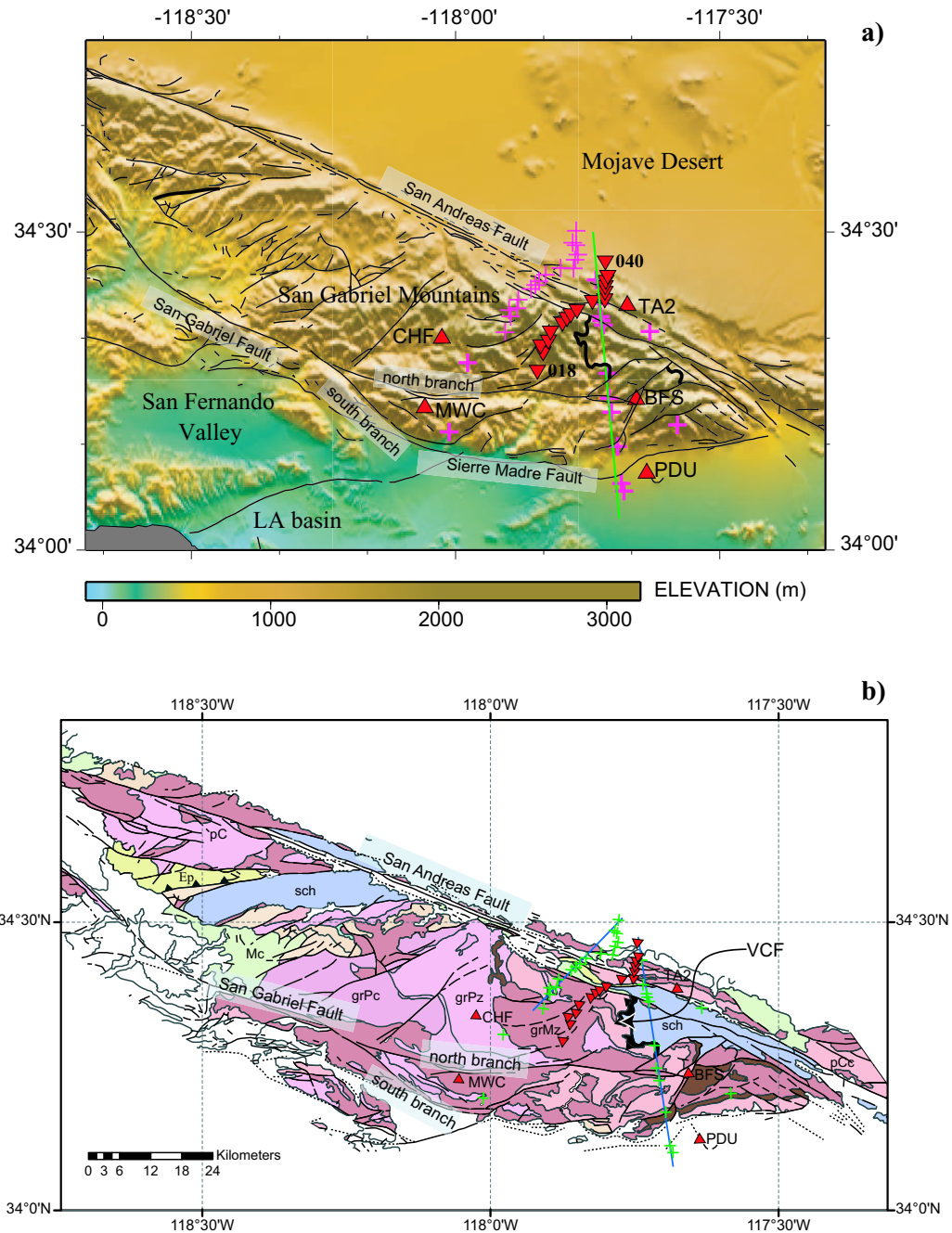


Figure 4.1 Topographic and revised geologic maps for the San Gabriel Mountains. In both maps, red triangles are the SCSN stations, red inverted triangles are the LARSE I stations. Crosses are the piercing points at 30 km for the SCSN station groups and NW group of LARSE I stations. The green (top) and blue lines (bottom) are the projected lines along which RF cross-sections are drawn in Figure 4.5. Major faults are marked on the map. VCF denotes Vicent Thrust Fault. Geologic units in the geological map are: grPc - Precambrian granitic rocks, grPz - Paleozoic and Permo-Triassic granitic rocks, grMz - Mesozoic granitic rocks, pCc - Precambrian igneous and metamorphic rock complex, pC - undivided Precambrian rocks, sch - Lower plate pelona schist, Ep - Paleocene marine sedimentary rocks, Mc - Miocene nonmarine sedimentary rocks.

that the deeper interface at about 40 km might be the Moho and thus support the deep Moho result of Kohler and Davis [1997]. Moho is observed to smoothly deepen from both the Mojave Desert and the Los Angeles basin to the eastern San Gabriel Mountains [Hafner et al. 1996] from the LARSE I reflection survey, however, no prominent PmP phase is observed beneath the eastern San Gabriel Mountains.

There are two problems with Zhu [2000], which might complicate the image. One is that lateral variations of the receiver functions in the direction perpendicular to the LARSE I line are not considered, which is incompatible with the large variations in the receiver functions with back azimuth observed for stations in the SGM (Chapter 3). Another problem is that all the available receiver functions are included in generating the image including those with low signal-to-noise ratio and basin stations which have large-amplitude reverberations that will generate artifacts in the image. For Kohler and Davis [1997], influence of the high-velocity anomaly body in the upper mantle, which was imaged by several tomography studies [Humphreys et al. 1984; Humphreys and Clayton 1990; Kohler 1999], was not considered, which could contribute a large portion of the arrival time anomaly.

In order to resolve the controversy, receiver functions (hereafter referred to as RF) for the three SCSN broadband stations in the eastern San Gabriel Mountains and the LARSE I passive stations were calculated and variations of the RFs with back azimuth are investigated. Only the northwest (NW) RF group for the LARSE I passive stations are considered due to variations of the RFs with back azimuth and the fact that not enough good events were recorded from other directions for them to be analyzed as an independent group. Synthetic RFs for models with lateral variations are calculated to help constrain the geometry of the Moho depth variation using a 2D finite difference modeling [Graves 1996].

4.2 Data

Since the regional study of the Moho depth variation by Zhu and Kanamori [2000], the number of SCSN stations has been nearly tripled, including two more stations in the eastern SGM (station BFS and PDU in Figure 4.1). To investigate the Moho structure beneath the SGM, back azimuth variations of the RFs for the available 3 SCSN stations in the eastern SGM are investigated, as well as the NW RF group of the LARSE I passive stations.

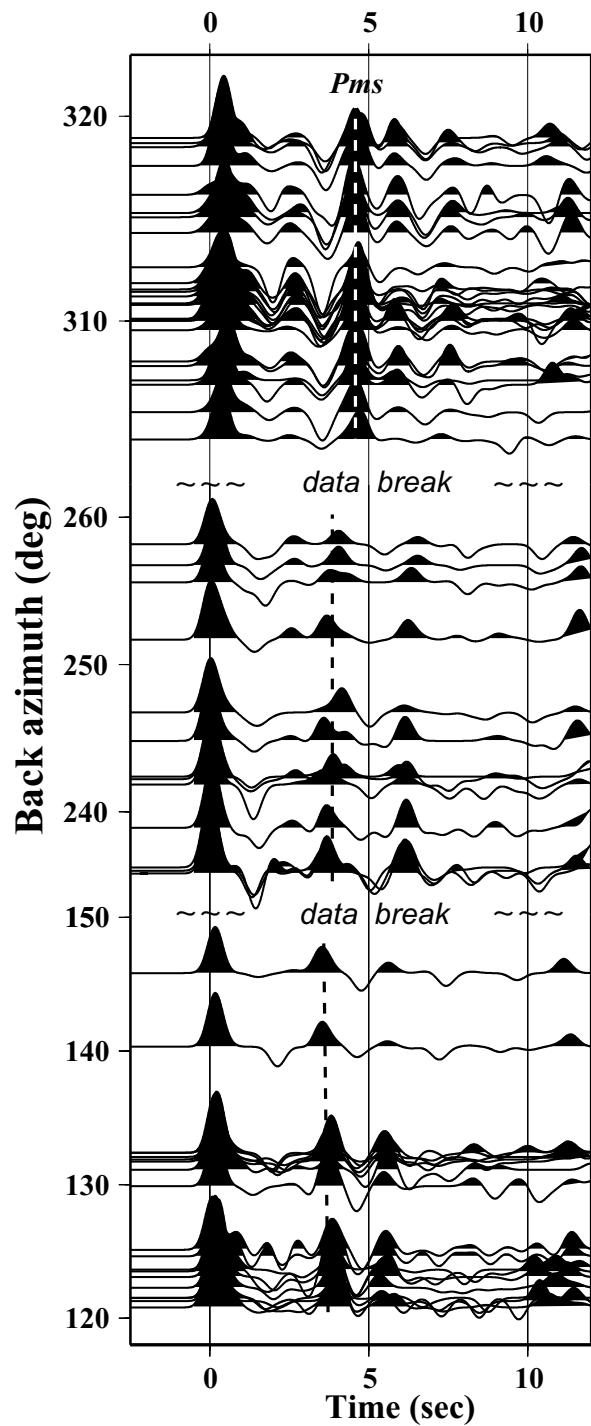


Figure 4.2 Radial receiver functions for station TA2 with Pms phase marked by the dashed lines. Note the large difference in the Pms arrival time for the different back azimuth groups—approximately 4.6 sec for events from NW, but 3.8–4.0 sec for events from SE and SW. Also, note the prominent later arrivals at ~ 5.5 sec and 6 sec for the SE and SW group respectively.

Large variations in the Pms arrival time are observed for station TA2 (Figure 4.2). Pms arrives at 4.6 sec for events from NW, and arrives at 3.6–3.9 sec for events from SE. This indicates a jump of 8-10 km within a distance of less than 15 km in the Moho if the average V_p/V_s ratio is assumed to be ~ 1.73 . An additional phase with slightly smaller amplitude is observed at 5.5 sec and 6.0 sec respectively for the SE and SW groups of the RFs. For station BFS, which is ~ 16 km south of station TA2, Pms phase is observed to change from a large-amplitude single pulse to smaller-amplitude double pulses as the ray parameter increases from 0.045 to 0.06 for the NW group RFs (Figure 4.3). The arrival time of the additional phase (Pds) decreases systematically with ray parameter. If the arrival time of the Pds phase is converted to depth using a uniform crustal velocity model, then a SE dipping midcrustal interface will be inferred to converge to the Moho from NW of station BFS. Synthetic RFs for such a model (Figure 4.4), however, do not fit the data. RFs for station #70 at the tip of the wedge, which is inferred to correspond to BFS in location, only have a single Pms pulse for all the ray parameters. The P to S converted phase from the dipping interface does not show up due to complications from dipping interfaces. The P to S converted phase generally has negligible amplitude from the up-dip direction due to the near perpendicular incidence of the P wave, which is discussed in several previous studies (Savage 1998; Peng and Humphreys 1997). RFs for an inner station #58, however, do show the transition from a single pulse to double pulses with increasing ray parameters. The RF variation pattern, however, is different from what was observed in the NW group of BFS since no systematic move-out of the Pds phase is observed. The additional Pds phase observed at #58 arises from the conversion across the flat portion of the additional crustal interface. Another difference between the synthetic RFs for this station and the data for station BFS is that double pulses are observed in RFs from the down-dip direction for the synthetics, while simple single pulse is observed for those of the SE station group of BFS.

RFs from the LARSE I data (Figure 4.5), which are ~ 15 km to the west of the SCSN stations (Figure 4.1), confirm the existence of a Moho step across the San Andreas Fault. Pms arrives at 4.5-4.7 sec and 4.0 sec respectively for stations to the immediate north (034–040 in Figure 4.5) and south (027–030) of the SAF, indicating the existence of a Moho step of ~ 4 -6 km across the SAF. In contrast to the SCSN stations, a late Pms arrival time of ~ 4.5 -4.7 sec is observed at three southern stations (018–022) beneath the central portion of the western SGM, indicating the existence of a deep Moho of ~ 35 -37 km. This interface corresponds very

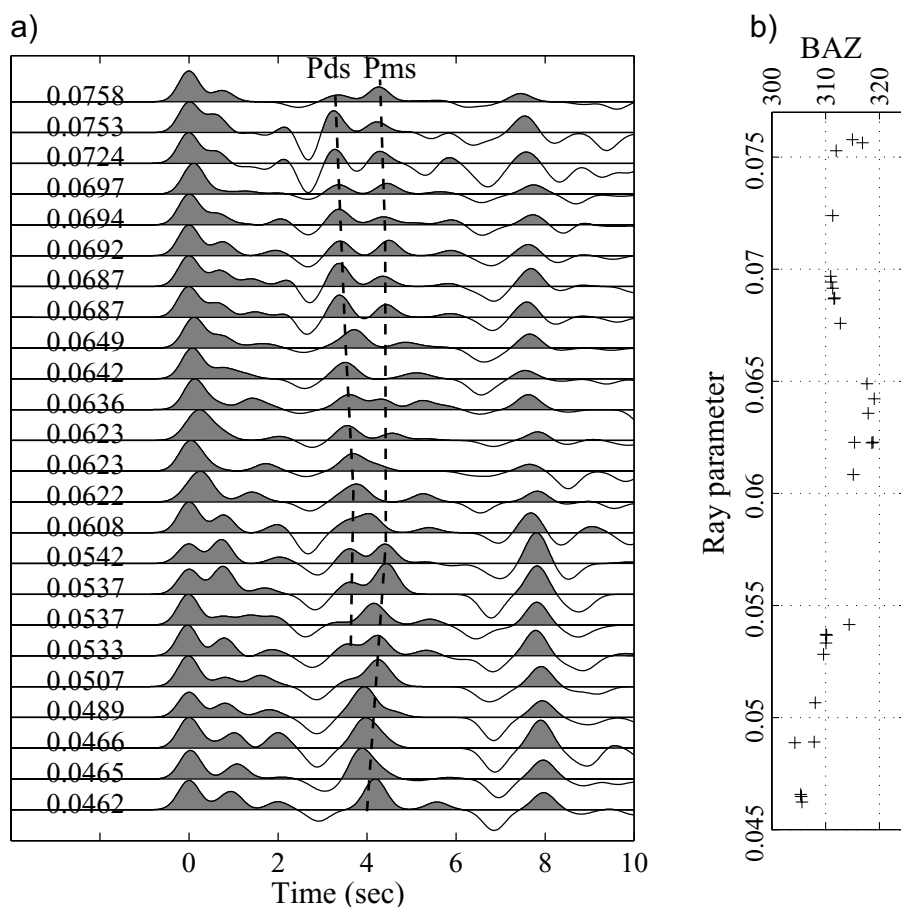


Figure 4.3 Variations of the Pms phase with ray parameter for the NW RF group of station BFS. Note that only one single large amplitude Pms phase exists at 4 sec for RFs with small ray parameters, but an additional phase appears for ray parameters larger than 0.05 and a systemic move-out of this additional phase (Pds) is observed—its arrival time decreases with ray parameter. The ray parameter for RF is marked at the beginning of each trace. back azimuths for the RFs are shown in (b) as plus signs. The low amplitudes for the Pms phase within the ray parameters within the range 0.06–0.065 is probably due to 3-D structures since they share a slightly larger back azimuths than other RFs.

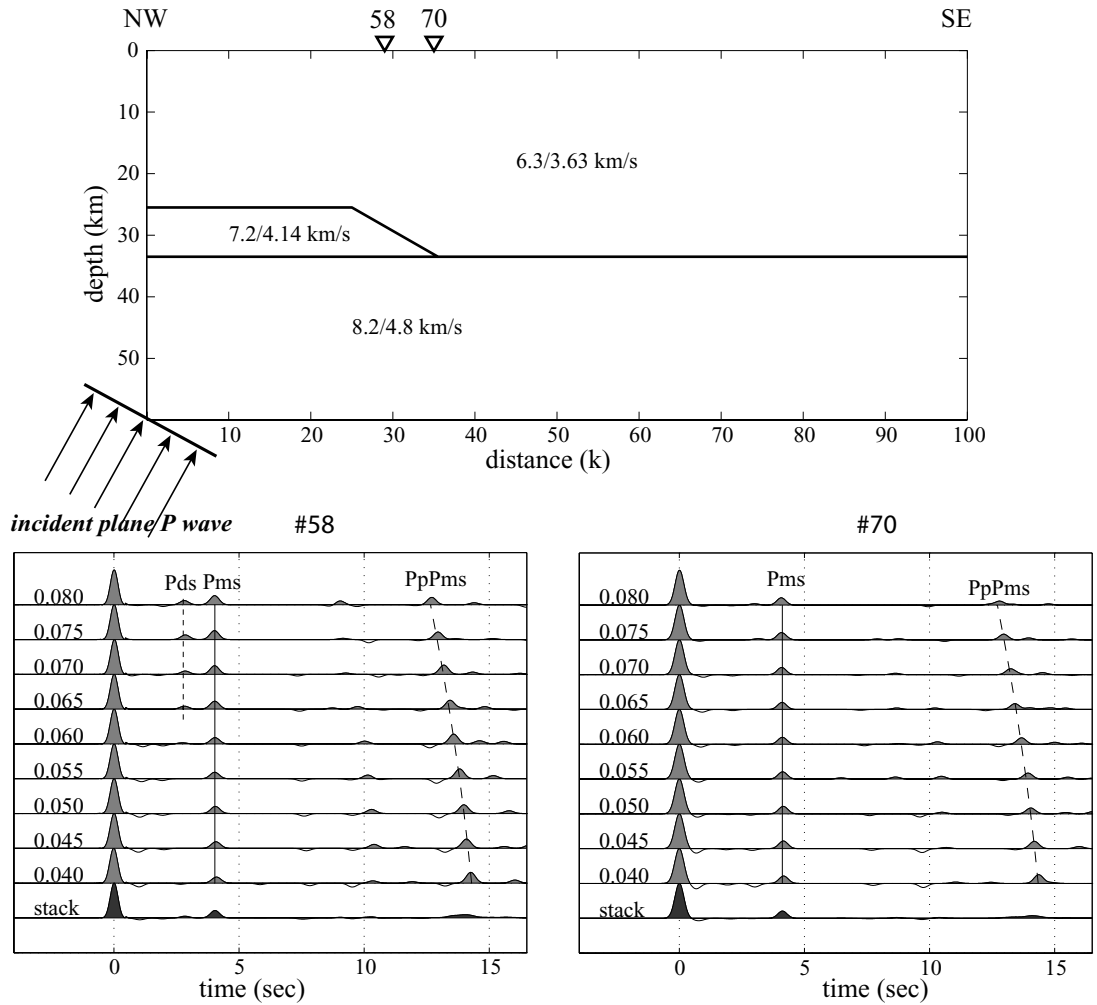


Figure 4.4 Synthetic RFs for a wedge-inserted model. Plane waves with varying incident angles corresponding to regularly spaced ray parameters in the range of [0.04, 0.08] were introduced at the left-bottom corner of the model. Velocity model is shown on the top, with the location of the two stations (#58, #70) marked on the top by triangles. RFs for station #58 are shown on the left, and those of #70 are shown on the right.

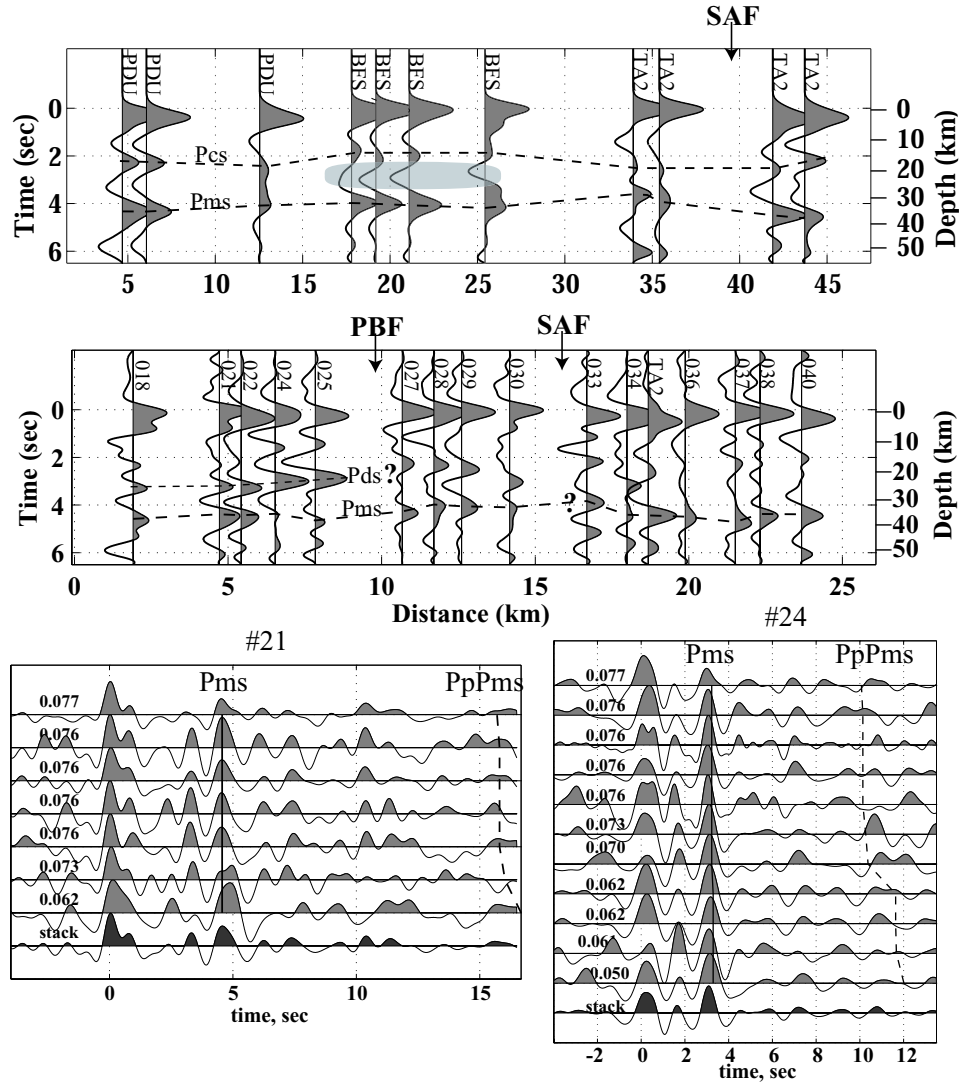


Figure 4.5 RF cross-sections along the two green lines in Figure 1. Note the difference in their distance scales. Relative constant Pms arrival times are observed for station groups within 22 km from the southern point along the SCSN profile (top). A fat Pms phase is observed at 25 km for the WNW BFS station group as a result of the average over the varying receiver functions shown in Figure 3. Slightly shallow Moho is observed for the two SW TA2 station groups at ~ 35 km. The shaded area represents the negative-gradient velocity interface. Note the large differences in the RFs along the LARSE I profile. Complications in the RFs for stations 033 and 034 probably result from the large lateral variations in the crustal structure across the San Andreas Fault. Stacking of two representative stations (#021 and #024) are shown on the bottom with the picked Pms and PpPms phases marked. Note that the picked PmPms multiples for station #024 are not well developed.

well with the deeper $\sim 35\text{--}37$ km interface at horizontal distance of ~ 10 km in Zhu's [2000] RF image, which was proposed to be Moho interface by others. However, large lateral variations in the RFs among the LARSE I stations can be seen from stations 018–022, 024–025 and 027–029. The large amplitude phase that appears at 2.8–3.0 sec for stations 024 and 025, was interpreted to be Moho Pms phase by Zhu [2000], as well as the earlier arrivals at ~ 3.0 sec for stations 018–022. In this study, the later interface at ~ 4.6 sec is interpreted to be Moho Pms for stations 018–022 due to the fact that similar RFs are observed at SCSN stations CHF and MWC to the west and amplitude of this later phase is larger and more consistent than the earlier one at ~ 3.0 sec for both station groups. An example of the RF group for station 021 is shown in Figure 4.5c. It is tempting to interpret the largest arrival at 2.8–3.0 sec on the RFs for stations 024 and 025 to be the Moho Pms (Figure 4.5d), however, there are two reasons that we think this may not be necessarily correct. The first is that there is evidence for a low-velocity zone just above this interface [Ryberg and Fuis 1998; Chapter 3] which would result in a larger velocity contrast across this one and thus might generate an anomalously large amplitude P-to-S converted phase, and second the true Pms phase, which could be the later, smaller arrival, might have its amplitude reduced by diffraction due to relief on the Moho. Since these two stations (024–025) are the only cases where such RF pattern is observed, we prefer not to draw a definite conclusion on which one is the Moho Pms. North of these two stations, the Pms arrival time is constant at ~ 4.0 sec (027–029), corresponding to a Moho depth of $\sim 31\text{--}33$ km.

In summary, a notch structure is inferred along the LARSE I profile, where the Moho shallows from 36–38 km and 34–37 km north of SAF and south of the Punchbowl Fault (PF), to a depth of 31–33 km for the sliver bounded by these two branches of the San Andreas Fault. The deep Moho of 36–39 km north of the SAF is inferred from stations (034–040), as well as the NW RF group of SCSN station TA2. The local root of 36–38 km for the western San Gabriel Mountains is inferred from the LARSE I data (018–022) and two SCSN stations further to the west. A shallow Moho of 31–33 km is inferred from the LARSE I station groups (027–030) for the sliver between the two branches of the San Andreas Fault, where the lower plate Pelona Schist is believed to reside at very shallow depths [Dibblee 1982c]. Possibility for the existence of a shallow Moho at similar depth is thus inferred for the Mt. Baldy block between stations TA2 and BFS, where the lower plate Pelona Schist is either exposed at surface or is believed to reside at very shallow depths [Dibblee 1982c]. The obviously earlier Pms arrival time for the

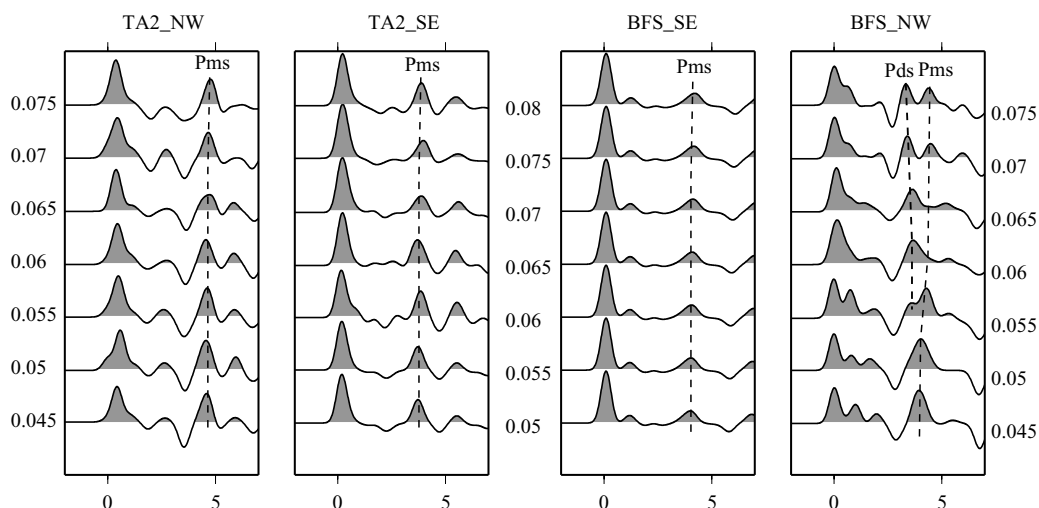


Figure 4.6 Summary of the receiver function data for the NW and SE groups of the two stations TA2 and BFS. Receiver functions for these four groups are binned to neighboring regularly spaced ray parameters for the purpose of direct comparison with the synthetics. Note that all events in the SE group of station BFS are included in each bin due to the small number of available good receiver functions.

SW groups of the SCSN station TA2 compared with other station groups to the north and south also support this inference. Thus, a step and probably a notch structure is inferred on the Moho along the SCSN profile.

4.3 Synthetic Models

Synthetic RFs for a model with a step in the Moho and one with a notch are calculated with plane waves incident at angles corresponding to the regularly spaced ray parameters (spacing is 0.005) in the range that matches the data ray parameters. The regularly spaced (in ray parameter) RF data are shown in Figure 4.6 for the purpose of direct comparison with synthetics. Synthetic RFs for the two cases mentioned above are shown in Figure 4.7. Comparison with the data indicates that synthetics for the notch structure fit the data very well, including the appearance of the additional diffraction phase at ~ 5.5 sec for the SE group of station 84, the transition from a single pulse to double pulses at ~ 4 sec with increasing ray parameters for 118-NW, and the simple arrivals for the other two station groups. The step structure, however, is not able to explain the complicated patterns observed in the BFS-NW since only one single large-amplitude Pms phase is observed for this group.

Synthetic RFs for three models with varied notch geometry in the Moho and one step model

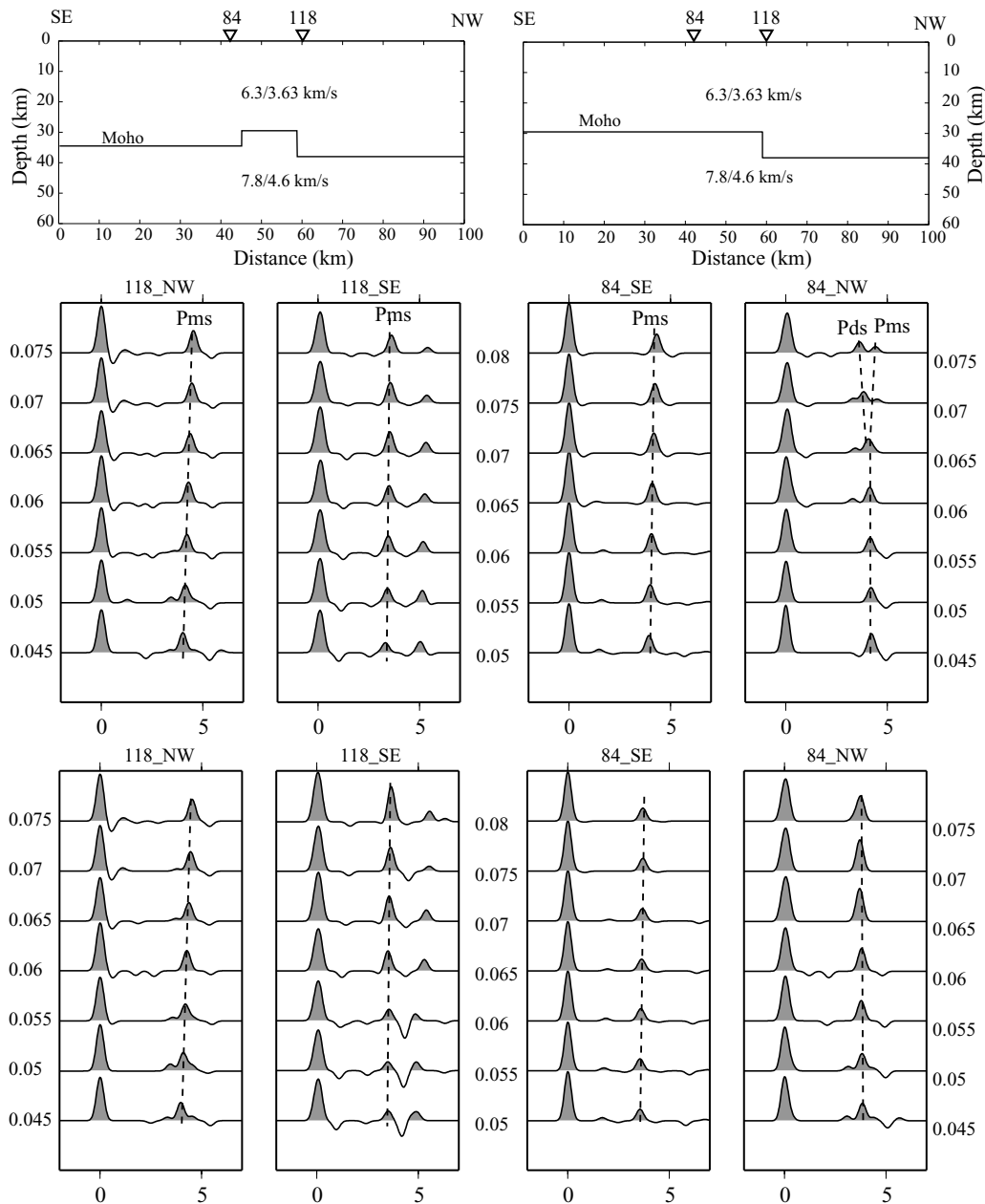


Figure 4.7 Synthetic RFs of two stations (118 and 84), corresponding to station TA2 and BFS in location, for a notch and a step model. The two models are shown on top. RFs for the notch structure (top left) are shown in the middle. The four columns correspond to TA2_NW, TA2_SE, BFS_SE, BFS_NW respectively and will be shown this way for the following figures. RFs for the step structure (top right) are shown at the bottom. Note the similarity of the synthetic RFs for the notch structure with the data show in Figure 4.6. The move-out pattern of the Pds phase for 84_NW is very similar to what was observed in the data. The Pds phase is absent in the corresponding station group for the step structure.

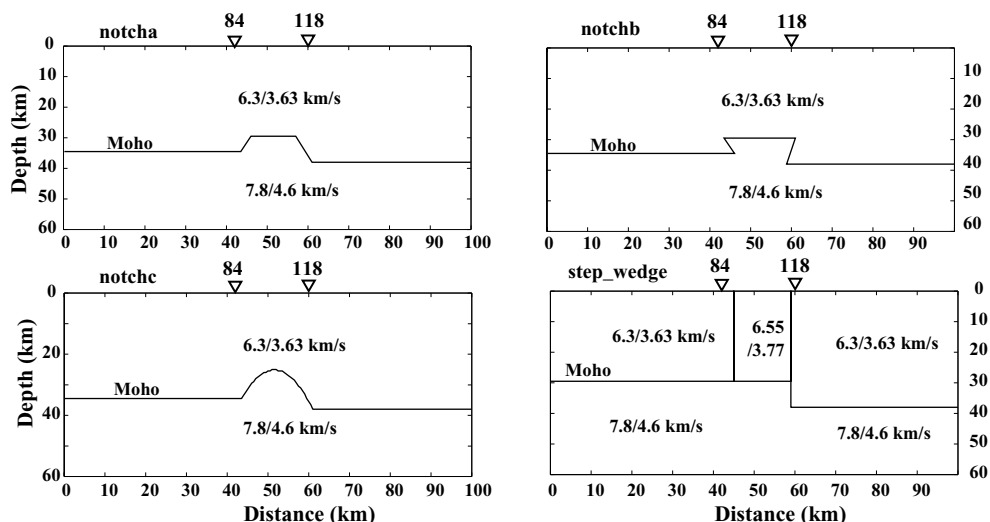


Figure 4.8 Geometries of four different models that were studied to help constrain the Moho geometry across the eastern San Gabriel Mountains. On the top left is a notch structure with steep normal faults on both sides (a). On the top right is notch structure with steep reverse faults (b). Dip angles for both cases are 60° . On the bottom left is a notch structure with a smooth curvature (c). On the bottom right is step structure with a high velocity material inserted between the two blocks (d).

with a high velocity block are calculated to help constrain geometry of the notch structure (Figure 4.8). Synthetic RFs for these 4 cases are shown in Figure 4.9. Synthetic RFs for both sharp-transit notch structures fit the data reasonably well, particularly with the prominent Pms phase and the comparable later Pds phase for TA2_SE, the branching out pattern of the Pds phase from Pms phase with ray parameters for BFS_NW and the simple single Pms phases for TA2_NW and BFS_SE. However, synthetics for the smoothed notch and the step-wedge structure do not fit the data, especially for BFS_NW. For the step-wedge geometry, no additional Pds phase branching out from the Pms phase is observed. The Pds phase only shows up for ray parameter 0.075 for the smoothed-notch structure.

Thus, the three flat-topped notch structures are the preferred models for the structure along the SCSN station profile. Even though there are some minor differences in the synthetics for these three preferred models, the differences are not prominent enough to distinguish among them. The synthetics do however rule out the smooth notch and the step-wedge as candidate model of the Moho topography and the exclusion of the step-wedge structure indicates that the patterns observed in the data could not be explained by lateral velocity heterogeneities.

In summary, synthetic RF modeling indicates that a notch structure is required on the Moho

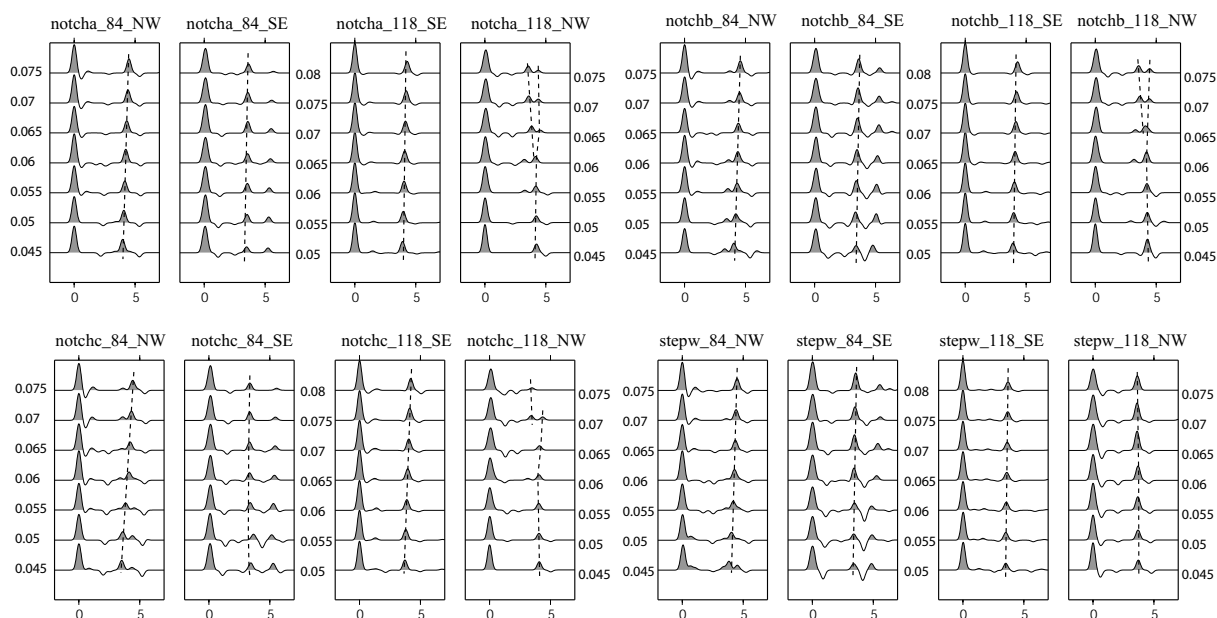


Figure 4.9 Synthetic receiver functions for the four models shown in Figure 4.8. The synthetic RFs are plotted in the same sequence as the models in Figure 4.8 with the synthetics for the notcha structure shown on the top left etc. Synthetics for each model is plotted in the same sequence as those in Figure 4.6.

in order to explain the complicated patterns observed in the data, and that a sharp-transit flat-topped notch is preferred compared with a smooth one.

4.4 Discussion

The common practice of estimating Moho depth from receiver functions is that RFs are stacked over back azimuths and ray parameters assuming a locally homogeneous crust and relatively flat Moho. In this study, however, the variations of RFs with back azimuth and ray parameter reveal an interesting Moho topography. The fact that a simple model (a notch structure on the Moho) is able to generate synthetic RFs that fit the complications in four RF station groups indicates that study of the Pms phase variations with back azimuth and ray parameters could provide valuable information about the large rapid lateral variations in the crustal structure with the support of synthetic RF modeling.

Boundaries of the shallow Moho inferred from this study align very well with the depth extension of the San Andreas Fault and the San Gabriel fault (Figure 4.10). One explanation for the Moho offsets across these two major faults is that it is caused by differential whole

crust uplifting among the blocks. Blythe et al. [2000] recently studied the erosion rate for the San Gabriel and San Bernardino Mountains from apatite fission-track and (U-Th)/He analyses. Their results indicate that distinct variations in the total amounts and rates of cooling exist between different fault-bounded blocks within the SGM and that the Mt. Baldy block (the block which we inferred to have shallow Moho) has the highest denudation rate, which can be interpreted as having the highest uplift rate. Within this block, the lower plate Pelona schist is either exposed at the surface or resides at shallow depth (Dibblee 1982c, Figure 5 profile B). Thus, differential uplifting does exist among the blocks, and might be the reason for the Moho offset across the two major faults. The nearly flat midcrustal interface beneath the three SCSN stations, however, would tend to argue against the whole crustal differential uplifting, but since the two blocks (the Mt. Baldy block to the north and the Sierra Madre block to the south) have very different evolution histories, it is possible that the midcrustal interfaces are not correlated to each other. Another possibility for the origin of the Moho offset is that it is an inherited feature, which means differences exist in crustal thickness among the blocks before they are juxtaposed together by the ~ 300 km strike slip movements along the major faults [Ehlig 1981]. Geochemistry studies [Ehlig 1981] indicate that the blocks bounded by the major faults in the San Gabriel Mountains belong to different terranes and have rather different evolution histories before they were juxtaposed together. We can not draw a conclusion about which mechanism is the main contribution factor of the Moho offsets across the two major faults from this study, but we do confirm the existence of a notch structure on the Moho.

The clear RFs obtained for the LARSE I stations and their correlation with the SCSN stations further to the west (Chapter 3) indicate that a local deep Moho of 36–39 km does exist in the western SGM, which corresponds to the deeper ~ 35 –37 km interface in Fig. 3 of Zhu [2000] at horizontal distance ranges of -18 to -10 km. It gets shallows to ~ 31 –33 km to the north across the Punchbowl fault and a very narrow notch structure is thus inferred along the LARSE I profile. The two interfaces at 28–31 km and 35–40 km at the southern end of the profile in Fig. 3 of Zhu [2000] are probably due to reverberations from sediment/basement boundary in the Los Angeles basin since thick sediments of 2–3 km are inferred by Zhu [2000].

The fact that a shallow Moho of 29–34 km exists in the western San Gabriel Mountains, where the elevation is the highest within the range indicates that the crust is not supported by Airy isostasy, but is most probably supported by regional or dynamic forces.

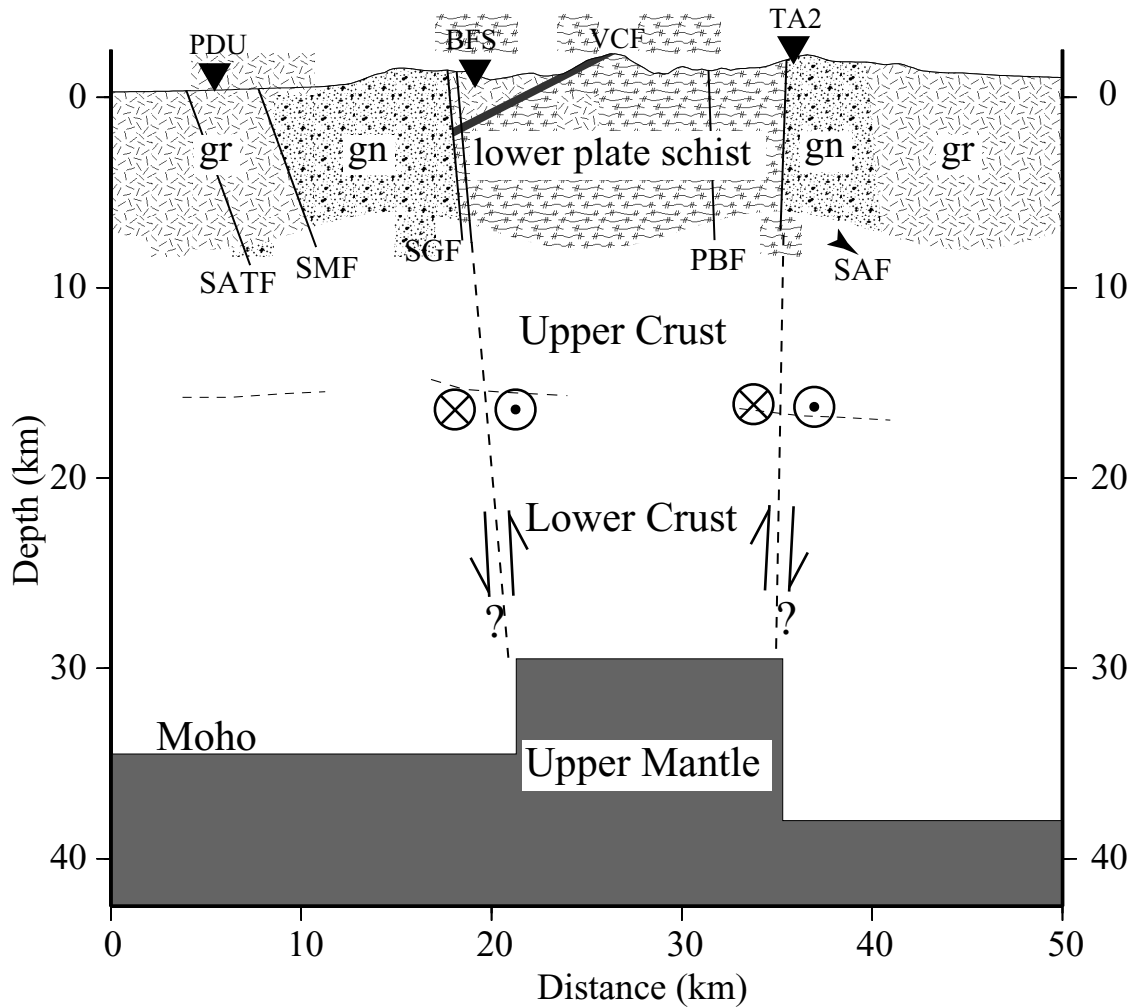


Figure 4.10 Model showing the alignment of the shallow Moho portion of the notch structure with the two major strike slip faults—the San Andreas Fault on the north and the San Gabriel Fault on the south, and its correlation with the surface exposure/near surface level of the lower plate Pelona schist. The petrologic unit in the upper crust is adopted from the cross-section B of Figure 5 in Dibblee [1982c].

4.5 Conclusions

Synthetic RF waveform modeling of the Pms phase variations with back azimuth and ray parameters for two stations in the eastern San Gabriel Mountains indicates that a notch structure exists on the Moho with shallow Moho beneath the Mt. Baldy block bounded by the San Andreas Fault in the north and the San Gabriel Fault in the south. Moho shallows from ~ 38 km north of the SAF, 34 km south of the SGF to a depth ~ 29 km beneath the Mt. Baldy block, the transition from the deep Moho on both sides to the shallow Moho in the center is relatively sharp. The Moho offset across the boundaries of the notch structure could be either related to differential uplifting of the different blocks bounded by the major faults or is the result of the ~ 300 km strike-slip movement along the major faults which juxtapose structurally very different blocks together.

Chapter 5

Conclusion

In this thesis, high resolution lateral variation of the crustal structure in Southern California is studied from densely distributed LARSE II refraction survey, back-azimuthal-grouped receiver function (RF) studies and synthetic RF waveform modeling. Large rapid variations in the crustal structure are imaged by all three studies. Variations in the upper crustal structure are directly correlated with the geologically mapped faults, which juxtapose very different rock units against each other. The influence of the movement along the major faults on the deep structure is also evident on the large lateral variation of the crustal structure and the Moho depth. Large offsets of 8–10 km are inferred across the San Andreas fault in the eastern San Gabriel Mountains, as well as an intermediate one of 4–6 km across the San Gabriel fault. The large differences in the crustal structure among station groups in the San Gabriel Mountains correlate very well with the surficial terrane distribution. The large offset across station JCS in the western Peninsula Ranges also correlates with the geologically mapped Elsinore fault.

Large-scale Moho depth distribution in the study area generally correlates very well with the tectonic evolution history the upper crust. Deep Moho is observed in the relatively intact Sierra Nevada, the western Peninsula Ranges and the San Bernardino Mountains batholiths, and shallow Moho is observed in the highly deformed and disrupted Mojave Desert province. Geothermal activities also seem to have some correlation with the subsurface structure. The shallowest Moho in the study area correlates with the highly extending Salton Trough and the topography low of the southern extension of the Death Valley fault zone in the Mojave Desert, where high heat flow and extensive Quaternary volcanic activities are observed. The transition from the shallow Moho beneath these weak crust area to the nearby rigid block is relatively sharp, such as the transition from Salton Trough to the western Peninsula Ranges. This indicates a sharp contrast in the physical properties of the crust between these two blocks.

Some features in the deep crustal structure that do not conform to the surficial expression is also observed, such as the deep Moho beneath station FUR in the surficially highly-extended

Death Valley area. Clear Pms and relatively well-developed multiples in the RFs for events from SW and SE (Appendix D) indicate the existence of a locally deep Moho, which is in contrast to highly extended surficial deformation. The current explanation for the accommodation mechanism of the large-scale extension in the Basin and Range province (BR) is by low-angle detachment faulting in the upper crust and ductile stretching and fluid-like flow in the mid-lower crust [Wernicke et al, 1996], which predicts a relatively flat Moho in the BR province. The existence of a locally deep Moho beneath station FUR indicates that decoupling might exist between the upper and the lower crust and that a revised kinematic model is needed.

This study also indicates that the eastern Mojave Desert to the east of the southern extension of the Death Valley fault zone is probably a very different tectonic province than the one to the west. The crustal structure is more complicated and partial melting might exist beneath this province.

Moho depth variation pattern does not directly correlate with the gravity field (compare Figure 3.6 and Figure 5.1), even though some features imaged by this thesis are supported by the gravity field, such as the correlation of the large Moho offset across the San Andreas Fault with a high gravity gradient from the Mojave Desert to the central Transverse Ranges. The large variation in the gravity field around station LDF in the Mojave Desert and JCS in the western Peninsula Ranges also correlates with the large difference in the in the crustal structure imaged across these two stations.

This study also provides some constraints on the strength of the crust. The existence of a deep Moho beneath the relatively intact Sierra Nevada and the western Peninsula Ranges indicates that the WNW movements of these two blocks involve the whole crust and that the crust is relatively strong, since both blocks have experienced large amount of WNW displacement during Cenozoic time and the western Peninsula Ranges province is currently on the Pacific plate. The large offsets among different blocks in these provinces and the San Gabriel Mountains also support the inference of a relatively strong crust.

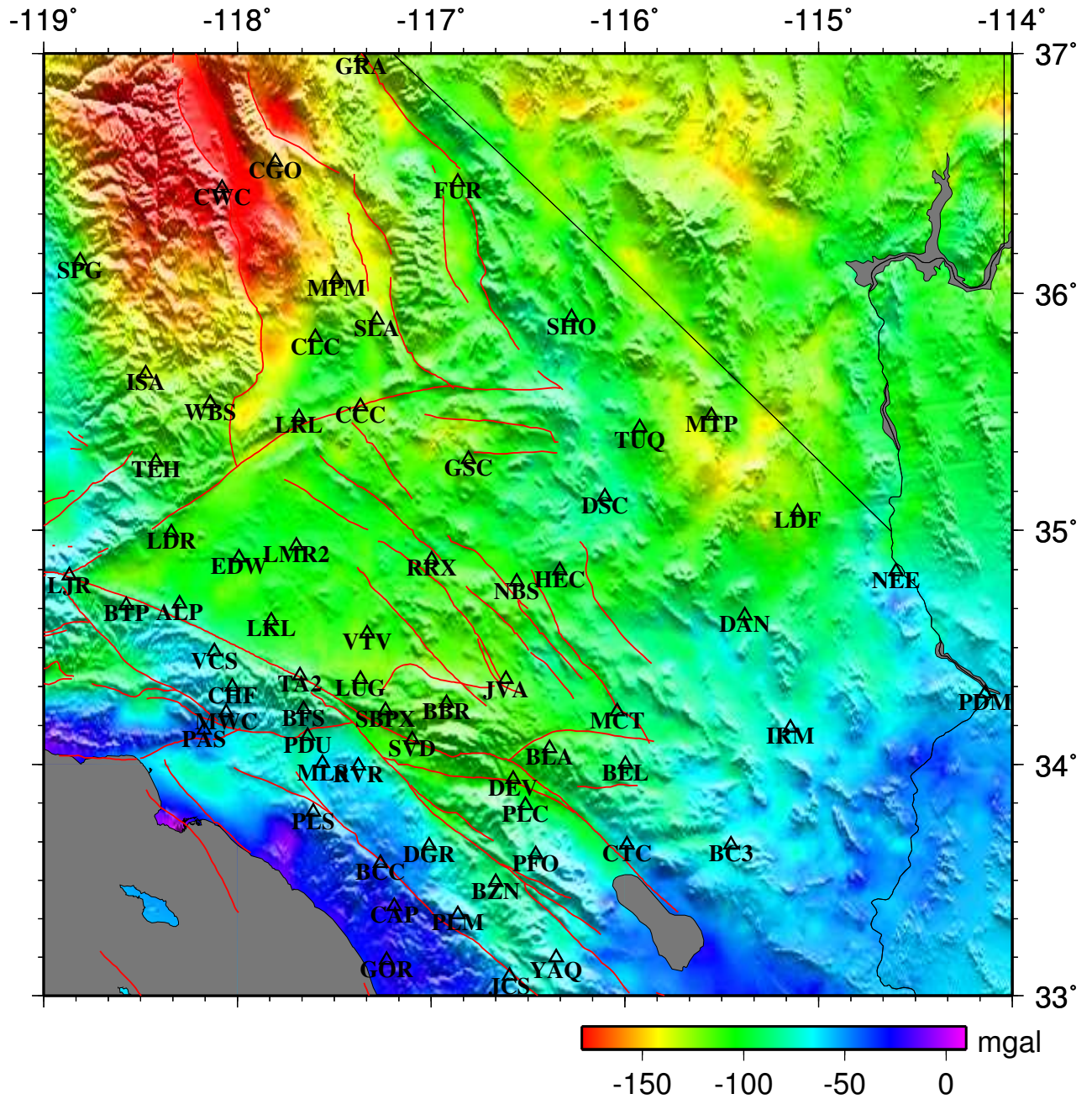


Figure 5.1 Complete Bouguer gravity anomaly for the study area. Black triangles are representative SCSN stations with station initials labeled.

Appendix A

Effect of Faults on First Arrivals

The complex patterns of first arrival branches due to a fault in a layer over a half-space model are shown in Figure 2.5. For shot #100, the true crossover point for the interface on the left side of the model is at the point R. However, the existence of the fault causes an additional kink point at A, which is the transition point between the headwave travelling along the half-space boundary on the left side and the diffraction phase emanating from the point K in the model. The diffraction phase appears as reverse branch in the first arrival time curve and this branch asymptotically approaches the half-space velocity on the right side of the model. As the shot nears the fault (i.e., #101 to #103), the true crossover point is not able to show up due to the sudden drop of the interface. The reverse branch, however, as the travel time for the diffraction phase from point K, shows up consistently, which gives rise the "pseudo" crossover points, such as A and P1. This reverse branch (curve ACM) is the first characteristic feature of faults (F1). It is important to note that the highest point on the ACM curve should be used to estimate the layer thickness of the footwall side when no true crossover points appear, and even then it may still under estimate the thickness if it has a time lower than the true crossover point.

When shots are close enough to the fault, that is when the fault is within the cross-over distance of the shot such as #104 to #108, the first arrival consists of the direct wave followed by the head wave travelling along the half-space boundary on the right side of the fault, as shown by branches L1 to L3. The travel time curve for each individual shot does not show any anomalous features. However, the curves as a group are different from those for a continuous flat-layered structure. The intercept times do not remain constant, but increase systematically with distances away from the fault (from L1 to L3). This is due to the difference in the distance from the source to the fault (travel path for the "pseudo" head wave branches, such as L1, is shown in the bottom panel. It travels first from shot #104 to point U, then along the right interface, and then back to the surface). This is another characteristic feature of faults (F3). We should note that we will significantly under estimate the thickness of the layer of the footwall

if we use the intercept points of these branches to estimate the layer thickness beneath the shot. The intercept point of shot #108 should give a reasonable estimate of the layer thickness for the hanging wall side however.

For shots on the hanging wall side of the fault, such as #110 to #113, the first arrival branches exhibit a normal cross-over point (E1-E3), but at a point (X) just to the left of the fault, the travel time curves of all the shots converge to each other and adopt a low apparent velocity—a velocity that approaches asymptotically to the velocity of the layer on the left side. Eventually at about the crossover distance of the left side interface away from the shot, the headwave phase travelling along the left side half-space boundary appears as first arrival and the travel time curve adopts the half-space velocity. The relatively slow diffracted phase between the two fast phases is the third characteristic of faults (F2) and it is due to the change of ray paths from headwaves along the right interface to a diffracted phase from the point U in the model. We can use the true crossover points like E1 to E3 to get a correct estimate of the layer thickness of the hanging wall if they exist.

The ray paths that give rise to the above three features are shown as arrowed lines in the velocity model in Figure 2.5. The middle panel shows the ray paths for the negative-slope segment ACM(F1). The bottom panel shows the reciprocal ray paths for shots from the footwall and the hanging wall. They give rise to the unusual low velocity segment feature(F2) and the systematically increasing intercept time head wave branches(F3).

The important points in the model are the layer piercing points (U for the hanging wall side, and K for the footwall side), which are closely related to the dip direction of the fault. The discontinuity of the interface in the velocity structure gives rise to the features in the first arrival data described above, and these break points control the location of the three features. Feature F1 depends on K, while features F2 and F3 depend on U. When the fault dips, these two points move laterally relative to one another, their corresponding features move with them. For the vertical fault described above (Figure 2.5), the kink point A of F1 is slightly to the hanging wall side of the fault, and the kink point X of F2 is $h \tan \theta$ away from the fault, with a distance between them being in the range of $h \tan \theta < D < 2h \tan \theta$. Here h is the thickness for the hanging wall, and θ is the critical angle.

For a steep normal faulted structure, the kink point A of F1 is on the footwall side, i.e., on the same side as U. This makes the distance between A and X much smaller than the vertical

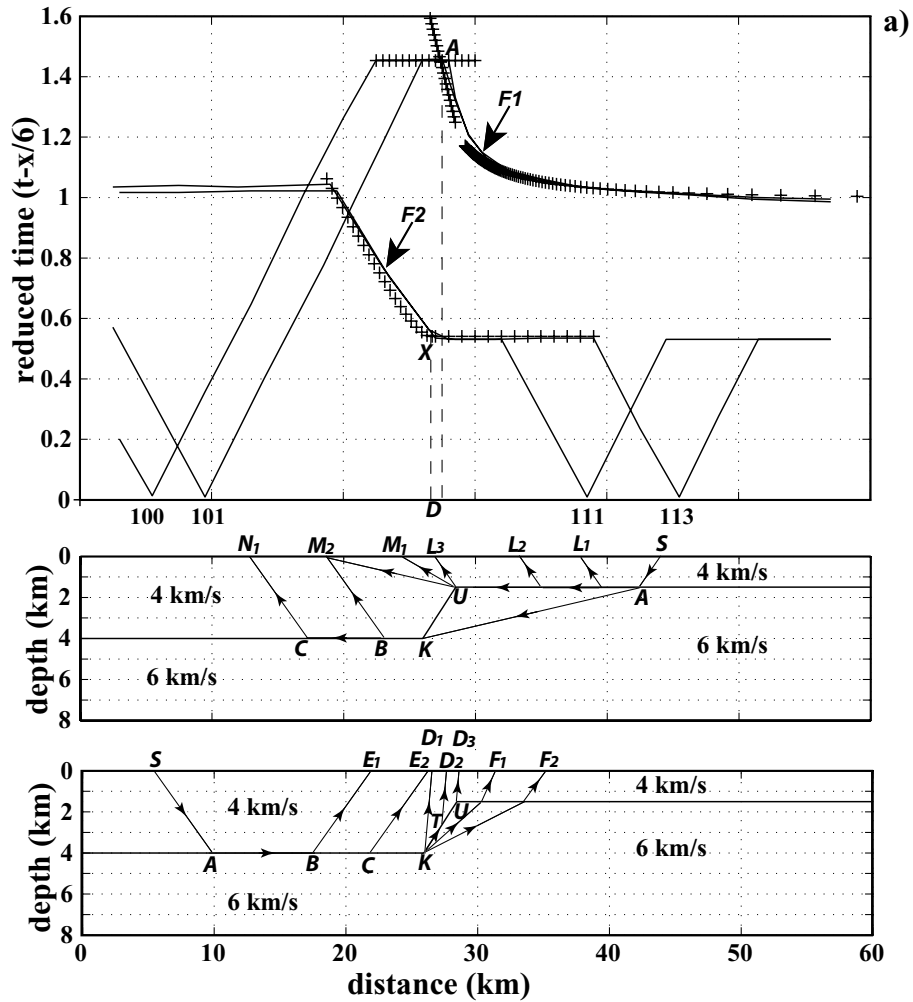


Figure A.1 Velocity models and synthetic first arrival picks for normal faulted and thrust faulted structures. On both plots, the solid line represents synthetic first arrivals from finite-difference modelling and the plus signs are the calculated travel times from ray theory. The ray paths for the calculation are shown the lower two panels. $F1$ and $F2$ in the upper panel represent the two diagnostic features discussed in the text. The middle panel shows the ray paths for different phases that appear as first arrival for a shot on the hanging wall, while the bottom panel shows those for a shot on the footwall. The top layer thickness of the hanging wall is designated as h . Note that the location of $F1$ (point A) is normally controlled by point K in the model, while $F2$ (point X) is controlled by point U . On the page is for a normal fault with a dip angle of 45° . Note that the distance between point A and X is much smaller than a vertical fault situation. Compare it with Figure 2.5. Here, $D < h \tan \theta$.

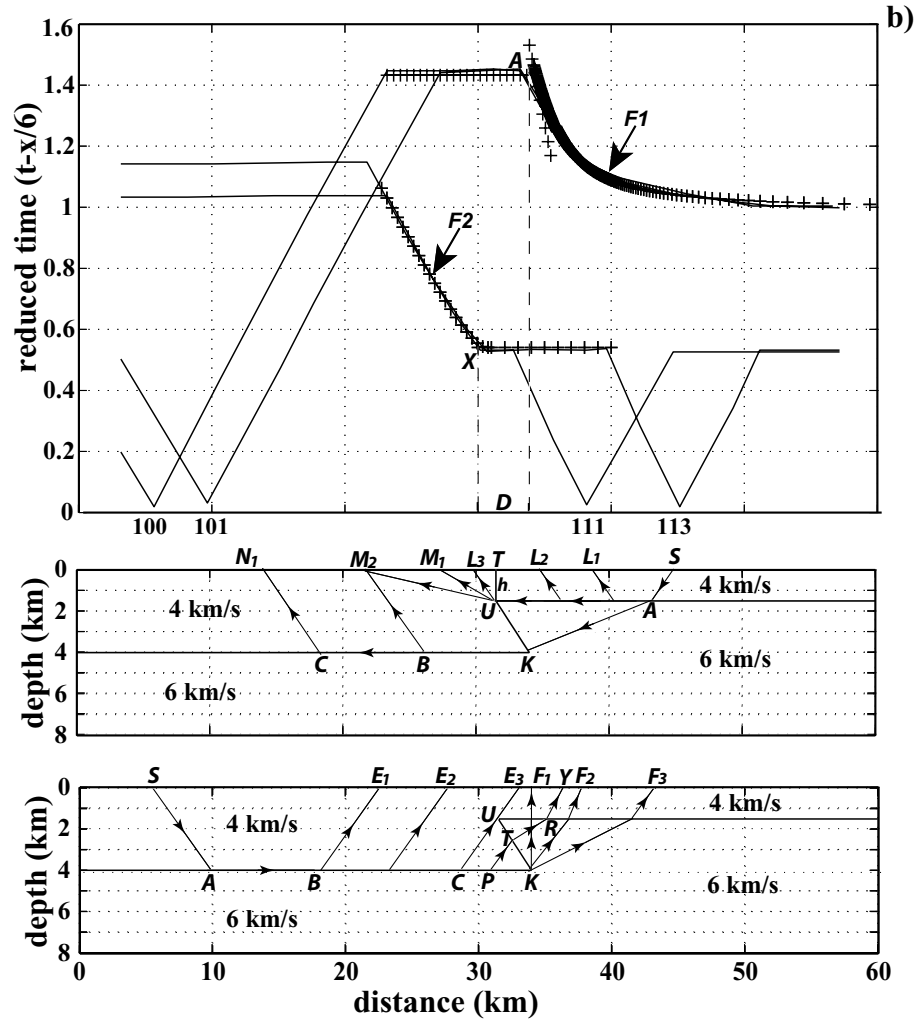
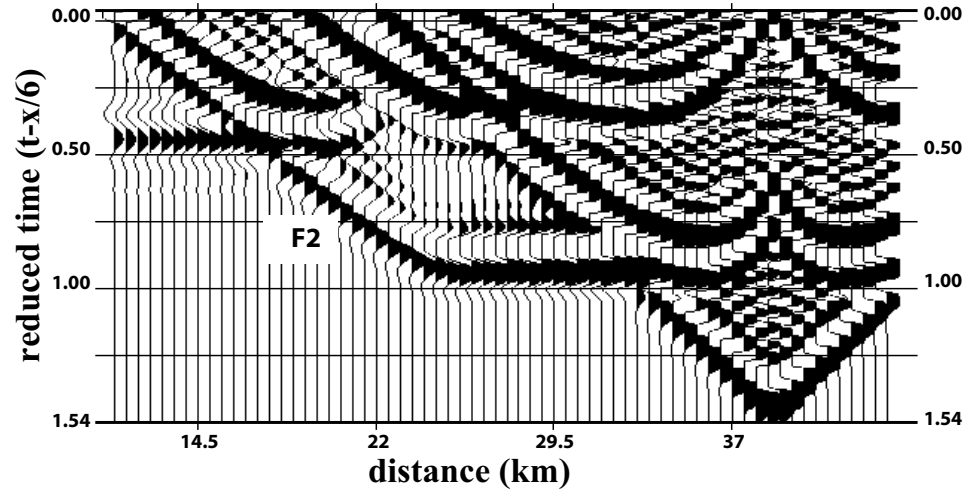


Figure A.1 (continued) On the page is for a steep thrust faulted structure (dip angle is 45°), the distance between point A and X is $D > 2h \tan \theta$. Relative position of A and X does not vary much with the dip angle. For normal fault situation, D varies with the dip angle, the smaller the dip angle, the smaller the distance. A and X might be aligned or reverse relative position for a shallow dipping normal fault.

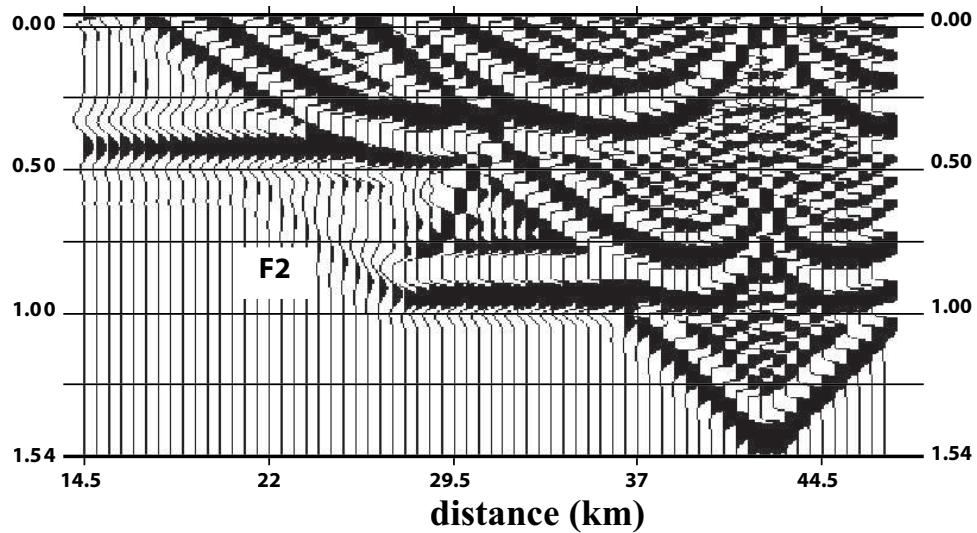
situation (compare Figure 2.5 and Figure A.1a). The two points might be aligned to the same ground point as is the case for the Pelona Fault or even reverse relative position when the dip angle of the fault gets shallower.

If the fault is a thrust fault (Figure A.1b), the kink point A of F1 is located considerably (at least $h \tan \theta$) to the hanging wall side of the fault. The position of point A in the arrival data is also controlled by point U in the model and the distance between the two kink points (X and A) is almost independent of the dip angle of the fault, with a value bigger than $2h \tan \theta$. As the dip angle gets smaller, the amplitude of the pulses consist of feature F2 in the waveform data gets smaller and almost invisible for a 30 dipping fault. From our finite difference modelling, amplitudes of the segment F2 are generally much smaller for a thrust faulted structure than that of a vertical or normal fault situation. Two synthetic seismograms for a thrust fault and normal fault are shown in Figure A.2.

In Figure A.1, the plus signs (+) denote travel time computed using the rays in the lower panels of the figures. They compare well with the travel time denoted by the solid lines, which are determined by finite-difference modelling.



(a)



(b)

Figure A.2 Amplitude comparison of the segment F2 for the two faulted structure in Figure A.1. Synthetic seismogram for the normal fault is shown in (a), while one synthetic shot gather from the thrust faulted structure is shown in (b). Note the amplitude difference for the segment F2. The amplitude for the normal case is much higher than that for the thrust fault. This amplitude difference is helpful in estimating the dip directions of faults for seismic surveys.

Appendix B

Receiver Functions for Individual Stations in the San Gabriel Mountains

Since large variations of the RFs with back azimuth are observed for most stations in the San Gabriel especially for those in the western San Gabriel Mountains (such as station VCS shown in Figure 3.3), all the radial and tangential RFs for the stations in the central Transverse Ranges are shown in the following pages. Check Figure 3.17 for station locations. Station PAS (Pasadena) is also shown as a reference.

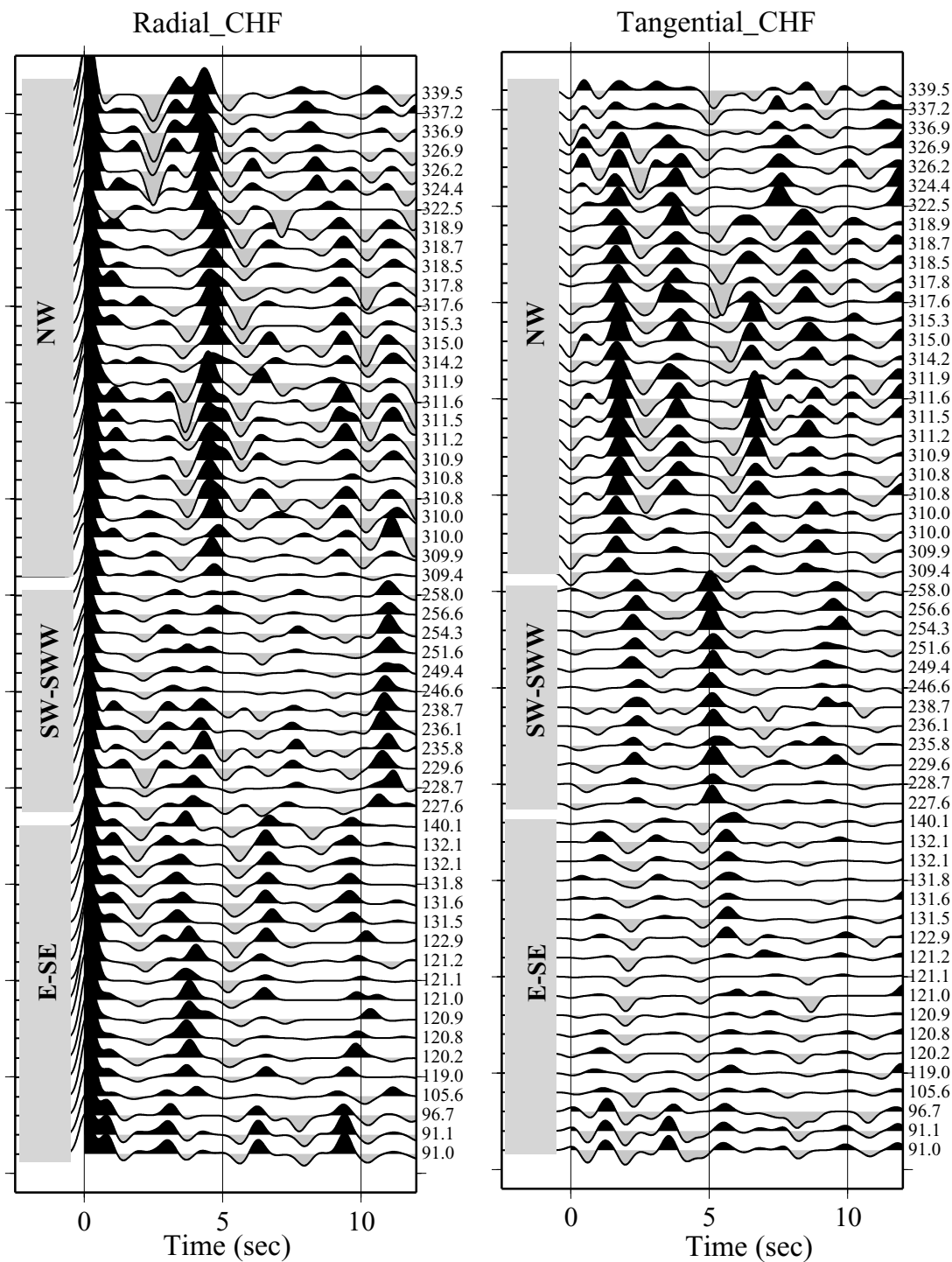


Figure B.1 Radial and tangential RFs for station CHF. Note the late Pms arrivals for the NW RFs with back azimuth less than 320° , which indicate the existence of a deep Moho.

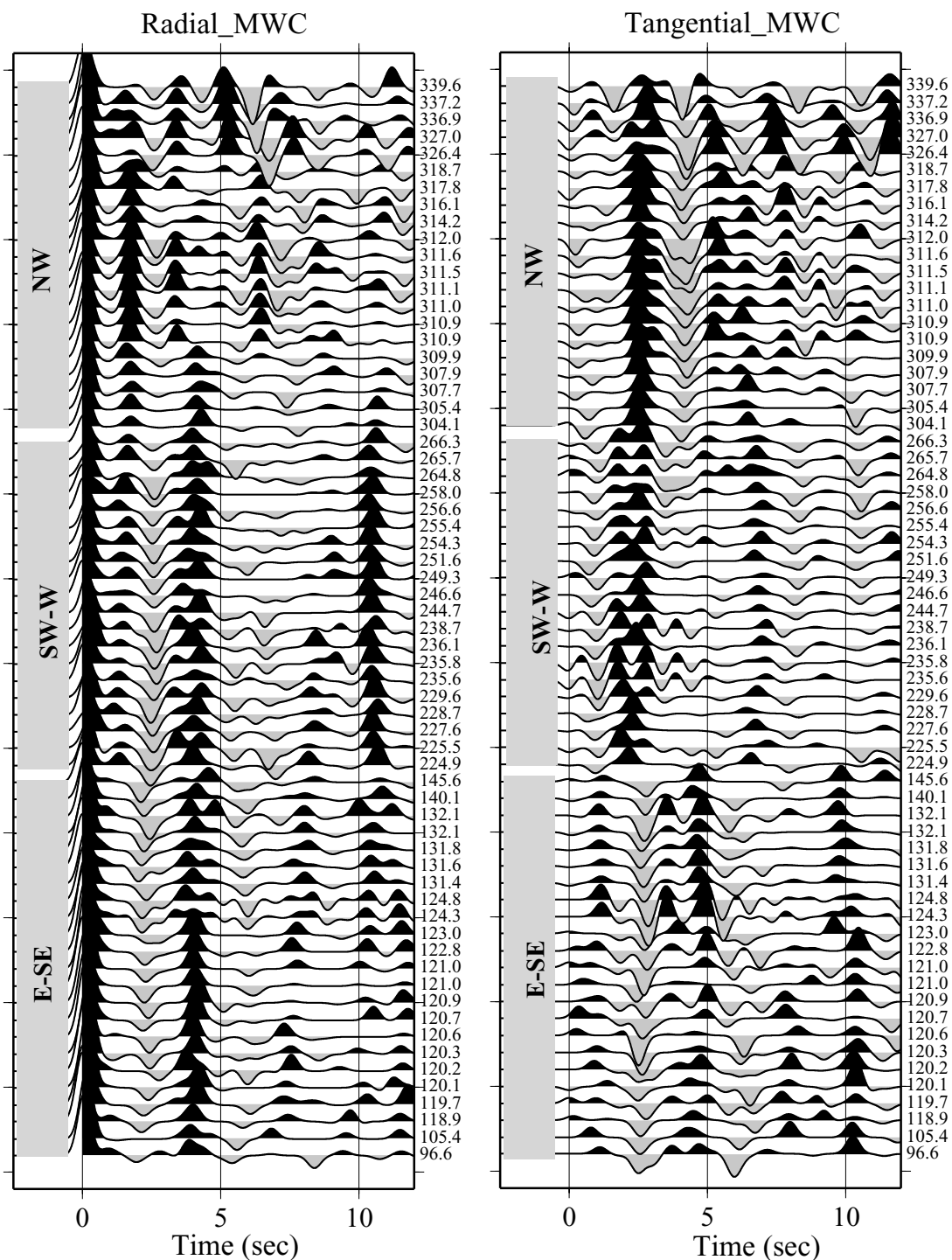


Figure B.2 Radial and tangential RFs for station MWC. Note the lack of Pms phase for part of the NW RFs with back azimuth in the range of 310° to 318° , which is probably due to complication in the deep structure across the north branch of the San Gabriel Fault (Figure 3.17). Late Pms arrival is observed for NW RFs with back azimuth larger than 318° indicating the existence of a local root here.

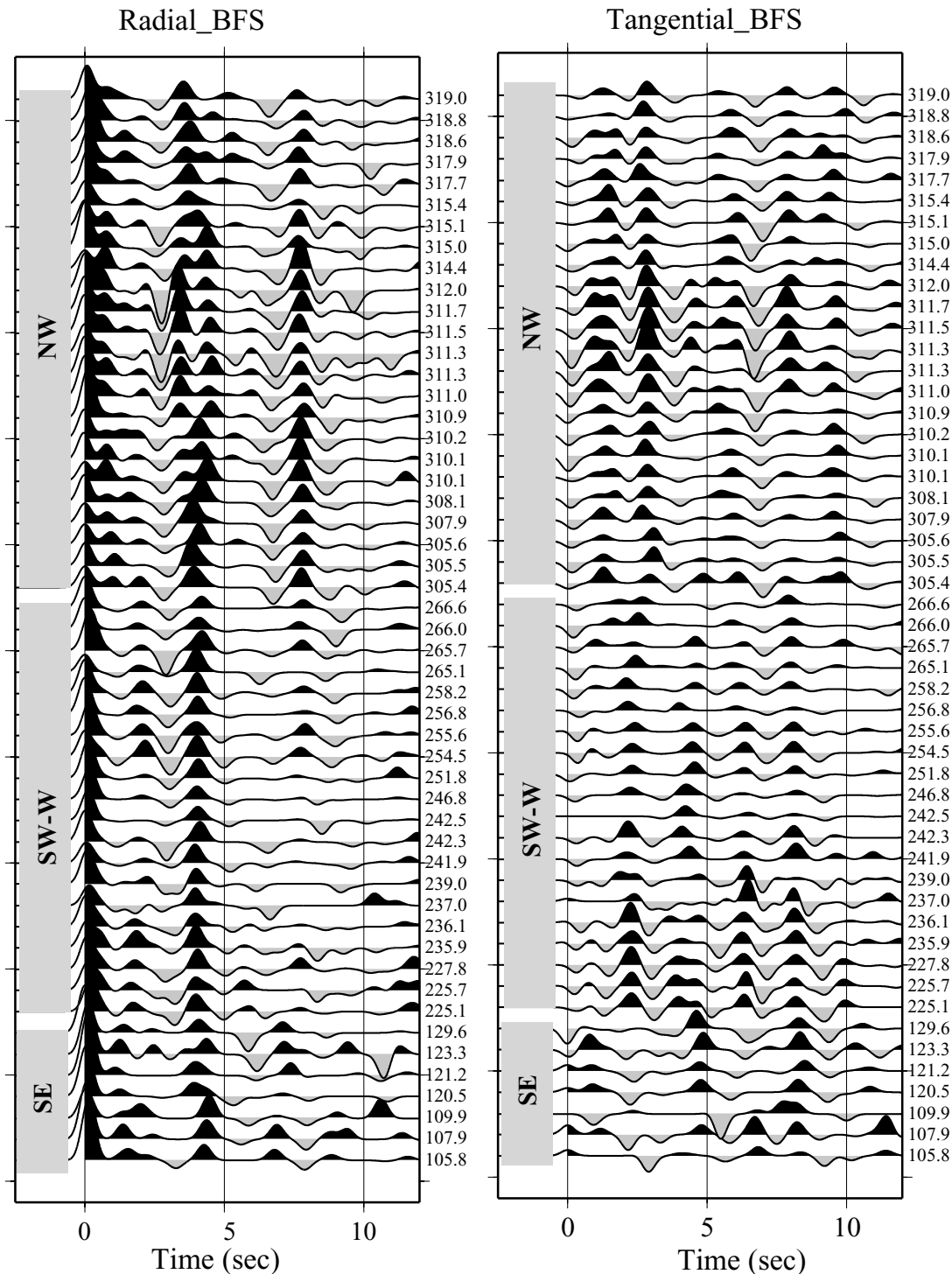


Figure B.3 Radial and tangential RFs for station BFS. Note the complications in the RFs for events from NW. This group of RFs vary systematically with ray parameter, which is shown in Figure 4.3 and is explained by the existence of a notch on the Moho.

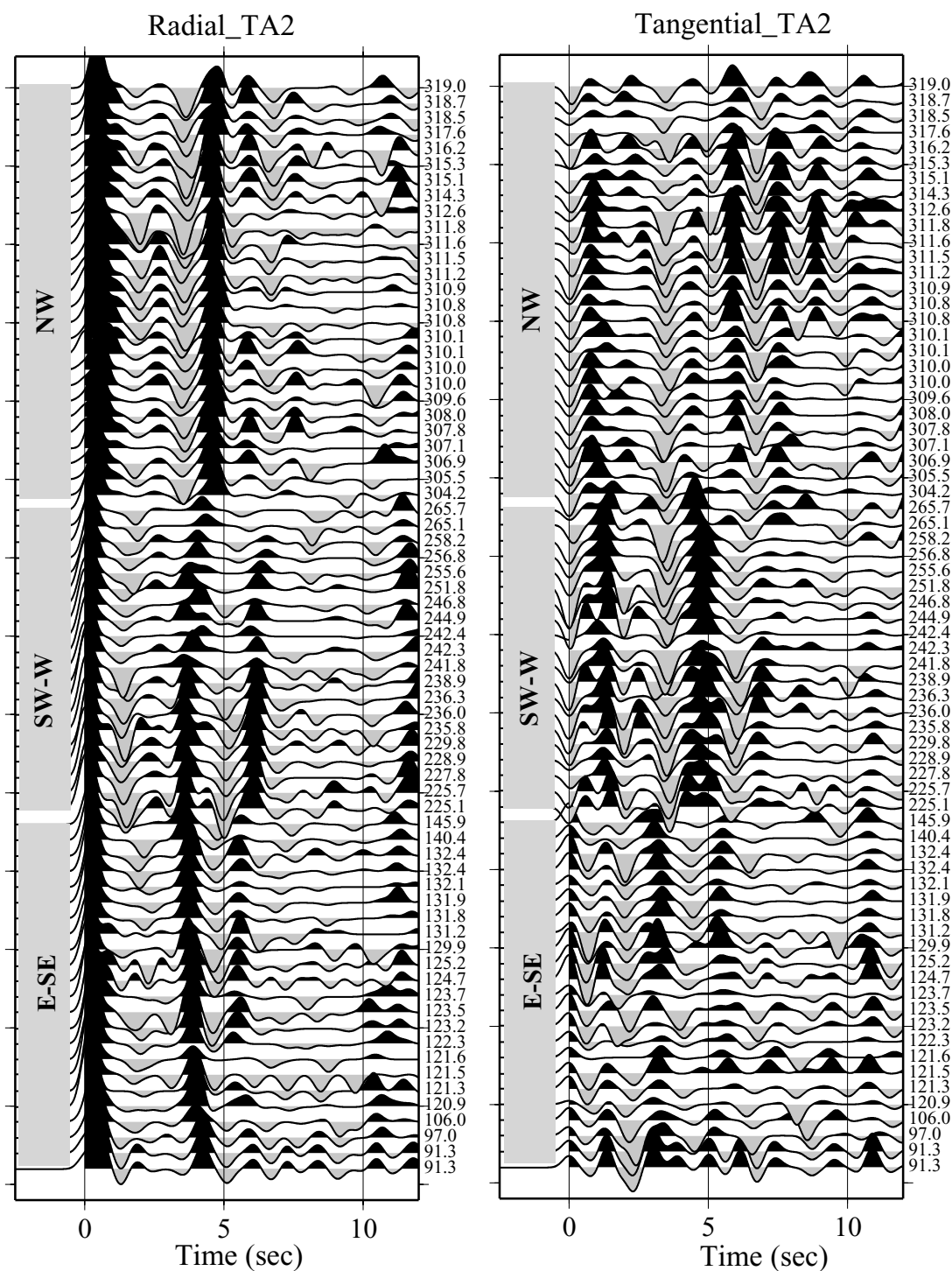


Figure B.4 Radial and tangential RFs for station TA2. Note the large difference in the Pms arrivals for the radial components for events from NW and those from SE and SW. Several relative large amplitude phases are observed in the tangential components indicating complications in crustal structure beneath this station.

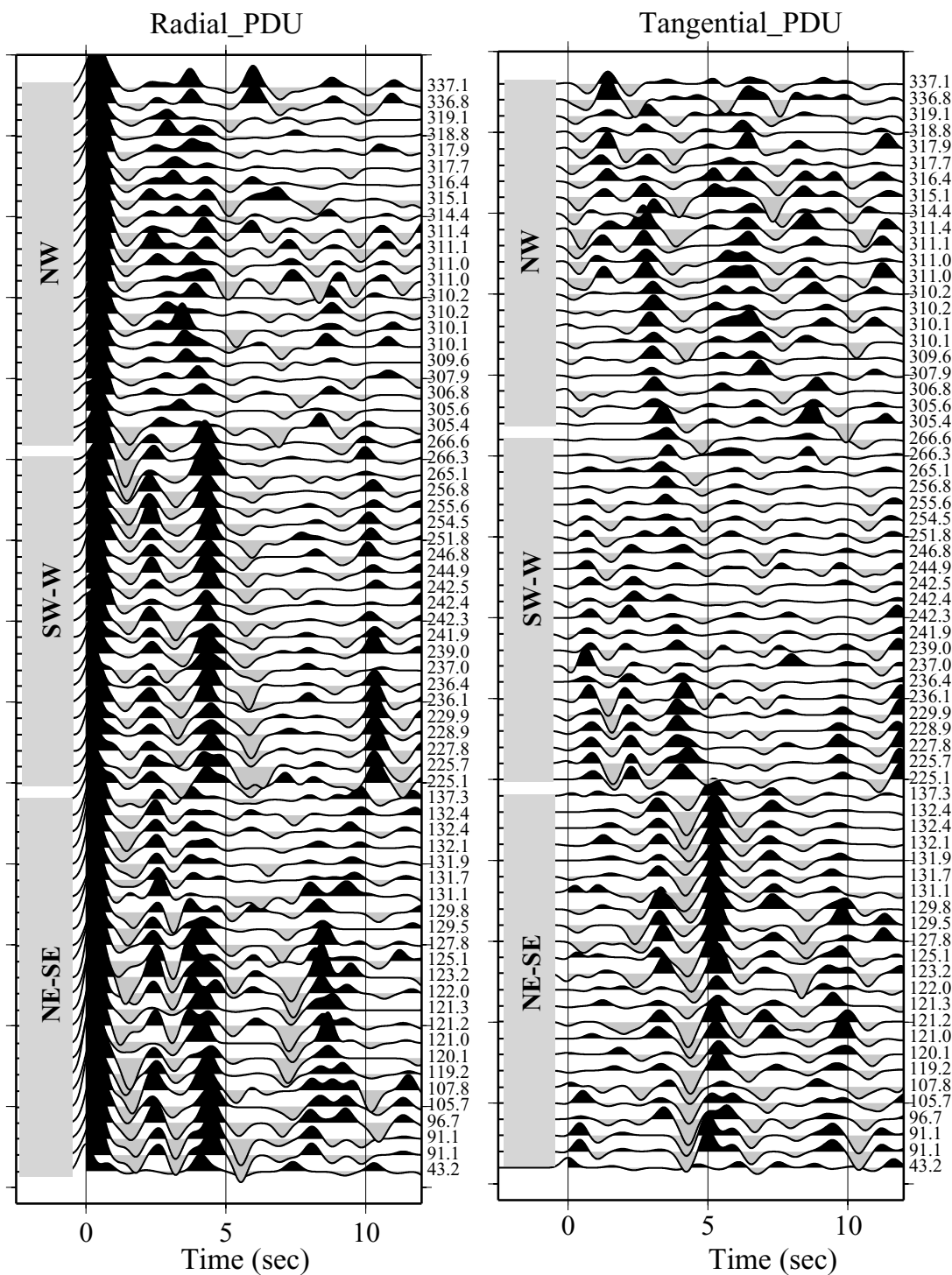


Figure B.5 Radial and tangential RFs for station PDU. Note the lack of consistent phases for the NW group probably as a result of complications in the crustal structure across the south bounding fault of the San Gabriel block—the Cucamonga thrust fault.

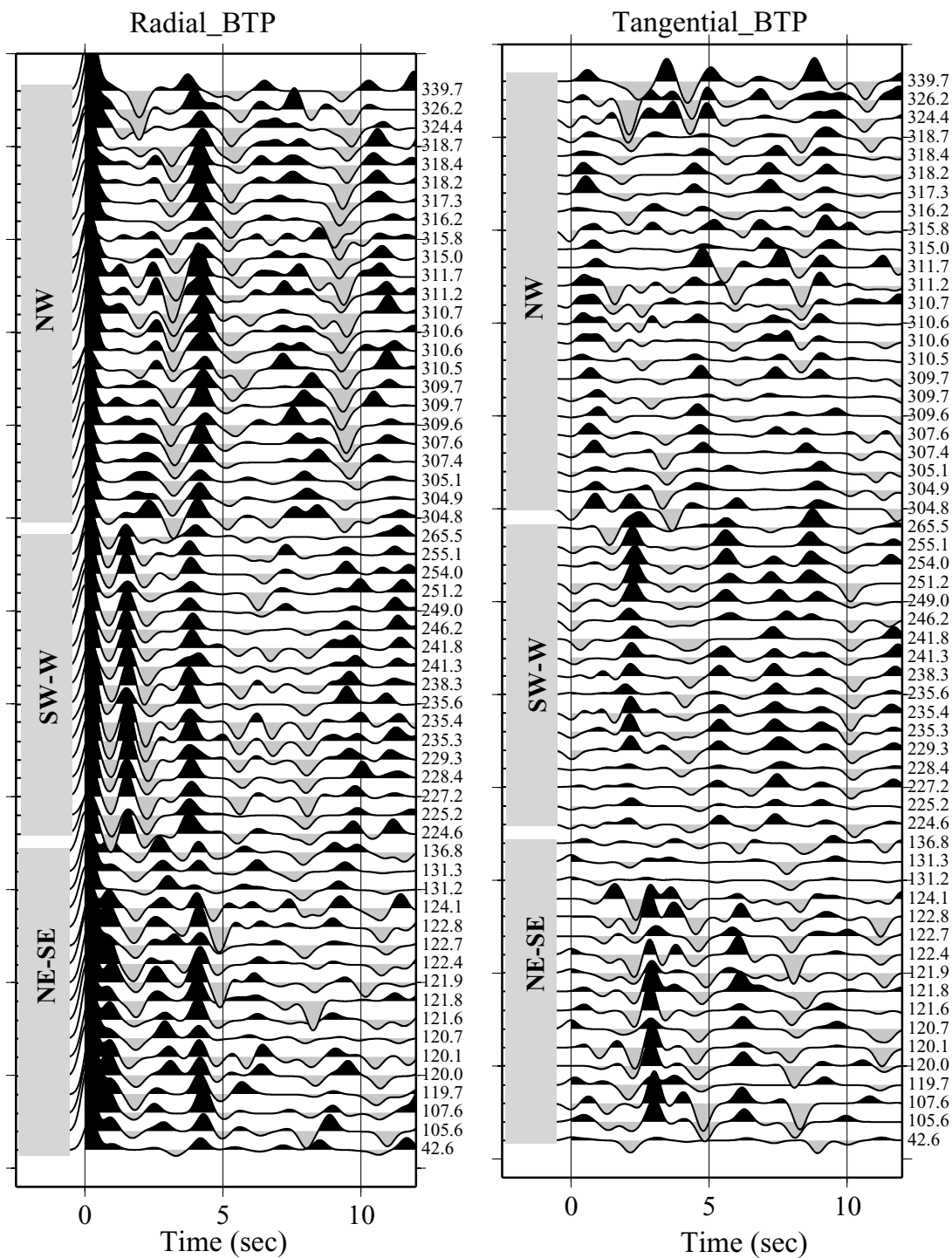


Figure B.6 Radial and tangential RFs for station BTP. Note the large difference in mid-crustal interfaces for the different back azimuthal groups.

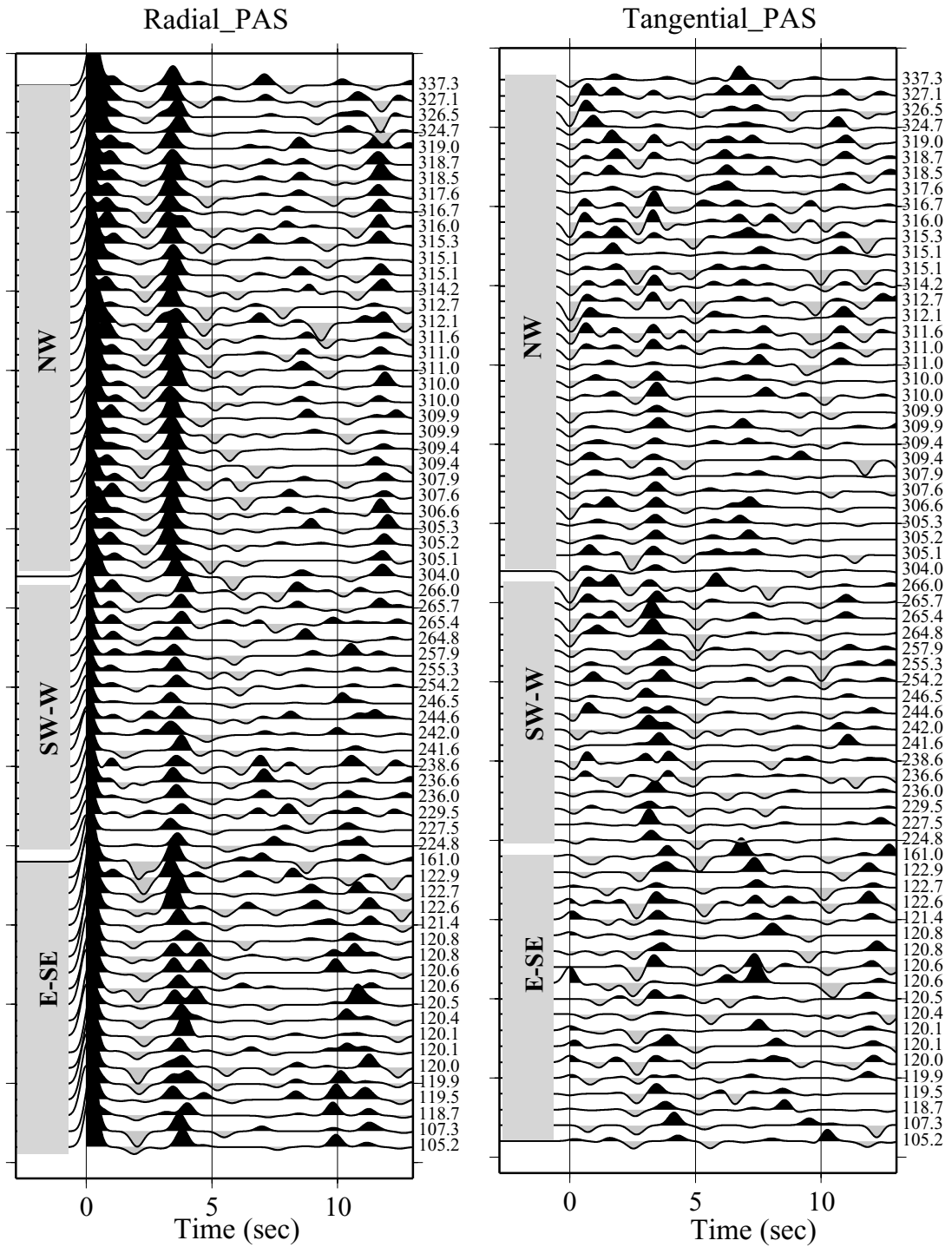


Figure B.7 Radial and tangential RFs for station PAS. Note that the positive phase arriving at around 12 sec for the NW RF group is the PpPms multiple.

Appendix C

Receiver Functions for Stations across the Salton Trough

C.1 Asymmetric Extension of the Salton Trough

In Chapter 3, asymmetric extension of the Salton Trough is presented in Figure 3.8, and the continental origin of the crust in the western Peninsula Ranges is inferred from the existence of a deep Moho beneath this range and its sharp transition to the shallow Moho beneath the Salton Trough. Involvement of the whole crust in the westward movement of western Peninsula Ranges (WPR) is thus inferred. Evidence for the strong coupling between the upper and lower crust can also be inferred from the large difference in the Moho depth among nearby stations within the WPR block. RF profiles for the three station groups separated by major faults in the WPR and one RF profile for station groups on the corresponding Mojave Desert side of the Salton Trough are shown in Figure C.2. Geologic station map for this study area is shown in Figure C.1

Large differences in the Pms arrival time for nearby station groups are observed in several places. One example is for stations DEV and PLC (Figure C.2), which are separated by the Banning fault. For station DEV, a relatively late Pms arrival time of ~ 4.2 is observed for all station groups, while an earlier Pms arrival time of 3.0–3.5 sec is observed for station PLC. Thus, a Moho offset of ~ 5 –8 km is inferred for these two stations that are ~ 15 km apart. A similar Pms arrival time difference is observed between stations GOR and DPP on the southern block (Profile S in Figure C.2). Stations located in the center of the intact WPR block, such as PLM, DPP, SDR and BAR, generally show a deeper Moho of 34–37 km, while stations close to the coast, such as BCC, CAP and GOR, and those close to the Salton Trough, such as PLC, AGA, TRO, BOR, YAQ, generally show a shallower Moho of less than 30 km. The large rapid variations in the Moho depth and the fact that a deep Moho exists in the center of WPR indicate

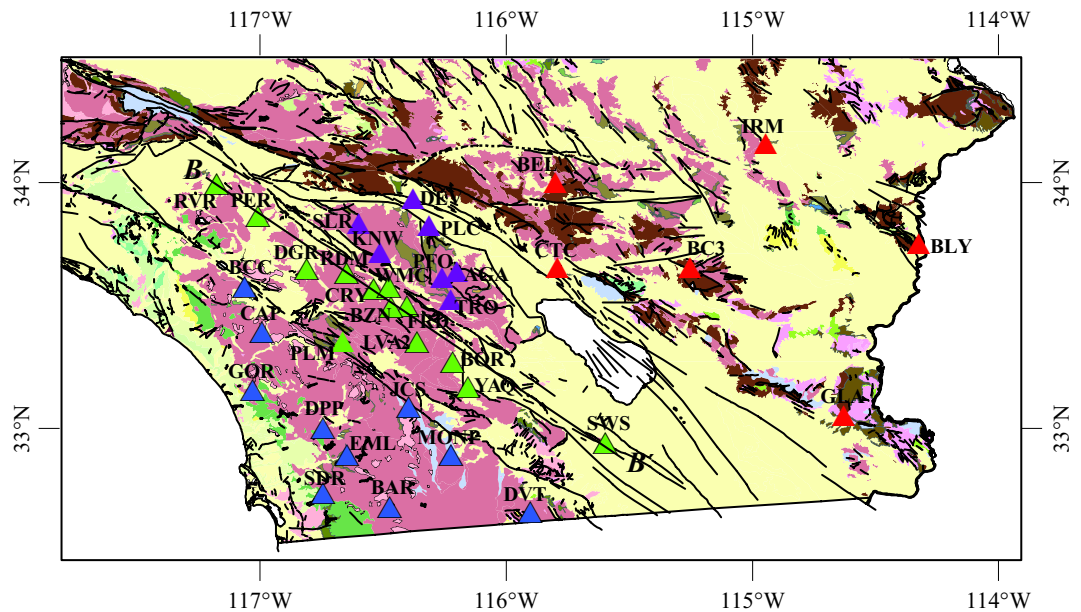


Figure C.1 Geological station map in the Peninsula Ranges. Color represents different rock units. Pink rose-colored rocks are Precambrian to Mesozoic granitic batholithic rocks. Green is Paleocene marine sedimentary rocks. Light blue is lower plate pelona schist and yellow is Quaternary sedimentary rocks. Station groups in the western Peninsula Ranges are divided into 3 groups separated by the major strike-slip faults

that the crust beneath the WPR is of continental origin and that the whole crust is relatively strong and is involved in the westward movement of the WPR block. Modifications of the continental crust, however, did occur at the edge of the block, especially close to the Salton Trough, where shallow Moho of 25–28 km is observed.

Asymmetric extension of the Salton Trough can be inferred by comparing the lateral variations of the Pms arrival times for the three western profiles with those on the eastern profile. For the 3 profiles on the west, transition from the shallow Moho at ~ 22 – 25 km beneath the Salton Trough to deeper Moho of ~ 33 – 37 km beneath the western Peninsular Ranges is rather sharp within a lateral distance of ≤ 40 km (such as along the central profile). The transition is very gradual to the east. Stations, such as IRM and BLY, that are ~ 100 km away from the axis of the Salton Trough still have a shallow Moho of 26–28 km.

C.2 RFs for Station JCS and Nearby Stations

Large difference in the Pms arrival time for the different back-azimuthal (BAZ) groups of the same station is also observed for several stations in the WPR, such as JCS at the north edge of

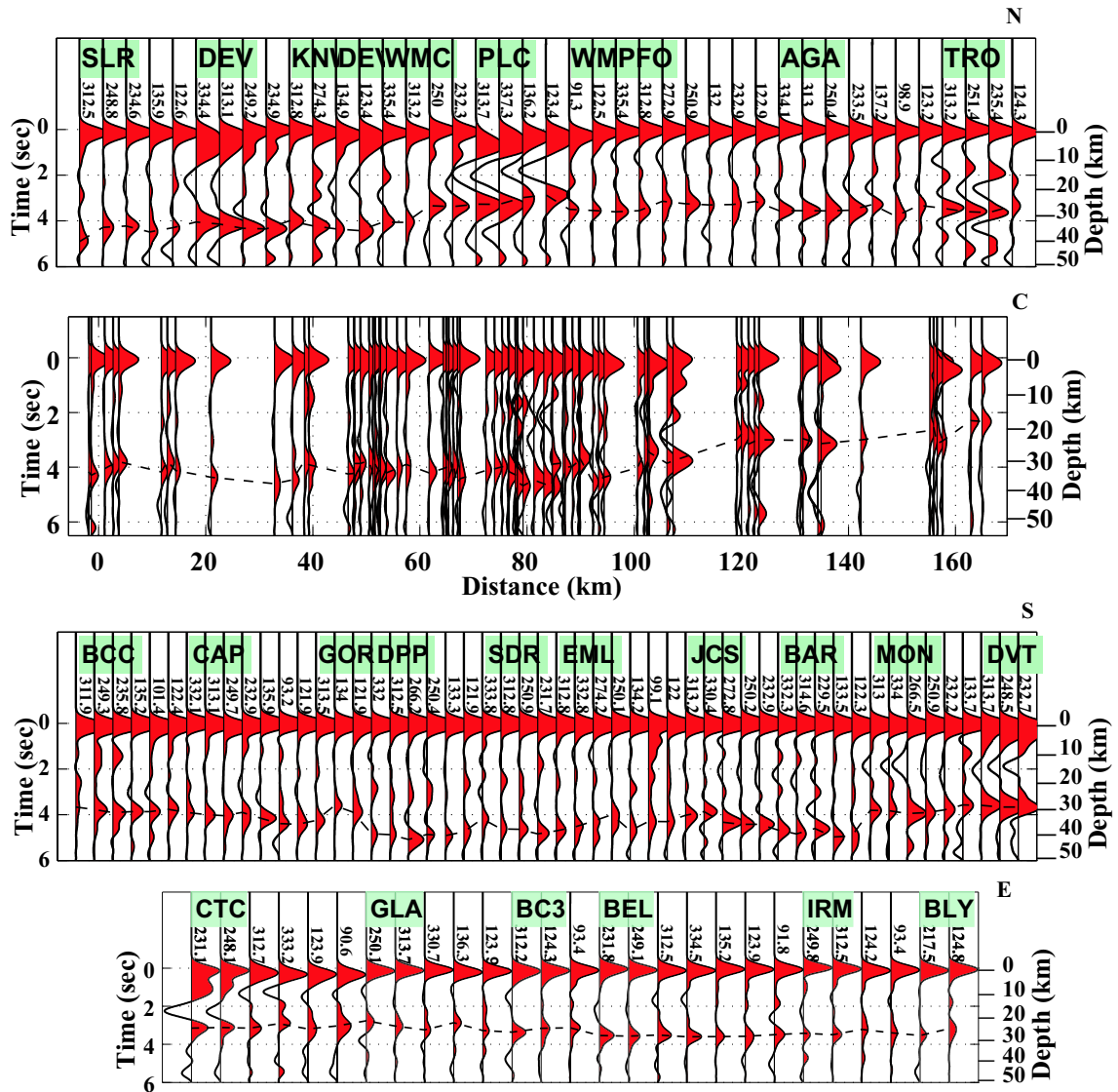


Figure C.2 Three RF profiles in the western Peninsula Ranges and one profile in the Mojave Desert to show the asymmetric extension of the Salton Trough. The N, C, S and E RF profiles are for stations in purple, green, blue and red in Figure C.1. The N and S RF groups are sorted according to their distance away from the Salton Trough. RF groups are projected onto line BB' for the central profile since stations in this central block are densely distributed. RF groups on the E profile are sorted according to their distance away from the Salton Trough, with stations closer to the Salton Trough shown on the left. Note that RF station groups for the N, S and E profiles are evenly spaced to show each individual trace. Dash lines in all profiles are the Pms phase marks. For the central profile, the apparent notch structure on the Moho at horizontal distance of ~ 90 km is due to difference in the Pms arrival in the direction perpendicular to the projected line BB' . Late Pms arrival is observed for station PLM at the southern edge of the central block, while earlier arrivals are observed for northern stations, such as BZN and FRD.

the southern block. RFs for the west BAZ groups have large Pms arrivals of 4.0–4.5 sec, while Pms arrives at ~ 3 sec for those from the east (Figure C.3). Moho piercing points for the east RF groups are located in the central block and are relatively closer to the Salton Trough where shallow Moho is observed. RFs for a nearby station (YAQ) at ~ 25 km to the east show early Pms arrivals of ~ 3 for events from all directions (Figure C.4), which confirms the existence of shallow Moho for the east BAZ groups of JCS. RFs for another station DPP, at ~ 33 km west of station JCS, show a similar deeper Moho of 34–37 km (Figure C.4) and thus the existence of deeper Moho for the west RF groups of JCS in the relatively intact western Peninsula Ranges is confirmed.

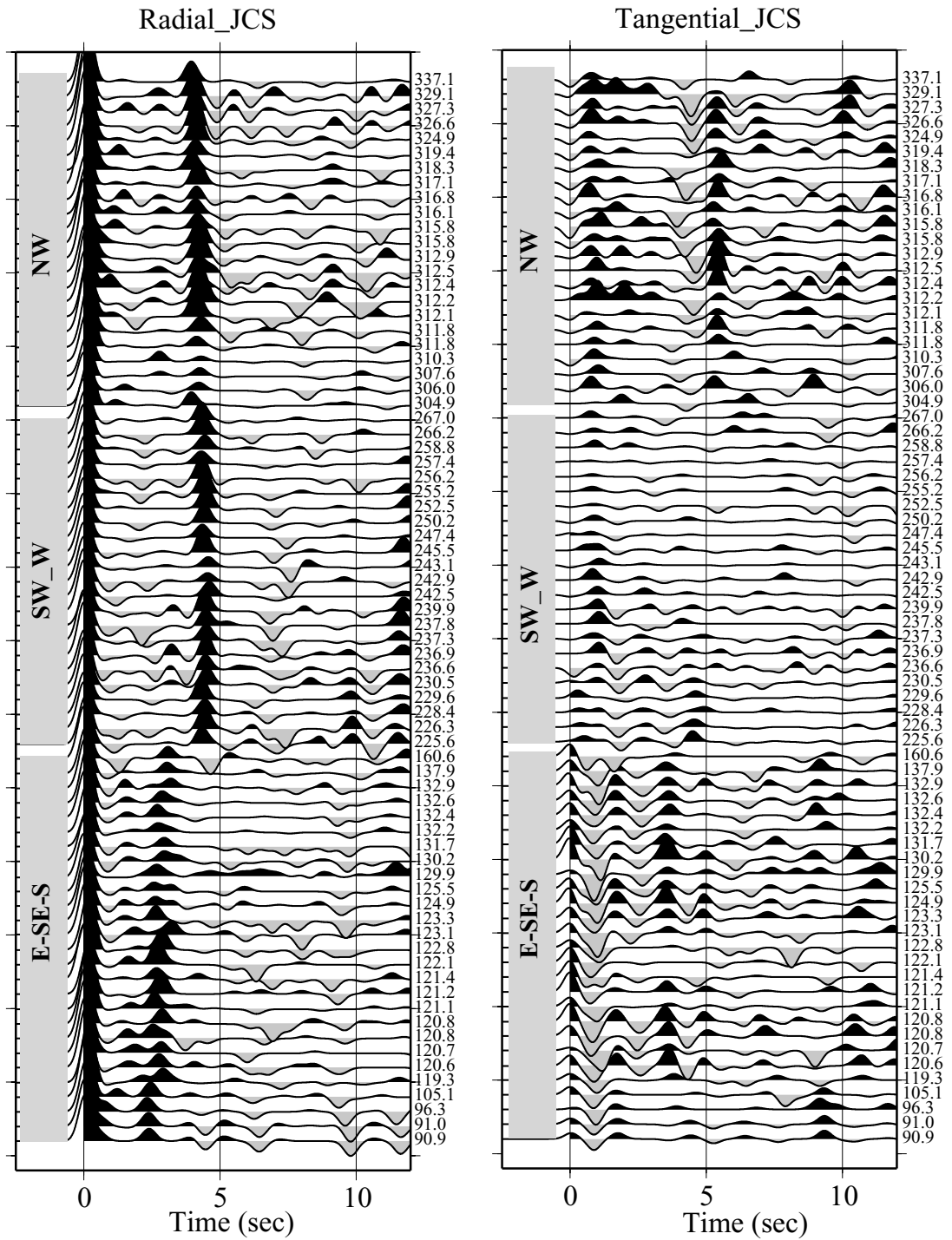


Figure C.3 Radial and tangential RFs for station JCS. RFs for both components are evenly spaced, but in the order of increasing back-azimuth from bottom to top. Note the low amplitude in the tangential components for the SW-W BAZ group and relatively larger amplitude for the E-SE-S and NW groups. The relatively large amplitude in the tangential component for the E-SE-S and NW groups indicates the existence of some complications in the crustal structure beneath this station.

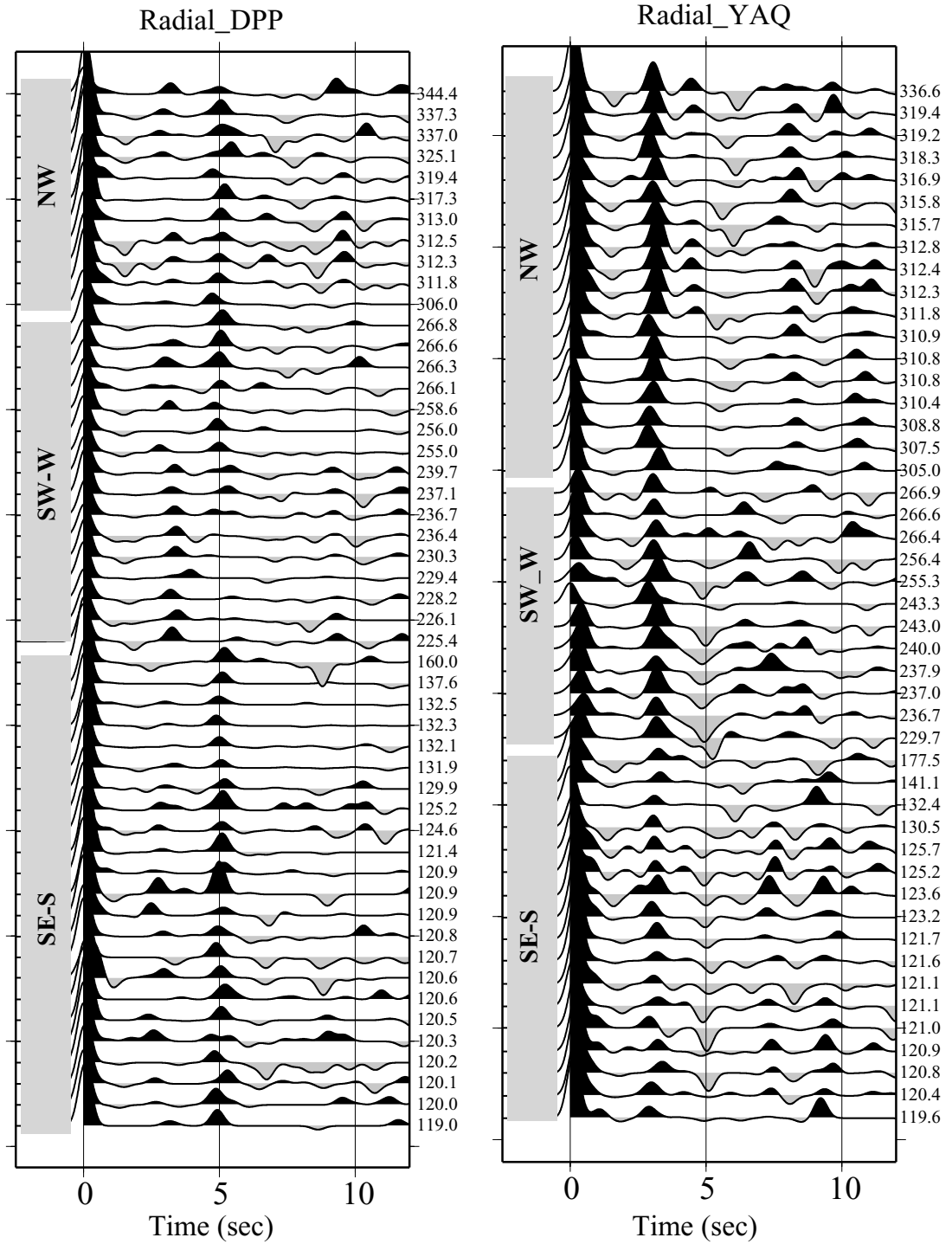


Figure C.4 Radial RFs for station DPP and JCS. Note the late Pms arrival differences for these two stations.

Appendix D

Anomalous Receiver Functions for Stations in the Mojave Desert and Sierra Nevada

Large variations in the receiver functions are also observed in several stations in the eastern Mojave Desert, Sierra Nevada and Walker lane area. Receiver functions for several representative stations are shown in the following sections.

D.1 Mojave Desert Stations

In chapter 3, large difference in the Pms arrival time with back azimuth is observed at two stations, DAN and LDF, in the eastern Mojave Desert. For station DAN, a large difference of ~ 1 sec is observed for events from NW and those from SE (Figure D.1. $[H, \kappa]$ domain grid search of one NW ([305, 323]) and one SE ([115, 130]) back azimuthal groups results in a Moho depth of 22 km and 32 km for them respectively. Both PpPms and PsPms multiples are well developed for the NW group and a well constrained (H, κ) combination is found for this group (Figure D.3). For the SE group, the PpPms multiple is prominent for most RFs, but PsPms multiple is not well developed probably due to weak lateral heterogeneity in the crustal structure. The (H, κ) combination is still relatively well defined and the Vp/Vs ratio is estimated to be within the range, [1.743, 1.825], which is similar to the estimation for the NW group [1.793, 1.9]. A Moho offset of ~ 10 km is thus inferred for these two station groups, which are ~ 15 km away from each other indicating that the Moho offset is very sharp. Relative large amplitude RFs are observed on the tangential components, which indicates that lateral heterogeneity or anisotropy might exist in the crustal structure beneath this station.

For station LDF, difference in the Pms arrival time for different back azimuthal groups is not as dramatic as those for station DAN, a minor difference of 0.2–0.3 sec is observed between

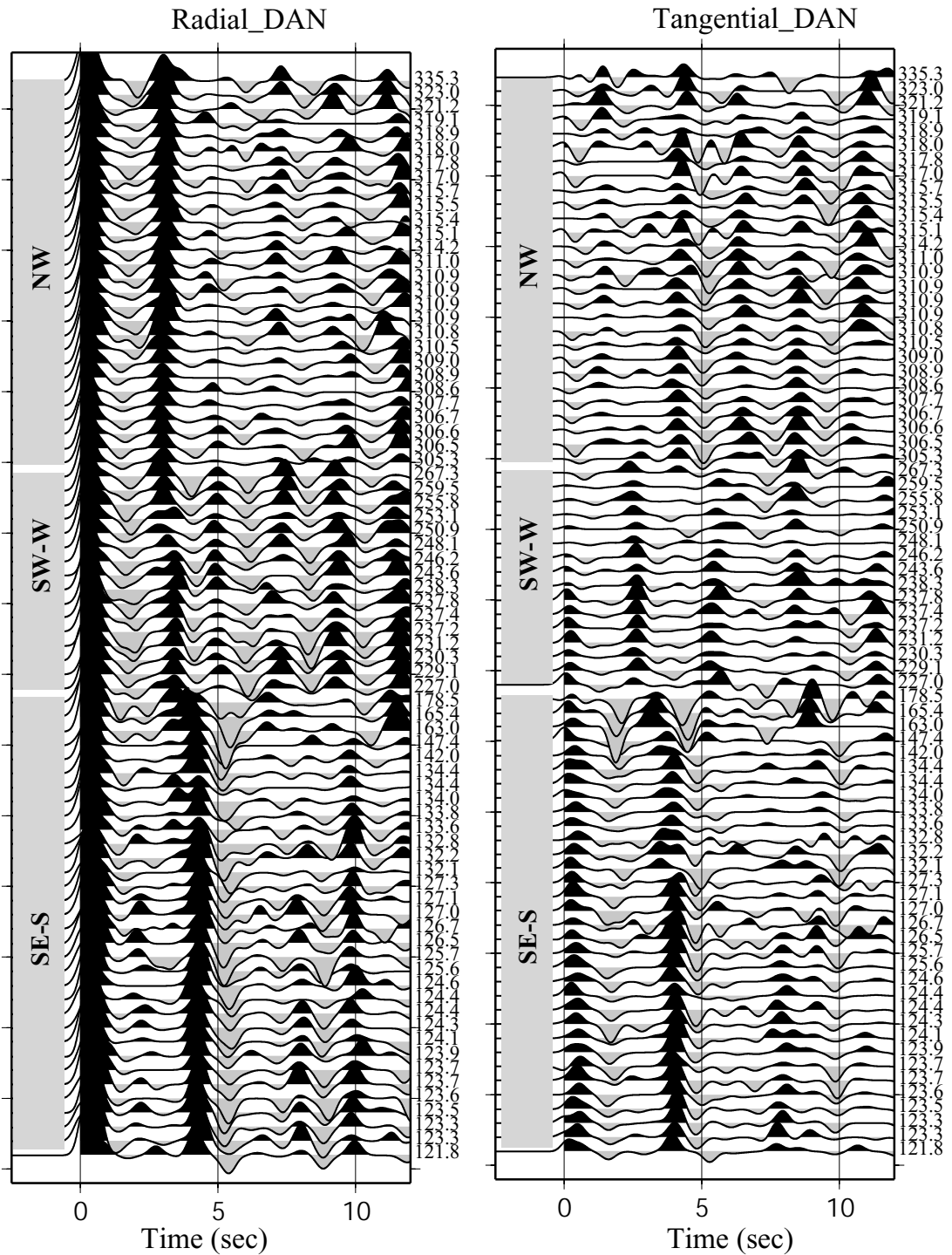


Figure D.1 Radial and tangential RFs for station DAN. Note the large difference in the Pms arrivals for stations from NW, SW-W and those from SE-S and the prominent negative pulse following Moho Pms for the SE-S group stations.

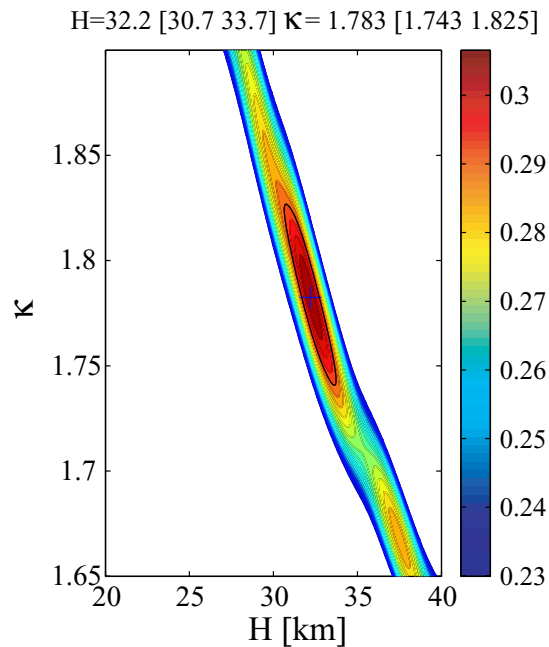
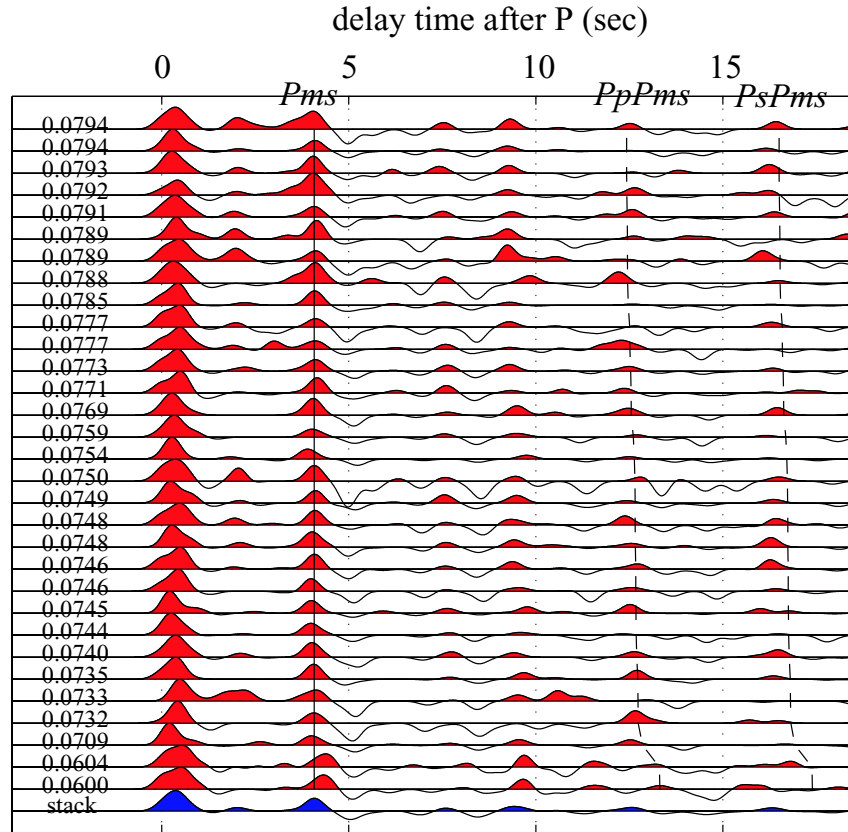


Figure D.2 Individual RF traces for the SE group of station DAN with the predicated arrival time of the three phases, Pms, PpPms and PsPms from the $[H, \kappa]$ domain grid search marked. Contour of the weighted summation function is shown on the bottom with the picked (H, κ) shown as a plus sign.

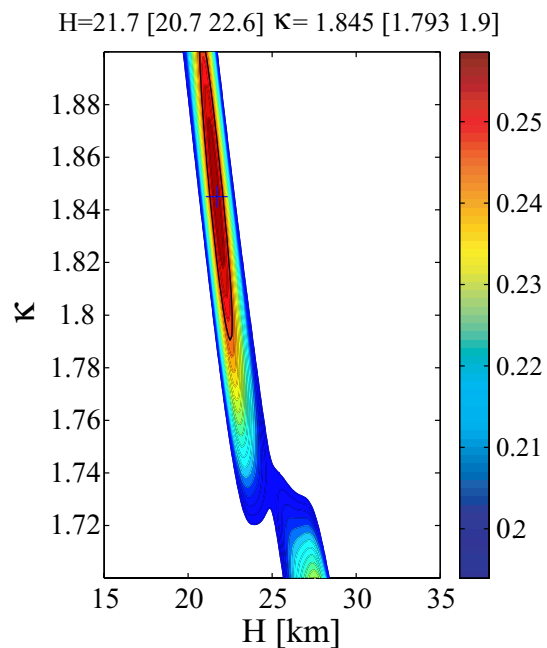
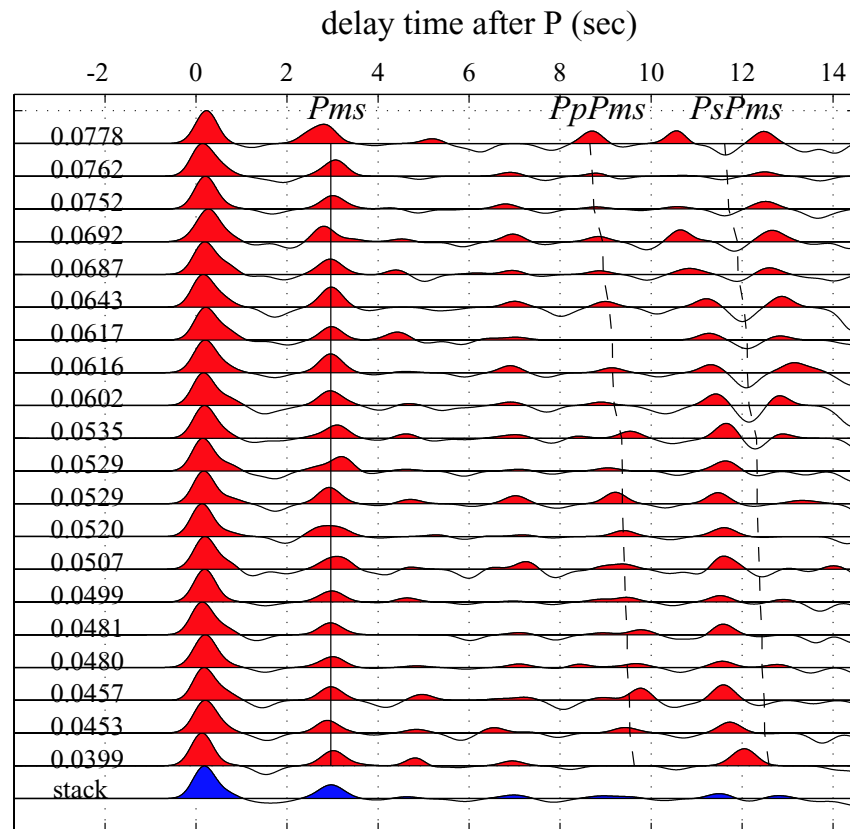


Figure D.3 Similar to Figure D.2, except only representative individual RF traces for the NW group of station DAN are shown. Note the early Pms arrival times for this group comparing with those of Figure D.2.

events from E-SE and those from NW and SW-W. The distinctive feature for this station is that a mid-crustal low-velocity zone and a relatively flat mid-crustal interface are observed, which are absent in other stations in the Mojave Desert, indicating the complexity of the crustal structure beneath this station. Interesting thing about the stacking of this station is that, for SE RF group Figure D.6 , it has a later Pms arrival time but a shallower Moho of ~ 27 km is inferred from the grid search due to the high Vp/Vs ratio (1.84) picked for this group, whereas a slightly deeper Moho of 30 km is inferred for the NW group due to the lower Vp/Vs value (1.70) (Figure D.5). PsPms multiples for the NW group are not well defined and more than one local maximum contours exist, so, the grid search for this group is probably not problematic even though the PpPms multiple is very prominent.

D.2 Sierra Nevada Stations

Nearby stations in the Sierra Nevada and Walker Lane area also show large differences in their Pms arrivals. One example is for stations ISA (Figure D.7) and WBS (Figure D.8) in the Tehachapi Mountains. The two stations are ~ 33 km apart with ISA in the middle of the Tehachapi Mountains and WBS on the border of the Sierra Nevada and the Walker Lane belt. Pms arrivals for station ISA are generally 0.4–0.6 sec later than those for station WBS, which, indicating the the existence of a Moho offset across the intact Sierra Nevada and the highly extended Walker Lane belt. Moho is relatively deeper beneath the intact Sierra Nevada and shallower in the highly extended Walker Lane belt. However, exceptions to this pattern are observed at station FUR, CGO and CWC.

Station FUR is located at junction of the Furnace Creek Fault and Death Valley Fault zone and is thus on a surficially highly extended area [Snow and Wernicke 2000]. But, RFs for this station imply the existence of a deep Moho at ~ 36 – 39 km, which is in contrast with previous COCORP studies [Allmendinger et al. 1983, 1987; Hauge et al. 1986; Hauser et al. 1987]. If the result is real, then the existence of a deep Moho in this highly extended Death Valley area will change the existing flat Moho picture beneath the Basin and Ranges established by the COCORP studies. Since there might be questions about the results for this station, radial and tangential RFs, as well as the stacking of the SE and SW groups are shown below.

A large difference in the Pms arrival time is observed at this station, with late arrivals of

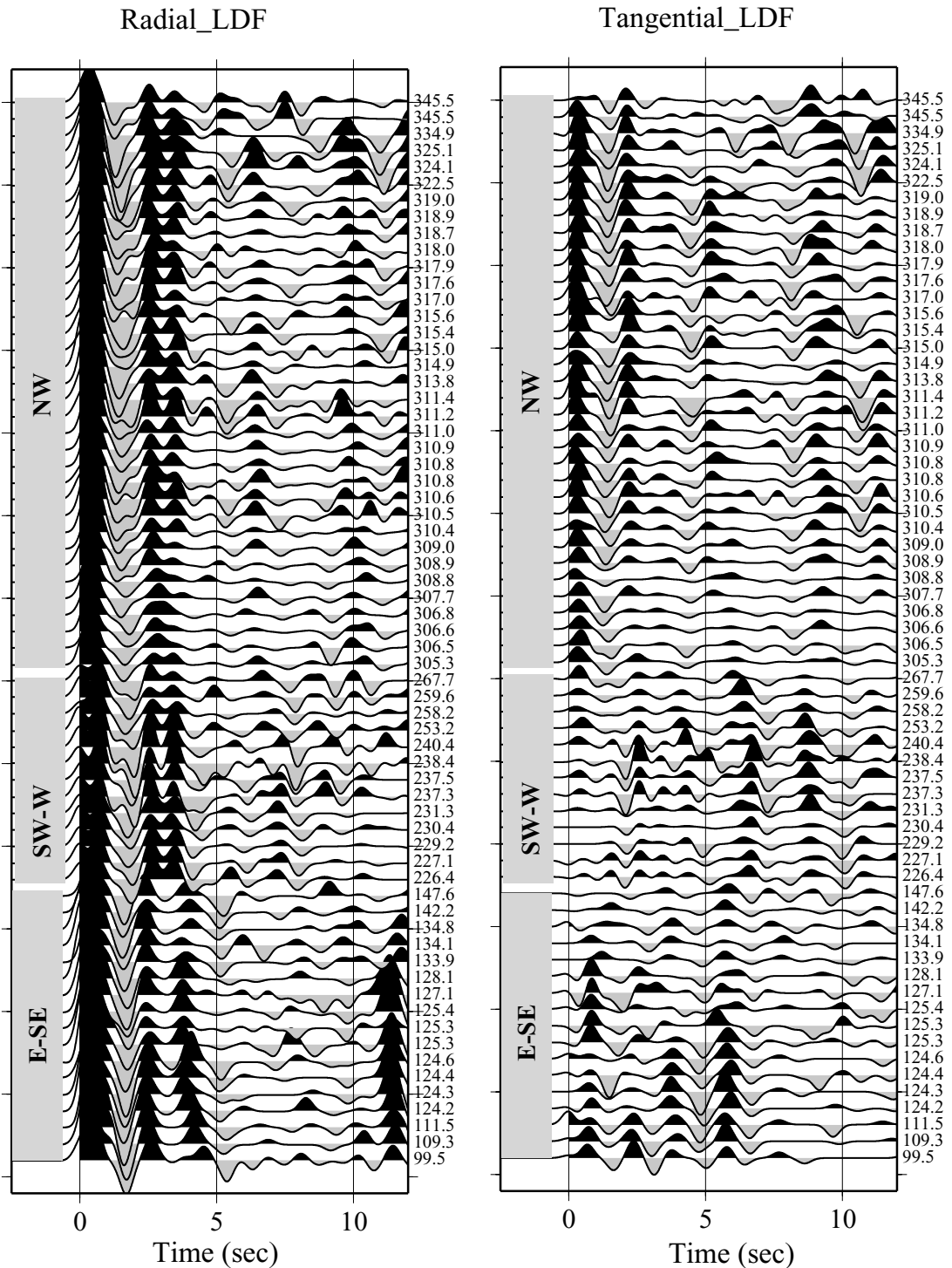


Figure D.4 Radial and tangential RFs for station LDF. Note the large difference in the Pms arrival times for events from NW, SW-W with those those from E-SE. Also note the prominent negative phase at ~ 1.5 sec and the following positive mid-crustal phases, which are absent in other station groups in the Mojave Desert.

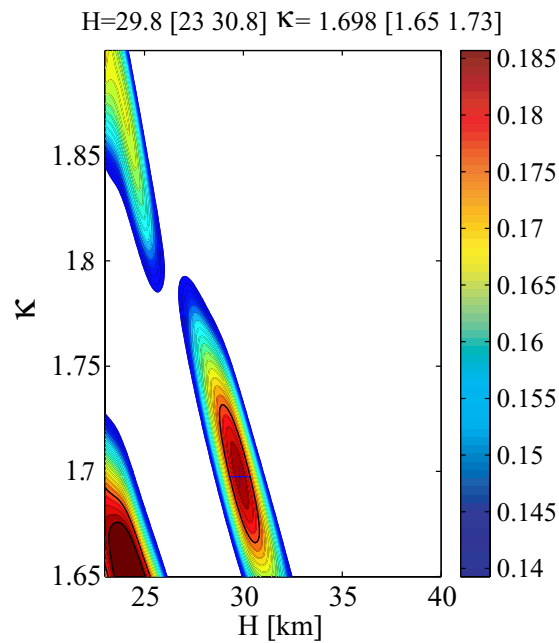
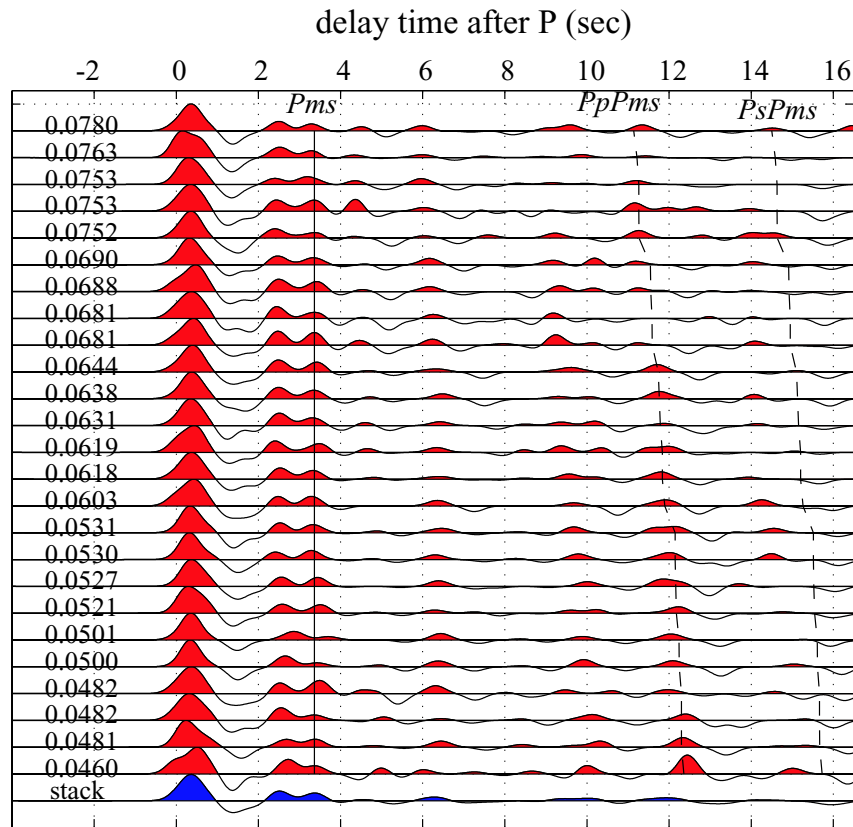


Figure D.5 Similar to Figure D.3, representative individual RF traces for the NW group of station LDF. Note the early P_{ms} arrival times and the relatively small V_p/V_s ratio for this group.

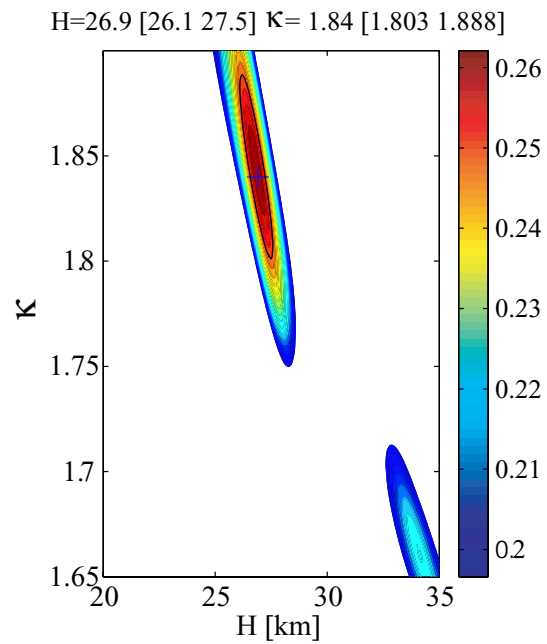
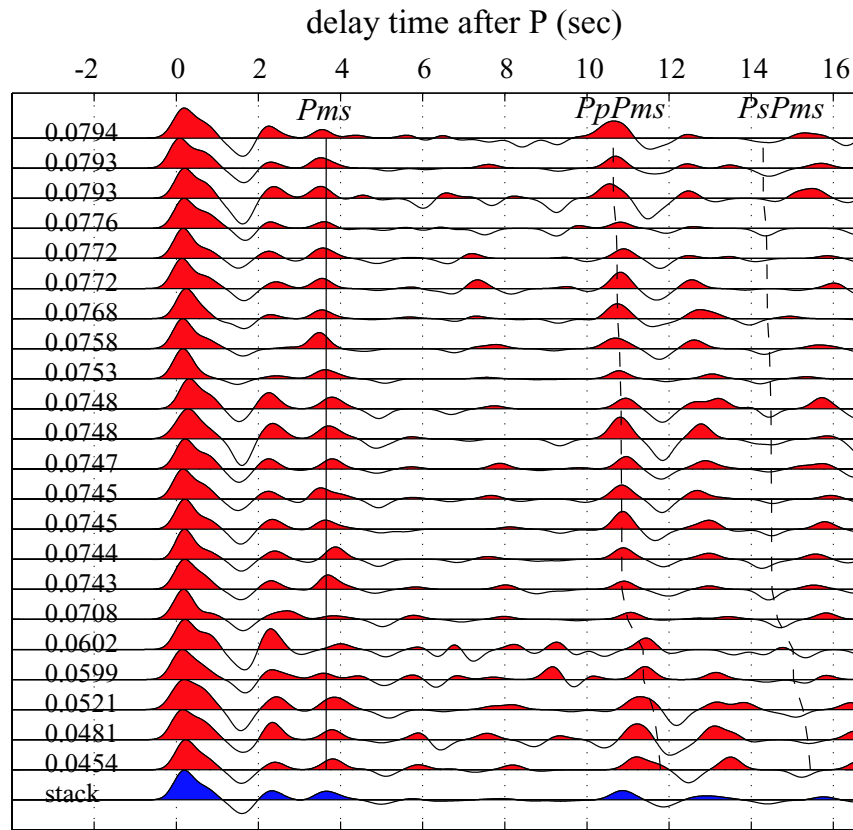


Figure D.6 Similar to Figure D.3, representative individual RF traces for the SE group of station LDF. Note the relatively late Pms arrival times and the large Vp/Vs ratio picked for this group.

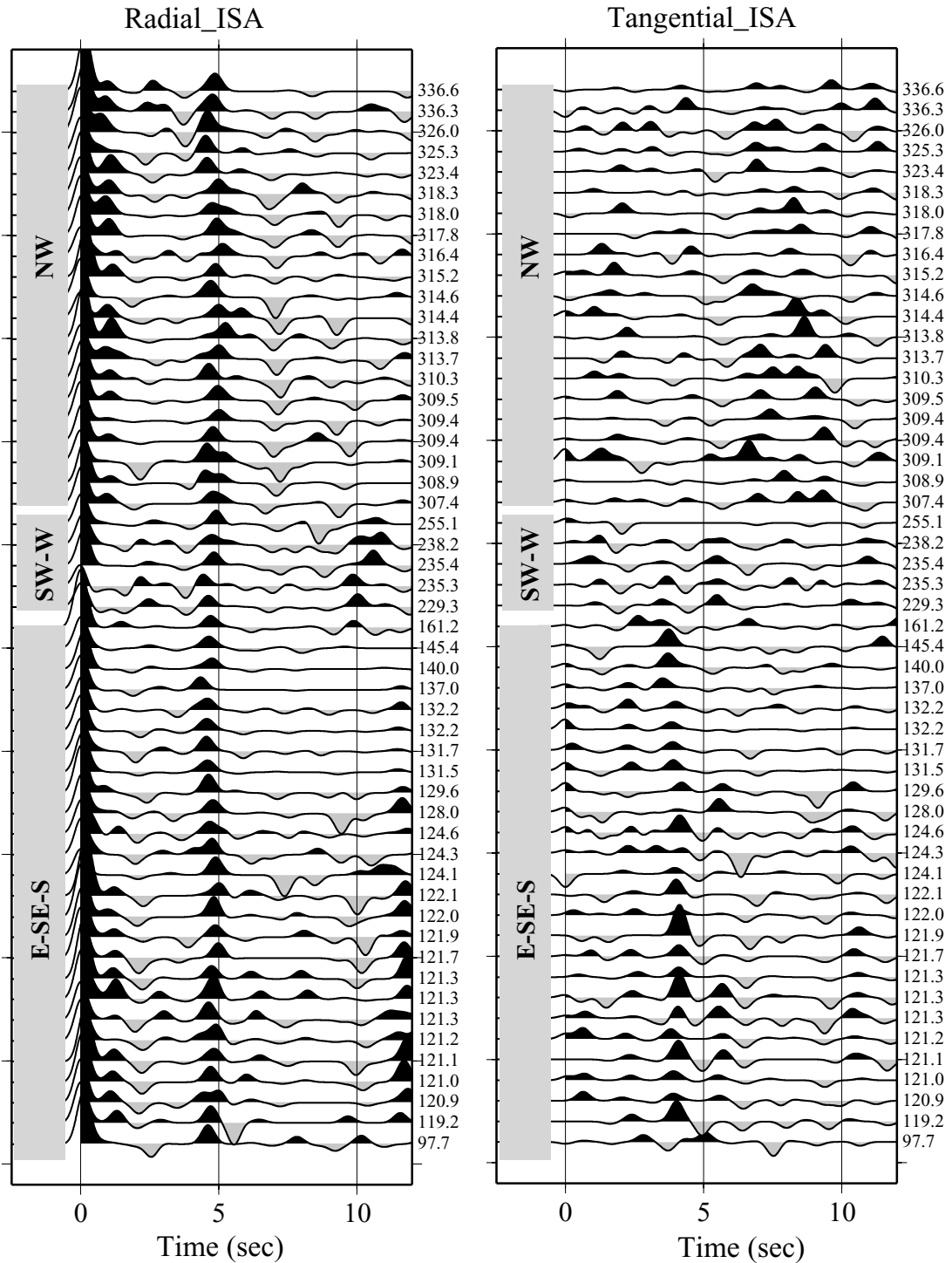


Figure D.7 Radial and tangential RFs for station ISA. Note the late Pms arrival times at ~ 4.5 - 4.7 sec on the radial components compared with the early Pms arrivals for station WBS, which is ~ 33 km to the SE (RFs are shown on Figure D.8). Amplitude of the tangential components is generally small indicating a relatively homogeneous structure beneath this station.

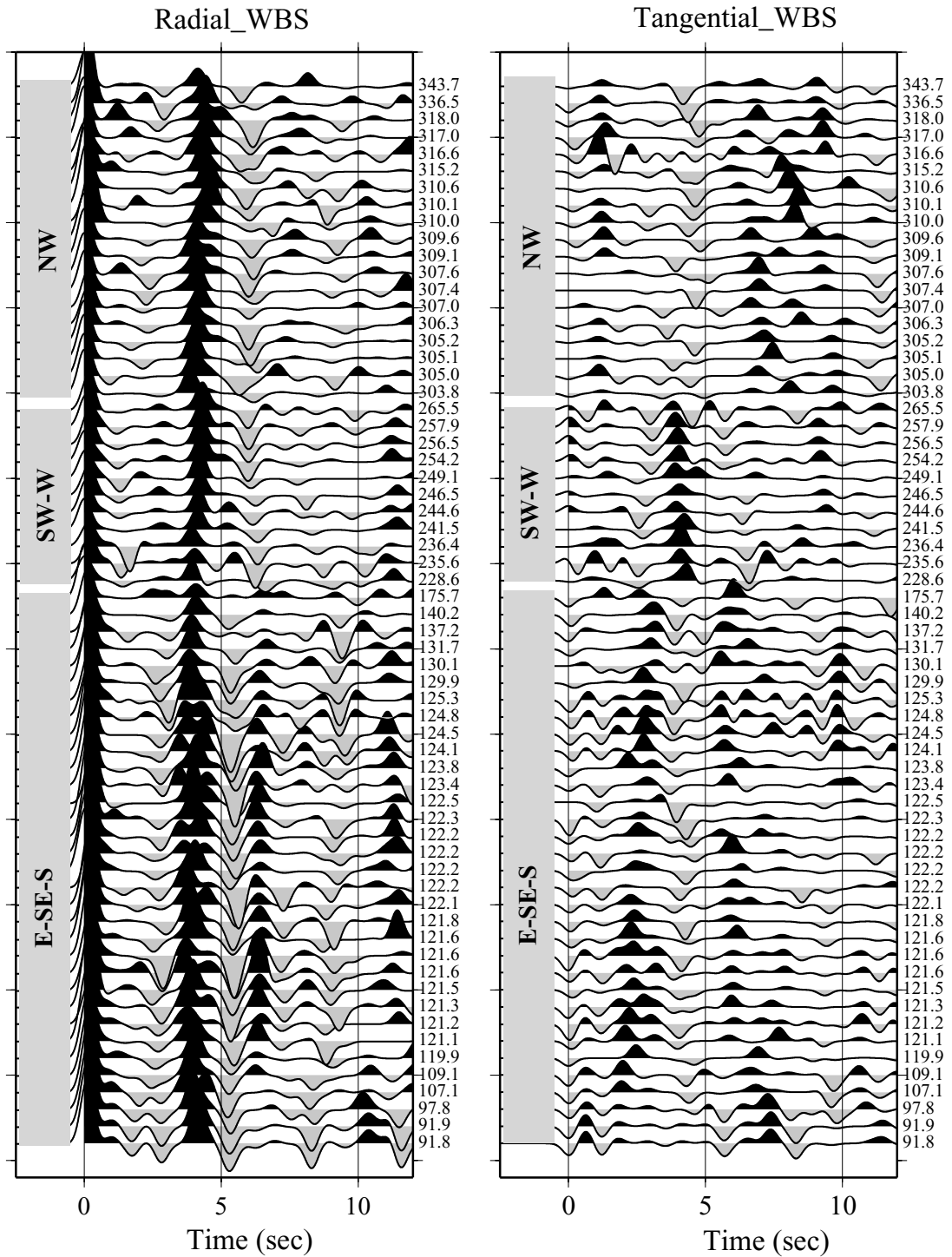


Figure D.8 Radial and tangential RFs for station WBS. Note the early Pms arrivals at ~ 4.0 - 4.2 sec on the radial components and complications in the RFs for events from SE close to the boundary between the relatively intact Sierra Nevada and the highly extended Walker Lane, indicating the existence of lateral heterogeneity to the SE of this station.

~ 5 sec from SW, early arrivals of ~ 4 sec from NW and intermediate arrivals of 4.5 sec for SE. Stacking of the SW and SE RF groups both result in a deep Moho of 39–40 km, but a large difference in the V_p/V_s ratio is inferred between these two groups. A large κ of 1.775 is inferred for the SW group, while a small κ of 1.68 is inferred for the SE group. The large difference in the V_p/V_s ratio for these two station groups poses some questions about the stacking results, but it can not be resolved from this study. A negative pulse at ~ 1.5 –2 sec is commonly observed at the radial component of this station (Figure D.8), amplitude variation of this phase on the radial and tangential components indicates that it is dipping to the SW.

Another example of relatively deeper Moho at a station in the highly extended Walker Lane belt is station CGO, which is in contrast to the shallower Moho at station CWC, which is on the eastern edge of the Sierra Nevada. RFs for station CGO generally have a later Pms arrival times than those of station CWC, indicating the existence of some decoupling between the upper crust and the lower crust in this area.

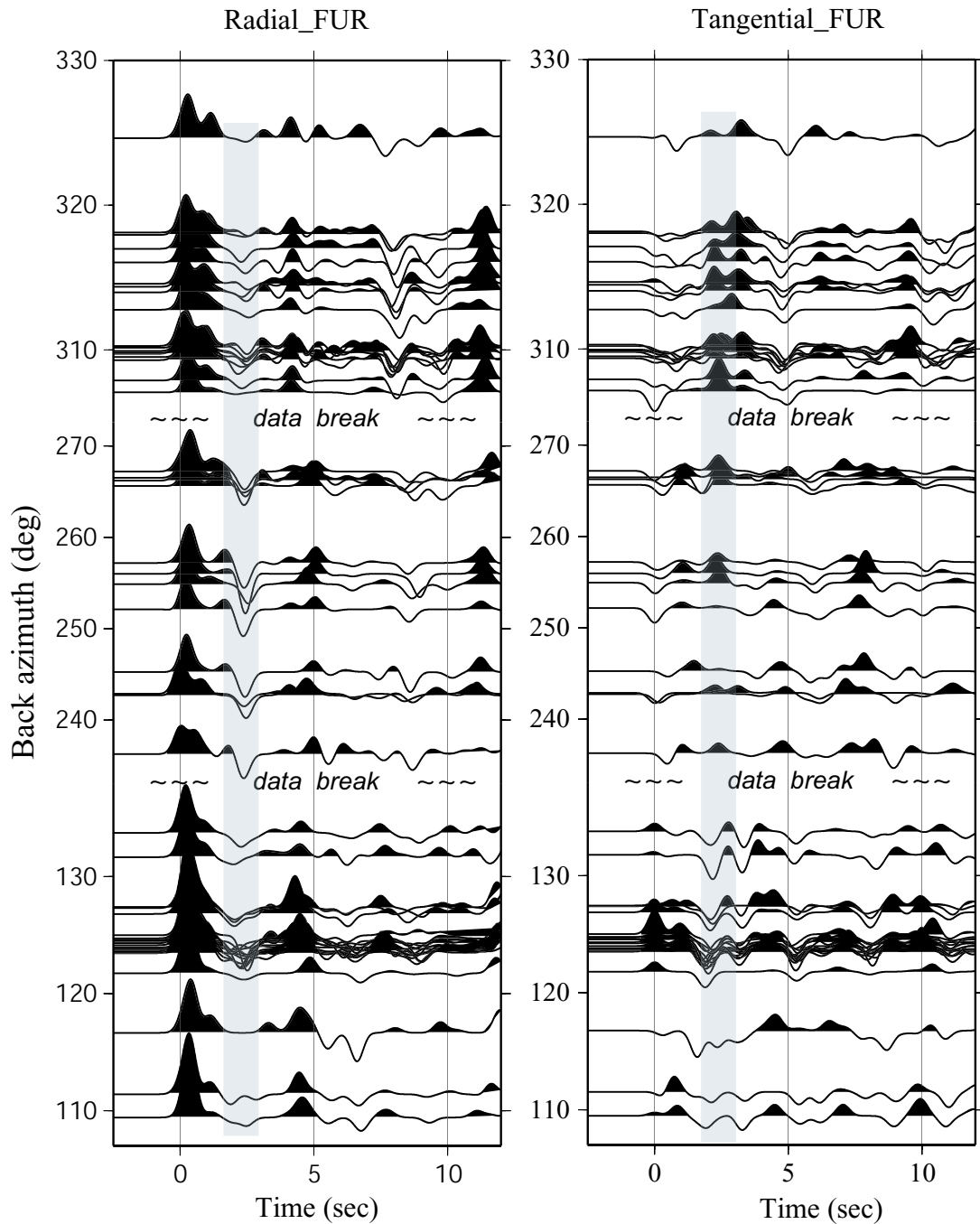


Figure D.9 Radial and tangential RFs for station FUR. Note the large difference in the Pms arrival times for events from NW, SE with those from SW-W. Also note the amplitude variations of the shaded negative phase on the radial component, with largest amplitude observed at SW direction. Polarity of this phase in the tangential component has a reversed polarity for events from NW and those from SE. Amplitude variation of this phase indicates that this velocity-decrease mid-crustal interface is dipping to the SW.

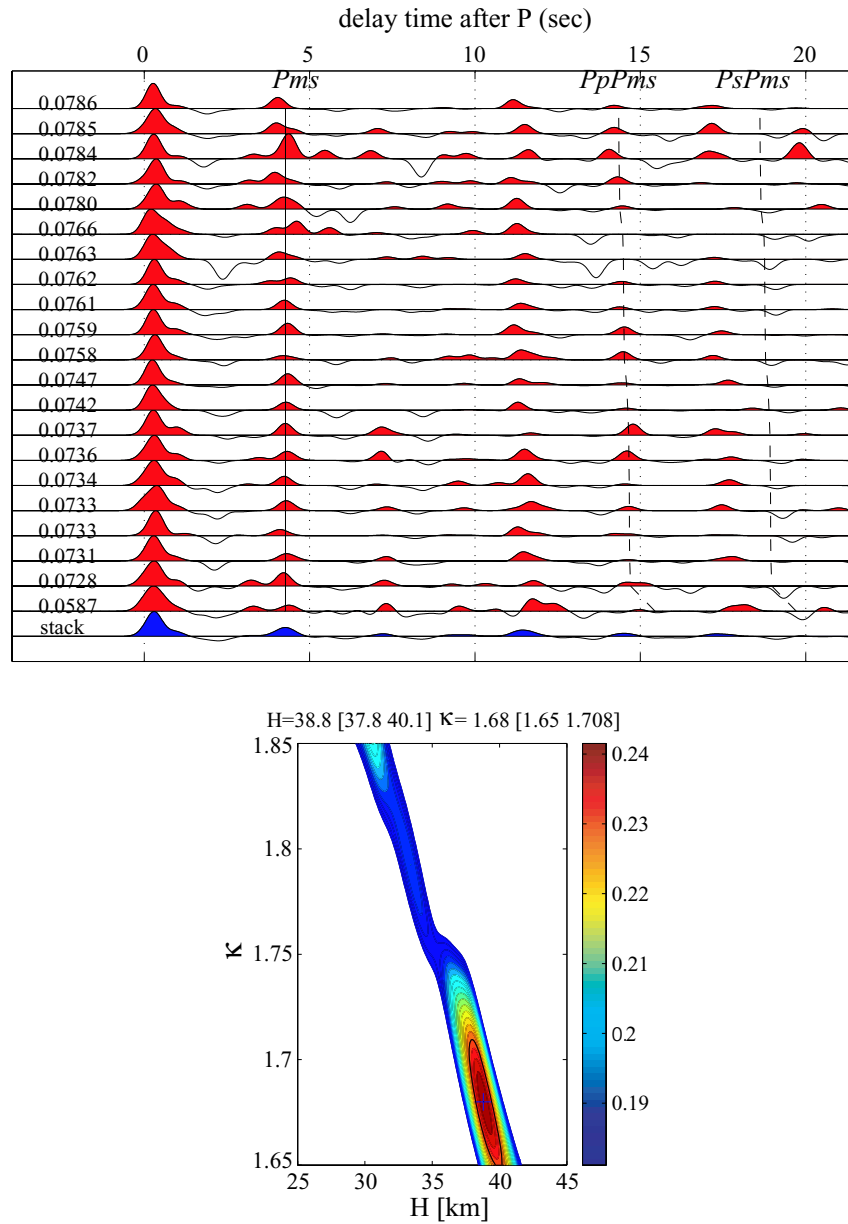


Figure D.10 Individual RF traces for the SE group of station FUR with the predicted arrival time of the three phases, *Pms*, *PpPms* and *PsPms* from the picked (H , κ) marked. Note the relatively prominent *PpPms* and *PsPms* multiples. The weighted summation function is shown on the bottom which picked a relative deep Moho of 38.8 km and a small V_p/V_s ratio of 1.68 for this group.

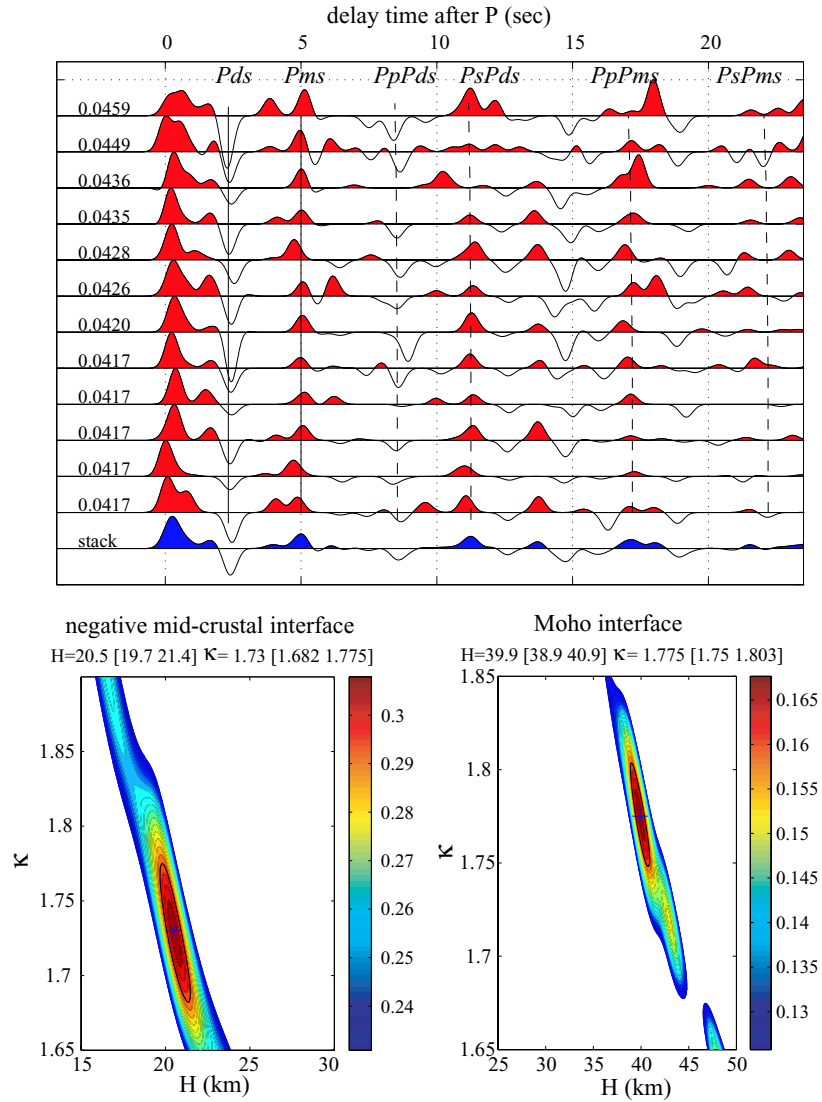


Figure D.11 Individual RF traces for the SW group of station FUR. Predicated arrival times of the three phases from both the Moho, Pms, PpPms and PsPms and the mid-crustal negative-gradient-velocity interface, Pds, PpPds, PsPds from the $[H, \kappa]$ domain grid search are marked. Note the multiples for the negative phase are very well developed. Contour map of the the weighted summation function for the negative-velocity-gradient interface is shown on the bottom left and that for the Moho shown on the bottom right. A deep Moho of 39.9 km and V_p/V_s ratio of 1.775 are inferred for this group. Note the PpPms multiple is not well developed and thus this group is not included in the regional Moho depth mapping of Figure 3.6.

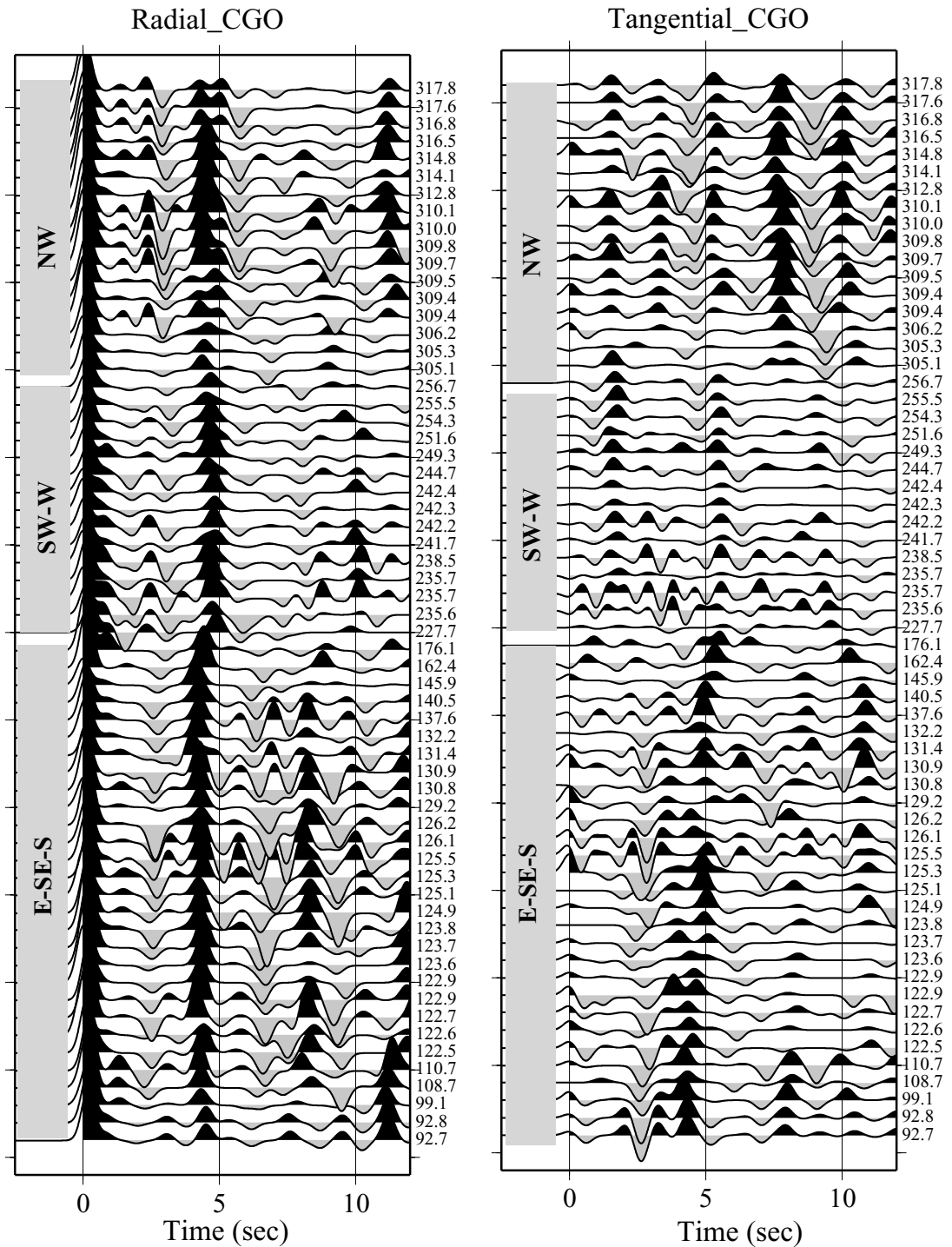


Figure D.12 Radial and tangential RFs for station CGO. Note the relatively late Pms arrivals at ~ 4.4 - 4.7 sec for events from SW-W, corresponding to a Moho depth of 34–36 km and the complicated RFs for events from NW on the radial components. Variations of the Radial RFs with back azimuth and the relatively large amplitude on the tangential components indicate the existence of lateral heterogeneity beneath this station, especially to the NW, approaching the boundary between the the relatively intact Sierra Nevada and the highly extended Walker Lane.

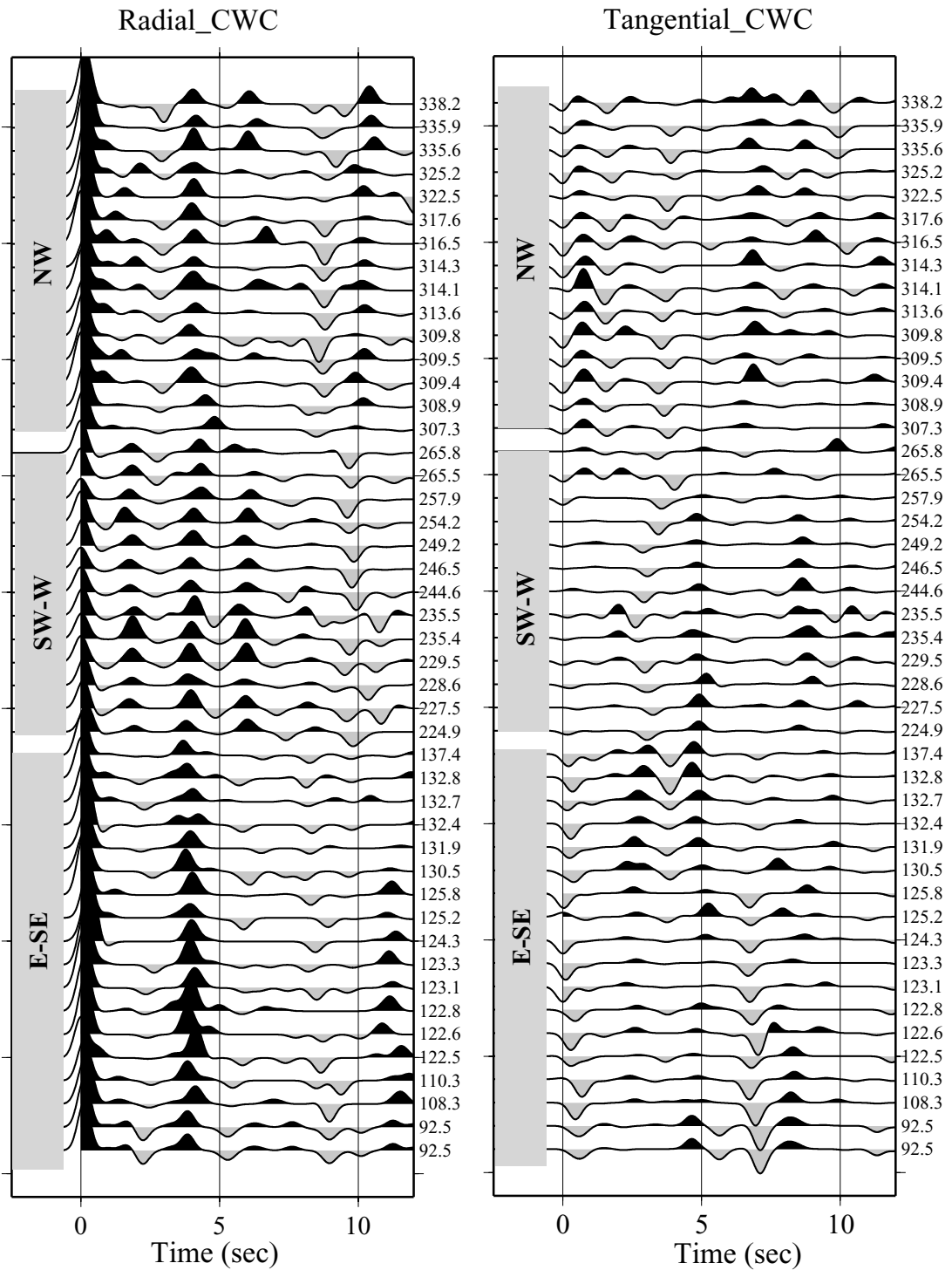


Figure D.13 Radial and tangential RFs for station CWC. Note the early Pms arrivals at ~ 3.9 - 4.1 sec on the radial components and the relatively small amplitudes on the tangential components.

Appendix E

Moho Depth and Vp/Vs Ratio for the Regional RF Study

In chapter 3, Moho depth for station groups with relatively well-developed multiples are shown in Figure 3.6. Since Vp/Vs ratio is very important in estimating the Moho depth using receiver function method. The estimated Vp/Vs ratio for the station groups in Figure 3.6 is shown below. Generally, station groups in the Coso geothermal area and the Peninsula Ranges have relatively larger Vp/Vs ratio (≥ 1.75), while those in the Mojave Desert show intermediate Vp/Vs ratio of around 1.75. No consistent pattern is observed for stations in the Sierra Nevada or the Coast Ranges. Station name, averaged back azimuth for the back azimuthal group, surface projection the Moho piercing points, the picked Moho depth H , Vp/Vs ratio κ , the uncertainty range for both parameters, total number of events for the group and elevation of the stations are shown in the following table.

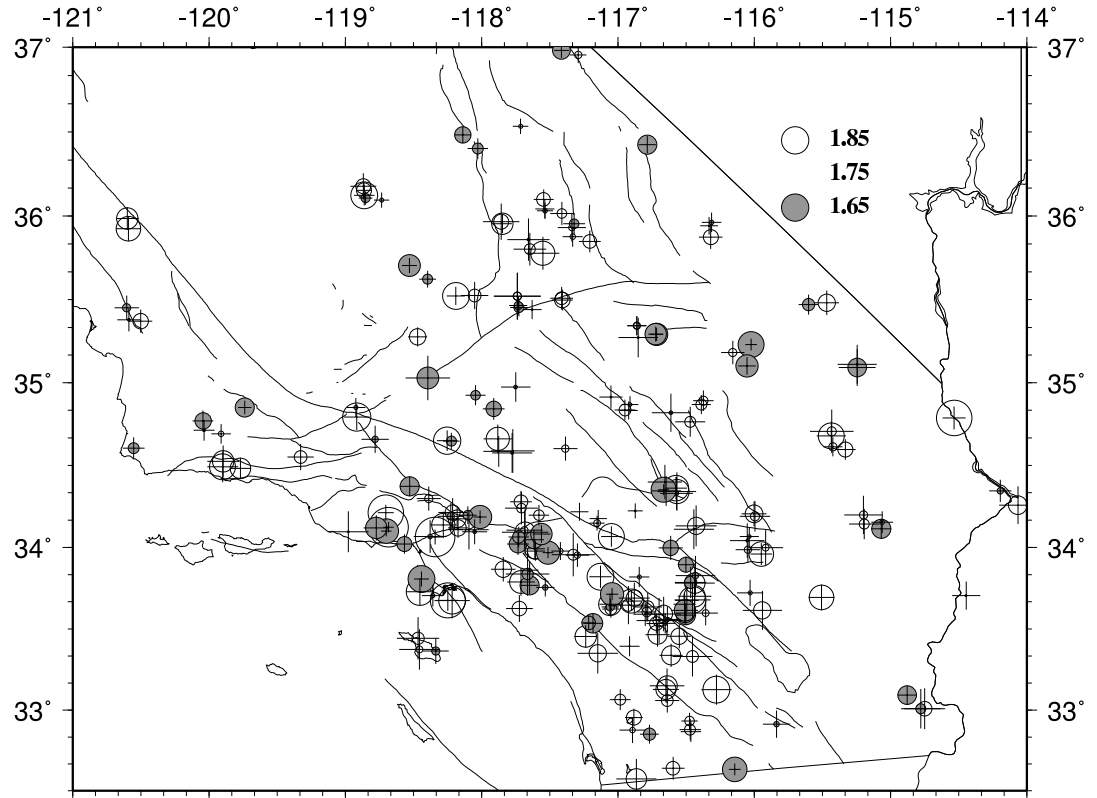


Figure E.1 Vp/Vs ratios for the station groups with relatively well-developed multiples that are shown in Figure 3.6. Size of the circle represents the value of the Vp/Vs ratio, which is directly proportional to its difference with 1.75 with Vp/Vs ratios smaller than 1.75 shaded.

Table E.1. Moho depth for the station groups from RF study

STA	BAZ	Lat	Long	H	H range	κ	κ range	# of RFs	Elev
AGA	137.2	33.597	-116.356	26.2	25.2-27.8	1.775	1.725-1.815	6	809
AGA	313.0	33.678	-116.453	26.0	24.2-28.1	1.848	1.780-1.912	36	809
AGA	334.1	33.701	-116.438	26.6	24.7-28.2	1.828	1.775-1.898	9	809
ALP	122.4	34.647	-118.222	34.2	33.3-35.0	1.713	1.682-1.743	35	753
ALP	134.6	34.650	-118.253	29.6	28.9-30.2	1.850	1.815-1.890	9	753
BAR	122.3	32.640	-116.596	38.2	37.1-39.2	1.800	1.765-1.848	31	496
BBR	134.6	34.223	-116.873	36.2	35.4-37.1	1.757	1.730-1.785	11	2069
BC3	312.2	33.694	-115.506	24.8	23.8-25.8	1.840	1.795-1.890	23	1050
BCC	122.3	33.535	-117.184	34.2	32.8-35.2	1.678	1.650-1.720	20	391
BCC	135.2	33.537	-117.215	34.1	33.5-34.8	1.700	1.672-1.725	9	391
BDM	122.6	37.916	-121.790	36.2	32.3-39.1	1.693	1.650-1.790	18	220
BEL	135.2	33.960	-115.949	26.5	25.8-27.5	1.840	1.800-1.880	9	1388
BEL	249.1	33.986	-116.046	28.4	27.1-29.6	1.777	1.735-1.825	9	1388
BEL	312.5	34.041	-116.051	28.6	26.7-31.3	1.760	1.693-1.820	37	1388
BEL	334.5	34.067	-116.036	29.2	28.1-30.3	1.763	1.727-1.797	6	1388
BEL	91.8	33.999	-115.917	27.9	25.6-29.2	1.775	1.735-1.863	9	1388
BFS	121.7	34.197	-117.580	31.7	30.8-32.7	1.788	1.750-1.825	16	1296
BFS	272.3	34.239	-117.709	32.1	29.2-33.3	1.785	1.745-1.865	6	1296
BFS	312.5	34.278	-117.712	32.4	31.2-33.5	1.800	1.763-1.843	33	1296
BKR	135.1	35.230	-116.023	28.1	27.3-28.7	1.655	1.650-1.693	14	275
BLA	313.6	34.111	-116.443	33.8	29.6-35.1	1.757	1.723-1.870	25	1214
BLA	333.9	34.132	-116.427	31.3	28.5-33.7	1.813	1.750-1.900	9	1214
BLY	124.8	33.705	-114.446	25.8	24.8-26.9	1.743	1.695-1.798	8	196
BOR	334.3	33.331	-116.453	23.3	21.9-25.8	1.793	1.708-1.855	9	227
BZN	233.2	33.465	-116.710	29.1	28.3-30.6	1.820	1.770-1.858	6	1301
BZN	313.4	33.533	-116.719	30.1	29.2-31.0	1.800	1.767-1.840	20	1301
BZN	336.4	33.552	-116.699	30.1	28.2-33.8	1.795	1.695-1.860	6	1301
CAP	135.2	33.350	-117.149	31.6	30.1-36.1	1.813	1.710-1.858	9	287
CAP	332.1	33.454	-117.237	29.2	28.0-30.1	1.828	1.787-1.870	9	287
CCC	232.5	35.498	-117.408	30.3	29.4-31.8	1.807	1.763-1.840	9	670
CCC	248.0	35.509	-117.413	30.6	29.8-32.3	1.797	1.750-1.833	9	670
CGO	102.8	36.534	-117.714	33.5	32.6-34.1	1.765	1.740-1.797	6	2804
CIA	120.4	33.364	-118.336	22.8	21.7-24.2	1.720	1.680-1.775	28	467
CIA	232.2	33.374	-118.457	18.5	16.9-19.6	1.775	1.717-1.865	7	467
CIA	312.2	33.442	-118.467	22.7	20.8-24.0	1.795	1.730-1.885	29	467
CLC	134.9	35.778	-117.551	26.0	25.0-27.3	1.838	1.777-1.898	10	775
CLC	250.5	35.802	-117.647	29.2	27.1-30.7	1.790	1.740-1.860	10	775
CLC	312.3	35.859	-117.656	28.2	26.1-31.2	1.760	1.680-1.835	37	775
CMB	310.8	38.079	-120.452	31.0	27.4-32.1	1.662	1.650-1.757	16	697
CPP	121.7	34.021	-117.733	30.2	28.8-32.0	1.685	1.650-1.730	12	205
CPP	86.4	34.064	-117.729	29.2	28.1-30.6	1.705	1.668-1.743	6	205
CRP	122.5	34.096	-118.051	31.3	29.9-32.7	1.737	1.693-1.785	13	233

Table E.1—Continued

STA	BAZ	Lat	Long	H	H range	κ	κ range	# of RFs	Elev
CRP	246.8	34.119	-118.174	27.5	26.8-28.2	1.810	1.775-1.848	6	233
CRP	311.5	34.175	-118.180	27.9	27.0-28.7	1.815	1.780-1.858	16	233
CRY	312.3	33.604	-116.789	32.0	31.2-32.7	1.785	1.753-1.823	37	1128
CRY	332.4	33.635	-116.781	32.1	29.5-33.0	1.795	1.765-1.870	6	1128
CTC	134.8	33.615	-115.941	20.6	19.7-22.2	1.813	1.730-1.873	7	503
CTC	333.2	33.721	-116.030	23.6	22.8-24.6	1.765	1.717-1.813	7	503
CVS	122.0	38.308	-122.384	23.4	22.4-24.4	1.730	1.682-1.783	21	295
CWC	133.0	36.401	-118.028	32.4	31.3-33.8	1.710	1.672-1.747	6	1553
CWC	312.0	36.483	-118.139	35.2	34.4-36.1	1.690	1.660-1.720	19	1553
DAN	135.2	34.596	-115.331	32.0	30.8-33.0	1.805	1.770-1.845	13	368
DAN	232.7	34.612	-115.423	27.1	26.5-27.7	1.780	1.745-1.815	9	368
DAN	312.5	34.678	-115.435	21.7	20.7-22.6	1.845	1.793-1.900	38	368
DAN	328.9	34.706	-115.431	22.6	21.6-23.6	1.783	1.705-1.865	6	368
DEC	313.6	34.298	-118.389	26.1	25.1-27.4	1.780	1.735-1.823	21	490
DEV	123.4	33.894	-116.501	39.3	38.3-40.4	1.695	1.665-1.725	21	302
DEV	334.4	33.997	-116.613	36.1	33.5-37.2	1.693	1.665-1.753	7	302
DGR	232.6	33.623	-117.052	32.8	32.0-33.6	1.793	1.765-1.828	10	650
DGR	249.9	33.635	-117.057	32.9	32.1-33.6	1.780	1.750-1.813	11	650
DGR	272.6	33.652	-117.059	31.6	30.8-32.4	1.833	1.795-1.873	6	650
DGR	335.3	33.713	-117.044	39.4	38.1-40.6	1.665	1.650-1.695	8	650
DGR	93.6	33.646	-116.924	31.9	30.9-35.8	1.795	1.698-1.838	9	650
DJJ	121.7	34.067	-118.379	27.8	26.2-29.2	1.733	1.675-1.795	30	215
DPP	332.0	33.064	-116.983	37.9	36.6-39.4	1.790	1.753-1.830	7	440
DSC	135.2	35.102	-116.054	26.0	25.1-26.7	1.668	1.650-1.715	7	283
DSC	311.6	35.182	-116.158	25.6	25.0-26.7	1.780	1.737-1.823	26	283
DVT	232.7	32.632	-116.143	34.3	33.0-35.2	1.660	1.650-1.693	6	881
EDW	122.1	34.842	-117.911	31.9	30.9-33.2	1.693	1.650-1.730	11	762
EDW	313.1	34.924	-118.045	30.4	29.3-31.5	1.715	1.680-1.753	22	762
EML	122.0	32.851	-116.769	37.7	36.9-38.6	1.705	1.668-1.737	28	152
EML	250.1	32.877	-116.894	32.1	30.3-33.0	1.770	1.735-1.830	7	152
EML	332.8	32.953	-116.884	34.9	34.1-35.8	1.805	1.773-1.838	9	152
FIG	120.6	34.691	-119.912	33.9	32.6-35.0	1.770	1.735-1.807	18	945
FIG	250.0	34.713	-120.037	29.4	28.3-30.5	1.760	1.723-1.800	10	945
FIG	311.9	34.769	-120.044	31.9	30.8-33.0	1.690	1.650-1.727	26	945
FMP	121.5	33.674	-118.217	21.0	19.8-22.7	1.848	1.770-1.900	35	52
FMP	134.4	33.676	-118.248	20.2	19.7-20.9	1.878	1.823-1.900	9	52
FRD	133.7	33.455	-116.551	26.4	25.7-27.1	1.810	1.767-1.855	9	1164
FRD	312.6	33.535	-116.654	30.9	29.8-32.1	1.735	1.698-1.773	38	1164
FRD	335.4	33.558	-116.637	30.0	28.5-31.3	1.760	1.717-1.813	8	1164
FUR	124.6	36.424	-116.785	38.8	37.8-40.1	1.680	1.650-1.708	21	-37
GLA	123.9	33.008	-114.750	25.3	24.1-28.2	1.803	1.708-1.858	26	610
GLA	136.3	33.009	-114.779	24.8	22.7-27.9	1.713	1.650-1.795	9	610

Table E.1—Continued

STA	BAZ	Lat	Long	H	H range	κ	κ range	# of RFs	Elev
GLA	313.7	33.092	-114.878	27.5	26.7-28.4	1.682	1.650-1.720	35	610
GRA	125.1	36.955	-117.292	37.2	36.4-38.0	1.777	1.747-1.807	10	622
GRA	248.9	36.981	-117.415	41.8	40.7-43.1	1.685	1.658-1.713	8	622
GSC	232.1	35.273	-116.851	27.3	25.0-28.5	1.743	1.695-1.840	9	1000
GSC	312.4	35.343	-116.861	29.3	28.2-30.4	1.777	1.743-1.815	36	1000
GSC	312.4	35.344	-116.862	29.4	28.5-30.4	1.773	1.737-1.805	36	1000
GSC	98.0	35.292	-116.717	30.1	29.5-30.7	1.668	1.650-1.698	6	1000
GSC	98.0	35.293	-116.724	30.0	29.3-30.6	1.672	1.650-1.705	6	1000
HEC	312.3	34.869	-116.389	28.6	27.8-29.4	1.790	1.755-1.825	39	920
HEC	333.4	34.892	-116.374	28.4	27.5-29.3	1.783	1.745-1.820	9	920
HLL	121.3	34.137	-118.282	26.6	25.6-27.8	1.835	1.785-1.882	24	193
HOPS	232.1	38.965	-123.118	31.6	30.7-32.7	1.717	1.680-1.755	6	299
HOPS	241.0	38.971	-123.122	31.9	31.0-32.9	1.695	1.658-1.735	10	299
IRM	124.2	34.114	-115.068	29.2	28.0-30.8	1.680	1.650-1.723	15	532
IRM	249.8	34.142	-115.193	26.9	25.0-27.5	1.787	1.753-1.865	6	532
IRM	312.5	34.198	-115.199	27.7	25.0-29.4	1.780	1.727-1.868	21	532
IRM	93.4	34.153	-115.062	28.6	27.9-29.4	1.733	1.693-1.773	6	532
ISA	122.8	35.623	-118.397	39.3	38.0-40.3	1.713	1.685-1.747	26	873
ISA	312.4	35.704	-118.530	43.6	42.3-44.7	1.670	1.650-1.705	20	873
JCC	121.9	40.782	-123.953	23.9	20.1-25.3	1.843	1.785-1.950	17	27
JCC	233.0	40.791	-124.077	28.7	26.2-29.8	1.693	1.652-1.767	8	27
JCC	302.5	40.848	-124.091	26.4	25.3-27.7	1.725	1.680-1.767	10	27
JCS	232.9	33.059	-116.639	34.5	33.1-36.4	1.793	1.745-1.833	10	1228
JCS	313.2	33.128	-116.649	30.3	28.8-31.5	1.823	1.783-1.878	31	1228
JCS	330.4	33.150	-116.639	29.1	27.1-31.0	1.823	1.765-1.892	7	1228
JRC	230.1	35.955	-117.848	29.9	29.1-30.8	1.828	1.793-1.862	6	1452
JRC	248.3	35.966	-117.857	31.7	27.8-33.0	1.805	1.767-1.900	10	1452
JVA	123.5	34.341	-116.567	27.9	26.9-30.9	1.838	1.747-1.888	30	873
JVA	135.2	34.330	-116.570	31.2	29.5-32.4	1.735	1.685-1.805	10	873
JVA	232.2	34.344	-116.647	29.5	28.2-32.1	1.773	1.705-1.815	9	873
JVA	251.3	34.352	-116.665	32.5	31.5-33.2	1.658	1.650-1.690	8	873
JVA	313.4	34.399	-116.655	30.2	27.2-31.3	1.755	1.717-1.843	24	873
JVA	99.5	34.361	-116.575	28.4	27.5-29.3	1.843	1.803-1.885	7	873
LDF	232.8	35.092	-115.245	30.0	26.3-31.5	1.682	1.650-1.785	9	1209
LDF	250.1	35.111	-115.245	27.9	25.8-30.6	1.743	1.670-1.813	12	1209
LDR	311.3	35.029	-118.395	31.9	26.4-33.2	1.670	1.650-1.813	32	1089
LFP	333.7	34.372	-118.528	24.6	23.6-25.6	1.680	1.650-1.723	7	135
LGU	99.7	34.096	-118.979	24.9	23.7-30.4	1.743	1.650-1.800	6	351
LJR	248.8	34.793	-118.916	34.6	33.8-37.4	1.853	1.785-1.880	9	1443
LJR	312.5	34.850	-118.924	34.7	33.6-35.9	1.765	1.730-1.800	20	1443
LKL	121.9	34.588	-117.771	31.4	27.6-33.3	1.753	1.703-1.863	14	810
LKL	136.0	34.575	-117.777	29.9	28.7-34.0	1.760	1.660-1.807	7	810

Table E.1—Continued

STA	BAZ	Lat	Long	H	H range	κ	κ range	# of RFs	Elev
LKL	232.9	34.585	-117.876	30.4	29.3-33.4	1.747	1.672-1.785	7	810
LKL	313.0	34.660	-117.882	29.2	27.6-30.4	1.835	1.790-1.895	12	810
LMR2	311.5	34.974	-117.751	29.0	27.4-31.0	1.737	1.685-1.793	13	964
LRL	132.5	35.441	-117.630	30.9	29.9-31.9	1.757	1.725-1.795	8	1341
LRL	232.7	35.453	-117.726	31.3	30.3-32.2	1.713	1.680-1.745	9	1341
LRL	248.9	35.465	-117.731	30.9	29.9-32.0	1.723	1.690-1.755	13	1341
LRL	248.9	35.465	-117.731	31.0	29.9-32.0	1.720	1.690-1.755	13	1341
LRL	311.8	35.521	-117.738	29.9	26.7-32.8	1.780	1.705-1.878	39	1341
LRL	311.8	35.521	-117.738	29.9	26.8-32.8	1.780	1.708-1.878	39	1341
LVA2	250.7	33.338	-116.610	29.1	28.0-30.6	1.820	1.775-1.860	9	1435
MCT	124.2	34.205	-116.002	25.5	25.0-26.9	1.815	1.763-1.855	28	623
MCT	134.2	34.190	-115.995	26.2	25.0-28.1	1.783	1.723-1.835	10	623
MHC	122.8	37.306	-121.572	19.0	18.1-19.9	1.840	1.787-1.908	13	1250
MHC	303.3	37.369	-121.695	24.4	23.7-25.1	1.767	1.713-1.820	6	1250
MHC	310.1	37.384	-121.706	23.1	21.6-24.2	1.783	1.733-1.845	16	1250
MHC	310.3	37.385	-121.707	23.1	21.7-24.1	1.780	1.733-1.843	18	1250
MLS	132.7	33.968	-117.513	33.2	32.5-33.8	1.665	1.650-1.690	7	199
MLS	232.6	33.978	-117.605	31.5	30.8-32.1	1.810	1.777-1.848	7	199
MLS	250.9	33.991	-117.611	31.6	30.6-32.6	1.823	1.787-1.860	6	199
MLS	313.0	34.047	-117.617	27.6	26.8-29.3	1.685	1.650-1.723	25	199
MONP	232.2	32.866	-116.465	31.2	30.4-31.9	1.750	1.715-1.790	9	1920
MONP	250.9	32.879	-116.471	30.6	29.4-31.4	1.790	1.755-1.833	11	1920
MONP	313.0	32.933	-116.475	30.0	28.9-30.0	1.785	1.765-1.825	29	1920
MPM	124.2	36.015	-117.411	29.5	28.4-30.7	1.785	1.743-1.828	29	1823
MPM	234.4	36.032	-117.535	31.2	30.5-32.1	1.733	1.705-1.763	7	1823
MPM	247.7	36.042	-117.537	30.9	30.0-32.4	1.753	1.715-1.785	9	1823
MPM	311.7	36.099	-117.546	31.6	30.5-32.7	1.800	1.765-1.838	34	1823
MPP	121.0	34.851	-119.738	34.9	33.9-35.6	1.680	1.655-1.705	25	1711
MTP	250.6	35.470	-115.602	26.7	25.7-27.7	1.705	1.670-1.743	7	1552
MTP	91.3	35.482	-115.468	25.7	24.8-27.1	1.813	1.763-1.853	7	1552
MWC	135.2	34.186	-118.012	35.5	34.7-36.2	1.665	1.650-1.698	9	1696
MWC	231.9	34.196	-118.101	35.6	34.7-36.5	1.715	1.685-1.750	10	1696
NBS	102.4	34.764	-116.470	29.6	27.8-31.4	1.790	1.740-1.850	6	590
NBS	312.1	34.819	-116.611	28.1	26.4-32.6	1.737	1.650-1.790	24	590
NEE	125.4	34.787	-114.534	25.9	25.1-27.1	1.880	1.828-1.912	24	139
OLP	121.9	32.574	-116.865	29.3	27.7-32.2	1.825	1.743-1.890	21	130
ORV	102.7	39.538	-121.410	37.0	35.6-38.3	1.717	1.685-1.753	6	334
ORV	123.8	39.515	-121.425	35.7	34.4-37.1	1.690	1.658-1.725	19	334
PAS	121.6	34.108	-118.093	27.6	25.0-29.0	1.755	1.708-1.853	31	257
PAS	312.2	34.189	-118.226	28.5	27.2-30.5	1.723	1.668-1.765	36	257
PAS	332.2	34.213	-118.213	25.6	25.0-27.4	1.805	1.743-1.848	7	257
PDM	126.0	34.257	-114.066	25.8	25.0-28.9	1.818	1.727-1.865	19	115

Table E.1—Continued

STA	BAZ	Lat	Long	H	H range	κ	κ range	# of RFs	Elev
PDM	313.5	34.345	-114.195	28.0	26.8-29.1	1.727	1.688-1.770	21	115
PDU	122.4	34.081	-117.561	33.4	32.5-34.2	1.672	1.650-1.715	34	446
PDU	231.8	34.093	-117.681	32.5	31.2-37.9	1.825	1.698-1.868	9	446
PDU	248.1	34.105	-117.686	34.5	31.0-36.1	1.777	1.737-1.870	11	446
PER	122.6	33.821	-117.128	32.7	31.3-33.9	1.848	1.813-1.895	16	468
PFO	232.9	33.585	-116.502	29.8	29.0-30.5	1.680	1.650-1.725	10	1259
PFO	250.9	33.598	-116.507	29.5	28.2-30.6	1.680	1.650-1.720	10	1259
PFO	272.9	33.614	-116.509	28.9	26.5-31.0	1.672	1.650-1.747	6	1259
PFO	312.8	33.652	-116.511	29.4	28.2-30.6	1.747	1.708-1.790	36	1259
PFO	335.4	33.675	-116.494	29.5	27.8-30.6	1.755	1.720-1.807	8	1259
PHL	134.9	35.371	-120.501	24.1	23.3-25.1	1.807	1.763-1.848	6	355
PHL	230.1	35.379	-120.589	25.9	24.8-26.9	1.740	1.700-1.785	6	355
PHL	312.2	35.451	-120.605	24.7	23.6-25.8	1.720	1.678-1.767	27	355
PKD	243.7	35.925	-120.592	28.0	26.5-29.1	1.840	1.800-1.892	7	583
PKD	311.4	35.986	-120.600	28.5	27.5-29.6	1.828	1.787-1.870	15	583
PLC	123.4	33.782	-116.436	21.0	19.1-22.5	1.825	1.753-1.900	22	96
PLC	136.2	33.785	-116.467	26.1	25.3-26.8	1.705	1.655-1.770	8	96
PLC	86.5	33.828	-116.431	25.9	25.0-27.3	1.727	1.658-1.803	6	96
PLM	312.7	33.394	-116.915	37.2	35.6-38.6	1.753	1.720-1.793	40	1691
PLS	122.1	33.755	-117.533	28.5	27.5-29.4	1.730	1.698-1.765	26	1181
PLS	230.4	33.767	-117.649	33.0	31.6-34.1	1.680	1.652-1.715	7	1181
PLS	312.9	33.837	-117.663	29.8	26.3-32.8	1.708	1.650-1.810	36	1181
PLS	333.7	33.861	-117.648	29.0	28.1-29.9	1.737	1.705-1.770	7	1181
RDM	134.0	33.590	-116.799	33.1	31.2-34.2	1.745	1.713-1.800	8	1365
RDM	312.9	33.671	-116.901	31.1	30.2-32.2	1.838	1.803-1.875	35	1365
RDM	335.9	33.690	-116.880	32.2	30.9-35.1	1.810	1.737-1.850	6	1365
RPV	134.8	33.705	-118.358	23.4	22.7-24.2	1.735	1.695-1.775	8	107
RPV	250.3	33.728	-118.453	25.8	24.4-26.8	1.850	1.800-1.900	13	107
RPV	334.6	33.807	-118.441	26.0	24.4-26.6	1.652	1.650-1.705	9	107
RRX	123.5	34.833	-116.921	31.9	31.1-32.7	1.745	1.710-1.777	31	650
RRX	134.8	34.836	-116.949	30.6	29.8-31.4	1.793	1.757-1.833	11	650
RRX	311.9	34.914	-117.051	32.8	31.4-34.0	1.757	1.720-1.805	35	650
RRX	94.8	34.869	-116.911	32.1	31.3-32.8	1.763	1.733-1.795	9	650
RVR	122.3	33.953	-117.298	33.0	31.9-34.2	1.773	1.727-1.813	30	232
RVR	135.2	33.955	-117.329	32.7	29.8-35.9	1.790	1.715-1.873	9	232
RVR	249.0	33.978	-117.423	31.2	30.3-32.2	1.770	1.737-1.803	11	232
SAO	232.4	36.735	-121.493	27.7	26.5-28.9	1.725	1.672-1.773	6	317
SAO	311.4	36.808	-121.509	34.9	33.9-36.1	1.698	1.662-1.730	18	317
SBC	311.8	34.482	-119.770	30.5	29.5-31.5	1.825	1.787-1.865	31	61
SBPX	248.9	34.217	-117.283	39.2	38.2-40.2	1.750	1.717-1.783	11	1845
SDP	311.8	34.604	-120.553	26.4	25.5-27.3	1.710	1.670-1.750	12	601
SHO	233.6	35.874	-116.319	28.0	27.1-28.9	1.805	1.763-1.850	9	451

Table E.1—Continued

STA	BAZ	Lat	Long	H	H range	κ	κ range	# of RFs	Elev
SHO	312.1	35.942	-116.332	30.0	29.4-30.7	1.755	1.720-1.785	36	451
SHO	334.1	35.963	-116.313	30.2	29.1-31.3	1.733	1.698-1.770	8	451
SLA	123.7	35.849	-117.206	29.2	28.1-30.1	1.800	1.765-1.845	30	1160
SLA	250.2	35.877	-117.332	29.5	28.5-30.4	1.770	1.733-1.807	10	1160
SLA	311.9	35.932	-117.339	28.8	27.4-30.5	1.773	1.720-1.823	41	1160
SLA	334.3	35.954	-117.321	30.3	29.0-31.5	1.715	1.675-1.755	8	1160
SLR	248.8	33.819	-116.844	34.6	33.4-35.6	1.765	1.733-1.807	7	1538
SND	312.8	33.592	-116.665	30.2	28.3-32.5	1.815	1.753-1.880	37	1358
SPF	121.1	34.020	-118.567	33.0	31.6-34.0	1.695	1.665-1.737	13	470
SPF	312.3	34.100	-118.700	28.5	27.7-29.1	1.660	1.650-1.688	33	470
SPF	334.5	34.123	-118.683	30.2	29.8-30.9	1.895	1.862-1.900	9	470
SPG	123.4	36.095	-118.734	39.6	38.7-40.6	1.765	1.737-1.793	22	279
SPG	230.2	36.108	-118.852	38.7	38.0-39.8	1.717	1.693-1.743	7	279
SPG	252.3	36.123	-118.862	36.7	35.9-37.4	1.848	1.815-1.890	9	279
SPG	291.4	36.153	-118.864	39.5	38.3-40.3	1.805	1.780-1.838	6	279
SPG	311.2	36.177	-118.868	39.6	36.9-40.9	1.805	1.775-1.870	31	279
SRN	121.6	33.788	-117.712	26.8	25.8-27.9	1.833	1.783-1.885	31	208
SRN	311.5	33.866	-117.841	29.2	28.1-30.6	1.810	1.763-1.853	31	208
STG	135.8	33.625	-117.724	29.1	28.2-30.0	1.803	1.755-1.853	7	22
SVD	133.1	34.067	-117.048	32.5	31.7-33.3	1.845	1.807-1.882	8	574
SVD	312.4	34.148	-117.153	38.0	37.0-38.8	1.775	1.750-1.805	25	574
SVD	331.1	34.176	-117.145	38.3	36.7-39.5	1.747	1.720-1.783	7	574
SWS	231.5	32.913	-115.837	25.8	24.7-27.3	1.730	1.680-1.780	6	108
SYP	120.5	34.491	-119.901	28.9	27.0-30.1	1.845	1.787-1.900	31	1223
SYP	93.7	34.524	-119.897	31.2	28.7-32.6	1.828	1.783-1.900	7	1223
TEH	249.8	35.276	-118.470	31.9	30.9-33.1	1.810	1.773-1.843	12	824
TOV	134.1	34.119	-118.774	28.0	27.0-28.7	1.672	1.650-1.743	9	302
USC	313.9	34.063	-118.341	30.3	29.8-31.3	1.895	1.845-1.900	17	17
VTV	311.9	34.602	-117.386	30.1	28.8-31.5	1.777	1.735-1.823	27	843
WBS	249.0	35.522	-118.189	30.8	29.9-31.8	1.848	1.815-1.882	8	1898
WBS	99.2	35.525	-118.051	30.6	29.7-32.2	1.797	1.743-1.843	7	1898
WDC	302.7	40.608	-122.598	23.1	22.5-23.8	1.828	1.777-1.875	8	268
WDC	309.1	40.624	-122.613	23.6	22.7-24.8	1.813	1.760-1.865	15	268
WGR	312.0	34.551	-119.328	25.4	24.7-26.2	1.797	1.745-1.842	29	575
WSS	312.2	34.212	-118.703	27.8	27.2-28.6	1.880	1.842-1.900	28	284
YAQ	122.8	33.126	-116.278	22.0	21.0-23.0	1.848	1.797-1.908	23	430
YBH	303.8	41.767	-122.779	37.8	37.0-38.6	1.725	1.698-1.755	6	1059
YBH	308.6	41.775	-122.783	38.2	37.1-39.1	1.723	1.695-1.753	6	1059

Bibliography

- Abers, G. A., A. Ferris, M. Craig, H. Davies, A. L. Lerner-Lam, J. C. Mutter, and B. Taylor, Mantle compensation of active metamorphic core complexes at Woodlark rift in Papua New Guinea, *Nature*, **418** (6900), 862–865, 2002.
- Allmendinger, R. W., J. W. Sharp, D. Vontish, L. Serpa, L. Brown, S. Kaufman, J. Oliver, and R. B. Smith, Cenozoic and Mesozoic Structure of the Eastern Basin and Range Province, Utah, from Cocorp Seismic-Reflection Data, *Geology*, **11** (9), 532–526, 1983.
- Allmendinger, R. W., T. A. Hauge, E. C. Hauser, C. J. Potter, S. L. Klemperer, K. D. Nelson, P. Knuepfer, and J. Oliver, Overview of the Cocorp 40-Degrees-N Transect, Western United-States—the Fabric of an Orogenic Belt, *Geol. Soc. Am. Bull.*, **98** (3), 308–319, 1987.
- Ammon, C. J., G. E. Randall, and G. Zandt, On the Nonuniqueness of Receiver Function Inversions, *J. Geophys. Res. and Planets*, **95** (B10), 15,303–15,318, 1990.
- Ammon, C. J., and G. Zandt, Receiver Structure beneath the Southern Mojave Block, California, *Bull. Seismo. Soc. Am.*, **83** (3), 737–755, 1993.
- Atwater, T. and J. Severinghaus, Tectonic maps of the northeast Pacific, in *The Geology of North America: the Eastern Pacific ocean and Hawaii*, ed. E. L. Winterer, D. M. Hussong and R. W. Decker, The Geological Society of America, Boulder, Colorado, USA, pp. 15–20, 1989.
- Atwater, T., Plate tectonic history of the northeast Pacific and western North America, in *The Geology of North America: the Eastern Pacific ocean and Hawaii*, ed. E. L. Winterer, D. M. Hussong and R. W. Decker, The Geological Society of America, Boulder, Colorado, USA, pp. 21–72, 1989.
- Atwater, T. and J. Stock, Pacific-North America Plate Tectonics of the Neogene Southwestern United States: An update, *Inter. Geol. Rev.*, **40** (5), 375–402, 1998.

- Bird, P. and R. W. Rosenstock, Kinematics of present crust and mantle flow in southern California, *Geol. Soc. Am. Bull.*, **95**, 946–957, 1984.
- Blythe, A. E., D. W. Burbank, K. A. Farley, and E. J. Fielding, Structural and topographic evolution of the central Transverse Ranges, California, from apatite fission-track, (U-Th)/He and digital elevation model analyses, *Basin Research*, **12** (2), 97–114, 2000.
- Burchfiel B. C., D. S. Cowan, and G. A. Davis, Tectonic overview of the Cordilleran orogen in the western United States, in *The Cordilleran Orogen: Conterminous U.S.*, ed. Burchfiel B. C., P. W. Lipman, and M. L. Zoback, Boulder, Colorado, Geological Society of America, pp. 407–427, 1992.
- Cheadle, M. J., B. L. Czuchra, T. Byrne, C. J. Ando, J. E. Oliver, L. D. Brown, S. Kaufman, P. E. Malin, and R. A. Phinney, The Deep Crustal Structure of the Mojave Desert, California, from Cocorp Seismic-Reflection Data, *Tectonics*, **5** (2), 293–320, 1986.
- Crouch, J. K., Neogene Tectonic Evolution of the California Continental Borderland and Western Transverse Ranges, *Geol. Soc. Am. Bull.*, **90** (4), 338–345, 1979.
- Crouch, J. K., and J. Suppe, Late Cenozoic Tectonic Evolution of the Los-Angeles Basin and Inner California Borderland—a Model for Core Complex Like Crustal Extension, *Geol. Soc. Am. Bull.*, **105** (11), 1415–1434, 1993.
- Devoogd, B., L. Serpa, and L. Brown, Crustal Extension and Magmatic Processes—Cocorp Profiles from Death-Valley and the Rio-Grande Rift, *Geol. Soc. Am. Bull.*, **100** (10), 1550–1567, 1988.
- Dickinson, W. R., Plate tectonics and the continental margin of California, in *The Geotectonic Development of California*, Rubey Vol. **I**, ed. W. G. Ernst, Prentice-Hall Inc., Englewood Cliffs, New Jersey, pp. 1–28, 1981.
- Dickinson W. R., Kinematics of Transrotational Tectonism in the California Transverse Ranges and its contribution to cumulative slip along the San Andreas Transform system, *Geol. Soc. Am. SPECIAL PAPER*, **305**, 1–46, 1996.

- Dibblee, T. W., Areal geology of the Western Mojave Desert California, *Geology and Mineral wealth of the California Transverse Ranges*, **10**, ed. D. L. Fife and J. A. Minch, pp. 78–93, 1967.
- Dibblee, T. W., Geology of the Castaic Block, the Mountains and Hills Northwest of the San Gabriel Mountains, Southern California, in *United States Geological Survey Professional Paper*, **522**, ed. T. W. Dibblee Jr., United States Government Printing Office, Washington, 1982a.
- Dibblee, T. W., Regional geology of the Transverse Ranges Province of southern California, in *Geology and Mineral wealth of the California Transverse Ranges*, **10**, ed. D. L. Fife and J. A. Minch South Coast Geological Society, Santa Ana, pp. 7–26, 1982b
- Dibblee, T. W., Geology of the San Gabriel Mountains, Southern California, in *Geology and Mineral wealth of the California Transverse Ranges*, **10**, ed. D. L. Fife and J. A. Minch, South Coast Geological Society, Santa Ana, pp. 131–147, 1982c
- Dibblee, T. W., Geologic Map of the Oat Mountain and Canoga park (North 1/2) Quadrangles, Los Angeles County, California: Dibblee Geological Foundation Map # DF-36, 1:24000, 1992.
- Dibblee, T. W., Geologic Map of the Newhall Quadrangle, Los Angeles County, California: Dibblee Geological Foundation Map # DF-56, 1:24000, 1996.
- Dibblee, T. W., Geologic Map of the Warm Springs Mountain Quadrangle, Los Angeles County, California: Dibblee Geological Foundation Map # DF-64, 1:24000, 1997a.
- Dibblee, T. W., Geologic Map of the Green Valley Quadrangle, Los Angeles County, California: Dibblee Geological Foundation Map # DF-65, 1:24000, 1997b.
- Dokka, R. K., and T. M. Ross, Collapse of Southwestern North-America and the Evolution of Early Miocene Detachment Faults, Metamorphic Core Complexes, the Sierra-Nevada Orogen, and the San-Andreas Fault System, *Geology*, **23** (12), 1075–1078, 1995.
- Dokka, R. K., and K. Y. Macaluso, Topographic effects of the Eastern California Shear Zone in the Mojave Desert, *J. Geophys. Res.*, **106** (B12), 30,625–30,644, 2001.

- Ehlig, P. L., Origin and Tectonic history of the basement terrane of the San Gabriel Mountains, Central Transverse Ranges, in *The Geotectonic Development of California*, Rubey Vol. I, pp. 253–283, ed. W. G. Ernst, Prentice-Hall, Englewood Cliffs, New Jersey, 1981
- Fliedner, M. M., S. Ruppert, P. E. Malin, S. K. Park, G. Jiracek, R. A. Phinney, J. B. Saleeby, B. Wernicke, R. Clayton, R. Keller, K. Miller, C. Jones, J. H. Luetgert, W. D. Mooney, H. Oliver, S. L. Klemperer, and G. A. Thompson, Three-dimensional crustal structure of the southern Sierra Nevada from seismic fan profiles and gravity modeling, *Geology*, **24** (4), 367–370, 1996.
- Fliedner, M. M., S. L. Klemperer, and N. I. Christensen, Three-dimensional seismic model of the Sierra Nevada arc, California, and its implications for crustal and upper mantle composition, *J. Geophys. Res.*, bf 105 (B5), 10,899–10,921, 2000.
- Fuis, G. S., T. Ryberg, N. J. Godfrey, D. A. Okaya, and J. M. Murphy, Crustal structure and tectonics from the Los Angeles basin to the Mojave Desert, southern California, *Geology*, **29** (1), 15–18, 2001.
- George, P. G., and R. K. Dokka, Major Late Cretaceous Cooling Events in the Eastern Peninsular Ranges, California, and Their Implications for Cordilleran Tectonics, *Geol. Soc. Am. Bull.*, **106** (7), 903–914, 1994.
- Godfrey, N. J., G. S. Fuis, V. Langenheim, D. A. Okaya, and T. M. Brocher, Lower crustal deformation beneath the central Transverse Ranges, southern California: Results from the Los Angeles Region Seismic Experiment, *J. Geophys. Res.*, **107** (B7), 2002.
- Hadley, D., Geophysical Investigations of the Structure and Tectonics of Southern California, PhD thesis, California Institute of Technology, Pasadena, 1978.
- Hadley, D., and H. Kanamori, Seismic Structure of Transverse Ranges, California, *Geol. Soc. Am. Bull.*, **88** (10), 1469–1478, 1977.
- Hadley, D., and H. Kanamori, Regional S-Wave Structure for Southern-California from the Analysis of Teleseismic Rayleigh-Waves, *Geophys. J. Roy. Astr. Soc.*, **58** (3), 655–666, 1979.

- Hafner, K., R. W. Clayton, and E. Hauksson, Mid and lower-crustal structure beneath the San Gabriel Mountains, CA (LARSE), *Eos Trans. AGU*, bf 77 (46), Fall Meet. Suppl., F738, 1996.
- Hauksson, E., and J. S. Haase, Three-dimensional V-P and V-P/V-S velocity models of the Los Angeles basin and central Transverse Ranges, California, *J. Geophys. Res.*, **102** (B3), 5423–5453, 1997.
- Hauksson, E., Crustal structure and seismicity distribution adjacent to the Pacific and North America plate boundary in southern California, *J. Geophys. Res.*, **105** (B6), 13,875–13,903, 2000.
- Hauge, T. A., R. W. Allmendinger, C. Caruso, E. C. Hauser, S. L. Klemperer, S. Opdyke, C. J. Potter, W. Sanford, L. Brown, S. Kaufman, and J. Oliver, Crustal Structure of Western Nevada from Cocorp Deep Seismic-Reflection Data, *Geol. Soc. Am. Bull.*, **98** (3), 320–329, 1987.
- Hauser, E., C. Potter, T. Hauge, S. Burgess, S. Burtch, J. Mutschler, R. Allmendinger, L. Brown, S. Kaufman, and J. Oliver, Crustal Structure of Eastern Nevada from Cocorp Deep Seismic-Reflection Data, *Geol. Soc. Am. Bull.*, **99** (6), 833–844, 1987.
- Hearn, T. M., Pn Travel-Times in Southern-California, *J. Geophys. Res.*, **89** (NB3), 1843–1855, 1984.
- Hearn, T. M., and R. W. Clayton, Lateral Velocity Variations in Southern California .1. Results for the Upper Crust from Pg Waves, *Bull. Seismo. Soc. Am.*, **76** (2), 495–509, 1986a.
- Hearn, T. M., and R. W. Clayton, Lateral Velocity Variations in Southern California .2. Results for the Lower Crust from Pn Waves, *Bull. Seismo. Soc. Am.*, **76** (2), 511–520, 1986b.
- Hearn, E. H., and E. D. Humphreys, Kinematics of the southern Walker Lane Belt and motion of the Sierra Nevada block, California, *J. Geophys. Res.*, **103** (B11), 27,033–27,049, 1998.
- Hendrix, E. D., and R. V. Ingersoll, Tectonics and Alluvial Sedimentation of the Upper Oligocene Lower Miocene Vasquez Formation, Soledad Basin, Southern-California, *Geol. Soc. Am. Bull.*, **98** (6), 647–663, 1987.

- Hornafius, J. S., B. P. Luyendyk, R. R. Terres, and M. J. Kamerling, Timing and Extent of Neogene Tectonic Rotation in the Western Transverse Ranges, California, *Geol. Soc. Am. Bull.*, **97**, (12), 1476–1487, 1986.
- Hjorleifsdottir, V., and Helmberger D, Velocity variations in the lower crust beneath the Mojave Desert, oral project at California Institute of Technology, 2001.
- Houseman, G. A., E. A. Neil, and M. D. Kohler, Lithospheric instability beneath the Transverse Ranges of California, *J. Geophys. Res.*, **105** (B7), 16,237–16,250, 2000.
- Humphreys, E., R. W. Clayton, and B. H. Hager, A Tomographic Image of Mantle Structure beneath Southern California, *Geophys. Res Lett.*, **11** (7), 625–627, 1984.
- Humphreys, E. D., and R. W. Clayton, Tomographic Image of the Southern California Mantle, *J. Geophys. Res. and Planets*, **95** (B12), 19,725–19,746, 1990.
- Humphreys, E. D., and B. H. Hager, A Kinematic Model for the Late Cenozoic Development of Southern California Crust and Upper Mantle, *J. Geophys. Res. and Planets*, **95** (B12), 19747–19762, 1990.
- Humphreys, E.D., Postlaramide Removal of the Farallon Slab, Western United-States, *Geology*, **23** (11), 987–990, 1995.
- Ichinose, G., S. Day, H. Magistrale, T. Prush, F. Vernon, and A. Edelman, Crustal thickness variations beneath the peninsular ranges, southern California, *Geophys. Res Lett.*, **23** (22), 3095–3098, 1996.
- Ingersoll, R. V., and P. E. Rumelhart, Three-stage evolution of the Los Angeles basin, southern California, *Geology*, **27**, 593–596, 1999.
- Jacobson, C. E., F. R. Oyarzabal, and G. B. Haxel, Subduction and exhumation of the Pelona-Orocopia-Rand schists, southern California, *Geology*, **24** (6), 547–550, 1996.
- Jacobson, C.E., Metamorphic convergence of the upper and lower plates of the Vincent thrust, San Gabriel Mountains, southern California, USA, *Journal of Metamorphic Geology*, **15** (1), 155–165, 1997.

- Jennings, C. W., and J. S. George, 1994, Fault activity map of California and adjacent areas, with locations and ages of recent volcanic eruptions, scale 1:750 000, California Dept. of Conservation, Division of Mines and Geology, Sacramento, California, USA.
- Jennings, C. W., 1975, Fault map of California with locations of volcanoes, thermal springs, and thermal wells, California Division of Mines and Geology, Sacramento, California, USA.
- Jones, C. H., H. Kanamori, and S. W. Roecker, Missing Roots and Mantle Drips—Regional P(N) and Teleseismic Arrival Times in the Southern Sierra-Nevada and Vicinity, California, *J. Geophys. Res.*, **99** (B3), 4567–4601, 1994.
- Jones, C. H., Is Extension in Death-Valley Accommodated by Thinning of the Mantle Lithosphere beneath the Sierra-Nevada, California, *Tectonics*, **6** (4), 449–473, 1987.
- Jones, C. H., and R. A. Phinney, Seismic structure of the lithosphere from teleseismic converted arrivals observed at small arrays in the southern Sierra Nevada and vicinity, California, *J. Geophys. Res.*, **103** (B5), 10,065–10,090, 1998.
- Kaufman, P. S., and L. H. Royden, Lower Crustal Flow in an Extensional Setting—Constraints from the Halloran Hills Region, Eastern Mojave Desert, California, *J. Geophys. Res.*, **99** (B8), 15,723–15,739, 1994.
- Kikuchi, M., and H. Kanamori, Inversion of complex body waves, *Bull. Seismo. Soc. Am.*, **72**(2) 491–506, 1982
- Klemperer, S. L., T. A., Hauge, E. C. Hauser, J. E. Oliver, C. J. Potter The Moho in the Northern Basin and Range Province, Nevada, Along the Cocorp 40-Degree-N Seismic-Reflection Transect, *Geol. Soc. Am. Bull.*, **97** (5), 603–618, 1986.
- Kohler, M. D., P. M. Davis, H. Liu, M. Benthien, S. Gao, G. S. Fuis, R. W. Clayton, D. Okaya, and J. Mori., Data Report for the 1993 Los Angeles Region Seismic Experiment (LARSE93), Southern California: A Passive Study from Seal Beach Northeastward through the Mojave Desert, *USGS Open File Report* 96–85, 1996.
- Kohler, M. D., and P. M. Davis, Crustal thickness variations in southern California from Los Angeles Region Seismic Experiment passive phase teleseismic travel times, *Bull. Seismo. Soc. Am.*, **87** (5), 1330–1344, 1997.

- Kohler, M. D., Lithospheric deformation beneath the San Gabriel Mountains in the southern California Transverse Ranges, *J. Geophys. Res.*, **104** (B7), 15,025–15,041, 1999.
- Langenheim, V. E., Gravity and aeromagnetic models along the Los Angeles region seismic experiment (LARSE I), California, *USGS Open File Report*, 99-388, 1999.
- Langston, C. A., Effect of Planar Dipping Structure on Source and Receiver Responses for Constant Ray Parameter, *Bull. Seismo. Soc. Am.*, **67** (4), 1029–1050, 1977.
- Langston, C. A., Scattering of Teleseismic Body Waves under Pasadena, California, *J. Geophys. Res. and Planets*, **94** (B2), 1935–1951, 1989.
- Lewis, J. L., S. M. Day, H. Magistrale, J. Eakins, and F. Vernon, Regional crustal thickness variations of the Peninsular Ranges, southern California, *Geology*, **28** (4), 303–306, 2000.
- Lewis, J. L., S. M. Day, H. Magistrale, R. R. Castro, L. Astiz, C. Rebollar, J. Eakins, F. L. Vernon, and J. N. Brune, Crustal thickness of the peninsular ranges and gulf extensional province in the Californias, *J. Geophys. Res.*, **106** (B7), 13,599–13,611, 2001.
- Li, Y. G., T. L. Henyey, and P. C. Leary, Seismic-Reflection Constraints on the Structure of the Crust beneath the San-Bernardino Mountains, Transverse Ranges, Southern California, *J. Geophys. Res.*, **97** (B6), 8817–8830, 1992.
- Ligorria, J. P., and C. J. Ammon, Iterative deconvolution and receiver-function estimation, *Bull. Seismo. Soc. Am.*, **89** (5), 1395–1400, 1999.
- Lutter, W. J., G. S. Fuis, C. H. Thurber, and J. Murphy, Tomographic images of the upper crust from the Los Angeles basin to the Mojave Desert, California: Results from the Los Angeles Region Seismic Experiment, *J. Geophys. Res.*, **104** (B11), 25,543–25,565, 1999.
- Luyendyk, B. P., M. Kamerling, and R. Terres, Geometric model for Neogene crustal rotations in southern California, *Geol. Soc. Am. Bull.*, **91**, 211–217, 1980.
- Luyendyk, B. P., A Model for Neogene Crustal Rotations, Transtension, and Transpression in Southern California, *Geol. Soc. Am. Bull.*, **103** (11), 1528–1536, 1991.

- Magistrale, H., H. Kanamori, and C. Jones, Forward and Inverse 3-Dimensional P-Wave Velocity Models of the Southern California Crust, *J. Geophys. Res.*, **97** (B10), 14,115–14,135, 1992.
- Malin, P. E., E. D. Goodman, T. L. Henyey, Y. G. Li, D. A. Okaya, and J. B. Saleeby, Significance of Seismic Reflections beneath a Tilted Exposure of Deep Continental-Crust, Tehachapi Mountains, California, *J. Geophys. Res.*, **100** (B2), 2069–2087, 1995.
- Muehlberger W. R. and H. S. Hill, Geology of the Central Sierra Pelona, Los Angeles County, California, *Am. Jour. Sci.*, **256** (9), 631–643, 1958.
- Nicholson, C., C. C. Sorlien, T. Atwater, J. C. Crowell, and B. P. Luyendyk, Microplate Capture, Rotation of the Western Transverse Ranges, and Initiation of the San Andreas Transform as a Low-Angle Fault System, *Geology*, **22** (6), 491–495, 1994.
- Owens, T. J., and G. Zandt, The Response of the Continental Crust-Mantle Boundary Observed on Broad-Band Teleseismic Receiver Functions, *Geophys Res Lett.*, **12** (10), 705–708, 1985.
- Pellerin, C. L. M., and N. I. Christensen, Interpretation of crustal seismic velocities in the San Gabriel-Mojave region, southern California, *Tectonophysics*, **286** (1-4), 253–271, 1998.
- Peng, X. H., and E. D. Humphreys, Moho dip and crustal anisotropy in northwestern Nevada from teleseismic receiver functions, *Bull. Seismo. Soc. Am.*, **87** (3), 745–754, 1997.
- Raikes, S. A., Regional Variations in Upper Mantle Structure beneath Southern-California, *Geophys. Journ. Roy. Astr. Soc.*, **63** (1), 187–216, 1980.
- Richards-Dinger, K. B., and P. M. Shearer, Estimating crustal thickness in southern California by stacking PmP arrivals, *J. Geophys. Res.*, **102** (B7), 15,211–15,224, 1997.
- Royden, L., Coupling and decoupling of crust and mantle in convergent orogens: Implications for strain partitioning in the crust, *J. Geophys. Res.*, **101** (B8), 17,679–17,705, 1996.
- Ryberg, T., and G. S. Fuis, The San Gabriel mountains bright reflective zone: possible evidence of young mid-crustal thrust faulting in southern California, *Tectonophysics*, **286** (1-4), 31–46, 1998.

- Saleeby, J., Segmentation of the Laramide Slab—evidence from the southern Sierra Nevada region, *Geol. Soc. Am. Bull.*, **115** (6), 655–668, 2003.
- Savage MK, Lower crustal anisotropy or dipping boundaries? Effects on receiver functions and a case study in New Zealand, *J. Geophys. R.*, **103** (B7), 15,069–15,087, 1998.
- Schulte-Pelkum, V., G. Monsalve, A. Sheehan, M.R. Pandey, S. Sapkota, R. Bilham, and F. Wu, Imaging the Indian subcontinent beneath the Himalaya, *Nature*, **435** (7046), 1222–1225, 2005.
- Serpa, L., B. Devoogd, L. Wright, J. Willemin, J. Oliver, E. Hauser, and B. Troxel, Structure of the Central Death-Valley Pull-Apart Basin and Vicinity from Cocorp Profiles in the Southern Great-Basin, *Geol. Soc. Am. Bull.*, **100** (9), 1437–1450, 1988.
- Snow, J. K., and B. P. Wernicke, Cenozoic tectonism in the central basin and range: Magnitude, rate, and distribution of upper crustal strain, *Amer. J. Sci.*, **300** (9), 659–719, 2000.
- Wang, K., T. Plank, J. D. Walker, and E. I. Smith, A mantle melting profile across the basin and range, SWUSA, *J. Geophys. Res.*, **107** (B1), 2002.
- Weldon, R., and E. Humphreys, A Kinematic Model of Southern California, *Tectonics*, **5** (1), 33–48, 1986.
- Wernicke, B., R. Clayton, M. Ducea, C. H. Jones, S. Park, S. Ruppert, J. Saleeby, J. K. Snow, L. Squires, M. Flidner, G. Jiracek, R. Keller, S. Klemperer, J. Luetgert, P. Malin, K. Miller, W. Mooney, H. Oliver, and R. Phinney, Origin of high mountains in the continents: The southern Sierra Nevada, *Science*, **271** (5246), 190–193, 1996.
- Wernicke B. and G. J. Axen, On the role of Isostasy in the Evolution of Normal-Fault Systems, *Geology*, **17** (9), 848–851, 1988.
- Wooley R. J. and V. E. Langenheim, Gravity data along LARSE (Los Angeles Region Seismic Experiment) II, Southern California, *USGS Open File Report*, 01-375, 2001.
- Wright, T. L., Structural Geology and tectonic evaluation of the Los Angeles basin, California, in *Active Margin Basins*, pp.35–134, ed. K. E. Biddle, *AAPG Mem.* **52**, 1991.

- Yan, Z. M., R. W. Clayton, and J. Saleeby, Seismic refraction evidence for steep faults cutting highly attenuated continental basement in the central Transverse ranges, California, *Geophys. J. Int.*, **160** (2), 651–666, 2005.
- Zandt, G., H. Gilbert, T. J. Owens, M. Ducea, J. Saleeby, and C. H. Jones, Active foundering of a continental arc root beneath the southern Sierra Nevada in California, *Nature*, **431** (7004), 41–46, 2004.
- Zhao, D. P., H. Kanamori, and E. Humphreys, Simultaneous inversion of local and teleseismic data for the crust and mantle structure of southern California, *Physics of the Earth and Planetary Interiors*, **93** (3-4), 191–214, 1996.
- Zhu, L. P., Crustal structure across the San Andreas Fault, southern California from teleseismic converted waves, *Earth and Planet. Sci. Lett.*, **179** (1), 183–190, 2000.
- Zhu, L. P., and H. Kanamori, Moho depth variation in southern California from teleseismic receiver functions, *J. Geophys. Res.*, **105** (B2), 2969–2980, 2000.
- Zhu, L. P., Deformation in the lower crust and downward extent of the San Andreas Fault as revealed by teleseismic waveforms, *Earth Planets and Space*, **54** (11), 1005–1010, 2002.